Study of structured catalysts for post-treatment of syngas produced by dried-wood gasification

Dolores Jurado Fuentes

UNIVERSITÉ DE STRASBOURG

ÉCOLE DOCTORALE DES SCIENCES CHIMIQUES

Institut de Chimie et Procédés pour l'Energie, l'Environnement et la Santé

THÈSE présentée par :

Dolores JURADO FUENTES

soutenue le : 18 décembre 2020

pour obtenir le grade de : Docteur de l'université de Strasbourg

Discipline/ Spécialité : Chimie/Catalyse hétérogène

Etude de catalyseurs structurés pour le post-traitement du gaz de synthèse issu de la gazéification de bois pressé

THÈSE dirigée par :

Mme ROGER Anne-Cécile	Professeur, Université de Strasbourg (ICPEES)
Mr THOMAS Sébastien	Maître de Conférences, Université de Strasbourg (ICPEES)

RAPPORTEURS :

Mr MONTES RAMÍREZ Mario	Professeur, Université du Pays Basque
Mr PHAM MING Doan	Docteur, IMT Mines Albi (Centre RAPSODEE)

AUTRES MEMBRES DU JURY :

Mme ROMERO SARRIA Francisca	Maître de Conférences, Université de Séville
Mme TSCHAMBER Valérie	Professeur, Université de Haute-Alsace (LGRE)

Acknowledgement

Como no podía ser de otra manera, empezaré agradeciendo a mis dos co-tutores de tesis, Profesora Anne-Cécile ROGER y Dr Sébastien THOMAS. Gracias por apostar por mí para este proyecto. Gracias a vosotros he tenido la oportunidad de crecer profesionalmente, pero, sobre todo, personalmente. Muchísimas gracias por vuestra dedicación y paciencia, que han hecho que mi trabajo fuese más ameno. Sinceramente, creo que he sido afortunada de haber tenido la oportunidad de trabajar mano a mano con dos maravillosas personas como vosotros. Gracias por la complicidad y por vuestra confianza. Siempre estaré abierta a una segunda visita (y colaboración) a la ciudad que me ha robado un pedacito de mi corazón, Estrasburgo.

Muchísimas gracias a los miembros del proyecto EBIPREP por cada reunión e intercambio de resultados que me ha permitido aprender mucho sobre distintas disciplinas científicas, aparte de catálisis. Gracias al team leader del proyecto, Profesor Andrea Wilke, por sus consejos post-defensa de tesis y por su eterna sonrisa en cada reunión.

Por supuesto, este trabajo de tesis jamás podría haberse llevado a cabo sin el gran maravilloso equipo que hay detrás. Muchísimas gracias a Clémence y Ksenia por su gran ayuda en cada problema técnico y a Benoît por su energía y alegría. A mis compañeros. Gracias a Valentin por ser el compañero de despacho más enrollado que podía tener, por tu ayuda en el laboratorio y como no, por tu maravillosa cerveza. Me gustaría agradecer a Isabelle, con la que coincidí durante unos meses. No me he reído más en mi vida que con Isabelle y sus bailes. No me podía olvidar de Andrea, buen científico, mejor persona. Increíble como una persona que conoces de poco tiempo puede llegar a ser un gran amigo. Andrea, gracias por aguantar mis agobios, mis dudas e inquietudes y un largo etc. Muchísimas gracias a Rogeria, Renata, Quianwen, Arno… por hacer mi estancia en el laboratorio bastante amena.

Millones de gracias a Cristina. Compañera de aventuras. Si esta tesis está terminada en cierto modo es gracias a ti. Sin duda alguna eres una de las personas que ha marcado mi experiencia en Estrasburgo. Muchísimas gracias por tu apoyo, por creer en mí incluso más que yo en mí misma, por las tonterías en el laboratorio y por cada cerveza fuera de él (con sus reflexiones incluidas). Gracias por ayudarme en mi crecimiento personal y aportar a mi propio autoconocimiento. Sin ti Estrasburgo no hubiese sido lo mismo. Espero que algún día nos volvamos a ver, bien sea haciendo ciencia o en la barra de un bar en

Cádiz. Ha sido un placer tenerte en mi vida. Te mereces lo mejor. ¡Ah! Y gracias por la música.

Muchísimas gracias al personal técnico del ICPEES, en particular a Christopher SUTTER, Christopher MELART y Dra. Vasiliki PAPAEFTHYMIOU por vuestra disposición y especialmente a Dr. Thierry DINTZER por amenizar las sesiones de microscopía hablándome de música, cámaras o de bicicletas. Cuando llegué no me respondías ni un mail y tres años después conseguí, no solo que me respondieras, sino que lo hicieras en español. Muchas gracias por tu paciencia, con personas como tú trabajar es muy fácil.

Me gustaría agradecer a todas esas personas que me han hecho mi estancia en Estrasburgo más agradable y divertida fuera de mi ámbito laboral. Entre ellos, Adri, muchísimas gracias por esa energía tan positiva que siempre desprendes y por tu forma de ver la VIDA. Elenia, eres especial, mi salvavidas de Estrasburgo. Bendita formación transversal que te puso en mi camino (para algo que hace bien el ecole doctorale…). Por desgracia para ti, siempre estarás en mi vida. Por último, a Matteo. Valor tuviste al decidir compartir piso conmigo en el periodo más complicado de mi tesis… Mil gracias por por tus comidas/cenas y tus tonterías que hacían mucho más liviana mi escritura.

Volviendo a mis orígenes, no me podré olvidar jamás de esa conversación en Reina Mercedes (Sevilla) en julio 2017 con Dra Francisca Romero-Sarria y el Profesor José Antonio Odriozola. Muchísimas gracias por vuestro empujón, sin él no hubiese disfrutado de esta experiencia. Sin olvidarme de la primera persona que apostó por mí. Nuría, muchisisisimas gracias por todo. Vale muchísimo como profesional y como persona.

No menos importante, mi familia y amigos que en la distancia siempre me han acompañado en este camino. Muchísimas gracias por vuestra fe ciega en mí, por apoyarme en todo lo que me proponía y me propongo. A mi prima, amiga, hermana Julia, mil gracias por tu paciencia y por siempre estar, eres única.

A mi Javi, mi compañero de vida. Muchísimas gracias por la lucha. Los dos sabemos que no ha sido fácil. Gracias por tu paciencia, tu templanza y por seguirme en cada locura. Gracias por tu confianza y por apostar por nosotros. Tu apoyo incondicional es fundamental, ya lo sabes. Seguimos remando.

Bienvenidos a mi tesis. Detrás de estas páginas hay mucha ciencia y algo de crecimiento personal.

Como dice Coldplay en una de sus canciones: “*Nobody said it was easy”*

Thesis content

List of figures

List of schemes

List of tables

RÉSUMÉ

Chapitre 1. *Introduction générale*

Au cours des dernières années, la production d'énergie à partir de la biomasse s'est développée en raison de son intérêt pour la préservation de l'environnement. En effet, elle permet de produire des biocarburants tout en réduisant les émissions de CO_2 [1]. Dans cette optique, le projet Interreg EBIPREP propose l'utilisation complète de la biomasse bois comme vecteur d'énergie renouvelable par deux procédés connectés : la production de biogaz et le procédé de gazéification thermique. Le premier procédé est cinétiquement lent et moins adapté aux matières premières lignocellulosiques, tandis que le second produit un gaz de synthèse de qualité altérée par la génération de composés organiques lourds appelés goudrons. Dans ce projet, les deux sous-procédés individuels sont combinés pour augmenter de manière significative l'efficacité globale par rapport aux procédés individuels.

L'objectif de la thèse est un des objectifs partiels du projet. Elle a pour but le développement d'un système catalytique pour la réduction des goudrons produits lors de la gazéification de la biomasse afin de générer un gaz de synthèse de haute qualité et d'éviter les inconvénients opérationnels causés par leur condensation dans les turbines et les lignes, en aval du réacteur de gazéification. Il a été largement démontré que les catalyseurs à base de nickel permettent de réformer les goudrons et de produire un gaz de synthèse de meilleure qualité. Néanmoins, ces types de systèmes catalytiques sont bien connus pour leur désactivation rapide par dépôt de carbone et frittage [2,3]. Dans ce travail, afin d'améliorer la gazéification du carbone et, par conséquent, la stabilité catalytique, trois oxydes mixtes différents à haute mobilité d'oxygène ($Ce_2Y_2O_7$ noté CY, $Ce_{0.63}Zr_{0.33}Sm_{0.04}O_2$ noté CZS et $La_{0.6}Sr_{0.4}Co_{0.2}Fe_{0.8}O_{3-\delta}$ noté LSCF) ont été préparés par une méthode pseudo sol-gel et ont été utilisés comme supports pour les catalyseurs à base de nickel. Outre l'étude du rôle du support catalytique dans le vaporeformage des goudrons, l'effet de la voie d'addition du Ni a également été étudié. L'activité des systèmes catalytiques en poudre a été testée en utilisant différentes molécules modèles de goudron, avec une composition molaire typique de gaz de synthèse ex-biomasse.

Chapitre 2. *Synthèse et caractérisation des systèmes catalytiques*

Une charge de Ni de 10 % en masse a été ajoutée par deux méthodes différentes conduisant à six systèmes catalytiques différents : ***(1)*** imprégnation humide de supports calcinés (Ni/CY, Ni/CZS et Ni/LSCF) ou ***(2)*** insertion directe au cours de la synthèse sol-gel (Ni-CY, Ni-CZS et Ni-LSCF). Les supports et les catalyseurs qui en résultent ont été

caractérisés par XRD (diffraction des rayons X), physisorption de N_2, H_2-TPR (réduction en température programmée), H_2-TPD (désorption d'H_2 en température programmée) et XPS (spectroscopie des photoélectrons X).

Les résultats des principales caractérisations des systèmes catalytiques synthétisés sont résumés dans le **tableau 1**. En général, la surface spécifique (SSA) est faible, en raison de la température de calcination élevée utilisée et varie de 10 à 22 $m^2\ g^{-1}$. Pour ce qui est de l'influence de la méthode d'addition du Ni sur les supports, on peut clairement distinguer deux tendances dans la SSA. Les catalyseurs à base de CY et de LSCF préparés par imprégnation au Ni (Ni/CY et Ni/LSCF) présentent une SSA plus élevée que les catalyseurs sol-gel respectifs (Ni-CY et Ni-LSCF), alors que l'effet inverse est observé pour les catalyseurs à base de CZS. La porosité peut être associée à la porosité interparticulaire en raison des faibles valeurs de volume poreux obtenues pour tous les matériaux. Une taille de particules de support oxyde similaire ($d_{support}$) a été déterminée pour tous les solides dans chaque système, quelle que soit la voie d'addition du Ni utilisée. Les tailles de particules des cristallites CZS, CY et LSCF sont respectivement d'environ 8-9 nm, 20-23 nm et 14-17 nm, alors qu'aucun lien avec la SSA ne peut être remarqué. En ce qui concerne la taille des particules des cristallites de NiO (d_{NiO}), une valeur légèrement plus faible a été obtenue pour le catalyseur sol-gel Ni-CZS (19 nm) par rapport au système Ni/CZS imprégné (24 nm), alors que l'inverse a été noté dans les catalyseurs CY, où le catalyseur Ni/CY imprégné présente la valeur de d_{NiO} la plus faible (8 nm) de tous les catalyseurs. Une taille de particules de 26 nm a été obtenue pour la phase NiO pour le catalyseur sol-gel Ni-LSCF, ce qui donne la valeur la plus élevée de tous les systèmes préparés. En ce qui concerne les paramètres de maille des supports oxydes, une diminution a été clairement constatée pour les matériaux sol-gel par rapport aux matériaux imprégnés équivalents. Ceci prouve l'existence de cations nickel partiellement insérés dans les structures d'oxydes mixtes (CZS, CY et LSCF) au sein des catalyseurs sol-gel, puisque les rayons ioniques de ces espèces sont inférieurs à ceux de Zr^{4+}, Y^{3+} et Fe^{3+}/Co^{3+} dans les mêmes coordinences (0.56 Å pour Ni^{3+} et 0.69 Å pour Ni^{2+}) [4]. Pour des raisons stériques, l'insertion d'ions Ni^{2+} est plus favorable. En outre, une amélioration remarquable de la réductibilité du support pour les catalyseurs sol-gel, pouvant être liée à la présence d'espèces partielles de Ni^{2+} dans les structures d'oxydes mixtes, est observée.

	SSA* ($m^2 \cdot g^{-1}$)	V_{pore} * ($cm^3 \cdot g^{-1}$)	$d_{support}$ ¥ (nm)	d_{NiO} ¥ (nm)	$a_{support}$ ¥ (Å)	Réductibilité du support± (%)
Ni/CY	22	0,18	23	8	5,387	30
Ni/CZS	15	0,05	8	24	5,314	60
Ni/LSCF	14	0,06	17	-	3,871	54
Ni-CY	12	0.09	20	14	5,381	35
Ni-CZS	22	0.08	9	19	5,301	86
Ni-LSCF	10	0.03	14	26	3,865	72

*obtenue par physisorption de N_2

¥calculés à partir des résultats DRX

±estimé partir de la consommation de H_2 des analyses TPR

Tableau 1. *Propriétés structurales et texturales des catalyseurs.*

Chapitre 3. *Conditions de prétraitement et tests catalytiques : catalyseurs en poudre*

L'activité des systèmes catalytiques en poudre a été testée en utilisant deux différentes molécules modèles de goudron, phénol et toluène, avec une composition molaire typique de gaz de synthèse ex-biomasse (2 % CH_4, 10 % H_2O, 12 % CO_2, 16 % H_2 et 20 % CO, complété par N_2). ***Le tableau 2*** montre les conditions spécifiques des différents tests catalytiques utilisées à l'échelle du laboratoire. Il est à souligner que la composition des gaz d'entrée a été choisie en fonction des conditions réelles de l'installation pilote de gazéification de biomasse, alors que la concentration d'entrée de goudron utilisée dans ce travail était plus élevée puisqu'ils ont été injectés un par un (voir ***tableau 2***). Les essais d'activité catalytique ont été réalisés dans des conditions isothermes à 400 ºC et/ou 550 ºC pendant 6 h.

	Laboratoire				Unité pilote		Rapport des teneurs
	$WHSV_{gaz}$ (h^{-1})	$WHSV_{goudron,\ Ni^0}$ (h^{-1})	H_2O/ $C_{goudron}$	Teneur en entrée ($g \cdot Nm^{-3}$)	$WHSV_{gaz}$ (h^{-1})	Teneur en entrée ($g \cdot Nm^{-3}$)	Labo/ pilote
Phénol	370	14	16,5	4,0	200-400	0,090	44
Toluène	370	26	7,7	13,4	200-400	0,350	40

Tableau 2. Résumé des conditions des tests catalytiques à l'échelle du laboratoire et comparaison avec les conditions des tests à l'échelle pilote

Avant l'évaluation des propriétés catalytiques, un prétraitement réducteur doit être effectué afin de générer des espèces de Ni^0 qui sont la phase active en vaporeformage des goudrons. Ainsi, deux conditions de prétraitement différentes ont été étudiées : (i) sous un

mélange H_2/N_2 et (ii) sous un mélange de gaz de synthèse (2 % CH_4, 10 % H_2O, 12 % CO_2, 16 % H_2 et 20 % CO, complété par N_2).

(i) Prétraitement sous un mélange H_2/N_2

La conversion du goudron et la sélectivité en carbone de surface pour les différents systèmes catalytiques sont reportées dans la ***figure 1***. Tout d'abord, l'effet de la température sur l'élimination des goudrons a été étudié pour le reformage du phénol (***figure 1 (a)***). Comme prévu, une augmentation de l'activité catalytique pour la conversion du phénol avec une augmentation de la température de la réaction a été mise en évidence. En outre, la sélectivité en carbone déposé tend à être moins élevée pour la plupart des catalyseurs à 550 ºC par rapport à 400 ºC en raison de la lente cinétique du processus de gazéification du carbone à basse température. Parmi tous les catalyseurs, Ni/CY et Ni-LSCF ont montré les meilleures performances catalytiques et le plus faible taux de dépôt de carbone dans le reformage du phénol à 550 ºC (conversion de 90 %). Suivent ensuite, les catalyseurs Ni/LSCF et Ni-CZS pour lesquels une conversion similaire a été atteinte (85 %) mais avec cependant une plus grande quantité de dépôts de carbone formée pour le matériau Ni/LSCF. Puisqu'à plus basse température la formation de carbone est favorable, induisant une désactivation catalytique rapide, l'activité catalytique en reformage du toluène n'a été évaluée qu'à 550ºC. Les résultats sont présentés dans la ***figure 1(b)***. Par rapport au reformage du phénol, une diminution de la conversion du toluène et une augmentation de la sélectivité en carbone ont été constatées pour la plupart des catalyseurs pendant le reformage du toluène. Ceci est cohérent avec les conditions sont plus sévères pour le reformage du toluène (plus forte teneur, rapport H_2O/C plus faible) que pour le phénol. Le même ordre de performance est observé en reformage du phénol et du toluène, le système Ni/CY étant le catalyseur le plus performant.

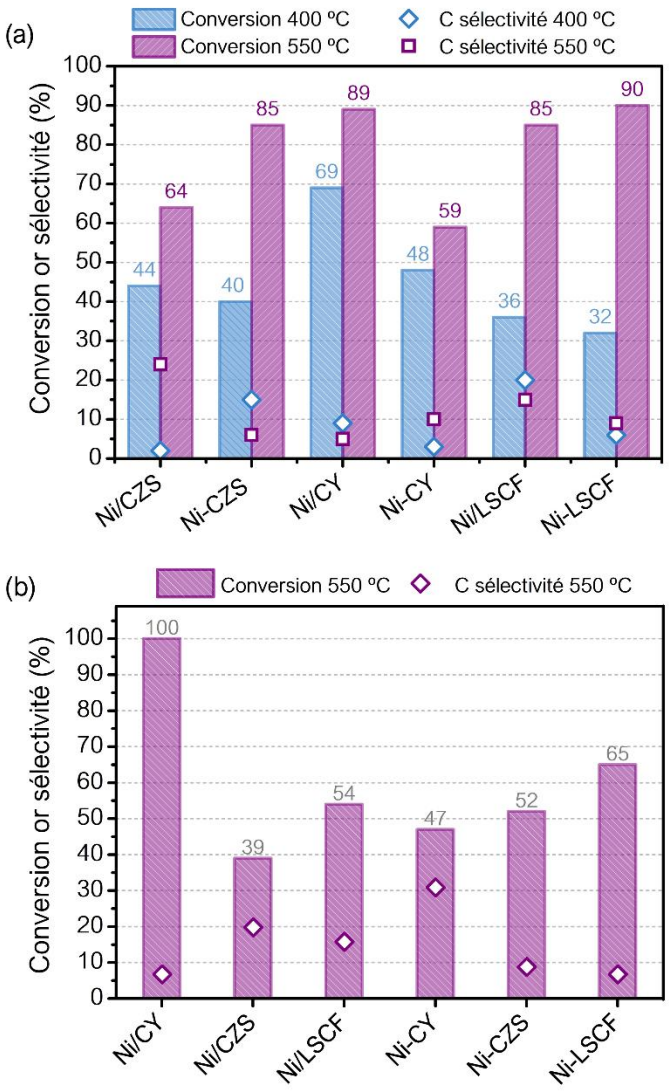

Figure 1. Conversion des goudrons et sélectivité en carbone des catalyseurs en poudre, prétraités sous atmosphère H_2/N_2 : *(a)* reformage du phénol à 400 et 550 °C et *(b)* reformage du toluène à 550 °C.

(ii) Prétraitement sous un mélange de gaz de synthèse

L'objectif de la thèse étant l'évaluation des catalyseurs à l'échelle pilote, en ligne d'un gazéifieur, donc un prétraitement de réduction *in situ* sous le mélange syngas ex-biomasse est visé.

La figure 2 montre le profil de consommation d'hydrogène des matériaux prétraités à 500 °C sous mélange de gaz de synthèse. Un pic principal situé à des températures d'environ 600 °C a été mis en évidence pour tous les matériaux, il est associé à la formation de CH_4 par réaction entre le carbone déposé à la surface et l'hydrogène (***figure 2 (a)***). En outre, des pics moins intenses peuvent également être détectés dans la plage de température comprise entre 100 et 500 °C (***figure 2 (a), encadré)***. Ces pics sont

généralement associés à la réduction de NiO en Ni^0 et les différences de température de réduction entre les catalyseurs mettent en évidence l'existence de différentes interactions Ni-support[5]. Les profils de réduction du catalyseur Ni-LSCF frais et prétraité sont similaires, la consommation de H_2 étant cependant inférieure pour le matériau prétraité (***figure 2 (b)).*** Ce fait pourrait suggérer que la réduction du NiO dans des conditions d'atmosphère de gaz de synthèse est très difficile pour ce catalyseur, contrairement aux autres échantillons à base de nickel.

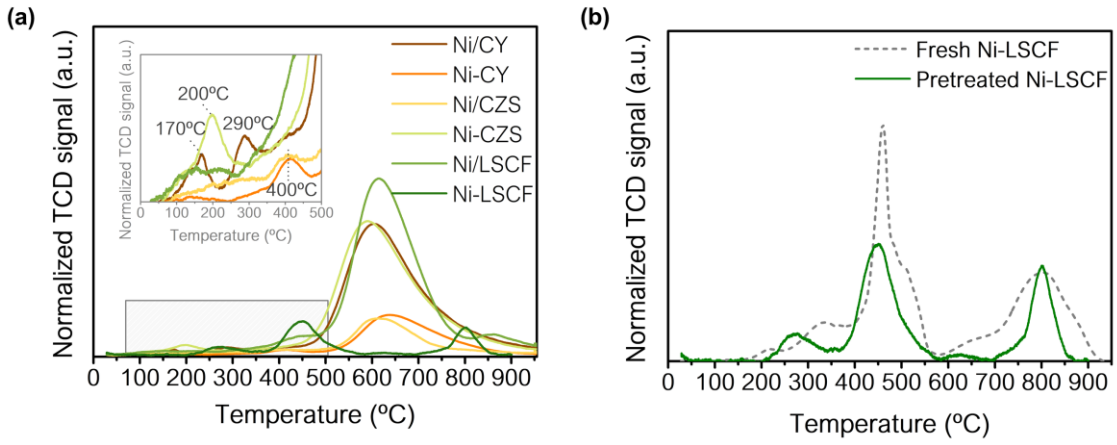

Figure 2. (a) profils de consommation d'H_2 des catalyseurs prétraités sous syngas ; (b) comparaison entre les profils de consommation d'H_2 de Ni-LSCF frais et traité sous syngas

En résumé, après un prétraitement réducteur sous H_2, les catalyseurs Ni/CY et Ni-LSCF permettent d'obtenir une meilleure activité catalytique en termes de conversion des goudrons et de sélectivité en carbone. Cependant, comme il a été mentionné précédemment, la réduction sous gaz de synthèse est difficile pour le catalyseur Ni-LSCF et la faible réduction de NiO semble être la cause de de la faible activité catalytique après activation sous syngas dans une installation pilote de gazéification. Son équivalent imprégné, le catalyseur Ni/LSCF, a conduit à une conversion des goudrons similaires mais avec une plus grande sélectivité en carbone. Il a néanmoins été choisi, avec le système Ni/CY, pour la structuration sur des extrudats de SiC afin de produire les catalyseurs pour les tests en unité pilote.

Chapitre 4. *Optimisation de la structuration catalytique par rapport aux extrudats à base de SiC et aux essais catalytiques.*

Le dépôt sur les extrudats de SiC des deux catalyseurs présentant la meilleure activité et dont la réduction sous syngas est efficace, Ni/CY et Ni/LSCF, a été optimisé afin

de produire des lits catalytiques destinés aux tests dans une installation pilote de gazéification. Des extrudats à base de SiC de formes et tailles diverses, présentés dans la ***figure 3,*** (anneaux R ou pastilles P de SiC de tailles différentes RSiC 8/5, RSiC5/3 et PSiC) a été utilisé.

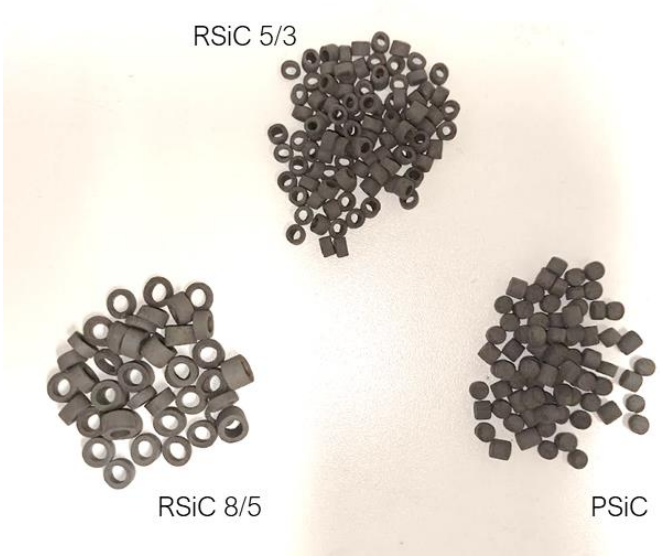

Figure 3. Extrudats à base de SiC de formes et tailles diverses

Les extrudats ont été imprégnés avec les supports, CY et LSFC, puis le dépôt de Ni a été effectué. La charge visée était de 54 $g_{support}/L_{lit}$ et 6 g_{Ni}^{0}/L_{lit}. L'influence de différents paramètres tels que la morphologie des extrudats de SiC, la concentration de la solution de précurseurs de support et la nature du solvant a été étudiée. Les résultats de cette étude pour certains de ces paramètres sont présentés dans le ***tableau 3,*** pour les deux catalyseurs.

En ce qui concerne les catalyseurs structurés Ni/LSCF, la quantité de LSCF déposée est étroitement liée à la morphologie du SiC et diminue dans l'ordre suivant : PSiC (73 g/L) > RSiC 5/3 (56 g/L) > RSiC 8/5 (47 g/L) pour deux imprégnations successives réalisées avec une solution à base d'acide propionique (0,30 M en cations) **(tableau *3)***. La même tendance est observée pour le dépôt de Ni, soulignant qu'une augmentation de la quantité de support imprégné favorisait le dépôt de Ni. Ainsi, la plus grande quantité de Ni déposée a été atteinte pour la forme PSiC (9,5 g/L). Le rapport Ni/support est proche pour les trois formes de SiC, variant de 0,13 à 0,15. Comme attendu, l'imprégnation du support à l'aide d'une solution à base d'eau, à une concentration plus élevée de 0,60 M en cations, a entraîné une augmentation de la quantité de LSCF déposée (78 g/L pour le RSiC 8/5eau contre 47 g/L pour le RSiC 8/5prop). Cependant, une quantité de Ni imprégné plus faible a été obtenue pour le RSiC 8/5eau, malgré une masse de support plus élevée. De ce fait, une

quantité de nickel/support plus faible a été obtenue pour le RSiC 8/5eau (0,06) que pour le RSiC 8/5prop (0,15).

Afin d'élucider le rôle du support dans l'activité catalytique, l'imprégnation du support CY à l'aide d'une solution aqueuse a été effectuée pour la morphologie du RSiC 8/5. L'imprégnation du support CY sur les extrudats RSiC 8/5 a été réalisée en utilisant une solution à base d'eau à 0,60 M en cations. Une masse plus faible de dépôt a été atteinte par rapport au support LSCF dans les mêmes conditions d'imprégnation, ce qui a conduit à un rapport Ni/support plus élevé (0,17 pour Ni/CY/RSiC 8/5 contre 0,06 pour Ni/LSCF/RSiC 8/5).

Par la suite, l'étude catalytique des catalyseurs structurés en reformage du toluène a été menée dans les mêmes conditions que pour les poudres, en maintenant dans tous les tests la charge de Ni^0 constante et en prétraitant sous gaz de synthèse.

	Solvant	Concentration de la solution de précurseur (M)	m_{supp}/L_{lit} (g/L) *	$m_{Ni}{}^0/ L_{lit}$ (g/L) ±	Ni^0/support
Ni/LSCF/PSiC	prop	0,30	72	9.5	0.13
Ni/LSCF/RSiC 5/3	prop	0,30	56	7.5	0.13
Ni/LSCF/RSiC 8/5	prop	0,30	47	7.2	0.15
Ni/LSCF/RSiC 8/5	eau	0,60	78	6.7	0.09
Ni/CY/RSiC 8/5	eau	0,60	45	7.7	0.17

*après deux imprégnations successives de solution de précurseur

±après deux imprégnations successives de solution 0,26 M de $Ni(NO_3)_2$

Tableau 3. Influence de la forme du SiC, du solvant et de la concentration de la solution de précurseur de support dans la préparation des catalyseurs structurés Ni/LSCF et Ni/CY.

La conversion du toluène et la sélectivité en carbone obtenues à l'échelle du laboratoire sur les catalyseurs structurés Ni/LSCF réduits en poudre sont présentées ***figure 4.*** Pour les catalyseurs obtenus par solution d'acide propionique, la conversion du toluène diminue dans l'ordre suivant : RSiC 8/5 (29 %) > RSiC 5/3 (25 %) > PSiC (21 %) et la tendance inverse est observée pour la sélectivité en carbone. Comme un rapport Ni^0/support similaire a été obtenu pour ces catalyseurs, les différences d'activité catalytique pourraient être associées à l'influence de la morphologie du SiC sur la dispersion du Ni. La morphologie du RSiC 8/5 apparait comme la plus favorable. L'utilisation de l'eau comme solvant, permettant des productions à grande échelle dans de meilleures conditions, conduit à une diminution de la conversion du toluène et à une augmentation notable de la sélectivité en carbone (RSiC $8/5_{eau}$ comparé à RSiC $8/5_{prop}$). En ce qui concerne le

catalyseur structuré Ni/CY, une conversion du toluène similaire à celle de son équivalent LSCF est obtenue (19 % Ni/CY/RSiC$_{eau}$ contre 22 % Ni/LSCF/RSiC$_{eau}$), tandis qu'une sélectivité plus faible en carbone a été constatée (10 % Ni/CY/RSiC contre 15 % Ni/LSCF/RSiC$_{eau}$).

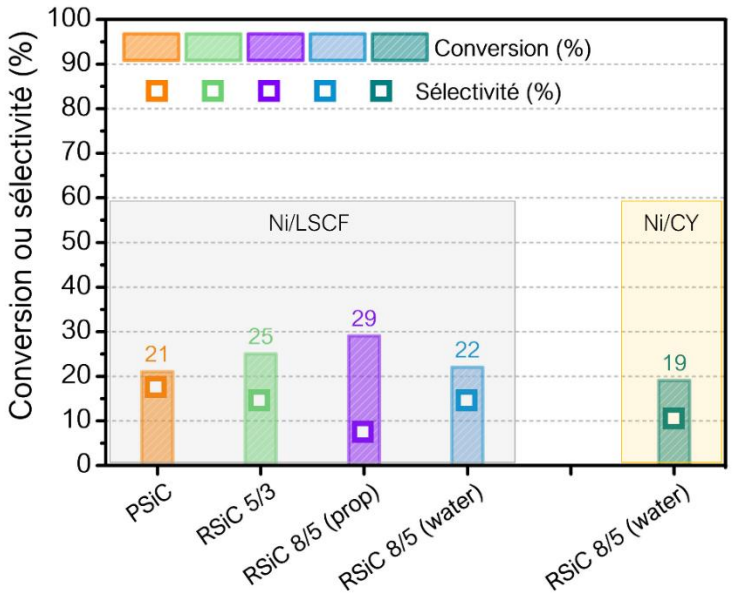

Figure 4. Conversion du toluène et sélectivité en carbone (550 ºC pendant 6h) des catalyseurs structurés prétraités sous atmosphère de gaz de synthèse

Chapitre 5. *Tests catalytiques dans l'installation pilote de gazéification de biomasse*

Sur la base des résultats catalytiques obtenus pour les catalyseurs structurés, les extrudats de morphologie RSiC 8/5 ont été utilisés pour une synthèse à plus grande échelle (1,2 L) en vue des tests en unité pilote. L'eau a été utilisé comme solvant en raison de sa faible toxicité par rapport à l'acide propionique. Puisque le système Ni/LSCF a montré des valeurs de sélectivité en carbone élevées et afin de diminuer la désactivation ainsi attendue, l'effet de l'ajout de ruthénium comme dopant de la phase métallique (1% de la masse du catalyseur contre 5 % environ pour le nickel) a été évalué. Ainsi, trois systèmes catalytiques différents ont été synthétisés et testés dans l'installation pilote de gazéification de biomasse : Ni/CY/RSiC 8/5, Ni/LSCF/RSiC 8/5 et RuNi/LSCF/RSiC 8/5.

Le tableau 4 présente les principales caractéristiques des lots synthétisés. Des performances similaires en matière de dépôt ont été constatées pour les imprégnations à grande échelle par rapport à celles effectuées à l'échelle laboratoire (voir *tableau 3*) : un rapport Ni/support plus élevé a été obtenu pour le catalyseur à base de CY. Les masses

totales de Ni° dans le lit catalytique (1,0 L) pour les différents essais dans l'unité pilote sont proches.

	Mise à l'échelle (lot de 1,2 L)				Lit catalytique dans l'unité pilote (1,0 L)		
	m_{supp}/V_{lit} (g/L)	m_{Ni^0}/V_{lit} (g/L)	Ni/support	Ni (%)	m_{totale} (g)	$m_{catalyseur}$ (g)	m_{Ni} (g)
Ni/CY/RSiC 8/5	44	6,0	0,14	12	455	40	4,8
Ni/LSCF/RSiC 5/3	79	5,0	0,06	6	508	72	4,3
RuNi/LSCF/RSiC 8/5	69	4,0	0,06	5	509	63	3,2

Tableau 4. Effet de l'augmentation d'échelle dans le dépôt de catalyseur et quantité de catalyseur utilisée dans l'essai en unité pilote

Les principales conditions des essais à l'échelle de l'usine pilote et l'efficacité catalytique des catalyseurs structurés préparés (exprimée ici par la conversion du toluène) sont résumées dans le ***tableau 5.*** Dans tous les cas les catalyseurs ont été activés par prétraitement *in situ* sous gaz de synthèse brut (issu de la gazéification en continu de copeaux de bois) à 500 ºC pendant 1h. Les goudrons ont été collectés simultanément en sortie directe du gazéifieur et dans le flux sortant du réacteur catalytique en ligne du gazéifieur, à différents temps d'opération, puis analysés.

Conformément aux résultats catalytiques à l'échelle du laboratoire, les catalyseurs Ni/CY ont montré une meilleure performance catalytique que le matériau Ni/LSCF nu (conversion de 38 % pour Ni/CY contre 4 % pour Ni/LSCF, après 1h de fonctionnement). En outre, l'ajout de Ru aux catalyseurs Ni/LSCF a largement amélioré l'efficacité de l'élimination des goudrons. En effet, la conversion du toluène la plus élevée (60 %) parmi les trois systèmes a pu être obtenue pour RuNi/LSCF. Par conséquent, l'activité catalytique de ce matériau a également été testée en utilisant une biomasse composée d'un mélange bois/résidus, résidus générés par le procédé de production de biogaz. Comme on peut l'observer, la présence de résidus dans la matière première a conduit à une teneur en goudrons du gaz de synthèse beaucoup plus élevée (1,09 $g \cdot Nm^{-3}$ comparé à 0,19 $g \cdot Nm^{-3}$) et, par conséquent, la conversion du toluène a chuté de 60 % (bois) à 24 % (bois/résidus).

	Type de biomasse	T_{cata} (ºC)	$WHSV_{gaz}$ (h^{-1})	Teneur en toluène en entrée ($g \cdot Nm^{-3}$)	Conversion du toluene (%)
Ni/CY/RSiC 8/5	Bois	510	460	0,38	38
Ni/LSCF/RSiC 5/3	Bois	532	250	0,22	4
RuNi/LSCF/RSiC 8/5	Bois	560	240	0,19	60
RuNi/LSCF/RSiC 8/5	Bois/résidus	565	60	1,09	24

Tableau 5. Activité catalytique des catalyseurs structurés à l'échelle pilote, après 1 heure de fonctionnement

Conclusion générale

De nombreuses études ont reporté l'utilisation de supports à forte mobilité d'oxygène comme alternative pour améliorer la résistance au dépôt de coke dans les catalyseurs à base de Ni. Dans cette idée, la synthèse de trois supports (CY, CZS et LSCF) a été effectuée par méthode pseudo sol-gel. La modification des propriétés physico-chimiques du support par la voie d'addition du Ni (imprégnation humide ou sol-gel en une étape) a été étudiée par plusieurs techniques de caractérisation. L'existence d'ions Ni^{2+} insérés dans la structure d'oxyde mixte du support a été mise en évidence pour les trois catalyseurs sol-gel (Ni-CY, Ni-CZS et Ni-LSCF). La présence de Ni^{2+} permet d'améliorer la réductibilité du support par rapport aux catalyseurs imprégnés équivalents. La surface spécifique la plus élevée (22 $m^2 \cdot g^{-1}$) et les particules de Ni les plus petites (8 nm) ont été obtenues pour le catalyseur Ni/CY.

La possibilité de prétraitement réducteur sous atmosphère de gaz de synthèse a été étudiée pour pouvoir être transposée à l'échelle de l'unité pilote. Comme il a été démontré, la plupart des catalyseurs peuvent être activés dans ces conditions. Seul le catalyseur Ni-LSCF n'est quasiment pas réduit par le syngas à 500 °C.

Les systèmes catalytiques en poudre ont été testés dans le reformage du phénol à deux températures de réaction (400 et 550 ºC) et en reformage du toluène à 550 °C. Dans les deux cas, la conversion du goudron a diminué selon l'ordre suivant : Ni/CY~Ni-LSCF > Ni/LSCF~Ni-CZS > Ni-CY > Ni/CZS. Compte tenu de la performance catalytique et de la possibilité de réduction sous atmosphère de gaz de synthèse, Ni/CY et Ni/LSCF ont été choisis pour le dépôt sur des extrudats à base de SiC en vue d'une utilisation en test pilote. Parmi les différentes morphologies de SiC étudiées, le RSiC 8/5 a donné les meilleurs résultats catalytiques en termes de conversion et de sélectivité en carbone. Par conséquent, afin d'étudier l'activité catalytique à l'échelle pilote, une synthèse des

catalyseurs structurés de RSiC 8/5 a été réalisée afin de produire 1,2 L des deux matériaux sélectionnés (Ni/CY/RSiC 8/5 et Ni/LSCF/RSiC 8/5). En outre, puisque Ni/LSCF présentait une faible résistance au dépôt de coke, l'ajout de Ru a été effectué afin d'éviter le processus de désactivation. Parmi tous les catalyseurs testés à l'échelle pilote, le système RuNi/LSCF/RSiC 8/5 présente la meilleure performance catalytique, avec une valeur de conversion du toluène de 60 %. Finalement, une diminution de la conversion du toluène de 60 % à 24 % a été mise en évidence, due à une très forte augmentation de la teneur totale en goudrons dans le syngas) en utilisant un mélange biomasse/résidus comme matière première de la biomasse.

Références

1. Molino, A.; Chianese, S.; Musmarra, D. Biomass gasification technology: The state of the art overview. *J. Energy Chem.* 2016, *25*, 10–25, doi:10.1016/j.jechem.2015.11.005.

2. Ashok, J.; Dewangan, N.; Das, S.; Hongmanorom, P.; Wai, M.H.; Tomishige, K.; Kawi, S. Recent progress in the development of catalysts for steam reforming of biomass tar model reaction. *Fuel Process. Technol.* 2020, *199*, 106252, doi:10.1016/j.fuproc.2019.106252.

3. Zhang, Z.; Liu, L.; Shen, B.; Wu, C. Preparation, modification and development of Ni-based catalysts for catalytic reforming of tar produced from biomass gasification. *Renew. Sustain. Energy Rev.* 2018, *94*, 1086–1109, doi:10.1016/j.rser.2018.07.010.

4. Shannon, R.D. Revised effective ionic radii and systematic studies of interatomic distances in halides and chalcogenides. *Acta Crystallogr. Sect. A* 1976, *32*, 751–767, doi:10.1107/S0567739476001551.

5. Iglesias, I.; Baronetti, G.; Alemany, L.; Mariño, F. Insight into Ni/Ce_{1-x} $Zr_xO_{2-\delta}$ support interplay for enhanced methane steam reforming. *Int. J. Hydrogen Energy* 2019, *44*, 3668–3680, doi:10.1016/j.ijhydene.2018.12.112.

CHAPTER 1
General Introduction

1.1. General context

The greenhouse gases (GHG) are components of the atmosphere, both natural or anthropogenic, which are able to absorb and emit radiation at specific wavelengths within the spectrum of infrared radiation emitted by the Earth's surface, the atmosphere and clouds. Thereby, an increase in the GHG levels in the atmosphere increase the heat near the surface of the Earth, causing temperatures rise. The main anthropogenic GHGs dealt by the Kyoto Protocol are CO_2, CH_4, N_2O as well as the fluorinated gases (PFC, HFC, SF_6 and NF_3).

A gradual increase of global GHG emissions over the period 1970 – 2012 from 24.3 Gton CO_{2eq}/year to 46.4 Gton CO_{2eq}/year can be appreciated in ***Figure 1.1.*** This increase is caused by the socio-economical enlargement, leading to an increase in the total economic demand. Along this period, a decrease of the proportion of CH_4 and N_2O into the global GHG emissions has been detected pointing out the CO_2 as the most problematic molecule. This tendency is associated to the industrialization of the emerging economies, reducing the agriculture activities (large share of N_2O and CH_4 emissions) and leading to a strong increase in fossil CO_2 emissions due to the energy and industrial sectors [1]. Considering the distribution of the GHG emitted in 2012, the 75% of the global warming effect can be attributed to the fossil CO_2 emissions and only the 25% of the global warming is associated to the other GHG emissions. The global warming owing to the increase of GHG levels in the atmosphere has been clearly perceived by the increases in global average temperature by 1 ºC (compared to the beginning of the 20th century) and rising global average sea level by 8 cm [2].

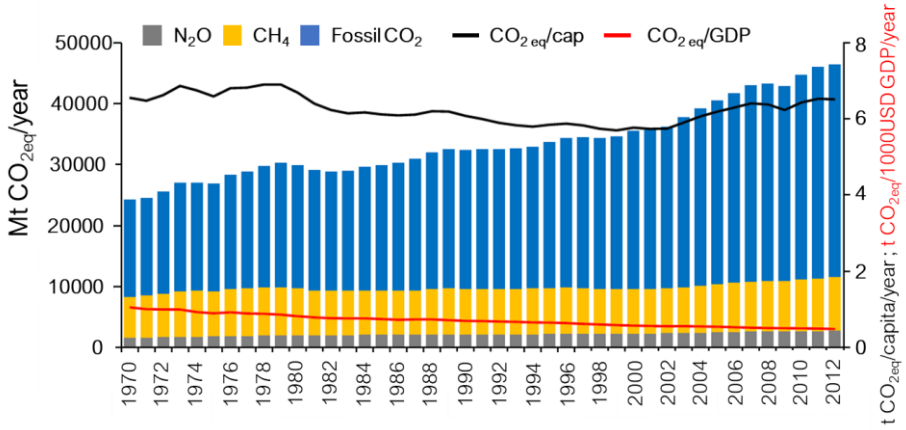

Figure 1.1. Global GHG emissions in the world (emissions from large scale biomass burning and the land use, land-use change and forestry sectors no included) [1]

The GHG emissions in the world classified by sector, shown in ***Figure 1.2 (a)***, evidences that the major anthropogenic emissions are associated to the energy production, being the cause of the 73% of the global GHG emissions. Indeed, this latter is mainly generated from fossil fuel sources (oil, coal and natural gas) as can be seen in ***Figure 1.2 (b),*** where the distribution of emissions by fuels linked to the global primary energy are presented. In 2016, fossil fuels accounted for 81% of the global primary energy supply, pointing out the existence of an energetic-economic system totally dependent on fossil fuels. Within this situation, different simulated scenarios related to the mitigation of the GHG emissions and their consequences on the global warming has been reported in literature. The *Energy Technology Perspective* (ETP) scenarios reported by the International Energy Agency (IEA) and displayed in ***Figure 1.3***, shows the projection of the anthropogenic CO_2 emissions between 1900-2050 and the corresponding increment of Earth's temperature. The average temperature of the year 1900 has been considered as reference. Three main scenarios labelled as 6 ºC Scenario (6DS), 4 ºC Scenario (4DS) and 2 ºC Scenario (2DS) can be found. The 6SD corresponds to the extension of the current trends, without any change in the economic-energetic system and would lo lead at least to a temperature increase of 6 ºC in the long term. The 4DS considers the stabilization of the current levels by a limitation of emissions and improvement of energy efficiency. In this scenario the temperature would rise by 4 ºC. Lastly, the 2DS is the most ambitious scenario. It sets the target of reducing energy-related CO_2 emissions by more than half in 2050 (compared to 2009). An 80% chance of limiting the average global temperature increase to 2 ºC is estimated through this scenario. This latter scenario implies a change in the energy sector as well as a reduction in the GHG emissions into the non-energy sectors.

The ambitious objective presented by 2DS has been considered in the Paris Agreement for containing the rise of global mean temperature by 2100. As described in the 2DS scenario, in order to reach this target an energetic transition will be required. The energetic transition is the structural change of the global energy sector, shifting from fossil-based systems (oil, coal and natural gas) to renewable energy sources. Thereby, the investment in the renewable energies and the improvement in energy storage might be the key drivers of the energy transition.

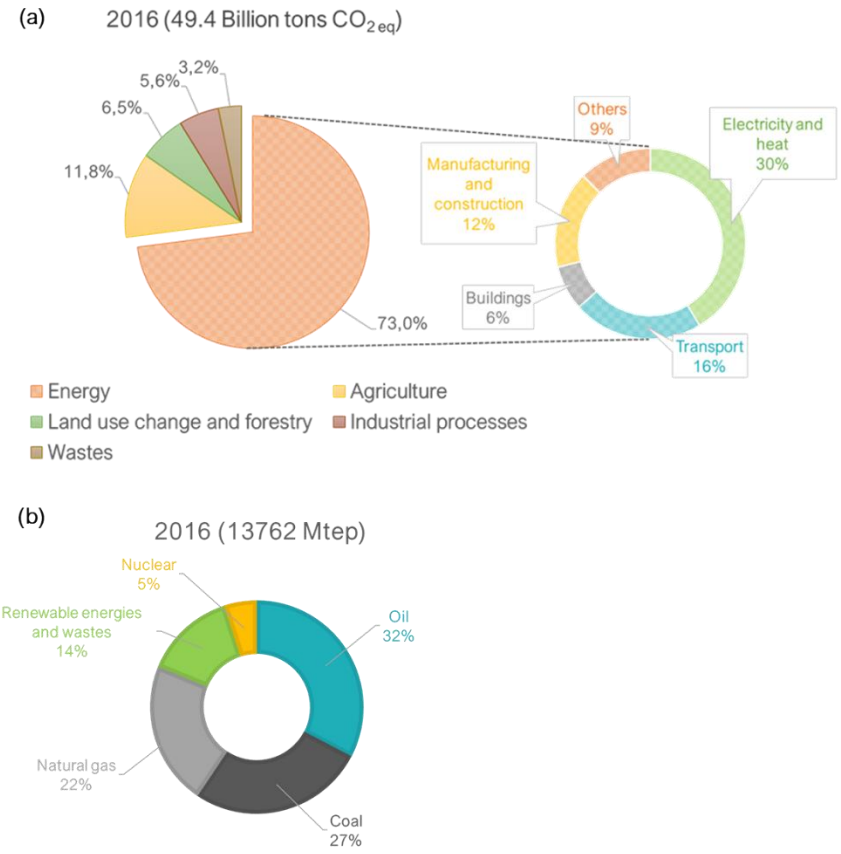

Figure 1.2. (a) World GHG emissions by sector in 2016 [3] and (b) World primary energy by source in 2016 [2]

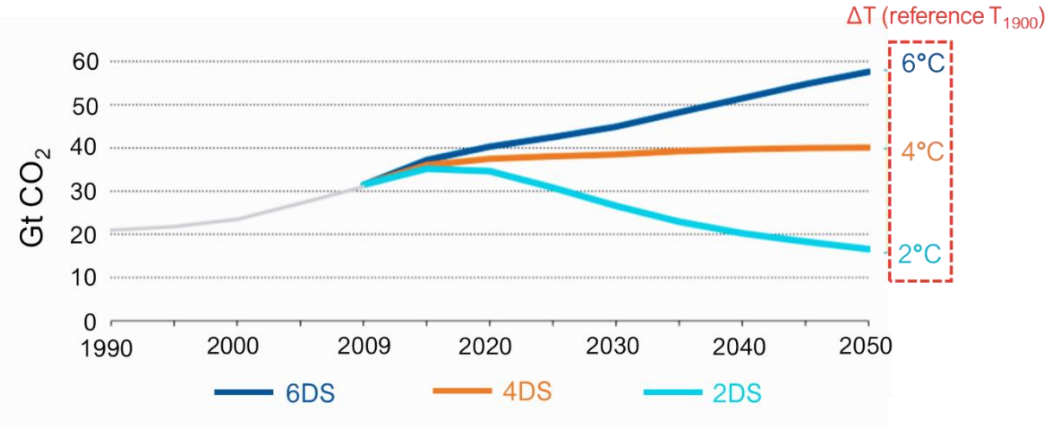

Figure 1.3. ETP 2012 scenario CO_2 emissions pathways [4]

1.1.1. Commitments of the European Union in the Paris Agreement

An ambitious economy-wide domestic target has been set by the European Council for 2030 [5]:

- A reduction by 40% of GHG emissions compared to 1990 levels
- A 27% share of renewables in gross final energy consumption

- An improvement in energy efficiency of 27%, meaning a reduction of 27% in primary energy consumption compared to 2007.

In this context, the contribution of the renewable energies in the total energy production became increasingly important in Europe along the years (***Figure 1.4***). As it can be seen, in 2017, the production energy from renewable sources (wind, solar and biomass) was for the first time slightly higher (679 TWh) than that produced from coal sources (669 TWh) [6]. Among the three renewable energies, wind energy generated the 54%, followed by biomass energy with a 29% and the solar energy, as the last, contributing in a 17%.

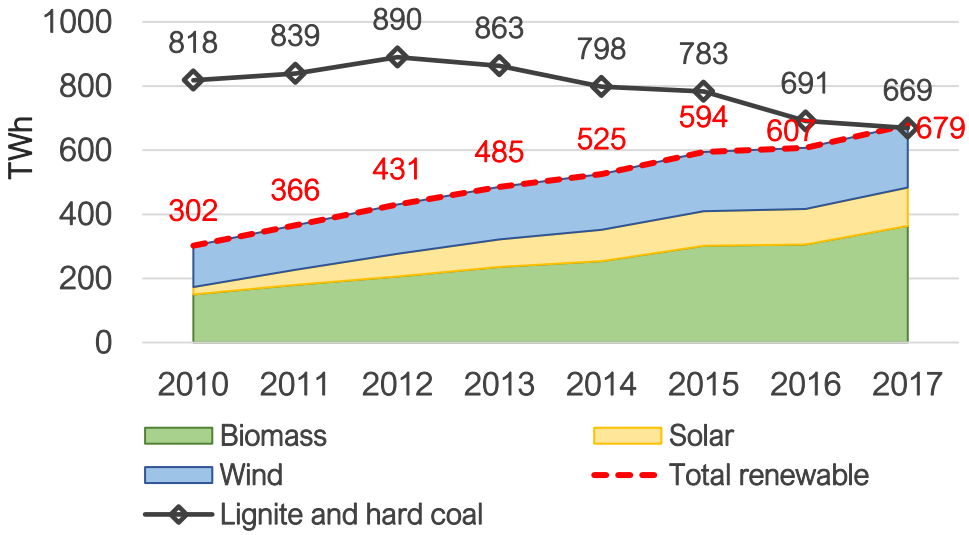

Figure 1.4. Energy production from renewables (wind + solar + biomass) and coal sources [6]

In the period 2000-2014, 46% of current EU-28 biomass power plants (42% bioenergy production capacity) were built with an increase in demand for solid biomass for energy use due to EU energy policy [7]. Bioenergy is the main source of renewable energy in EU in terms of gross final consumption, contributing to 59% of all renewables and to 10 % of all energy sources to the gross final consumption in 2016 (***Figure 1.5***) [8]. 75% of the bioenergy produced is consumed by the heating and cooling sector. Bioelectricity and biofuels represent the 13% and 12% of the bioenergy produced. In 2015, the heat production from biogas was mostly located in: Germany (1.6 Mtep), Italy (0.25 Mtep) France (0.16 Mtep) and UK (0.16 Mtep) [9]. Regarding the gross consumption of bioenergy, Germany, France, Italy, Sweden and the UK are the top five EU Member States.

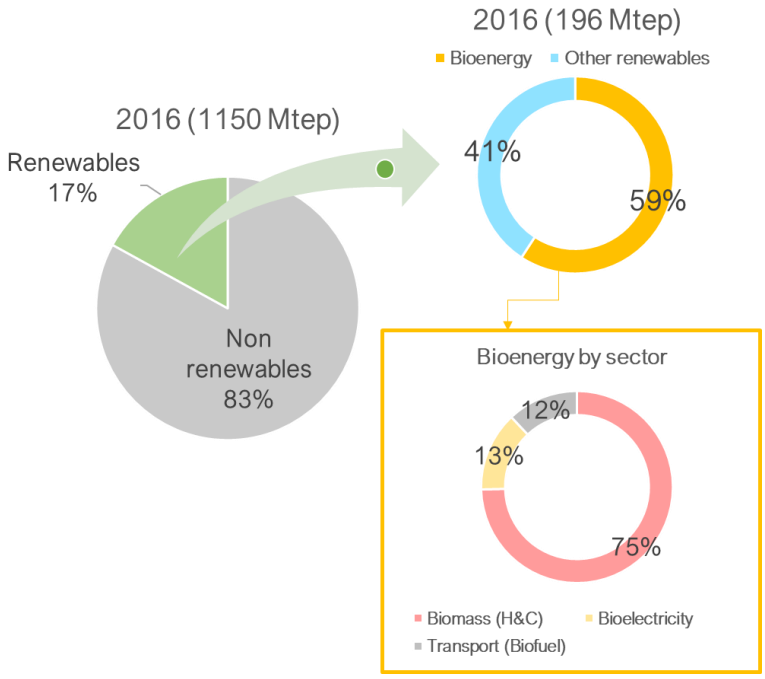

Figure 1.5. Share of renewables in the EU gross final energy consumption in 2016. The bioenergy contribution [8].

Wind and solar energy are, as well, large renewable sources for electricity generation as it can be observed in ***Figure 1.4***. However, these sources are variable and intermittent, since the amount of energy generated changes by geography and upon time, not only at the scale of season. Thereby, a reliable steady power generation cannot be only provided by wind and solar energies [10]. The combination of wind and/or solar power plants with a fast reacting backup power, able to produce electricity when the wind is not blowing or the sun light intensity is limited by weather conditions, is one of the solutions. In contrast to wind and solar energies, biomass energy is characterized by its easy availability from the geography point of view and no dependency on the season. Therefore, biomass power could be used as a backup power to compensate these energy fluctuations.

To conclude, bioenergy can play a significant role as flexible energy producer, balancing the power systems based on variable renewable energy sources as wind or solar. The key condition of bioenergy progress is the availability of reliable, affordable and sustainable biomass [11]. The production and use of biomass comprise a chain of several steps from the growing and harvesting of feedstocks, processing, conversion and distribution of bioenergy vectors to their final use. Thus, the environmental performance of biomass as energy carrier depends on the specific characteristic of those intermediary steps. A good management of the bioenergy pathways might lead to an important

greenhouse gas saving as well as it should ensure food security and protecting ecosystems and the deforestation, degradation of habitats and loss of biodiversity.

1.2. Biomass: general aspects

1.2.1. Definition of biomass

Owing to the diversity of the materials, usage and origin, the definition of biomass can change. The 2009/28/EC European Directive defines biomass as "the biodegradable fraction of products, waste and residues of biological origin from agriculture (including vegetal and animal substances), forestry and related industries, including fisheries and the aquaculture, as well as the biodegradable fraction of industrial and municipal wastes". Zang *et al.* [12] defined biomass as "a stored source of solar energy in the form of chemical energy, which can be released when the chemical bonds between adjacent oxygen, carbon and hydrogen molecules are broken by various biological and thermochemical process".

1.2.2. Biomass composition

Generally, biomass is composed by a mixture of cellulose, hemicellulose, lignin, lipids, proteins and simple sugars, being the three formers the main components [12–14]. The typical level of the main compounds (cellulose, hemicellulose and lignin) in biomass are shown in ***Table 1.1.*** Inorganic elements and water fraction are as well found in the biomass composition. As concern to the elemental composition, carbon (~40-45 wt% (wet)) and oxygen (40 wt% (wet)) are the major elements, constituting the 80-85% of the weight of a biomass [15]. Additionally, some traces of hydrogen, nitrogen, sulphurs and chlorine are present.

Component	Percentage dry basis (%)	Description
Cellulose	40-60	A linear chain of glucose linked by β-glycosidic linkage. High molecular weight (≥106 $g.mol^{-1}$)
Hemicellulose	20-40	Short chains of sugars. Lower molecular weight than cellulose.
Lignine	10-25	Biopolymer rich in polyphenolic components that provide structural integrity to plants. Amorphous structure

Table 1.1. Typical levels of cellulose, hemicellulose and lignin in biomass

1.2.3. Biomass sources

Wood, energy crops as well as agricultural and forest residues are considered as the main biomass sources [12,13]. Furthermore, food processing wastes, sewage sludge

and organic components of the municipal solid wastes (MSW) are also other biomass resources.

In the EU, the wood biomass from forests and other wooded land are the main biomass sources. As it can be seen in ***Figure 1.6,*** a direct energy supply of 32% and indirect supply of 28% is produced from the aforementioned sources. Around 27% is generated from agricultural biomass (agricultural crops and by-products) and a share of 12% in energy supply is originated from wastes (municipal or industrial).

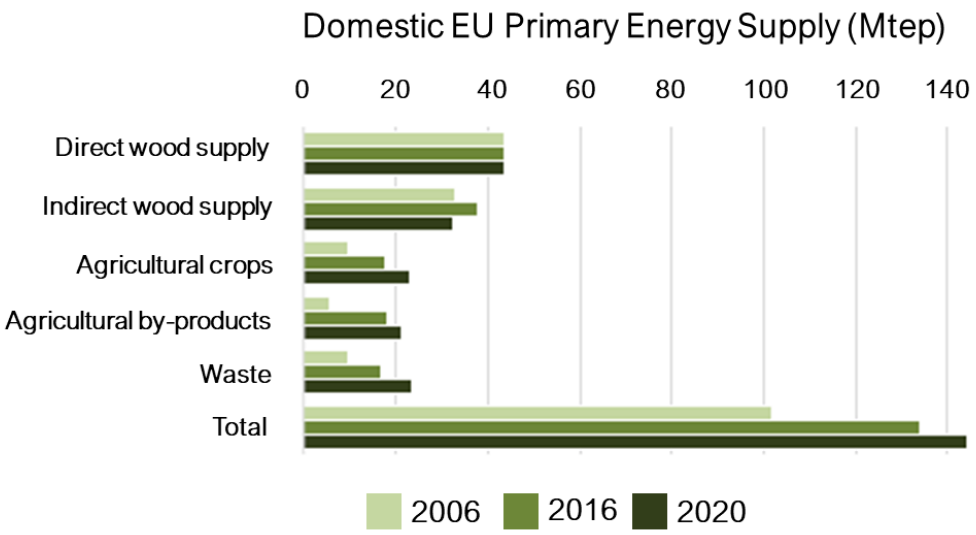

Figure 1.6. Domestic biomass supplied for energy in 2006, 2016 (EU country data) and projections for 2020 (according to the projections in the National Renewable Energy Action Plans) [8]

Wood pellets became an important energy carrier at large scale and over long distances, owing to their high energy density (average heating value of 17.5 GJ/ton corresponding to 26.3 GJ/$m^3_{apparent}$) [8]. The UE was one of the principal manufacturers, producing 50% of the global production (29 million tons in 2016), and also the main consumer globally (23 million tons) [8]. Within the European Member States, the consumption of wood pellets is banked on imports as well as on the residential sector for heating and for energy production.

1.2.4. Biomass conversion processes

A large variety of liquid and gaseous fuels can be generated from biomass. The biomass conversion processes for energy production have been widely categorized into two main groups: biological and thermochemical processes (see ***Scheme 1.1***) [12–14,16]. The thermochemical conversion is suitable for feedstocks with low moisture content and normally needs high temperatures and displays high conversion rates [17]. Combustion,

pyrolysis and gasification are the most common thermochemical processes to produce energy from biomass. On the contrary, the biological conversions require low temperatures and show lower reaction rates compared to the thermochemical ones. Feedstocks with high moisture content are the desired candidates for these processes [17]. The fermentation and anaerobic digestion are the principal processes used among the biological conversions.

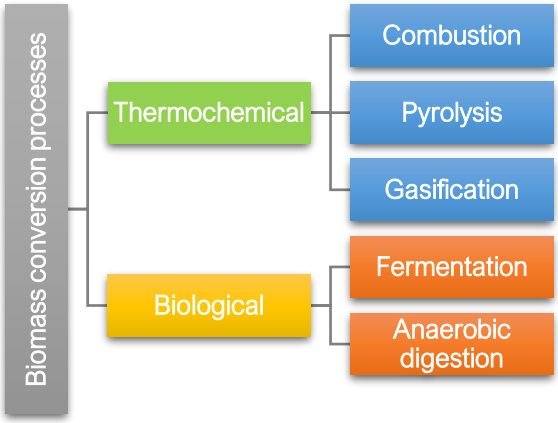

Scheme 1.1. Classification of the main biomass conversion processes for energy production

As previously mentioned, the thermochemical processes are generally more efficient than biochemical/biological processes in terms of the reaction time required (few seconds or minutes in thermochemical vs few days, week or longer for biochemical/biological processes) but also because of their higher ability to convert most of the organic compounds. For instance, lignin materials are considered as non-fermentable component of biomass and thereby, their complete decomposition via biological approaches is harder than via thermochemical ones [12,17]. The background of the thermochemical processes (combustion, pyrolysis and gasification) is described in the following section.

1.3. Thermochemical biomass conversion

1.3.1. Combustion

Combustion consists in the oxidation of biomass at high temperatures (1200 -1800 ºC) using the adequate amount of oxygen to convert it into heat energy, water and carbon dioxide through a chain of successive exothermic reactions [12,17]. The heat energy generated is directly used or transformed into electricity. No additional useful intermediates such a, gas, liquid or solid fuels are produced through this thermochemical process.

Combustion is the most developed and broadly used process for biomass conversion, generating the 97% of the bioenergy in the world [13]. In general, a biomass combustion plant, using wood and forest residues as feedstock, provides between 20 to 50 MW with an electrical efficiency of 25-30% [13]. Different biomass feedstocks can be used at combustion plants such as wood, dry leaves, hard vegetables, rice husk…[18]

1.3.2. Pyrolysis

Pyrolysis is the conversion of biomass into liquid bio-oil, solid charcoal or fuel gas/syngas (mixture containing CO, H_2, CO_2 and CH_4) products by thermal decomposition of the biomass in the absence or in presence of low amount of oxidizing agent at low-intermediate temperatures (400 – 700 ºC). A good management of the operating conditions can lead to the preferential production of one of the three products, usually solid or liquid fuel, optimizing its yield. The pyrolysis process is usually carried out in two steps:

(i) The pre-pyrolysis (120-200 ºC): breaking of weakness bonds, formation of free radicals and carbonyl groups, evaporation of the water fraction and formation of CO_2 and CO.

(ii) Pyrolysis step: is highly reliant on the reaction temperature and residence time. Based on the residence time, this step can be further classified into slow and fast pyrolysis.

The slow pyrolysis is conducted at relative low temperature (400 ºC) and, thereby, requires long reaction and conversion times of the biomass (solid residence time: 600 – 6000 s) [13,16,19]. The solid charcoal is the major product obtained through this process and it can be used in several sectors, i.e. in household (heating), chemical (production of absorbent, active carbon …) and pharmaceutics [19]. On the contrary, the fast pyrolysis occurs at higher temperatures (500 – 600 ºC), leading to a rapid conversion of the biomass, with short contact time (solid residence time: 0.5 – 5 s), into vapors that are subsequently condensated into dark liquid product (bio-oil) [13,16,19,20]. The production of this liquid fraction is up to 70-80 wt% of the biomass used [13]. This kind of pyrolytic process provides a proportion of 60% of bio-oil, 20% of bio-coal and 20% syngas [13,20]. The liquid fuel (bio-oil) can be stored and used in sectors such as heating and electricity generation. To date, pyrolysis of biomass is largely used for the production of bio-oil for the production of energy through co-generators [13].

1.3.3. Gasification

Gasification is the thermochemical conversion of biomass into a syngas, through partial oxidation using oxygen/air as gasification agent. Commonly, 35% of the oxidizing agent required for full combustion is used in this process along with high temperatures.[12,21]. Other gasification agents, such as steam, can be employed, producing a fuel gas with high H_2/CO ratio by endothermic reactions (steam gasification). However, the main drawback of steam as gasification agent is the high energy requirement that must be supplied by external sources [21].

The biomass gasification involves a several thermochemical processes closely interconnected. The stages of a typical gasification process with air as gasification agent is shown in *Scheme 1.2.* The process begins with the evaporation of the moisture content present in the biomass feedstock (drying, 120 – 200 ºC). Afterwards, thermal decomposition of dry biomass in absence of oxygen or air occurs (pyrolysis, 200 – 500 ºC) and its volatile components are vaporized producing a gas mixture composed of H_2, CO, CO_2, CH_4, light hydrocarbons and steam. As consequence, biomass is reduced to char, while gaseous hydrocarbons condense at low temperature producing liquid tars. In the combustion zone (800 – 1000 ºC), CO_2, CO and steam are formed from partial or complete oxidation of the products generated in the pyrolisis (gases, tars and char) through exothermic reactions with oxygen from air. These exothermic reactions rise the temperature and, consequently, reduction reaction are favoured, obtaining a fuel gas rich in H_2, CO_2, CO and CH_4 and residues as char and tars.

Many operating conditions such as, type of gasifier, biomass feedstock, moisture degree of the biomass and gasification agent influence the composition of the end-gas. Generally, air gasification leads to a gas with low heating value (4 – 6 $MJ \cdot Nm^3$) whereas steam/oxygen gasification produces syngas with medium heating value (10 – 14 $MJ \cdot Nm^{-3}$) [22,23]. In contrast with the pyrolysis, the gaseous phase is the main product obtained by gasification due to the higher temperatures used in gasification (5% of bio-oil, 10% of bio-coal and 85% syngas) [24].

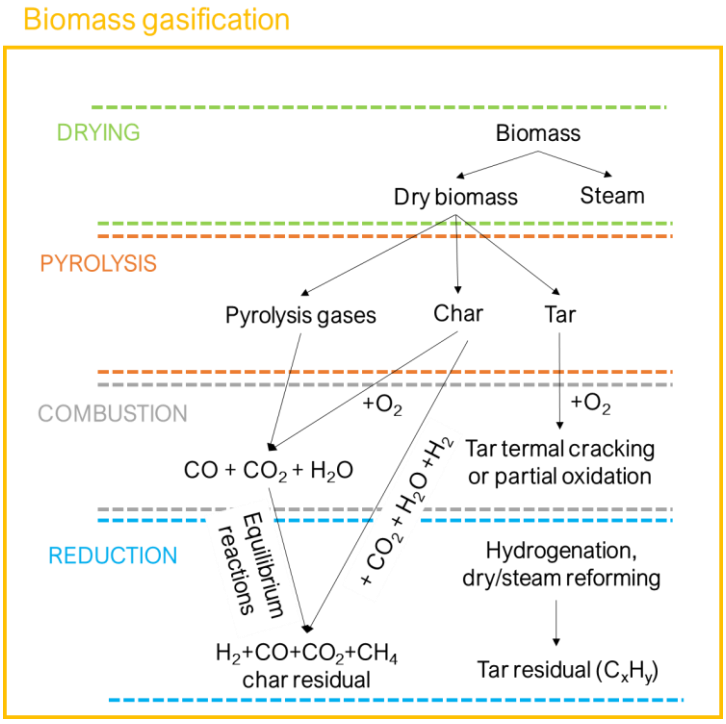

Scheme 1.2. Thermochemical processes involved in biomass gasification (from Valderrama Ríos *et al.* [25])

A summary of the primary and secondary products generated through the thermochemical conversion process is shown in ***Scheme 1.3.*** A direct heat generation is obtained by biomass combustion, while the pyrolysis processes are mostly focused in the generation of bio-coal and/or bio-oils. Gasification as biomass conversion process brings wider possibilities than combustion and pyrolysis since it leads to the conversion of biomass into a valuable gas product (syngas) that can be used as chemical and energetic vector. Besides, the gas produced by biomass gasification can be used for the production of second generation of biofuels as well as for the generation of energy [12,22].

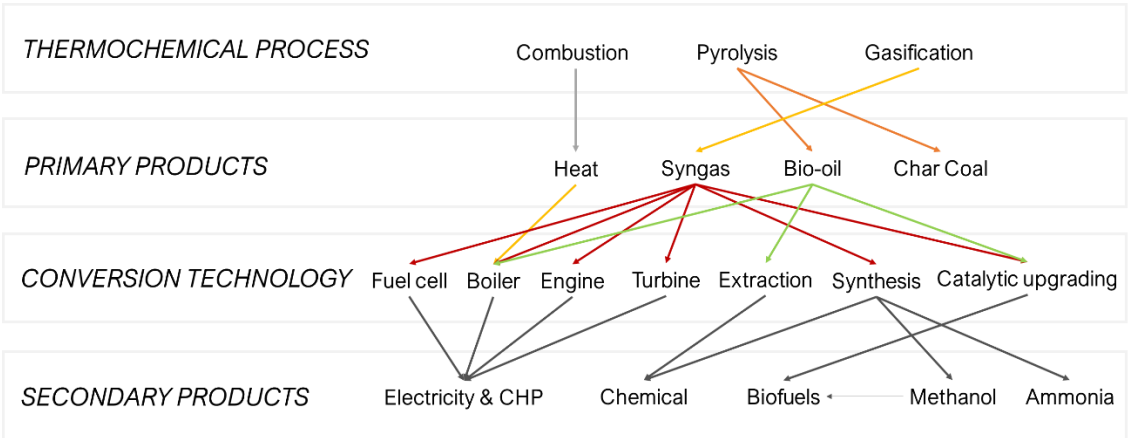

Scheme 1.3. Summary of the thermochemical conversion processes and products (adapted from ref. [26])

1.3.3.1. Gasification technology

The reactors used on an industrial scale to carry out the biomass gasification, commonly called gasifiers, differ one from another concerning various aspects [26]:

(1) Mode of contact between the feedstock and the gasification agent
(2) Mode and rate of heat transfer
(3) Residence time of the feedstock in the reaction zone

The gasifiers are adapted according to the application of the gasification products and optimized to improve their efficiency [26]. Studies about the type of gasifier used in Europe, United States and Canada have evidenced that 75% of the reactors are co-current fixed-bed reactors, 20% are fluidized bed reactors, 2.5% are counter-current fixed-bed reactors and the rest are categorized into the other kinds of gasifiers [27]. Thus, the main characteristics of the most used gasifier in industry are detailed in this section.

- *Fixed-bed reactors*

These reactors usually produce low heating valued syngas. They are appropriate for small or medium-scale thermal applications [12]. Fixed bed gasifiers comprise updraft (counter-current) and downdraft (co-current) configurations. In the formers, the feed moves downwards with respect to the gasification agent and then the product gas moves upward, whereas in the latter, both, the feed and the product gas are moved downward.

Updraft gasifiers produce gas with high tar content since the tars do not have the opportunity to pass through the combustion zone where the temperature is high enough to decompose them. Nowadays, most of these type of reactors have been decommissioned because of the environmental issues, like water pollution from tar residues [12,26]. Downdraft gasifier is one of the most used fixed-bed gasification systems. By comparing to updraft configuration, the produced tars can be partially converted through thermal cracking since the product gas passes through the combustion zone. Consequently, the tar content in the product gas is significantly reduced in downdraft gasifier.

- *Fluidized-bed reactors*

Fluidized bed reactors can be categorized into bubbling fluidized gasifiers and circulating fluidized gasifiers. A bed of inert granular material (sand) is placed into the reactor and held in a condition of fluidization when the gasification agent is introduced bottom-up from the bed through a distribution grid. The inert solid behaves as a liquid and is continuously stirred by the presence of gas bubbles, ensuring a uniform condition of exchange of matter and heat between the solid and the gas [26]. In the circulating fluidized

gasifier, the hot bed material is circulated between a cyclone separator and the gasifier. During the circulation, the bed material along with produced char go back to the reactor, while the ashes are separated and removed from the system [12].

Compared to fixed bed reactors, fluidized bed provides a more homogenous temperature inside the reactor. Additionally, fluidized bed gasifiers can be sized efficiently for middle and large scale [12,26].

1.3.3.2. Biomass gasification products and downstream processes

Generally, as prior described, two main products are obtained from biomass gasification process: solid phase and gas/vapor phase. The solid phase is largely composed by ashes and un-reacted char. The char proportion (lower than 1 wt%) is very low compared to the total ash amount generated [26]. The gas/vapor phase, well known as syngas, comprises a non-condensable gas phase (mixture of H_2, CO, CO_2, CH_4 and light hydrocarbons) and condensables products. Other components in minor level such as NH_3, HCl and H_2S can also be part of the gas phase and their level depend on the biomass composition [26,28]. Special consideration is needed for the condensable phase, called tar, since it is made of several organic compounds that, once condensed, may be considered as viscous oil.

The syngas produced through biomass gasification can be used in many ways, including direct use in internal or external combustion engines, for electricity production, in solid fuel cells (SOFC), in the production of second generation of biofuel through Fischer-Tropsch or the synthesis of chemical products as methanol [22,29,30]. In function of the final application, the syngas must meet several specific quality limitations that have to be taken into consideration. For instance, a H_2-rich syngas is needed for its application in SOFC technology, while specific hydrogen to carbon monoxide (H_2/CO) ratios are required for the biofuels and chemical products production. However, the raw syngas generated by gasification is composed by CO, H_2, CH_4, CO_2 and H_2O, and by-products such tars, inorganic compounds and solid particles. Among these impurities, the generation of tars and their presence in the raw syngas are a great drawback into the biomass gasification sector from the operating point of view and the further syngas application.

Tars formed during the gasification will condense quickly at temperature below their dew point (~ 300 ºC), bringing many operational and environmental problems, counting the clog and corrosion of pipeline and device, and the generation of waste water with high

content in phenolic compounds. [12,22,25,30]. Thereby, the presence of tars result in a decrease in the efficiency of the process and a consequent increase system operational cost [31]. Besides the operational issues, the presence of tar limits the use of the syngas in some downstream applications. As can be seen in ***Table 1.2.,*** the tolerance of the syngas-using processes on these secondary products is strongly variable. Thereby, a syngas purification/cleaning system to reach the requirements for a specific application is fully needed. Accordingly, the general aspects of tar compounds as well as the processes that can be conducted to reduce their content in the syngas will be discussed in the following sections.

Application	Tar content ($mg \cdot Nm^{-3}$)
Direct combustion	No specified
Internal combustion engine	< 100
Gas turbine	< 5.0
Synthesis of methanol	< 0.1
Compressors	50 – 500
Fuel Cells	< 1.0

Table 1.2. Tolerance limit on tar content for various applications [25]

1.4. Tar compounds: general aspects

1.4.1. Tar definition and maturation

According to the tar measurement protocol published by the International Energy Agency (IEA), the Directorate General for Energy of the European Commission (DG XVII) and the Energy Department of the United States, tars are defined as "all hydrocarbons with molecular weight higher than benzene" [32]. Other definition widely used in literature is the concept of tar as a mixture of condensable hydrocarbons, involving from single to five-rings aromatic compounds together with oxygenated compounds and complex Polycyclic Aromatic Hydrocarbons (PAHs) [25,33,34].

1.4.2. Tar formation

As aforementioned, tar formation is mostly formed along the pyrolysis step due to the decomposition of the lignocellulosic biomass. The oxygenated hydrocarbons are the major components formed in this step due to the high content of oxygen atoms in cellulose and hemicellulose structure [35]. Other aromatic compounds arise as result of the pyrolysis of lignin, mainly bi- or tri-functional phenols (cresol, xylenol…) [26]. Afterwards, as consequence of the increase in temperature and the presence of oxidant (air, oxygen or steam), these oxygenated hydrocarbons can be decomposed to light hydrocarbons,

aromatics and olefins which are later transformed to higher hydrocarbons and larger PAH. *Scheme 1.4* shows the tar formation in function of temperature reported by Elliott in 1988 [36]. An enhancement in structural stability of the compounds when temperature rises up can be observed. Thereby, temperature is one of the key factors for tar formation and distribution.

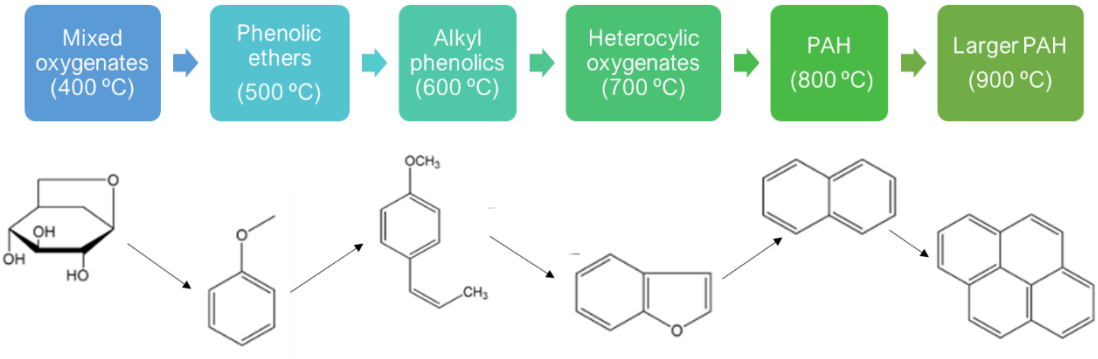

Scheme 1.4. Tar maturation process in function of temperature [35]

1.4.3. Tar classification

In the literature, two ways of classifying tar are found. One is referred to the process conditions in which compounds are formed and the other one considers the physical tar properties such as tar water solubility and tar condensation. Thus, according to the process conditions, tars were categorized into four product classes by Milne *et al.* [37]:

(i) Primary products: formed during the pyrolysis through decomposition of biomass building blocks (cellulose, hemicellulose and lignin) and are composed of acid, sugars, alcohols, aldehydes, …

(ii) Secondary products: resulting from primary tar rearrangement at temperatures above 500 ºC, generating heavier molecules such as olefins and phenolics compounds

(iii) Alkyl tertiary products: involve methyl derivatives of aromatic compounds (methyl acenaphthylene, indene, …)

(iv) Condensed tertiary products: largely PAH

The Energy Research Center of the Netherlands (ECN), the Applied Scientific Research Center of Netherlands (TNO of the Dutch Toegepast Natuurwetenschappelijk Onderzoek) and the University of Twente Netherlands developed a tar classification based on the chemical structure, solubility and condensability in the framework of the project

"Primary measures for the reduction of tar production in fluidized-bed gasifiers" [38]. As can be found in ***Table 1.3,*** tar compounds are classified into five categories, including GC-undetectable, heterocyclic, light aromatics, light PAH component and heavy PAH components.

Tar class	Name	Property	Representative compounds
1	GC-undetectable	Very heavy, cannot be detected by GC	-
2	Heterocyclic	Containing hetero atoms, highly water-soluble compounds	Pyridine, phenol, cresols, quinolone…
3	Light aromatic (1 ring)	Hydrocarbons with single ring Do not pose a problem regarding condensability and solubility	Toluene, ethylbenzene, xylene, styrene…
4	Light PAH compounds (2-3 rings)	Condensation at low temperature even at low concentrations	Indene, naphthalene, fluorene, phenanthrene…
5	Heavy PAH compounds (4 – 7 rings)	Condensation at high temperatures and low concentrations	Fluoranthene, pyrene, perylene, coronene…

Table 1.3. Tar classification from ECN-TNO-UT [38]

1.4.4. Tar composition from biomass gasification

A typical tar composition in syngas produced by biomass gasification is presented in ***Figure 1.7.*** However, the type of reactor, biomass feedstock and its moisture degree, reaction temperature and residence time of the biomass in the reactor are some of the factors that influence the tar composition. Several investigations evidenced that each type of biomass used in a gasification process exhibits its own reactivity with different thermal degradation kinetics and product characteristic [39,40]. For instance, tar formation and distribution for the gasification of cellulose, hemicellulose and lignin have been studied by Yu et al. [40]. The authors observed that the highest tar yield with more stable components was displayed by lignin gasification. Other studies reported the tar distribution in function of the reaction temperature. As it can be observed in ***Figure 1.8.***, the conversion of primary tar into smaller non-condensable molecules and secondary tar begins at temperature above 500 ºC, while primary tars are fully converted at higher temperatures and tertiary tars is produced [37].

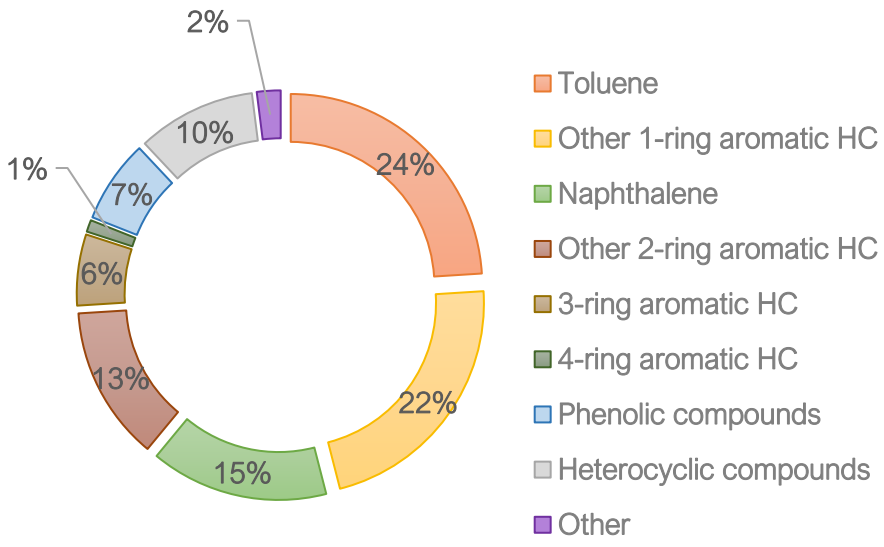

Figure 1.7. Typical biomass tar composition [25,35]

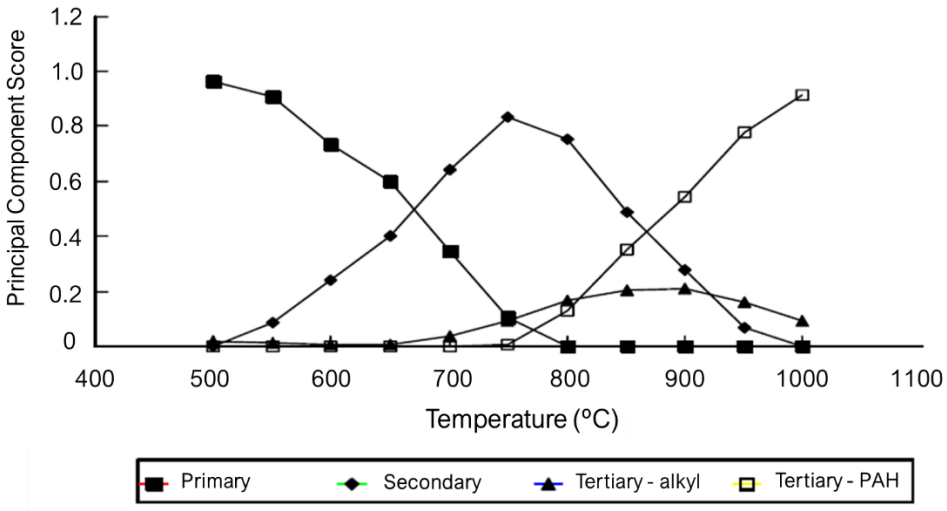

Figure 1.8. Tar distribution as a function of temperature (adapted from ref [37])

1.5. Tar removal

In this context, an efficient and economical method for the reduction of tar content in the product syngas is desired into this research area. Based on the location of the tar removal into the gasification plant, the methods could be classified into two groups: *in situ* methods, known as primary methods and downstream methods, called secondary methods.

1.5.1. Primary methods

These methods are carried out during the gasification process, to inhibit the formation or to reduce the tar generated in the gasifier. Utopian concept of these primary methods is the idea to completely remove the tar without the use of a secondary treatment.

In order to well reduce the tar content, an optimization of operating conditions and a proper design of the gasifier reactor are mandatory. As well, the use of additives, such as catalysts, into the gasification reaction can be complementary option [33].

1.5.1.1. Operation conditions

The carbon conversion, product syngas composition as well as tar formation and composition are directly linked to the operating conditions of the gasification process. The key operational factors are temperature, pressure, gasification agent, additives-catalysts used and mass ratio between fuel and gasification agent [25,33]. Some of these parameters will be discussed in this section. It should be stressed that the selection of these parameters is closely dependent on the type of gasifier used.

Gasification temperature not only modifies the tar composition through influencing the chemical reactions involved, but also affects the amount of tar formed during the gasification process. A summary of the influence of the gasification temperature in the product syngas characteristic is shown in ***Scheme 1.5.*** High operating temperature (> 800 ºC) in the gasifier is required to attain a high carbon conversion of biomass and then a product gas with low tar content [41]. Besides tar, temperature has also an impact on the formation of NH_3 and NO_x. It has been evidenced that the level of these two species in the product syngas decreases with the increase of temperature [42]. Nevertheless, as it evidenced in ***Scheme 1.3.,*** the use of high temperatures decreases the gas heating value and increase the risk of sintering. Thereby a good compromise between the tar content and these other parameters might to be found. Additionally, other factor that determine the gasification temperature is the kind of feedstock used.

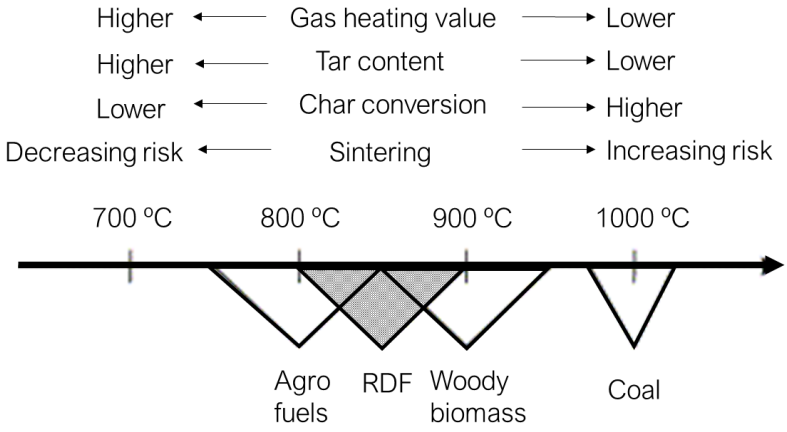

Scheme 1.5. Gasification temperature for various feedstocks and the influence of the gasification temperature in the product syngas characteristics [33]

Other factor that plays an important role in the tar formation is the gasification agent used (oxygen, air or steam) since the selectivity of the gasification reactions varies with the gasifying media. A higher tar content was reached using steam and the lowest when air was supplied [43]. The promotion of tar formation using steam as gasification agent has been related to the decrease of temperature resulting from the steam addition. Additionally, the heating value is as well affected by the type of gasification agent. As prior reported, lower heating value of the generated syngas is attained with air since the product syngas is diluted by nitrogen [33].

The residence time of the biomass into the reactor and the mass ratio between fuel and gasification agent are other parameters that must be considered to produce a syngas with low tar content using primary methods.

1.5.1.2. Gasifier design

The syngas characteristics in function of the type of gasifier are listed in ***Table 1.4.*** As it can be observed, the gasifier type and design influence the tar content in the product syngas generated. However, as prior discussed, other variables as feedstock, temperature, gasification agent… affect the tar content, then, the differences in tar content shown in ***Table 1.4.*** cannot be only associated to the type of gasifier.

An improvement in the syngas quality has been evidenced through modifications in the gasifier design. For instance, the injection of a secondary air above the biomass feeding point in a fluidized bed resulted in a reduction of tar content of 90%, using a gasification temperature around 840 – 880 ºC [44]. Additionally, the use of two stages in the gasifier design appears to be relevant in the production of clean syngas [45,46]. This concept is based on the separation of the pyrolysis and reduction zone, thus, the tar formed in the pyrolysis process (first stage) are later decomposed in the reduction zone (second stage). The combination of different reaction zones using multi-stage processes leads to improve the gasification efficiency and the product gas quality [33].

Gasifier type	Scale (MW)	LHV ($MJ \cdot Nm^{-3}$)	Tar ($g \cdot Nm^{-3}$)	Particle ($g \cdot Nm^{-3}$)
Updraft fixed bed	0.1 – 30	4.0 – 5.6	30 – 150	0.1 – 1
Downdraft fixed bed	0.01 – 8	< 6	0.01 – 0.5	0.1 – 8
Bubbling fluidized bed	1 – 80	3.5 – 5.0	1.5 – 10	12 – 16
Circulating fluidized bed	10 – 100	3.6 – 5.9	5 – 50	20 – 100
Dual fluidized bed	> 50	> 10	1.5 – 20	12 – 16

Table 1.4. Influence of the structure and type of gasifier in the product gas characteristics [30]

1.5.2. Secondary methods

Secondary methods for tar removal can be divided into two categories:

(i) Physical/mechanical methods (ceramic candle filters or wet scrubber)

(ii) Thermochemical methods (thermal cracking, partial oxidation or catalytic processes)

1.5.2.1. Physical/mechanical methods

The physical methods are subdivided into two other categories: dry and wet cleaning methods. The dry methods are conducted at 200 – 500 ºC temperature range, whereas the wet methods are performed after cooling, in the range of 20 – 60 ºC [25,34]. Generally, they are mainly used to capture particles and tar in a condensed form *via* inertia collision, interception, diffusion, electrostatic force and/or gravity [30]. Cyclone, rotating particles separators, electrostatic precipitators, filters and scrubbers are the typical equipment used.

Wet cleaning systems widely used in many gasification pilot plants to remove contaminants and tar are the water scrubbers. As tar is mostly composed by a mixture of non water-soluble compounds, water is not the most accurate scrubbing medium for tar removal. Thereby, other kind of absorbents, especially hydrophobic adsorbent, should be more effective for tar absorption [47]. The main drawbacks of the wet methods are the sewage produced as by-product that will cause a secondary pollution [21]. Then, a treatment and disposal of waste fluids and sludge has also to be performed in the case of wet cleaning method. The dry methods have advantages for wide adaptability of tar, high removal efficiency and lower price than wet cleaning methods. Despite the dry cleaning

methods solve the problem of wastewaters, the complex filtration equipment, their high cost and the inconvenient of operation-running lifetime delayed their development [21].

Another drawback of these cleaning method is the generation of solid and liquid wastes largely composed by aromatic hydrocarbons. These compounds have been identified as carcinogens, mutagens and teratogens. Therefore, strict safety procedures are required for their post-treatment. Most important, the tar energy is loss when these physical methods are used. Currently, catalytic hot gas filters for elimination of tar has been developed, upgrading the produced syngas through the combination of the filtration (particles removal) and the catalytic cracking of tars [25,34].

1.5.2.2. Thermochemical methods

1.5.2.2.1. Thermal cracking and partial oxidation

This method can be applied only in the reactors with high temperature zones. Tars are very stable compounds and, generally refractory to cracking by thermal treatment. Thereby, thermal cracking of tar needs the use of high temperatures (> 1100 ºC) and/or increase the gas residence time, producing large amount of soot [48]. For economic and operational reasons, thermal cracking is not an attractive method for tar removal at large-scale gasification systems [25]. While for the partial oxidation approach, the main issues is the balance between the fuel gas quality and removal efficiency, since some useful gas components such as H_2 or CO could be potentially oxidized once an excess of air is supplied [30].

1.5.2.2.2. Catalytic processes

Contrary to the physical methods, based only in the elimination of tars from the produced gas, the use of catalyst leads to an increase in the overall efficiency of the gasification process, since tar can be converted into energetic gaseous products [29,30,35]. In addition, catalytic conversion of tar reduces the reaction temperature compared to the high temperature conventional cracking.

Up to now, steam reforming of tar has received special attention, since the tar can be effectively removed and simultaneously converted into H_2, CH_4 and CO [49]. Afterwards, the produced CO can further react with the steam *via* water gas shift reaction to produce a H_2-rich syngas (see ***Figure 1.9***) [50].

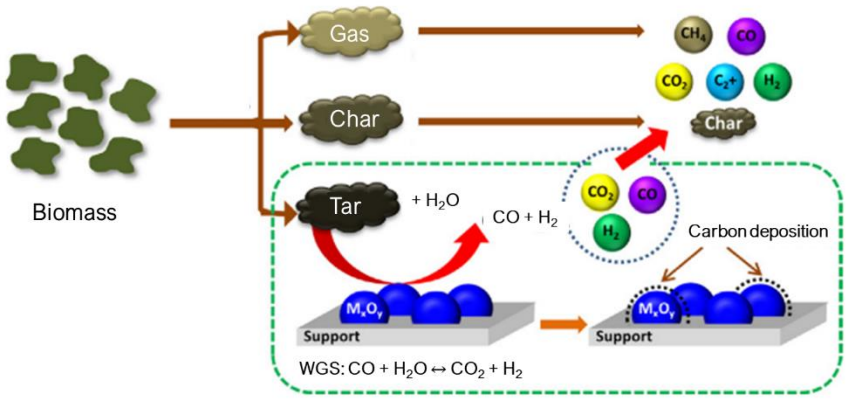

Figure 1.9. Tar abatement through catalytic steam reforming (M_xO_y represents a metal oxide catalyst) [35]

Two approaches are considered for the catalytic tar reforming: (i) the catalyst is directly added into the gasifier reactor along with the biomass feedstock and, (ii) a downstream catalytic reactor is used [25]. The former approach can be included as one of the primary methods used for tar reduction. Despite the use of a second reactor displays high effectiveness in tar removal, it is often considered as an expensive and complex process for small and medium scale systems [35].

1.6. General aspects of catalytic systems for steam reforming of tars

The selection of the catalytic systems for steam reforming of tar, as primary or secondary catalyst, should be based on the following standards [29,34,35,51]:

- High efficiency on tar removal
- Suitable ratio of desired product (such as syngas)
- High resistance to deactivation by sintering, coking and/or fouling
- Easy regeneration
- Considerable mechanical strength for the commercial application
- Low cost and easy availability

Many catalytic formulations have been investigated in the literature for tar abatement through reforming reactions. The catalysts has been divided by El-Rub *et al.* into two main groups [52]:

(i) *Minerals,* which are available in nature and can be directly used or post-treated using physical treatment as calcination. Calcined rocks (calcite, magnesite, calcined dolomite), olivine and clay minerals are typical mineral

catalysts. These types of catalysts are typically used as a primary catalyst in a in-bed reactor.

(ii) *Synthetic catalysts,* which are chemically synthesized and relatively more expensive than the minerals. Within these groups are char, synthetic zeolite, alkali metal carbonates, activated alumina and supported-metal catalysts (Ni, Pt, Rh, Ru,…)

Supported-metal catalysts such as Rh, Ni and Co have been considered as an attractive option due to their high catalytic tar reforming at low temperatures, despite their high cost [53]. Furthermore, these catalysts are active in other parallel reactions such catalytic reforming of methane and of other light hydrocarbons, which upgrades even more the product syngas. Some of them, like Ni, can also catalyse the decomposition of NH_3 contaminants, reducing its level into the obtained syngas [54].

1.6.1. Supported-metal catalysts

Generally, supported-metal catalysts are composed by a metal phase (active phase) dispersed over a mixed oxide (catalytic support). A comparative studied of the different active phases used into the literature for reforming reaction will be presented below.

1.6.1.1. Active phases

The catalytic activity in methane reforming have been widely investigated for a series of transition metals using Ni, Ru, Rh, Pt, Pd, Ir as active phase [55–58]. A general agreement in the activity order, for both, dry (CO_2) and steam (H_2O) reforming was observed:

$$Ru \sim Rh > Ni \sim Ir > Pd \sim Pt$$

Tomishige *et al.*[59] studied the activity of several metals supported on CeO_2-SiO_2 for steam reforming of tars at 550 and 650 ºC using the same metal loading. They observed differences in catalytic activity tendency among the catalysts with the temperature. Whereas at low temperature (550 ºC) the catalytic activity decreased as follows: Rh > Pt > Pd > Ni ~ Ru; at higher temperature (650 ºC) nickel supported catalysts resulted to be more active than Pt and Pd, leading to the following tendency: Rh > Ni > Pd > Pt > Ru.

Nickel is the most widespread transition metal in the industrial catalysts used for steam and dry reforming reactions. Commercial nickel reforming catalysts is used for biomass gasification for tar reforming owing to its acceptable activity in heavy and light hydrocarbons steam reforming and its low cost [60]. Moreover, some researches

highlighted the ability of Ni based catalysts for ammonia decomposition. Noble metals are usually much expensive to be used in conventional industrial reformers [58].

Although their high activity in tar removal, supported-metal catalysts are prone to undergo deactivation owing to sintering, coke deposition and/or surface poisoning with sulphur, alkali metals or chlorine [51,53,60]. Therefore, the design and development of catalyst with high activity and resistance to catalytic deactivation are the main issues for catalytic reforming of tar. Metal-supported catalysts have been mainly used as secondary catalysts in a downstream reactor in form of ring (for instance, catalysts from BASF), or in monolithic structure, although there are some studies that used these type of catalysts as primary catalysts.

A deep study about the design of catalytic systems (influence of catalytic support, preparation method, addition of promoters…) as well as about the tar reforming (model molecules, catalytic test conditions, reaction atmosphere…) found in the literature will be presented along following chapters of the present work.

1.7. Efficient Use of Biomass for low Emission Production of Renewable Energy and biotechnological valuable Products (EBIPREP) project

The targeted EU climate and energy policy goals require that renewable energy become the main source of energy supply in the close future. In order to reach this ambitious goal, it is appropriate to link conventional and renewable energy or, better, combine and optimise sustainable individual processes intelligently.

Accordingly, the scope of this project is the development such sustainable subprocesses for the energy production using wooden biomass, which is the most significant renewable resources in Grand-Est and Black Forest region. Many sawmill owners are looking for an economic alternative based on the production and trade of wood chips generated from wood resides. To economize the energy- and cost-intensive drying process of wood chips, an innovative mechanical dewatering process has been developed by the company Bohnert. Consequently, a huge amount of liquid (200-250 L/ton fresh wood chips) rich in mineral components, named “wood juice”, is generated and treated as wastewater and, then, it has to be disposed in the sewage plant.

In EBIPREP project, specialists in biotechnology (UAS Offenburg), thermochemical conversion (UAS Offenburg), catalysis (University of Strasburg, UNISTRA), sensor

technology (UAS Karlsruhe) and environmental impact (UHA Mulhouse) joined to develop new solutions for the usage of the wood chips and the wood juice obtained during the mechanical drying process of biomass. The academic and industrial partners involve in EBIPREP project are presented in *Scheme 1.6.*

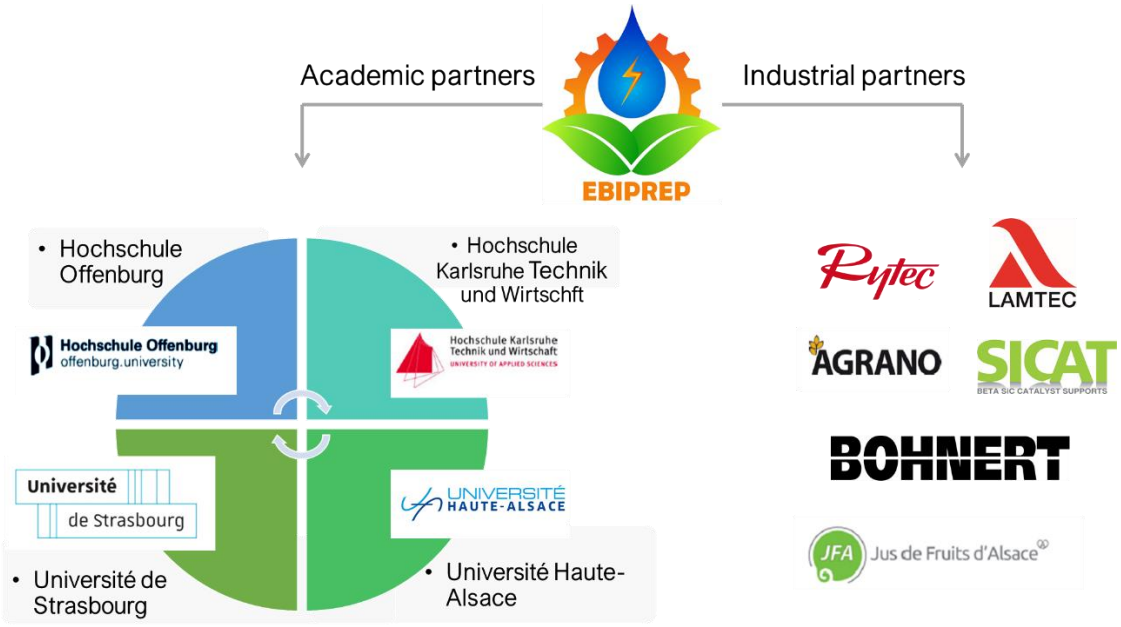

Scheme 1.6. Partners involve in EBIPREP project

The central aim of the project is the complete utilization of wood biomass as a renewable energy carrier by two biomass conversion processes: biotechnological processes, based on biomass fermentation and biogas production, and thermochemical process, based on thermal biomass gasification. Both individual processes show advantages and disadvantages. Biotechnological processes (fermentation and biogas production) produces a high-quality product gas (also from wet biomass as feedstock), but the process displays a slow production kinetic and, as aforementioned, it is less suitable for lignocellulosic feedstocks. By contrast, biomass gasification process generates a lower - quality product gas than the biotechnological processes, nevertheless, feedstocks are quickly converted and almost completely.

This project proposes the combination of both individual biomass conversion subprocesses in order to enhance significantly the overall efficiency compared to the single processes. The concept is presented in *Scheme 1.7*: the mechanical dewatered wood chips are implemented in the biomass gasifier to be converted into syngas. The wood juice are treated through two biotechnological processes: (i) used in biogas plants as a mineral-rich co-substrate in combination with the residues of fruit juice production or as single substrate or (ii) used in biofermentation as a nutrient source in the production of valuable bioproducts

such as, yeast or enzymes. Afterwards, the dried residues from these two biotechnological processes along with the wood chips are introduced into the gasifier. The thermal use of these residues opens the advantage to shorten the residence time in biogas reactor or reduce the reactor size. Then, the overall efficiency of this combined processes would increase compared to the single ones. The biogas and the syngas are unified and constitute the product gas of the overall process, that could be used for heat and electricity generation.

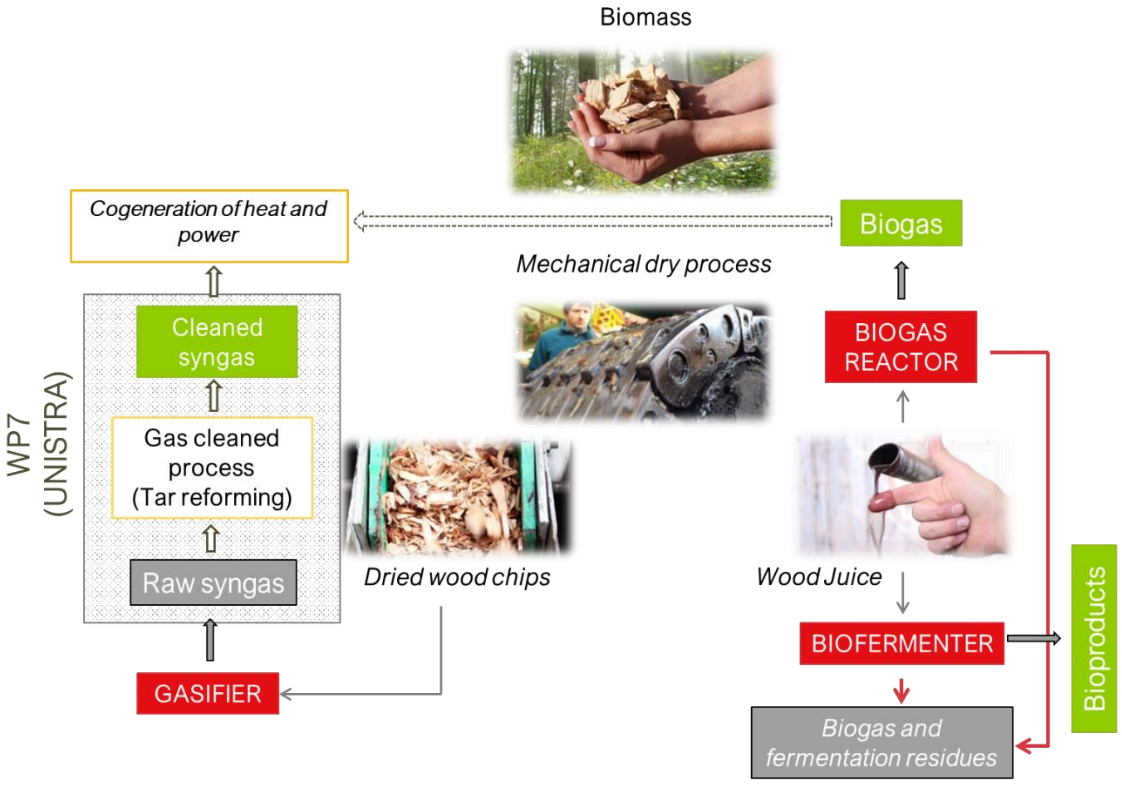

Scheme 1.7. Overall process for the efficient use of biomass for sustainable production of energy and high valuable bioproducts

1.7.1. Role of UNISTRA into EBIPREP

As presented in literature, the condensation of tar generated during biomass gasification process is one of the most important issues of this thermochemical process, causing clogging of pipes, sensors… but also disrupting the downstream applications. Catalytic reforming as a gas cleaning treatment of the raw syngas seems to be an attractive alternative to limit the environmental impact of biomass use and enhance the product gas quality. Many types of catalysts have shown a potential for tar removal, nevertheless no formulation that meets the high requirements (high activity, resistance to catalytic deactivation, easy regeneration…) are currently available. For these reasons, the role of UNISTRA in EBIPREP project is the development of catalytic materials to meet these specifics needs.

1.8. Objectives of this PhD work

In the framework of EBIPREP project, the main objective of this thesis is the development of a competitive catalytic systems for gas cleaning treatment after biomass gasification process.

The present PhD work deals with the synthesis and characterization of nickel supported catalysts for tar reforming reactions. The catalytic supports under study are based on mixed oxides with high oxygen mobility in order to limit the formation of carbon deposition from tar decomposition through carbon gasification. The choice of the support's compositions will be detailed along the following chapters. Afterwards, the catalytic activity of the synthesized catalysts in tar abatement is evaluated using model tar molecules, phenol and toluene, at laboratory scale. As the main aim of the work is the catalytic application under real biomass gasification conditions at large scale, an exhaustive optimization of the catalytic structuration over β-SiC-based extrudates has been conducted in order to choose the best parameters for the preparation of structured catalysts at large scale. The best powdered catalysts, in terms of catalytic activity and stability, have been selected and structured over β-SiC-based extrudates. The catalytic activity and stability of these structured catalysts have been as well evaluated at laboratory scale. Lastly, the structured catalysts at large scale were prepared and tested under real biomass gasification conditions at medium pilot plant scale. As one of the goals of EBIPREP project is the incorporation of the residues generated during the biotechnological processes into the gasifier, catalytic tests using wood chips and mixture wood chips + residues as biomass feedstocks in the gasifier were performed.

This manuscript is divided into five chapters:

- *Chapter 1 – General introduction*: overview of the use of biomass as renewable energy carrier. Particularly, the limitation of biomass gasification as thermochemical conversion to generate energy and the possible alternatives to reduce or improve these limitations, being catalytic reforming an attractive way for the improvement the overall efficiency.

- *Chapter 2 – Synthesis and characterization of catalytic systems:* the synthesis of nickel supported over CeO_2-ZrO_2-Sm_2O_3, CeO_2-Y_2O_3 and La_2O_3-SrO-Co_2O_3-Fe_2O_3 mixed oxides, using two ways for adding the active phase. The characterization results are shown and discussed in order to determine the effect of the Ni addition pathway in the physico-chemical properties of the mixed oxide supports.

- *Chapter 3 – Pre-treatment conditions and catalytic tests: powdered systems:* the effect of the addition pathway and the different catalytic supports in the catalytic activity and stability in tar reforming reaction using two tar model molecules (phenol and toluene) is presented. Pre-treatment conditions under different atmosphere (H_2 or syngas) and their influence of the catalytic activity and stability are also discussed. The three catalysts that display the better catalytic activity and stability in steam reforming of tar at laboratory scale are selected for the subsequent structuration.

- *Chapter 4 – Optimization of catalytic structuration over SiC-based extrudates and catalytic tests:* the optimization of the catalytic structuration parameters and the characterization of the structured catalysts are presented. In order to evaluate the impact of the structuration in the catalytic efficiency in tar removal, catalytic test at laboratory scale using toluene as tar model molecule is shown. Lastly, a comparison between the structured catalysts obtained at small scale and those at large scale to elucidate possible modifications due to the scale up process is also reported. Three batches of 1.2 L based on the three best catalysts selected were prepared for the catalytic test under real conditions in a pilot plant.

- *Chapter 5 – Catalytic test at biomass gasification pilot plant scale:* complete the research with the study of the catalytic performance of the three selected catalysts under real conditions at biomass gasification pilot plant scale. As prior mentioned,

studies of the catalytic efficiency in tar removal using wood chips and a mixture with residues from biogas reactor are presented. As well, studies of *in situ* catalytic regeneration and its influence in the catalytic activity can be found in this chapter.

CHAPTER 2

SYNTHESIS AND CHARACTERIZATION OF CATALYTIC SYSTEMS

Abstract

As presented in the general introduction, Ni-supported catalysts have been widely used in industrial scale for tar abatement. Despite their high activity in tar reforming, these catalysts easily undergo catalytic deactivation due to the severe reaction conditions.

In this context, a deep state of art about the optimization of Ni-based catalysts reported in the literature to enhance their resistance to catalytic deactivation is detailed in the present chapter. Based on this, Ni supported samples over three different mixed oxides with high oxygen mobility have been synthesized and the active phase of Ni was added through two pathways. The textural and physicochemical properties of the prepared catalysts are presented and discussed in order to elucidate the possible modifications in the support properties caused by the addition method and to further explain their catalytic behaviour. Besides, some operation conditions as the reduction pre-treatment are determined from the characterization results.

2.1. Introduction

Nickel-based catalysts have been widely used for tar reforming due to the high activity/cost ratio of nickel. Their high activity is associated with the fact that metallic nickel easily promotes tar decomposition by activation and cleavage of C-C, C-H and O-H bonds [51,52,61,62]. Besides, other molecules that can participate in tar reforming as H_2O and CO_2 can be also activated by these catalytic materials [35]. Thus, numerous commercial nickel-based catalysts, commonly supported over alumina (Al_2O_3), are available for tar abatement [63–65]. For instance, Coll *et al.* [64] have studied the decomposition of five different tar model molecules (benzene, toluene, naphthalene, anthracene and pyrene) over two commercial nickel-based materials (UCI G90-C and ICI 46-1) and their tendency to coke deposition. Park *et al.* [66] evaluated the activity of a commercial CH_4 reforming catalyst, FCR-4 (12 wt% Ni/α-Al_2O_3), in toluene reforming reaction at 600 ºC for 100 h introducing 30 mg/Nm^3 of toluene. A decrease in toluene conversion from 78.9% to 45.3% over the reaction time was found. The carbon deposits have been evaluated by SEM and TGA analysis from which the authors concluded that the loss of activity was due to structurated carbon blocking of the active sites. In other study, Laositipojana *et al.* [67] studied a Ni/Al_2O_3 catalyst for ethanol reforming to generated H_2-rich syngas. They observed a quick deactivation and a decline of H_2 selectivity by more than 30% within 20 min. Additionally, a large amount of carbon deposition was found for the catalyst.

Despite the high activity in catalytic tar removal exhibited by Ni-based catalysts, it should be stressed that gasification conditions (high temperatures, high pressure steam, presence of impurities, particles, ashes…) create a harsh environment for these catalytic materials. Then, nickel reforming catalysts must face several challenges as consequences of these conditions, including sulphur poisoning, carbon formation and sintering, which are closely linked [51,68,69]. The deposition/encapsulation of carbon over the active metal sites and the metal sintering in steam rich environment have been recognised as the main catalytic deactivation processes of Ni-based catalysts. Therefore, the development of efficient catalytic materials with high activity and resistance to deactivation produced by metal sintering and/or coke formation is crucial for catalytic reforming of tar.

The catalytic performance in term of activity and stability of Ni-based catalysts generally depends on many different parameters, such as the metallic nickel loading, the method of synthesis, the nature of the support and the addition of promoters (alkali metals) and/or dopants (noble metals).

The metal-support interaction as well as the active particle size and its dispersion are strongly influenced by the nickel loading. For instance, Artetxe *et al.* [70] carried out a catalytic steam reforming of six different tar model compounds (phenol, toluene, methyl naphthalene, indene, anisole and furfural) over Ni/Al_2O_3 catalysts with 5, 10, 20 and 40 wt% nickel loading. Whereas the tar conversion and H_2 formation increased with the increase of Ni loading from 5% to 20%, these values decreased with increasing Ni up to 40%. The mentioned decrease is caused by a larger Ni particle size and lower specific surface area of the catalyst. Simultaneously, the formation of coke was increased with the increase of Ni content and reached its maximum for the 40 wt% Ni catalyst. Similarly, Li *et al.* [71] found that an increase in Ni loading favours the activity of the catalyst, but do not avoid the deactivation in acetic acid steam reforming. They observed that nickel particles probably form aggregations during the synthesis process when Ni content are higher than 20 wt%. Then, large size particles are formed, giving faster metal sintering and coke deposition on the catalyst. Additionally, Yue *et al.* [72] suggested that lower tar conversion for high Ni contents is related to an increase in Ni particle size and the subsequence decrease in its specific surface area.

The choice of catalyst supports is another important parameter that can enhance the catalytic performance [69,73,74]. Many studies have been focused on the effect of catalyst support on the performance of Ni-based catalysts [51]. The dispersion of Ni on the support improves metallic Ni surface, avoid the nickel agglomeration by sintering, and could promote carbon gasification process [74]. Thus, the properties of a catalyst such as reducibility, metal dispersion, mechanical strength and/or thermal stability might be influenced by acidity/basicity, specific surface area, pore structure and electronic structure of the support [51,65,69]. Additionally, the support plays roles during catalytic reaction offering adsorption sites to the reactants and interacting with active metals.

2.1.1. Support

Many supports have been widely used to disperse the nickel particles. These supports could be mainly classified in the literature into five categories: (i) acid supports (Al_2O_3); (ii) natural pre-treated minerals (calcined olivines, dolomites, calcites); (iii) mesostructured and highly ordered zeolites and silicas (SBA-15, ZSM-5, MCM-41,…); (iv) synthetic mineral-like supports (spinels, hydrotalcites, …) and (v) supports with high oxygen mobility (CeO_2, doped CeO_2, perovskites…). Here after, an overview of the main characteristics of each category is presented.

2.1.1.1. Acid supports

As it has been above mentioned, alumina is the most typical support for nickel-based catalysts for tar reforming reactions due to its good mechanical strength, chemical/physical stability, and high specific surface area which might enhance the dispersion of the active metal phase. However, alumina-supported nickel catalysts are easily deactivated by sintering and carbon deposition, since its acidic character favour reactions such as, hydrocarbon dehydration, thus, promoting the coke formation [75]. An enhancement of the catalytic stability of these catalysts by doping Al_2O_3 with other mixed oxides such as MgO, CaO, Fe_2O_3, CeO_2 or La_2O_3 among others, have been observed by different authors [72,76–79]. These additives lead to higher nickel dispersion due to the stronger metal-support interaction. Moreover, a decrease in the acidity (case of basic oxides as CaO and MgO) improves also the resistance to coke formation and, in case of redox metal oxides, to the presence of oxygen vacancies might promote the carbon gasification process.

2.1.1.2. Natural (pre-treated) minerals

Natural minerals, such as dolomites, olivines and calcites have been employed as supports of tar steam reforming catalysts, due to their low cost, their non toxicity, their availability and their high activity at high temperatures [51,80]. Dolomite presents a general chemical formula $Ca,Mg(CO_3)_2$ and generally contains 30 wt% CaO, 21 wt% MgO, 45 wt% CO_2 and trace amounts of minerals such as SiO_2, Fe_2O_3 and Al_2O_3 [47,51]. It has been reported that calcined dolomite is more active in terms of tar reduction than the un-calcined dolomite due to its larger surface area and higher oxide content at the surface [81–83]. For instance, Hu *et al.* [83] studied the effect of calcination of dolomite, as well as olivine, as downstream catalysts in steam gasification of apricot stone and found that calcined dolomite is the most effective catalyst among all tested catalysts for increasing the H_2 content in the resulting syngas. Moreover, the addition of Ni in calcined dolomite favoured the tar reduction. In addition, Chang *et al.* [84] observed that the yield increased by 33% for H_2, by 7% for syngas production whereas a decrease of 59% of CH_4 yield were observed over a Ni/dolomite at 900 ºC compared with calcined dolomite catalysts without Ni loading. Xu *et al.* [85] have carried out chemical loop reforming of toluene over 20 wt% of CuO, NiO and Fe_2O_3 supported on calcined dolomite. Among all catalysts, they observed that NiO/dolomite exhibited the highest syngas purity under different reactions conditions. Additionally, this catalyst showed the lowest carbon deposition, the best regeneration and cycle performance. Calcined dolomite-based materials exhibit high activity for decomposition of phenols and oxygenated compounds. However, the catalysts are less

effective for PAHs removal formed in air-blown gasification [54,81]. In addition, calcined dolomite has some limits in its application in fluidized bed reactor, associated to the easy attrition due to its soft and fragile properties [86]. Olivine is mainly a silicate mineral in which magnesium and iron cations are set in the silicate tetrahedrals. The general formula of natural olivine is $(Mg,Fe)_2SiO_4$ [47,51,87]. Apart of the main advantages of natural minerals, olivine is characterized by its high attrition resistance compared to dolomite. It can provide good resistance to attrition even at high temperature. Thus, olivine is of great interest for the *in situ* tar abatement in fluidized bed biomass gasification applications [87]. However, olivine shows slightly lower activity in biomass gasification and tar reforming than dolomite. Therefore, the addition of some metals to olivine can improve its tar reforming activity. In this sense, the activity in tar removal of olivine-supported Ni catalyst was demonstrated by several studies. Świerczyński *et al.* [88] found a higher catalytic activity for Ni/olivine catalyst, with higher selectivity of H_2 and CO and lower carbon deposition, compared with bare olivine. Similarly, Michel *et al.* [89] have tested olivine and Ni/olivine in steam reforming of α-methylnaphthalene as tar model compound, observing an increase in α-methylnaphthalene conversion for Ni/olivine related to bare olivine.

2.1.1.3. Mesostructured and highly ordered zeolites

Mesostructured and highly ordered zeolites, silica and alumina-silica are considered acid catalysts. Zeolites are crystalline aluminosilicates linked through oxygen atoms, producing a three-dimensional network with channels and cavities of molecular dimensions [90,91]. Among the properties of zeolites as heterogeneous catalysts it can be highlighted [92]: (a) high surface area; (b) molecular dimensions of the pores; (c) adjustable acidity; (d) high thermal/hydrothermal stability; (e) high resistance to nitrogen and sulphur compounds; and (f) easy regeneration ability. Other advantages of zeolites are their relatively low price, and the knowledge gained about them from long used in fluid catalytic cracking (FCC) units. Nevertheless, one of the main disadvantages of these materials is the rapid deactivation by coke deposition owing to their acidity [52,93]. The confinement effect of mesoporous materials can stabilize the Ni particles during reduction process, increasing the long-term stability [94]. Thus, the combination of zeolites with Ni properties can lead to a catalytic material with high potential in tar abatement. Tang *et al.* [95] studied the effect of Ni loading (6, 9, 12 and 15 wt%) over HF-modified ZSM-5, labelled as FZ5, in toluene steam reforming. They observed that 9Ni/FZ5 was the best catalyst in toluene steam reforming at 650 ºC, leading to the highest H_2 yield and the lowest amount of carbon deposits. This good performance has been related to the high metal dispersion found on this catalyst. Ye *et al.*

[96] investigated the effect of the acidity of the support MCM-41 on Ni/MCM-41 catalyst in biomass gasification. They concluded that the more acidic the sites, the higher the amount of H_2 generated. Nonetheless, the carbon formation was also promoted.

2.1.1.4. Synthetic minerals

Others Ni-based catalyst formulations with a good catalytic performance in tar steam reforming are the Ni supported over synthetic minerals such as hydrotalcite, palygorskite or mayenite. This kind of support provides small metal nanoparticles, then, high metal dispersion due to their strong metal-support interaction [51,69,97]. Li *et al.* [98] investigated the influence of the composition and reduction pre-treatment of Ni/Mg/Al catalysts obtained from hydrotalcite precursors for steam reforming of tars coming from pyrolysis of biomass. The characterization results showed the formation of nanocomposite between Ni metal and Mg(Ni,Al)O particles resulting in relatively small Ni particles and low coke formation. Chen *et al.* [99] investigated the effect of Ni loading (0, 2, 5 and 8 wt%) in Ni/palygorskite (Ni/PG) catalyst, reaction temperature (650, 750 and 800 ºC) and inlet CO_2/toluene ratio on H_2 yield and carbon deposition during toluene dry reforming. In general, Ni5/PG and Ni8/PG exhibited the best H_2 yields. In addition, they observed a decrease in the H_2 yield and in carbon deposition with the increase in temperature and in CO_2/toluene ratio.

2.1.1.5. Supports with high oxygen mobility

The oxygen mobility and oxygen storage capacity are support properties with an important role in the activity and stability in reforming reactions [69,100]. Supports with high concentration of oxygen vacancies and mobile oxygen species in the support structure can promote the water activation during steam reforming reaction and thereby boost the gasification of carbon species deposit *via* oxygen supply to the active phase.

Considering the importance of oxygen mobility in reforming reaction, a literature research focused on the ionic conducting ceramics or solid electrolytes widely developed for technologies applications such as, solid oxide fuel cells (SOCF) or batteries, has been carried out. Among the wide variety of solid electrolytes, fluorite-type electrolytes and perovskite structure oxides are the most common oxygen-ions conductor [101–103]. Fluorite-type electrolytes are the conventional fast oxide-ion conduction materials. Industrially, the most extensively used and investigated are the solid solutions like AO_2-A'O or AO_2-A''$_2O_3$, where A are tetravalent cations (Zr^{4+}, Ce^{4+}, Hg^{4+}, Th^{4+}) and A' and A'' are di- and trivalent cations (Ca^{2+}, Sr^{2+}, Ba^{2+}, Sc^{3+}, Y^{3+}…) [102]. Among them, although yttria-stabilized ZrO_2 (YSZ) is the electrolyte material par excellence for SOFC applications, Ce-based electrolytes based on Sm_2O_3- or Gd_2O_3-doped CeO_2 constitute a promising

alternative as electrolytes for intermediate temperature SOFC, exhibiting higher ionic conductivity than YSZ solids [103]. Concerning to the perovskite structure electrolytes, it has been also considered a promising ionic ceramic material widely used in solid-state electrochemistry as electrodes and electrolytes. Within these materials, lanthanum-transition metal oxides substituted by alkaline earth metals stand out owing to their electrical, magnetic and catalytic properties [101,102].

According to the latter and to the fact that reducible oxides such as ceria- and perovskite- based materials are well-known for their high lattice oxygen mobility, the influence of the oxygen mobility in the steam reforming of tar will be discussed in the following sections for these two latter types of materials.

- *Ceria-based supports*

Ceria shows a high lattice oxygen mobility and oxygen storage capacity (OSC) due to its peculiar property of being able to stabilize both Ce^{4+} and Ce^{3+} cations in its fluorite structure [104,105]. The presence of Ce^{3+} ions leads to the creation of oxygen vacancies, where water can be activated and oxygen species can be absorbed. Afterwards, these oxygen species can diffuse to the active metal-ceria interface and contribute to the reaction by removing the carbon deposit by gasification process [69]. An enhancement of catalytic performance and coke resistance during steam reforming of tar by CeO_2 as a promoter or as a bare support has been reported in many studies. For instance, Zhang *et al.* [106] investigated the effect of Ce doping over Ni/γ-Al_2O_3 in tar reforming and they found that a 5 wt% of Ce-doped γ-Al_2O_3 supported Ni sample led to the best catalytic performance. Accordingly Ashok *et al.* [107] showed that the addition of CeO_2 to Ni/Ca-Al oxide improved the catalytic performance in toluene steam reforming and inhibited the coke formation. Garcia-Garcia *et al.* [108] observed that the highest H_2 yield in steam reforming of m-cresol at 700 ºC was reached for Ni supported on CeO_2 among Ni supported on γ-Al_2O_3, α-Al_2O_3, olivine sand, zircon sand and La_2O_3/γ-Al_2O_3. However, some drawbacks as the thermal sintering of CeO_2 particles at high temperatures, leading to a decline of oxygen mobility, which is linked to the OSC and catalytic activity have been found for pure CeO_2. Thus, the enhancement of the oxygen mobility and thermal stability as well as the improvement of bulk reducibility induced by doping CeO_2 with isovalent/aliovalent cations have received a great deal attention in order to improve the catalytic performance [109]. The incorporation of isovalent cations with smaller ionic radius than Ce^{4+} such as Zr^{4+}, Hf^{4+}, Tb^{4+} etc. improves the thermal stability and also increases the dynamic OSC [110]. The dynamic OSC reflects the most reactive oxygen species and available oxygen ions, mainly linked to the surface

oxygen and oxygen vacancies and it is closely related to the mobility of oxygen [110]. As it has been described in the literature, the higher oxygen mobility and concentration of oxygen vacancies, the better the dynamic OSC [110–112]. Doping CeO_2 with smaller isovalent cations weakens the metal-oxygen interaction into the lattice due to the formation of longer M-O bonds, thereby making oxygen ions more mobile [113,114]. Therefore, the introduction of smaller isovalent non-reductible cations into ceria lattice enhances OSC by generating intrinsic oxygen vacancies (*Equation 2.1*), promoting the oxygen mobility by enhancing the Ce^{4+}/Ce^{3+} redox process [115].

$$2Ce^{4+} + O_O^x \leftrightarrow \frac{1}{2}O_2(g) + 2Ce^{3+} + V_0^{\bullet\bullet} \qquad \textit{Equation 2.1}$$

, where Ce_{Ce}^x is the ceria cation on the Ce site with neutral charge, O_O^x is oxygen anion in the place of oxygen anion in the ceria lattice, Ce_{Ce}' is Ce cations on Ce sites with an electron and $V_0^{\bullet\bullet}$ is a compensating oxygen vacancy doubly positive charged. It should be noted that this oxygen vacancy formation is a consequence of the system maintaining charge neutrality as part of the doping process.

Among all isovalent cations found in the literature, Zr-doped ceria (CeO_2-ZrO_2) solid solution is the most widely used in industry due to its high thermal resistance, higher reduction efficiency of redox couple Ce^{4+}/Ce^{3+} and better OSC compared to those of pure ceria [110]. For instance, Maia *et al*. [116] studied the influence of Zr-doped ceria supports in $Ni/Ce_xZr_{x-1}O_2$ systems during steam reforming of glycerol and reported that the best activity and stability exhibited by $Ni/Ce_{0.5}Zr_{0.5}O_2$ was directly correlated with the highest oxygen storage capacity result, thus a better oxygen mobility, among the different Ce/Zr studied. Ocampo *et al*. [117] studied the effect of Ni loading on $Ce_{0.72}Zr_{0.28}O_2$ material in carbon dioxide methanation and found that partial substitution of Zr^{4+} by Ni^{2+} improved the redox properties of the support, giving rise to better catalytic performance and stability.

Recently, the use of aliovalent elements (trivalent and/or divalent cations) as dopants into the CeO_2 lattice has received much attention. In addition to increasing the intrinsic oxygen vacancies of bare ceria by doping by aliovalent non-reducible cations such as Gd^{3+}, La^{3+}, Y^{3+}, Sm^{3+}, Eu^{3+} etc., additional extrinsic oxygen vacancies are also formed when these cations substitute Ce^{4+} in the lattice (*Equation 2.2*). These vacancies might increase the diffusion rate of lattice oxygen species, thus enhancing the ease with which the oxide can adsorb/release oxygen [118,119].Thus, Lucia *et al.* [120] reported that an enhancement in ionic conductivity might be expected when ceria is doped with cations with low association energies as it is the case of yttrium (Y^{3+}) and any rare-earth (RE^{3+}) dopants. In this condition,

the doped ceria should show a good ionic conductivity since the oxygen ions are theoretically free to move at low dopant content. Laobuthee *et al.* [104] showed an improvement in the reducibility and OSC of $Ce_xSm_{1-x}O_2$ using a small amount of Sm, as well as an increase of the H_2 yield during toluene steam reforming for $Ce_{0.85}Sm_{0.15}O_2$ compared to bare CeO_2. A higher Sm content resulted in a decrease in the OSC along with a decrease in catalytic activity, possibly due to the inability to form a pure solid solution structure.

$$M_2O_3 \leftrightarrow 2M'_{Ce} + 3O_O^x + V_0^{\bullet\bullet} \qquad \textit{Equation 2.2}$$

, where M is the trivalent cation, M'_{Ce} is the trivalent cation on the Ce cation site with an electron, O_O^x oxygen anion on the oxygen anion site into ceria structure and $V_0^{\bullet\bullet}$ is a compensating oxygen vacancy doubly positive charged.

Similarly, doping CeZr mixed oxides with rare earth (RE^{3+}) such as Gd^{3+}, Sm^{3+}, Eu^{3+} etc. upgrades OSC, redox properties and thermal resistance compared to single oxides, since the replacement of Ce^{4+} with RE^{3+} ions would result in additional oxygen vacancies [121–123]. Thereby, these oxygen vacancies could improve the diffusion rate of oxygen species [122,123]. Besides that, the ionic radius of all RE elements are larger than Zr^{4+} (0.84 Å in 8-fold coordination) resulting in a more effective stabilization of fluorite type structure. Harshini *et al.* [121] studied the influence of Tb into CeZr mixed oxide ($Ce_{0.75-x}Zr_{0.25}Tb_xO_2$, x = 0.0–0.2) using a Ni-based catalyst in propane steam reforming. An increase in the OSC were found for Tb-containing CZ oxides compared to the bare CZ and the performance of the catalysts were directly associated to the determined OSC. The catalyst with highest OSC exhibited the best catalytic performance and stability in propane steam reforming.

- *Perovskite-based supports*

Perovskite-based materials become important type of materials within the mixed oxide category due to their high thermal stability, ionic conductivity, electron mobility and redox properties [124,125]. The general formula of perovskite is ABO_3, where A is commonly a lanthanide, alkaline or alkaline-earth cation and B is any transition metal cations as Mn, Co, Fe, Ni, etc. Considering a utopic cubic perovskite unit cell (space group Pm3m), the larger cation (A) are coordinated with 12 oxygen anions whereas the smaller cation (B) coordinates with 6 oxygen anions. Experimentally, the partial substitution of A or B site metals by other ions with different valence and/or cationic radius provokes a distortion in the crystalline structure providing structural defects in the lattice [126,127]. These structural defects lead to the formation of oxygen vacancies and, hence, to a high content of mobile

oxygen species. Then, a more general formula, $A_{1-x}A'_xB_{1-y}B'_yO_{3\pm\delta}$, has been reported for these kinds of mixed oxides. The many possible substitutions at both A and B sites offers a wide flexibility in terms of adapting and tuning of their physicochemical properties. For instance, incorporation of reducible transition metal such as Co, Mn or Fe cations into the B sites supplies redox active sites that could promote catalytic reactions [125,128,129]. Furthermore, a partial substitution of A-sites with other elements as Sr, Ca, Ba cations can generate oxygen vacancies into the structure and enhance oxygen mobility [130,131]. As the possible composition of a perovskite oxide is almost infinite, this section will be mainly focused on the role of lanthanum-containing (La-based) perovskites oxides in tar reforming, since they have been the most commonly investigated and have shown an outstanding performance in different types of catalytic reactions like CO oxidation, methanol and NO conversion [124,125].

Partial insertion of alkaline earth element (Ca^{2+} or Sr^{2+}) or a lanthanide aliovalent cation (Ce^{4+}) substituting La^{3+} into the A sites induces oxygen nonstoichiometry into the perovskite structure, improving the oxygen mobility and thus, enhancing the catalytic performance [132]. Owing to the atomic size, strontium (Sr) has been widely used as a dopant on the A-site, generating $La_{1-x}Sr_xMO_3$ (M = Fe, Co, Al…) oxides [125,133]. Divalent strontium partially inserted into La^{3+} sites leads to oxygen vacancies formation. In addition, the introduction of high valence M cations into the B-site such as Fe, Cr, Co, favours oxygen and electron transfer. Accordingly, the best catalytic activity and coke resistance in steam reforming of toluene has been reported by Oemar *et al.* [126] for $Ni/La_{0.8}Sr_{0.2}AlO_3$, among $Ni/LaAlO_3$, $Ni/La_{0.8}Sr_{0.2}AlO_3$, Ni/La_2O_3 and $Ni/\alpha\text{-}Al_2O_3$ materials. The characterization of the catalysts showed that the high catalytic performance of $Ni/La_{0.8}Sr_{0.2}AlO_3$ would be associated to the lattice distortion as a consequence of Sr doping, since it generated higher content of oxygen vacancies at the surface of the catalyst. As well, the effect of a Mg, Ca and Sr doping of 20% into $LaNi_{0.8}Fe_{0.2}O_3$ (LNFO) in steam reforming of toluene has been reported [134]. The catalytic activity decreased with the following order: Sr-doped LNFO > Ca-doped LNFO > Mg-doped LNFO, whereas the deposited carbon exhibited the opposite tendency: Sr-doped LNFO < Ca-doped LNFO < Mg-doped LNFO. Thus, the enhancement in the catalytic activity and resistance to coke deposition promoted by the higher number of active sites and lattice oxygen species has been evidenced for Sr-doped LNFO material. Sekine *et al.* [135] studied the effect of different alkaline-earth metals (Sr, Ba and Ca) on $Ni/LaAlO_3$ catalyst in steam reforming of toluene and found that the catalyst with Sr doping of 30% into $LaAlO_3$ structure led to the best catalytic activity and the lowest amount of deposit carbon. Transient isotopic tests using $H_2{}^{18}O$ were carried over

$Ni/LaAlO_3$, $Ni/Sr/LaAlO_3$ and $Ni/La_{0.7}Sr_{0.3}AlO_3$ in order to determine the promotion mechanism. The results showed that ^{16}O products from the redox of the lattice oxygen in the catalyst and $H_2{}^{18}O$ were only observed over the $Ni/La_{0.7}Sr_{0.3}AlO_3$ catalyst. Hence, the partial substitution of La by Sr cations into the perovskite structure activate lattice oxygen species to promote the toluene reforming and suppression of carbon deposition.

2.1.2. Preparation method

The preparation method can have a strong impact in the physicochemical properties (specific surface area, pore volume, dispersion of the active phase) of synthesized catalysts and thereby plays a crucial role in the catalytic performance. Many studies report the optimization of the preparation method by changing the synthesis route, calcination temperature, adjusting the Ni loadings and/or the ratio Ni/promoter etc. The impregnation method has been considered as the most conventional method for catalyst synthesis. A catalytic material with large metal particles, weak metal-support interaction and heterogeneity in the composition of the catalysts is typically obtained by this method [136–139]. Furthermore, other synthesis methods such as sol-gel [140,141], colloidal [142], ammonia evaporation [143], co-precipitation, hydrothermal synthesis [144] have been reported as promising alternatives for catalyst preparation.

Wang *et al.* [145] found that Ni-based catalysts synthesized by co-precipitation method exhibited smaller metal nanoparticles, higher dispersion and stronger metal-support interaction than that obtained by wet impregnation, resulting in a more stabilized structure. Blanco *et al*. [140] evidenced a higher catalytic performance in terms of tar conversion and H_2 production for sol-gel Ni/SiO_2 catalyst compared to the corresponding impregnated sample. This was attributed to higher specific surface area and lower pore size obtained with the sol-gel prepared catalyst [140]. Accordingly, Ocampo *et al.* [117,146] investigated the CO_2 methanation over Ni-Ce-Zr mixed oxide synthesized via one-step pseudo sol-gel method. A higher methane yield and better stability was found for the sol-gel Ni-CZ catalyst compared to the equivalent material prepared by impregnation, Ni/CZ. This enhancement in the catalytic performance by one-step pseudo sol-gel method was attributed to the partial Ni^{2+} insertion into the CZ mixed oxide structure.

2.1.3. Modification of Ni-based catalysts

The catalytic performance of Ni based catalysts in steam reforming can be also modified by the addition of several promoters (alloying with other transition metals and noble metals, incorporating rare earth, alkaline-earth metals and alkali metals) [51]. Noble metals display high catalytic activity, good resistance to coke deposition and sulfur tolerance in

steam reforming process. As it is well known, noble metals (Pt, Rh, Ru, Ir, Au, etc.) exhibit faster carbon gasification kinetic than transition metals and their low carbon solubility in their bulk avoids the growth of carbon at the surface [147]. Therefore, the doping of Ni-based catalysts by noble metals could enhance the resistance to carbon deposition and thereby improve the catalytic stability.

Salehi *et al.* [148] studied the effect of adding ruthenium to a conventional Ni/Al_2O_3 catalysts on the H_2 production in catalytic steam reforming of bio-oil at different temperatures. An increase in the H_2 yield and carbon conversion was found for all Ru-containing catalysts. Additionally, the effect of Ru doping was noteworthy at lower temperatures in terms of H_2 yield and carbon conversion. Chen *et al.* [149] showed the catalytic behaviour of monometallic and bimetallic Ni catalysts (Ni-Fe, Ni-Cu, IrNi, RhNi, PtNi, RuNi, AuNi and PdNi) in steam reforming of tars. An improvement of the catalytic activity due to the addition of noble metals have been observed, and PdNi provided the best performance among the noble metal-containing catalysts. This highest performance should be associated to the promotion of Ni reduction and Ni dispersion. Other studies reported that the active Ni sites could be stabilized in the reduced state under reaction conditions with the incorporation of noble metals, resulting in the increase of tar conversion and decline of coke deposits [150,151]. Moreover, some investigations proved that deactivation process by sintering of Ni-based catalysts could be decreased by the presence of noble metals (NM) due to Ni-NM alloy formation [152,153].

2.2. Choice of catalytic systems and preparation method

The state of the art of Ni-based catalysts for steam reforming of tar highlights the importance of both the catalytic support and the preparation method in the resulting catalytic performance. Supports with high oxygen mobility and OSC capacity are considered promising materials in tar abatement through steam reforming reaction. The use of these kind of support might improve the resistance to coke deposition over the surface of the Ni-based catalysts, thus, enhances the lifetime of the catalytic system. Additionally, the preparation method of the catalysts and the pathway used for adding the active phase strongly influence the physicochemical properties of the catalytic system and thus its catalytic behavior.

According to literature, fluorite- and perovskite-based materials are promising ionic conductors ceramics displaying high oxygen ion conductivity. This property makes these kinds of materials attractive for their use as catalytic support in reforming reaction for inhibiting catalytic deactivation thru coke formation. Among them, Ce-based oxides and La-

based oxides have been received special attention on catalysis applications. Indeed, many researches based their investigation in the improvement of these two mixed oxides. Taking that into account, in the present work, Ce-and La-based oxides have been selected as catalytic supports. As above mentioned upgrades in other works, the increase of oxygen vacancy content in Ce-based supports by doping of bare ceria with cations of different chemical nature is aimed. Hence, samarium-doped CeZr mixed oxide, $Ce_{0.63}Zr_{0.33}Sm_{0.04}O_{2-\delta}$, and yttrium-doped ceria, $Ce_2Y_2O_7$, as two different doped ceria-based supports were prepared. Concerning the perovskite-based support, the partial insertion of Sr into La-site in La-based materials showed improved catalytic activity and resistance of coke deposition by enhanced oxygen mobility [134,135]. Moreover, the incorporation of reducible transition metals as Co, Fe, Mn at the B-site provides redox active sites that determine the adsorption and desorption of hydroxide ions and, therefore it might promote the steam activation during steam reforming reaction [125,128]. Considering that, the synthesis of a La-based perovskite with the following composition: $La_{0.6}Sr_{0.4}Co_{0.2}Fe_{0.8}O_{3-\delta}$ has been carried out.

As regard to the synthesis method, sol-gel methods lead to an easy formation of mixed oxides materials as well as to an easy deposition of the catalysts over catalytic substrate during catalytic structuration. Considering that this synthesis method has been widely used and optimized in our research group, and the fact that the final objective of this work is the catalytic structuration at large scale, the synthesis of the catalytic supports has been carried out using a sol-gel method.

In our research group, Ni-Ce mixed oxide systems have been highly investigated in several catalytic reactions due to their high efficiency and stability related to the enhancement of ceria redox properties as a consequence of the strong Ni-Ce interactions [117,146]. Thus, the addition of Ni (10 wt% Ni^0) has been studied through two synthesis routes: its direct incorporation in the material by a one-step pseudo sol-gel method and its deposition by conventional wet impregnation on the three supports prepared by the pseudo sol-gel method. Additionally, the addition of Ru (1 wt% Ru^0) by wet impregnation over one of the resulting catalysts has been performed to elucidate the influence of noble metal doping on the catalytic activity and on the formation of carbon.

2.3. Partial objectives

In this chapter, the different syntheses are detailed, and the characterization results of the different materials are presented and discussed in order to determine the effect of the synthesis method on their physicochemical properties.

The characterization techniques used in this work are: N_2 physisorption, XRD, H_2-TPR, XPS and H_2 chemisorption and H_2-TPD

2.4. Synthesis of the catalytic systems

The nomenclature and theoretical mass composition of the synthesized supports and catalytic systems have been described in ***Table 2.1***. Catalytic systems based on two kind of fluorite-based supports, labelled as CZS and CY, and one perovskite-based support, labelled as LSCF, are investigated. The '/' symbol is associated to the addition of the active phase by wet impregnation, whereas '-' symbol is related to the addition through "one-spot" pseudo sol-gel method.

Support/catalysts	Nomenclature	Ni (%)	Ce (%)	Zr (%)	Sm (%)
$Ce_{0.63}Zr_{0.33}Sm_{0.04}O_{2-\delta}$	CZS	-	71	24	5
$Ni/Ce_{0.63}Zr_{0.33}Sm_{0.04}O_{2-\delta}$	Ni/CZS	10	64	22	4
$Ni\text{-}Ce_{0.63}Zr_{0.33}Sm_{0.04}O_{2-\delta}$	Ni-CZS	10	64	22	4

	Nomenclature	Ni (%)	Ce (%)	Y (%)
$Ce_2Y_2O_7$	CY	-	60	40
$Ni/\ Ce_2Y_2O_7$	Ni/CY	10	55	35
$Ni\text{-}Ce_2Y_2O_7$	Ni-CY	10	55	35

	Nomenclature	Ni (%)	Ru (%)	La (%)	Sr (%)	Co (%)	Fe (%)
$La_{0.6}Sr_{0.4}Co_{0.2}Fe_{0.8}O_{3-\delta}$	LSCF	-	-	48	20	7	26
$Ni/La_{0.6}Sr_{0.4}Co_{0.2}Fe_{0.8}O_{3-\delta}$	Ni/LSCF	10	-	43	18	6	23
$Ni\text{-}La_{0.6}Sr_{0.4}Co_{0.2}Fe_{0.8}O_{3-\delta}$	Ni-LSCF	10	-	43	18	6	23
$Ru\text{-}Ni/La_{0.6}Sr_{0.4}Co_{0.2}Fe_{0.8}O_{3-\delta}$	RuNi/LSCF	10	1	43	18	6	23

Table 2.1. Nomenclature and theoretical mass composition

2.4.1. Synthesis of catalytic supports by pseudo sol-gel method: CZS, CY and LSCF

The synthesis of the different supports has been carried out using the "pseudo sol-gel" method based on the thermal decomposition of the related mixed propionate precursor. This method is also well known as "propionates" or "resin" method (***Figure 2.1***) [154–156]. The metallo-organic salts used as starting salts were separately dissolved in propionic acid with a concentration of 0.12 $mol{\cdot}L^{-1}$ in order to generate the individual metallic propionates. The starting salts used in this work were: cerium (III) acetate sesquihydrate, zirconium (IV) acetylacetonate, samarium (III) acetate and yttrium (III)

acetate for the synthesis of CZS and CY supports; and lanthanum (III) acetate, strontium (II) acetate, cobalt (II) acetate and iron (II) acetate for LSCF support. The resulting solutions were mixed in a round bottom flask equipped with a condenser column under reflux for 2 h to generate the mixed propionates by oligomerisation process. Afterwards, the excess of solvent was removed through a distillation leading to a mixed resin and this resulting resin was dried under air at 100 ºC and then calcined in air at 800 ºC for 6 h using a heating ramp of 2 ºC·min^{-1}.

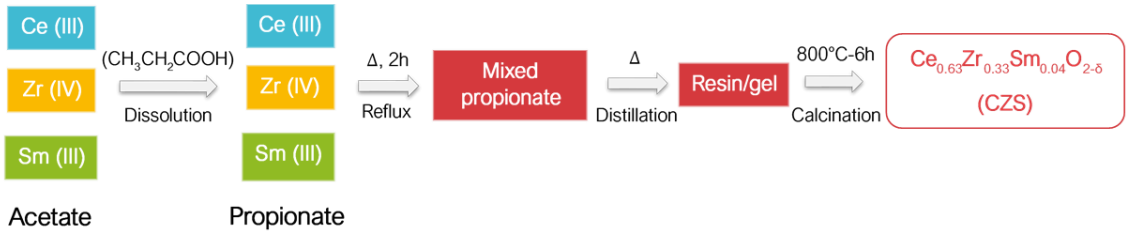

Figure 2.1. Steps of pseudo sol-gel synthesis (CZS synthesis as example).

2.4.2. Addition of the active phase

A Ni^0 loading of 10 wt% was added by two different pathways: (1) directly by *pseudo sol-gel method synthesis* (coded Ni-CZS, Ni-CY and Ni-LSCF) or (2) by *wet impregnation* of the calcined mixed oxides (coded Ni/CZS, Ni/CY and Ni/LSCF). In both cases, nickel (II) nitrate tetrahydrate was used as a starting salt. In the first case, the nickel salt was dissolved in propionic acid and the solution was mixed with the others in the pseudo sol-gel route above-described for the support preparation. In the second case, the nickel salt was dissolved in ethanol and then mixed with the support employing 3.5 mL solution/g support. The mixture was magnetically stirred for 20 min and dried at 100 ºC until complete evaporation of the solvent. Lastly, the metal-impregnated oxide was calcined under air at 500 ºC for 6 h using a heating ramp of 5 ºC·min^{-1}. A loading of 1 wt% Ru^0 was added in the case of RuNi/LSCF by a second wet impregnation of the calcined Ni/LSCF catalyst using ruthenium (III) acetylacetonate as a starting salt. The resulting Ru-impregnated oxide was calcined using the same temperature program than for nickel wet impregnation described before.

2.5. Characterization results

2.5.1. Nitrogen physisorption

The adsorption-desorption isotherms of the supports, CZS, CY and LSCF, and of the resulting catalysts, are plotted in ***Figure 2.2***. A type IV isotherm with a hysteresis loop H2 type, associated to samples with mesoporous structure, typically linked to or interparticle

space, is observed for CZS-based materials (***Figure 2.2 (a)***). As it can be noticed, the impregnated catalyst Ni/CZS presents an isotherm shape similar to that of the support CZS, whereas two consecutive hysteresis loops are observed in the case of the sol-gel catalyst Ni-CZS. This phenomenon highlights the existence of two different pore sizes in the sol-gel catalyst. The pore size distribution obtained by BJH desorption method is reported in ***Figure 2.2 (a), inset*** for CZS-based solids. A homogeneous pore size distribution is found for CZS and Ni/CZS, while two clearly different pore size mainly centered at 11 nm and 29 nm are distinguished for Ni-CZS. Concerning CY-based materials (***Figure 2.2. (b)***), type IV isotherms with a hysteresis loop of H1 type, characteristic of solids with narrow pore distribution or with spherical particles with homogeneous size and distribution, are found. In this case, the shape of the isotherm is not modified by the nickel addition pathway. Contrary to CZS systems, a homogeneous pore size distribution can be evidenced for CY systems (***Figure 2.2 (b), inset***), centered around 30-33 nm for both nickel containing materials, Ni/CY and Ni-CY, and around 50 nm for the support, CY. The average pore size is reported below for all solids, since only the pore size with higher probability can be deduced from the graph. Likewise, LSCF-based materials also show a type IV isotherm with a hysteresis H1 type loop. No modification of the isotherm shape due to nickel or ruthenium addition is evidenced in these systems. Regarding the pore size distribution, no narrow distributions was observed for these materials (***Figure 2.2 (c), inset***). Then, as it is expected in perovskite-based materials calcined at high temperature, the existence of hysteresis in these systems can be attributed to the presence of spherical particles, typical of non-porous solids. Generally, the presence of interparticular mesopores (2 nm < D_{pore}< 50 nm) prevailed for the three different systems.

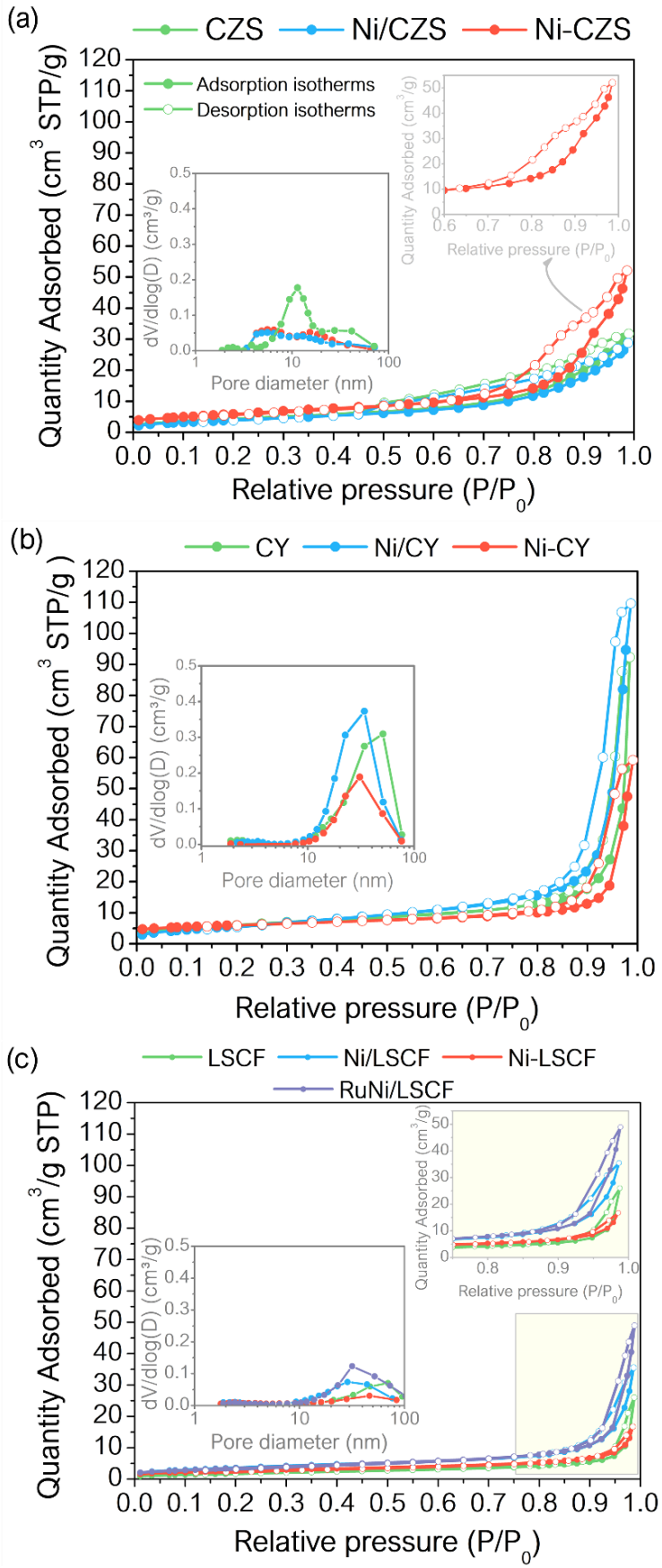

Figure 2.2. Adsorption-desorption isotherms and pore size distributions of synthesized materials: (a) CZS-, (b) CY- and (c) LSCF-based systems

The textural properties of the obtained materials are summarized in *Table 2.2*. As it can be expected, the specific surface area (SSA) is low for all materials due to the high calcination temperature used to synthesize the mixed oxides and varied from 7 to 22 $m^2 \cdot g^{-1}$. The addition of nickel by one step sol-gel leads to the best textural properties for CZS-based materials, achieving the highest SSA (22 $m^2 \cdot g^{-1}$) as well as the highest pore volume (V_{pore}) (0.08 $cm^3 \cdot g^{-1}$) and average pore diameter (D_{pore}) (13 nm). The impregnated catalyst, Ni/CZS, exhibited same textural properties than the support with a SSA of 15 and 16 $m^2 \cdot g^{-1}$, respectively. Opposite effect has been observed for CY based systems, for which the sol-gel catalyst, Ni-CY, shows the lowest SSA (12 $m^2 \cdot g^{-1}$) and pore volume (0.09 $cm^{-3} \cdot g^{-1}$) compared to the support, CY, which exhibits equivalent properties compared to the impregnated sample, Ni/CY. Similar to CZS materials, the nickel impregnation does not have influence on the textural properties of the support, reaching same values of SSA of 22 $m^2 \cdot g^{-1}$ for both materials. No significant differences in the average pore diameter can be noticed for CY materials, displaying values from 23 to 27 nm. Concerning LSCF-based materials, the values of SSA observed, from 9 to 14 $m^2 \cdot g^{-1}$, are consistent with those found in literature for these materials synthesized by sol-gel method [125,156–158]. An enhancement of the SSA was noted for both nickel containing LSCF solids, where the impregnated catalyst, Ni/LSCF, shows the highest value (14 $m^2 \cdot g^{-1}$) compared to its equivalent sol-gel catalyst (10 $m^2 \cdot g^{-1}$) and to the support (7 $m^2 \cdot g^{-1}$). Slightly higher pore volume is also observed for the impregnated catalyst (0.06 $cm^{-3} \cdot g^{-1}$) than for the bare support (0.04 $cm^{-3} \cdot g^{-1}$), whereas similar value is found in the case of the sol-gel catalyst (0.03 $cm^{-3} \cdot g^{-1}$). Additionally, lower average pore diameter is determined for both Ni-containing materials compared to the support. Lastly, the addition of ruthenium over Ni/LSCF does not alter SSA, while an increase of the pore volume and diameter can be noticed compared to Ni/LSCF. Generally, considering the low values attained for the pore volume, the porosity can be associated to an interparticle porosity for all materials.

Samples	SSA ($m^2 \cdot g^{-1}$)	V_{pore} ($cm^3 \cdot g^{-1}$)	D_{pore} (nm)
CZS	16	0.05	8
Ni/CZS	15	0.05	8
Ni-CZS	22	0.08	13
CY	22	0.14	26
Ni/CY	22	0.18	23
Ni-CY	12	0.09	27
LSCF	7	0.04	20
Ni/LSCF	14	0.06	17
Ni-LSCF	10	0.03	12
RuNi/LSCF	13	0.08	22

Table 2.2. Textural properties of synthesized materials

2.5.2. X-ray diffraction (XRD)

The X-ray diffractograms of the support and the corresponding catalytic systems are given in ***Figure 2.3***. The diffractograms of CZS–based materials (***Figure 2.3 (a)***) show a typical cubic fluorite structure related to $Ce_{0.6}Zr_{0.4}O_2$ (JPCD 00-038-1439) mixed oxide, with no noticeable samarium oxide phase. The samarium might be integrated into the CZ mixed oxide structure, however its presence as a single oxide cannot be completely rejected since the XRD pattern of Sm_2O_3 oxide associated to a cubic phase (JCPDS 00-42-1461) shows diffractogram peaks close to those related to CZ. Additionally, the theoretical amount of samarium in the support is fairly low, representing 5 wt% (***Table 2.1***). An additional phase corresponding to cubic NiO structure (JPCDS 03-065-2901) is evidenced in the Ni-containing CZS catalysts reflections (Ni/CZS and Ni-CZS), exhibiting lower relative intensity for the sol-gel catalyst, Ni-CZS, than for the equivalent impregnated, Ni/CZS. The lower relative NiO intensity and the shift to higher 2θ for the diffraction lines of the support displayed for Ni-CZS compared to Ni/CZS and CZS (***inset 2.3 (a)***) can evidence the partial insertion of Ni cations into the CZS structure when nickel is introduced by sol-gel method. This Ni insertion into the mixed oxide structure is favored by the formation of Ni-Ce-Zr-Sm mixed propionate precursor through the sol-gel method, leading to a homogeneous mixture at atomic level. Other studies has been as well remarked the existence of inserted Ni^{2+} species into doped Ce-based mixed oxide structure [146,159]. Regarding the CY–based materials (***Figure 2.3 (b)***), higher crystallinity than CZS, with mainly a cubic fluorite structure associated to $Ce_2Y_2O_7$ (JPCD 00-009-0286), is found for the support. In addition, a well-defined diffractogram peak centered at 2θ~ 96º related to (511) reticular plane has been widely associated in literature as typical of a pyrochlore structure [160–162]. Therefore, although the main crystalline structure is related to the fluorite one, the formation of a pyrochlore structure in minor proportion could be assumed. As for CZS systems, a cubic

NiO phase is observed in the two nickel containing solids, and a shift to higher 2θ in the sol-gel catalyst, Ni-CY, (***inset 2.3 (b)***) highlights the Ni^{2+} insertion into the CY structure for this catalytic system. Similar NiO relative intensity is displayed for both Ni-containing CY materials (Ni/CY and Ni-CY) which stresses out that relatively less nickel insertion through sol-gel method occurs in this case. This different behavior compared to Ni-CZS catalyst indicate that the Ni insertion is less favored with CY than with CZS mixed oxide structure. Concerning LSCF-based materials (***Figure 2.3 (c)***), two different crystalline phases can be noted in the LSCF support diffractogram. The phase with higher relative intensity is related to a perovskite structure with orthorhombic symmetry ($La_{0.7}Sr_{0.3}Fe_{0.7}Co_{0.3}O_3$, JPCD 01-089-1268) being, thus, the predominant crystalline phase in the support LSCF. The other phase corresponds to the formation of the cubic lanthanum oxide (La_2O_3, JPCD 01-083-1344). It indicates that the insertion of La^{3+} ions into the LSCF mixed oxide structure is not complete. No presence of other phase related to Sr-, Co or Fe-single/mixed oxides structures are detected in the diffractogram of the support, suggesting the formation of a poor lanthanum perovskite structure compared with the theoretical one. The perovskite structure is still detected in both Ni/RuNi containing catalytic systems ((Ru)Ni/LSCF and Ni-LSCF), whereas La_2O_3 phase does no longer appear. The crystalline phase associated to NiO is clearly observed for the sol-gel catalyst (Ni-LSCF) but not visible for the equivalent impregnated (Ni/LSCF). Focusing on the peak position linked to the reticular plane (112) of the perovskite structure (***inset 2.3.(c)***), it can be also discerned a shift to higher 2θ for the sol-gel catalyst compared to the support and the equivalent impregnated one. Likewise, the partial insertion of $Ni^{2+/3+}$ ions into the perovskite structure through one step sol-gel method is also promoted. For steric reasons, the partial insertion of Ni ions is highly favored in the B-site cations as Ni^{3+} into the LSCF mixed oxide [163]. The non-detection of both, NiO and La_2O_3 phase, for Ni/LSCF catalyst indicates that Ni form a secondary perovskite structure with the excess of La_2O_3 ($LaNiO_3$) observed in the diffractogram of support. This phase is not noticeable since the XRD pattern of $LaNiO_3$ related to a hexagonal phase displays diffraction peaks close to those associated to LSCF. However, the presence of a low content of "free" NiO species below the detection limit cannot be rejected for Ni/LSCF. The non-presence of La_2O_3 phase for Ni-LSCF catalysts suggest that the partial Ni insertion through sol-gel promotes also the introduction of La into the LSCF structure. Similar to Ni/LSCF, no phase related to NiO or La_2O_3 can be detected for RuNi/LSCF, which might suggest, once again, that the formation of $LaNiO_3$ perovskite phase through wetness impregnation is highly feasible. No noticeable RuO_2 phase is appreciated in the diffractogram of RuNi/LSCF due to its low content (theoretically 1 wt%, see ***Table 2.1***).

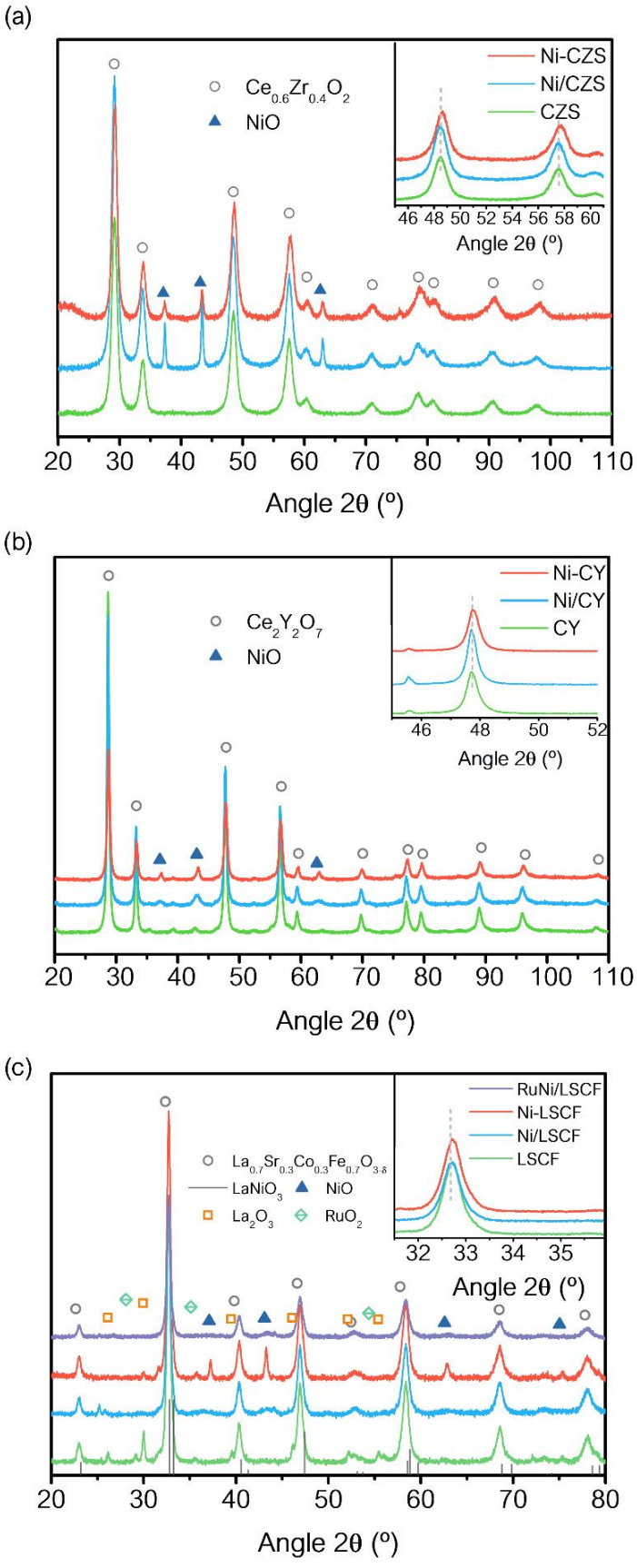

Figure 2.3. Diffractograms of synthesized materials: (a) CZS-, (b) CY- and (c) LSCF-based systems

The crystalline particle size of the synthesized supports ($d_{support}$) and of NiO (d_{NiO}) as well as support lattice parameter ($a_{support}$) calculated assuming a cubic structure (equations described in *Annex*, section C) are displayed in ***Table 2.3*** for the obtained materials. The crystalline size of the supports ($d_{support}$) has been estimated using the FWHM of the (111) and (200) as h, k, l indexes related to the reticular planes of well-defined diffractogram peaks placed at 2θ~29 and 34º, respectively, for Ce-based materials (CZS and CY). In the case of LSCF based materials, the FWHM of the (112) and (204) reticular planes linked to the diffractogram peaks place at 2θ~ 33 and 58º was used.

Generally, no modification in the support particle size ($d_{support}$) associated to the Ni addition pathway can be appreciated. The CZS, CY and LSCF crystallites particle sizes are, respectively, around 8-9 nm, 20-23 nm and 14-17 nm. No link with SSA can be noticed. Regarding the NiO crystallites particle size (d_{NiO}), a moderately smaller value was found for sol-gel Ni-CZS catalyst (19 nm) compared to the impregnated Ni/CZS (24 nm), while the opposite was noted for the CY catalysts, where the impregnated Ni/CY catalyst presents the lowest d_{NiO} (8 nm) among all the catalysts. Regarding LSCF-based materials, a crystalline particle size of 26 nm was reached for NiO phase for the sol-gel Ni-LSCF catalyst, leading to the highest value. No direct link between the nickel particle sizes and its dispersion can be established since the nickel insertion is favored for the sol-gel system, as it has been discussed above.

The support lattice parameter ($a_{support}$) has been averaged out for Ce-based materials (CZS and CY systems) using (111) and (200) as h, k, l indexes related to the reticular planes of well-defined diffractogram peaks placed at 2θ ≈ 29º and 34º, respectively. A reduced support lattice parameter considering a cubic structure has been defined for LSCF-based materials (see *Annex, section C*). In that case, reticular planes (112), (004) and (204) associated to diffractogram peaks located at 2θ ≈ 33º, 40º and 58º were used.

Regarding CZS- and CY-based materials, lower value than that of the cubic lattice parameter of pure ceria (5.404 Å) were expected for bare CZS (5.312 Å) and CY (5.387 Å) mixed oxide, as a result of the cell contraction by Zr^{4+} and Y^{3+} incorporation as solid solution, according to Vegard's law. This contraction in CZS oxide is due to the substitutional Zr^{4+} cations with smaller ionic radius (0.84 Å in 8-fold coordination) than that of Ce^{4+} (0.97 Å in 8-fold coordination) [164]. The opposite effect is expected with Sm^{3+} substitution in the unit cell (1.08 Å in 8-fold coordination). However, the atomic proportion Zr^{4+}/Sm^{3+} of 33/4 leads to a mean radius of 0.87 Å, still much lower than 0.97 Å. As regards CY oxides, the ionic

radius of Y^{3+} (1.02 Å in 8-fold coordination) is higher than Ce^{4+} one, then cell expansion would be expected. Despite that, a cell contraction is noticeable for CY mixed oxide. This fact is in concordance with several computational studies, where two correlative effects of how trivalent dopants affect the CeO_2 lattice distortion might be considered: (i) contraction by electrostatic interaction associated to oxygen vacancies formation and (ii) expansion due to steric effect which is linked to the differences in the ionic radius between the host and dopant cations [120]. The electrostatic interaction, thus, a contraction in the CeO_2 lattice, dominates when the dopant ionic radius is below 1.03 Å [165,166], as it is the case for Y^{3+}.

In order to compare LSCF lattice parameter with other analogous material, the normalized unit cell of $La_{0.6}Sr_{0.8}Co_{0.2}Fe_{0.8}O_3$ (94.83 $Å^3$) calculated from their corresponding lattice parameter obtained from Riertveld analysis by Banerjee *et al.* has been considered for the estimation of its reduced lattice parameter (4.560 Å), used as reference value. As expected by the presence of La_2O_3 in the diffractogram of bare LSCF (***Figure 2.3 (c)***), a much lower lattice parameter is displayed for LSCF material of the present study (3.872 Å) than the reference perovskite, which is explained by the no complete incorporation of La^{3+} cations into the perovskite structure.

Generally, among the nickel containing materials, the Ni and Ru-Ni impregnation has not significative influence on the support lattice parameter, whereas a decrease is clearly noteworthy for the one step sol-gel materials. As prior observed for the three sol-gel catalysts (***inset 2.3 (a), (b) and (c)***), the existence of nickel cations ions partially inserted into the mixed oxide structures (CZS, CY and LSCF) lead to shift to higher 2θ due to the decrease in the lattice parameter, since the ionic radius of these species in 8-fold coordination (0.56 Å for Ni^{3+} and 0.69 for Ni^{2+}) are smaller than Zr^{4+}, Y^{3+}, Co^{3+} (0.68 Å) and Fe^{3+} (0.78 Å) ones [164]. For steric reason, the insertion of nickel as Ni^{2+} is more probable in the case of Ce-mixed oxides, whereas the Ni^{3+} insertion is highly favored for La-based oxides. As expected, a minor decrease is noticeable for Ni-CY (5.381 Å) and Ni-LSCF (3.865 Å) materials than that Ni-CZS (5.301 Å) in comparison with the equivalent bare supports, CY (5.387 Å), LSCF (3.872 Å) and CZS (5.312 Å), respectively. This fact is in accordance with the relative NiO intensity displayed for Ni-CY compared to their equivalent impregnated catalysts (***Figure 2.3 (b)***), exhibiting similar relative NiO intensity than Ni/CY. Therefore, a possible rejection of Ni by CY mixed oxide structure may be assumed since ionic radius of Ni^{2+} species are rather small compared to that of Y^{3+}.

	$d_{support}$ (nm)	d_{NiO} (nm)*	$a_{support}$ (Å)
CZS	9	-	5.312
Ni/CZS	8	24	5.314
Ni-CZS	9	19	5.301
CY	21	-	5.387
Ni/CY	23	8	5.387
Ni-CY	20	14	5.381
LSCF	15	-	3.872
Ni/LSCF	17	-	3.871
Ni-LSCF	14	26	3.865
RuNi/LSCF	14	-	3.876

* Estimated by the FWHM of the (111) and (200) as h, k, l indexes related to the reticular planes of well-defined diffractogram peaks placed at 2θ~37 and 43º, respectively, by using the Sherrer's equation for NiO phase.

Table 2.3. Structural properties of the synthesized materials

2.5.3. Temperature programmed reduction (H_2-TPR)

The H_2-TPR profiles of the synthesized materials are displayed in ***Figure 2.4***. Additionally, the support reducibilities are shown in ***Table 2.4*** for the investigated systems. The support reducibility was calculated considering the following assumptions: (1) the theoretical mass composition of the supports described in ***Table 2.1***; (2) the theoretical amount of NiO is fully reduced to Ni^0; (3) cerium, cobalt and iron are the reducible species and are present initially in their oxidized form (Ce^{4+}, Co^{3+} and Fe^{3+}) for Ce- and La-based supports, respectively.

A main peak centered around 620 ºC with a weak shoulder around 500 ºC is found for bare CZS mixed oxide (***Figure 2.4 (a)***), ascribed to the well-known labile and/or surface and bulk oxygen reduction of CeO_2, respectively [146,167]. Typically, these two reduction temperatures have been reported in the literature around 530 and 820 ºC for bare CeO_2 [168–170]. Thus, the presence of Sm^{3+}/Zr^{4+} into the mixed oxide promotes the reduction of CeO_2, shifting its corresponding reduction profile to lower temperature [171,172]. Similar reduction profile, slightly shifted to lower temperature and, with a noteworthy lower hydrogen consumption than CZS mixed oxide, is obtained for CY mixed oxide (***Figure 2.4 (b)***). This points out the low reducibility capacity (***Table 2.4***) of CY (13%) mixed oxide in comparison with the CZS one (49%). As it has been widely reported in the literature, introduction of oxygen vacancies into ceria oxide structure can be carried out by two main processes: (i) reduction of Ce^{4+} species to form intrinsic oxygen vacancies and (ii) use of aliovalent dopant to generate extrinsic oxygen vacancies due to charge neutrality mechanism [115,119,173]. Then, Wang *et al.* [174] have studied the effect of yttria doping level in ceria mixed oxide, highlighting a lower reducibility of yttria-doped ceria systems

compared to the bare ceria oxide. They evidenced, using EPR and XPS, the formation of extrinsic oxygen anion vacancies with a simultaneous decrease of intrinsic ones as a result of the substitution of the host Ce^{4+} ions by Y^{3+} cations. Thereby, the ability of ceria to lose its lattice oxygen and, as a consequence, to form Ce^{3+} species is inhibited. In order to well explain the process, they considered the formation of intrinsic oxygen vacancies through the reduction process of ceria by the following redox process:

$$2Ce^{4+} + O_O^x \leftrightarrow \frac{1}{2}O_2(g) + 2Ce^{3+} + V_0^{\bullet\bullet} \qquad \textit{Equation 2.3}$$

,where O_O^x is an oxygen anion of ceria lattice and $V_0^{\bullet\bullet}$ is a doubly positive charged oxygen vacancy. By doping with yttria, an additional oxygen is removed from the oxide structure and an extrinsic oxygen vacancy are generated according to *Equation 2.4.* In this case, the reaction of *Equation 2.3* is shifted to the left, leading to a lower amount of Ce^{3+} in the bulk structure and a decrease of the reducibility of ceria is observed. Therefore, the differences in ceria reducibility found for CY and CZS could be associated to the fact that Zr^{4+} doping promotes the formation of intrinsic oxygen vacancies into the ceria structure favoring the Ce^{3+}/Ce^{4+} redox process, whereas this redox process is inhibited by the introduction of extrinsic oxygen vacancies to compensate the effective negative charge by Y^{3+} doping, leading to a decrease in the support reducibility.

$$Y_2O_3 \leftrightarrow 2Y'_{Ce} + 3O_O + V_0^{\bullet\bullet} \qquad \textit{Equation 2.4}$$

Concerning the Ni-containing materials, a H_2-TPR profile with a main peak centered between 350-400 ºC was obtained for both impregnated catalysts, Ni/CZS and Ni/CY, located at higher temperature for Ni/CY catalyst. This peak has been widely related to Ni^{2+} reduction to Ni^0 process [146,175–177]. In addition, two different peaks can be deduced at lower temperature and are connected to the existence of different NiO-support interactions [117,146]. It can be also assumed, through the rise of the support reducibility of Ni/CZS (60%) and Ni/CY (30%) catalyst compared to bare CZS (49%) and CY (13%) mixed oxides, respectively (***Table 2.4***), that nickel-ceria reduction takes place simultaneously, since the reduction of NiO enhances the reduction of surface Ce^{4+}.

A different TPR profile has been observed within the sol-gel resulting catalyst, Ni-CZS. Three reduction zones can be distinguished for Ni-CZS catalyst: at low (T ~ 300-450 ºC), intermediate (T ~ 450-550 ºC) and high (T > 550 ºC) temperature. The lower temperature peak has been frequently associated to the consumption of reactive oxygen species caused by the redox system Ni^{2+}/Ni^0 and Ce^{4+}/Ce^{3+} (*Equations 2.5-2.6*) [146,167,175], whereas the peak at around 400 ºC is the well-known Ni^{2+} reduction to Ni^0

of bulk NiO, previously observed in the impregnated catalyst [117,146]. The intermediate zone, between 450-550 °C, is associated to the surface/bulk reduction of CeO_2 as well as to the reduction of Ni^{2+} species in strong interaction with the support [146]. This fact confirms the partial Ni^{2+} insertion into CZS mixed oxide, facilitated by the formation of the mixed propionate precursor by means of sol-gel method, prior evidenced by XRD results. The last zone of reduction around 600 ºC corresponds to the reduction of bulk Ce^{4+}, shifted to lower temperature, compared to the bare support, due to the presence of nickel which, after reduction, helps the reduction of the support.

$$Ni^{2+} + O^{2-} + H_2 \rightarrow Ni^0 + H_2O + \square \qquad \textit{Equation 2.5}$$

$$2Ce^{4+} + Ni^0 \rightarrow 2Ce^{3+} + Ni^{2+} \qquad \textit{Equation 2.6}$$

where □ is an anionic vacancy.

Regarding the TPR profile of Ni-CY sol-gel catalyst (***Figure 2.4 (b)***), two peaks are located at higher temperature than those correlated to the impregnated catalyst (Ni/CY). One of these peaks appears around 400 ºC, associated to the bulk NiO reduction to Ni^0, while the peak centered around 450 ºC can be ascribed to Ni^{2+} species with stronger Ni-support interaction as a result of Ni^{2+} introduction into the mixed oxide structure, promoted by the synthesis based on the formation of Ni-Ce-Y mixed propionate precursor. However, comparing TPR profiles of both Ce-based sol-gel catalysts (Ni-CZS and Ni-CY), it seems that the Ni^{2+} insertion is not well enhanced into CY oxide structure probably caused by the Y^{3+} insertion into the CeO_2. Yamazaki *et al*. [178] showed that the oxygen vacancy formation by trivalent cations doped ceria is associated with the dopant concentration. They observed that the higher M^{3+} concentration the smaller was the inter atomic distance M^{3+}-O and linked this decrease to the formation of one and/or two oxygen vacancies by means of two and/or four inserted M^{3+} cations at dilute or high dopant concentration, respectively. Considering the latter, the stabilization of inserted Ni^{2+} ions could be limited in the CY oxide due to the enlargement of the ceria lattice by the presence of trivalent. This fact it can also be verified considering the calculated support reducibility (***Table 2.4***). It can be noticed that the presence of inserted Ni^{2+} species into both sol-gel catalysts promotes the support reducibility, since the calculated support reducibility increases compared to the corresponding impregnated catalysts. This increase is much lower for the CY-based systems (35% for Ni-CY *vs* 30% Ni/CY) than for CZS-based ones (86% for Ni-CZS *vs* 60% for Ni/CZS). Additionally, this tendency is in concordance with the support lattice parameters listed in ***Table 2.3,*** in which the decrease of the lattice parameter of the Ni-

containing sol-gel catalysts with respect to the corresponding support was much lower for Ni-CY (compared to CY) than for Ni-CZS (compared to CZS). Hence, a limitation in the partial insertion of Ni into CY mixed oxide structure can be concluded.

Complex H_2-TPR profiles have been found for LSCF-based materials (***Figure 2.4 (c)***). As it has been reported in the literature, the reduction processes into a perovskite system are commonly linked to B-site cations reduction, since the A-site cations reduction under experimental conditions is rather difficult [179,180]. Generally, a reduction profile divided in two regions (*regions I* and *II*) can be distinguished for the support (LSCF) and the equivalent catalytic systems (Ni/LSCF, Ni-LSCF and RuNi/LSCF). Regarding the LSCF mixed oxide reduction profile, the *regions I* and *II* have been widely associated to Co^{3+} and Fe^{3+} reduction, respectively [158,179,181]. The former is observed at low temperature, between 250- 550 ºC, and the latter at higher one, from 700 to 950 ºC. Two main peaks located at maximum temperatures of 380 and 490 ºC were noted in the *region I*, being commonly associated to the next two reduction steps [182,183]: (1) $Co^{3+} \rightarrow Co^{2+}$ and (2) $Co^{2+} \rightarrow Co^{0}$. Concerning the second region, only one peak at high temperature, 850 ºC, linked to the $Fe^{3+} \rightarrow Fe^{0}$ reduction is detected [158,180,181]. The high temperature reduction of these species has been associated to high stability of Fe^{3+} in the octahedral sites of a perovskite structure [180]. In addition, the separation between the two regions found at temperature range around 550-700 ºC can lead to the formation of stable partial reduced cobalt-containing perovskite under this reducing experimental condition [158]. Whereas similar shapes of the reduction profiles are achieved for the impregnated catalyst, Ni/LSCF, some differences are observed in the *region I* for the equivalent sol-gel system, Ni-LSCF. The likely formation of $LaNiO_3$ phase for Ni/LSCF catalyst observed by XRD leads to a complex reduction process (even more complex than for the bare support). Likewise, two peaks centered close to the temperatures above mentioned (385 and 475 ºC) are observed for the impregnated material, Ni/LSCF, in the *region I,* with an additional peak placed at lower temperature, 290 ºC. Two reduction steps have been mainly reported for the complete reduction of $LaNiO_3$ perovskite. Lin *et al.* [184] found two reduction peaks at 392 ºC and 528 ºC for $LaNiO_3$ phase. The reduction at low temperature was ascribed to the reduction of $LaNiO_3$ to Ni^0 and La_2NiO_4 spinel (*Equation 2.7*) and the one located at higher temperature to the reduction of the spinel phase, resulting in the complete reduction of Ni^0 and the formation of La_2O_3 (*Equation 2.8*). Oemar *et al*. [185] ascribed the first reduction peak at 350-450 ºC to the reduction of $LaNiO_3$ where Ni^{3+} is reduced to Ni^{2+} with the formation of a $La_2Ni_2O_5$ phase and the second one, at around 550 ºC, to the reduction of NiO, generating La_2O_3. In addition, Pereñiguez *et al.* [186] observed the formation of free NiO during the

synthesis of $LaNiO_3$ solid by EXAFS and attributed a shoulder reduction peak located at low temperature (425 ºC) to the reduction of NiO species to Ni^0 and the peak at high temperature (495 ºC) to the reduction of $LaNiO_3$.

$$LaNiO_3 + H_2 \rightarrow La_2NiO_4 + Ni + 2H_2O \qquad \textit{Equation 2.7}$$

$$La_2NiO_4 + H_2 \rightarrow La_2O_3 + Ni + H_2O \qquad \textit{Equation 2.8}$$

Considering the latter, the peak located at lowest temperature might be linked to the reduction of free particle of NiO with weak Ni-support interaction or to the reduction of $LaNiO_3$ into La_2NiO_4 and Ni [187]. The shift to lower temperature compared to what found into the literature (around 350 – 400 ºC) might be due to the presence of other reducible species, such as Co^{3+} or Fe^{3+} that can favor the reduction of $LaNiO_3$ perovskite. Moreover, the two-peak detected in the *region I* might be associated to the decomposition of the La_2NiO_3 spinel to Ni^0 and La_2O_3 oxide along with the reduction of Co^{3+} species. The noticeable increase in the H_2 consumption into the *region I* suggested the simultaneous reduction of Co^{3+} and the remaining Ni^{2+} species as spinel structure (La_2NiO_4). Besides, a shift of the *region I* to lower temperature with a noteworthy increase in the H_2 consumption of the peak at lower temperature (240 ºC) compared to Ni/LSCF has been evidenced for RuNi/LSCF catalyst. This increase in the H_2 consumption at 240 ºC for RuNi/LSCF underlines that Ni reduction is promoted by the addition of Ru over Ni/LSCF catalyst.

Relating to the sol-gel material, the *region I* is shifted to higher temperature compared to the impregnated catalyst, Ni/LSCF and bare LSCF mixed oxide, probably associated to the presence of inserted Ni ions species. A main reduction peak centered at 460 ºC could be mostly due to the Ni^{2+} reduction species to Ni^0 with strong Ni-support interaction [188,189]. Different shoulder peaks probably linked to Co^{3+} reduction can be as well distinguished in this region. The number and nature of Co^{3+} species have been associated in the literature to the distortion of the perovskite lattice and oxygen defect that could be highly sensitive to the preparation method and calcination conditions of the perovskite [190,191]. The presence of more oxygen defects in the bulk can lead to more inhomogeneous Co^{3+} species and, consequently, to multiple reduction peaks [191,192]. Therefore, the detailed understanding of the different reduction processes of Co species in these perovskite-type systems becomes difficult. Within the *region II*, the peak related to Fe^{3+} reduction is shifted to lower temperature in both Ni- and RuNi-containing materials (Ni/LSCF, Ni-LSCF and RuNi/LSCF) with respect to the bare support. Thus, Ni addition could promote the support reducibility, becoming remarkable for the sol-gel catalyst,

increasing from 29% to 54% in the case of impregnated and up to 72% for the sol-gel system. No modification in the support reducibility was detected for RuNi/LSCF compared to Ni/LSCF. Then, the addition of Ru favored the Ni reduction, shifting the reduction peaks of these latter species to lower temperature, but no improvement in the support reducibility was remarkable compared to Ni/LSCF.

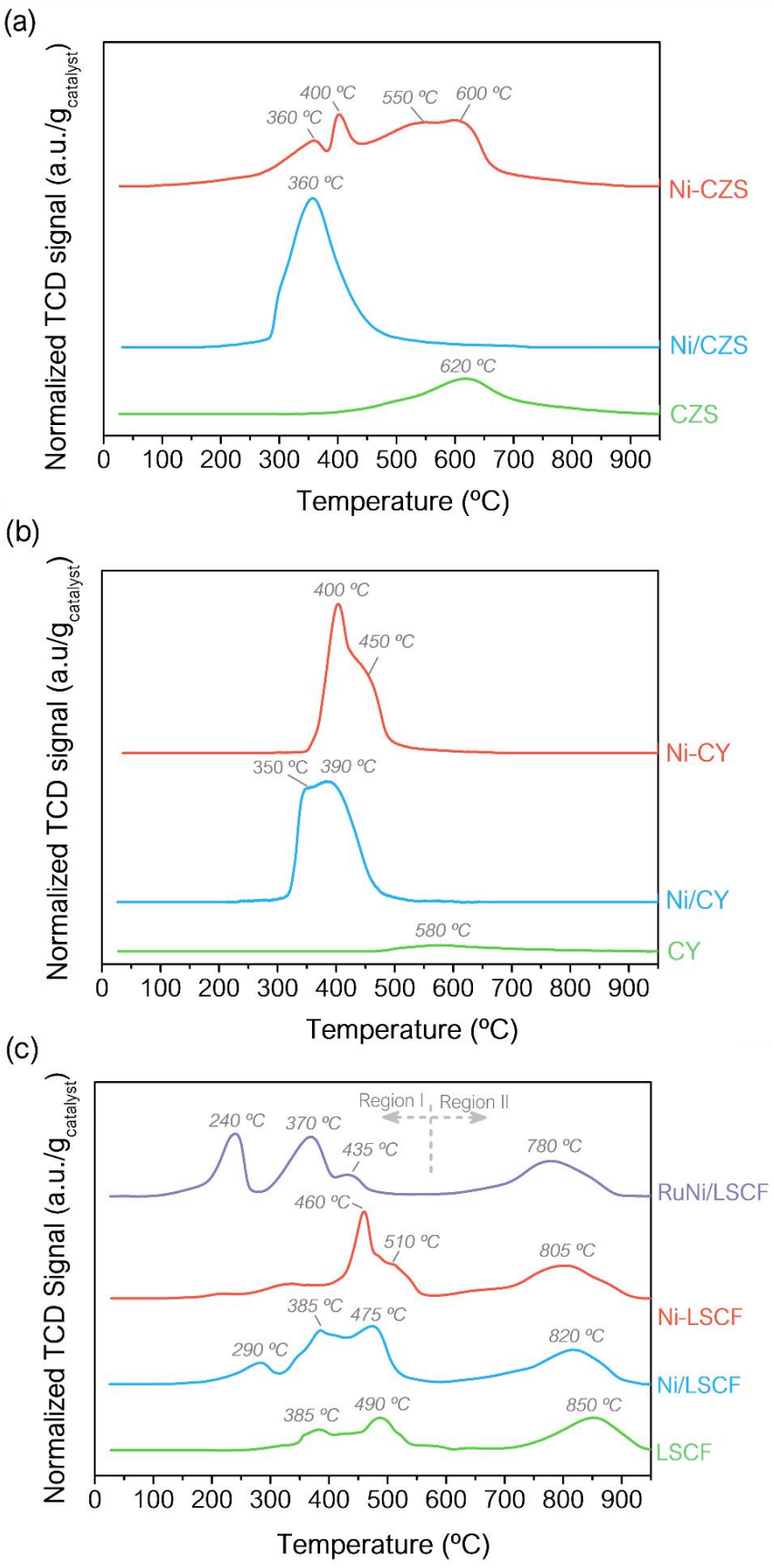

Figure 2.4. H_2-TPR profile of the synthesized materials: (a) CZS-, (b) CY- and (c) LSCF-based systems

	Support reducibility (%)
CZS	49
Ni/CZS	60
Ni-CZS	86
CY	13
Ni/CY	30
Ni-CY	35
LSCF	29
Ni/LSCF	54
Ni-LSCF	72
RuNi/LSCF	56

Table 2.4. Support reducibility of synthesized materials

A reduction pretreatment should be performed prior to the catalytic test in order to generate the active phase (Ni^0) in steam reforming of tar. Therefore, as it can be deduced by the H_2-TPR profiles (***Figure 2.4***) above discussed, a reduction pretreatment at 600ºC would lead to the complete reduction of NiO to Ni^0 and the partial reduction of ceria in the case of CZS and CY- based materials. Whereas a partial reduced cobalt-containing perovskite would be expected to be generated considering the H_2-TPR profile of LSCF based materials.

2.5.4. X-ray photoelectron spectroscopy (XPS)

The deconvoluted XPS spectra of Ce 3d and Ni 2p regions are given in ***Figure 2.5*** for the synthesized Ce-based materials. Generally, eight components have been found by performing a peak fitting deconvolution within the Ce 3d spectra of both CZS- and CY-based materials from 920 to 870 eV (***Figure 2.5 (a) and (b)***, respectively). Two series of four components have been found, labeled *v, v', v'', v''' and u, u', u'', u'''* associated to Ce $3d_{5/2}$ and Ce $3d_{3/2}$ levels, respectively [193–195]. According to other studies, the doublet (*v', u'*) is associated to Ce^{3+} species, while the others are ascribed to Ce^{4+} ones [193,194]. This points out the co-existence of Ce^{4+}/Ce^{3+} oxidation states at the surface of both CZS and CY supports. Comparing Ce 3d spectra of both CZS and CY supports, a shift to lower binding energy is noted in CY spectra, i.e., peak u''' is located at 916.4 eV *vs* 915.6 eV for CZS and CY, respectively. This observation indicates the higher electronic density around Ce atoms for CY than that for CZS, since yttrium's electronegativity is slightly lower than zirconium's one. Focusing on Ni-containing mixed oxides, the lower relative intensities in Ce 3d observed for impregnated catalysts (Ni/CZS and Ni/CY) compared to the bare supports is evidenced, being severe for Ni/CZS. In addition, the Ni $2p_{1/2}$ sat (879.3 eV), linked to Ni^{2+} state, can even be clearly detected in the Ce 3d range for the latter solid (***Figure 2.5 (a)***). This point is in accordance with the strong intensity detected in Ni 2p region (from 875 to

840 eV) among the impregnated catalysts, emphasizing the presence of high Ni content on the surface. Within the Ni 2p region, peaks at 853-854 eV and its satellite peak at 859-860 linked to Ni $2p_{1/2}$ level and, peak at 870-871 eV associated to Ni $2p_{3/2}$ levels are clearly distinguished for the impregnated catalysts. These peaks can be associated to Ni^{2+} oxidation state [105,167]. Nevertheless, an opposite behavior regarding the intensities within the Ce 3d and Ni 2p region was found for the sol-gel catalysts. The spectrum shape of the sol-gel solids (Ni-CZS and Ni-CY) seems to be similar to the corresponding bare support. The decrease in intensity of the Ni 2p orbital peaks detected for the sol-gel materials stands out a lower Ni^{2+} surface content than the corresponding impregnated one. This fact suggests, once again, that the partial insertion of Ni^{2+} species into the mixed oxide structures has been favored by mean of sol-gel route synthesis, as it was prior discussed in the XRD and H_2-TPR results. Consequently, a shift to higher binding energy within Ce 3d spectra owing to lesser electronic density around Ce atoms compared to the bare support caused by the partial Ni^{2+} insertion into the Ce-based support structures (CZS and CY) through one step sol-gel method is noticeable.

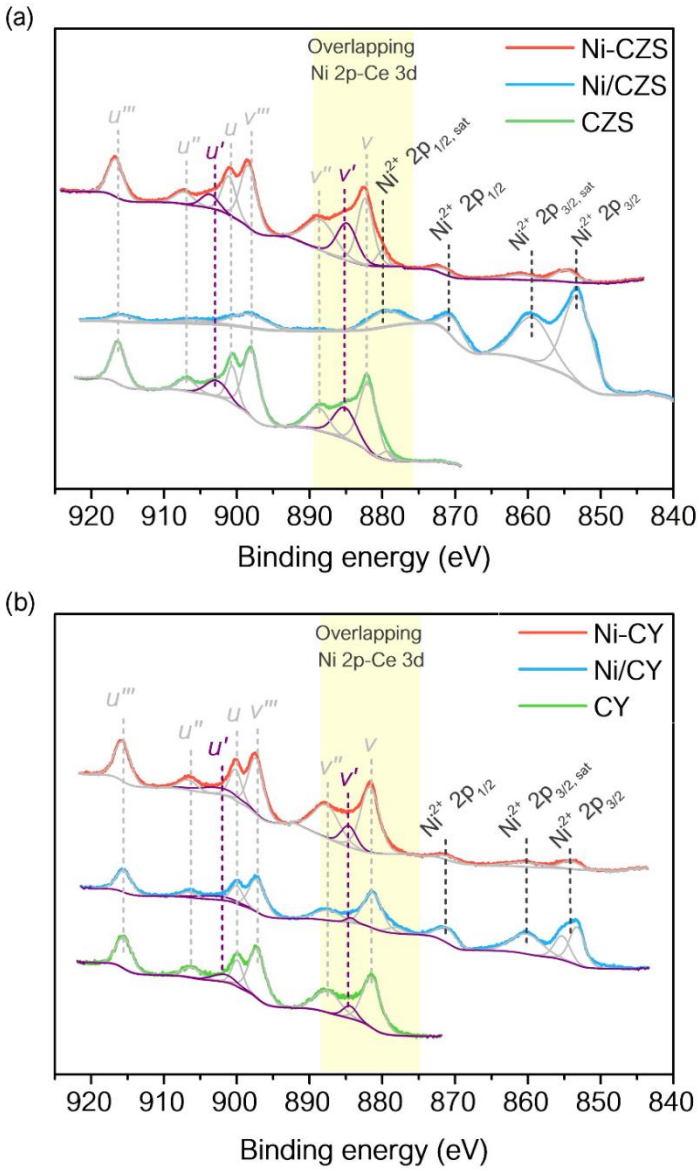

Figure 2.5. XPS of the synthesized Ce-based materials. Ce 3d – Ni 2p region for (a) CZS and (b) CY- based materials

Concerning LSCF-based materials, the deconvoluted XPS spectra of Ni 2p – La 3d along with Co 2p and Fe 2p region are presented in ***Figure 2.6.*** Thus, peaks located at 850.4 and 834.0 eV linked to $3d_{3/2}$ and $3d_{5/2}$ orbital components of La^{3+} state are found for the bare support (***Figure 2.6. (a)***) [156,196,197]. Additionally, the remaining peaks centered at 866.6, 854.9 and 838.2 eV have been widely associated to the different satellite peaks of La^{3+} species [196]. The appearance of such satellite peaks as well as their relative intensity and the binding energy separation are highly susceptible to the chemical coordination environment of La atoms and is supposed to arise from ligand-to-metal charge transfer process leading to a highly complex spectrum [196,198,199]. Two peaks are evidences in

the Co 2p region (***Figure 2.6. (b)***), both indicates the presence of Co^{2+} species at the surface of the bare support. Thus, the corresponding $2p_{3/2}$ orbital component is located at 781.6 eV and its satellite peak at 786.3 eV [199]. Eventually, components at around 711.9 eV and 725.4 eV belong to Fe^{3+} species are observed in the deconvoluted Fe 2p region for LSCF (***Figure 2.6. (c)***) [199].

As regard to the Ni containing mixed oxides, a shift to lower BE compared to the support is found for the $3d_{3/2}$ and $3d_{5/2}$ orbital components within the La 3d region for both catalysts (***Figure 2.6 (a)***). Thus, the $3d_{3/2}$ orbital component are placed at 849.5 eV for both catalysts whereas the $3d_{5/2}$ orbital component are located at 837.0 eV for Ni/LSCF and at 836.3 eV for Ni-LSCF. Similar to the bare LSCF, these peaks are related to the presence of La^{3+} species in both Ni containing catalysts. As expected, differences between the two Ni containing catalysts can be seen within the Ni 2p region (875 - 840 eV) in ***Figure 2.6. (a)***. The $2p_{3/2}$ and $2p_{1/2}$ orbital components linked to Ni species are clearly discerned for Ni/LSCF material. The peaks located at 853.4 and 860.3 eV have been extendedly linked to $2p_{3/2}$ orbital component and its satellite characteristic of Ni^{2+} species. The peak at 873.6 eV were associated to the $2p_{1/2}$ satellite peak, also distinctive of Ni^{2+} species. Besides, the peak placed at 854.8 eV, in the $2p_{3/2}$ orbital component of Ni has been linked by Chen *et al.* [200] to the presence of Ni^{3+} species (see ***Figure 2.6 (a), inset***). Similarly, the peak found in the $2p_{1/2}$ orbital component at 871.8 eV has been related to the presence of Ni^{3+} species by Pereñíguez *et al.* [186] in their XPS studies carried out over $LaNiO_3$ perovskite. Despite that, it must be remarked that XPS cannot be used as a definitive proof of the existence of $LaNiO_3$, since Ni^{2+} and Ni^{3+} are difficult to discriminate, especially considering the overlapping of La 3d peaks and Ni $2p_{3/2}$ peaks. Thereby, based on the prior results revealed by XRD and H_2-TPR analysis along with the presence of a $Ni^{2+/3+}$ mixture at the surface deduced by XPS analysis, the formation of $LaNiO_3$ as secondary phase can be assumed for Ni/LSCF. Mainly two peaks can be appreciated into the Ni 2p region for Ni-LSCF catalyst, associated to the $2p_{3/2}$ orbital component (853.6 eV) and its corresponding satellite (862.4 eV). These peaks highlight the presence of low amount of Ni^{2+} species at the surface of this catalyst. No such peaks related to Ni^{3+} species are noticeable in this region, suggesting that nickel atoms are preferentially in the bulk of the structure rather than the surface for Ni-LSCF. This fact confirms, once again, the promotion of Ni insertion into the mixed oxide structure through the sol-gel method.

Generally, within the Co 2p region (***Figure 2.6 (b)***), peak associated to Co^{2+} are appreciated for both catalysts, Ni/LSCF and Ni-LSCF. Peak at 779.3 eV related to $2p_{3/2}$ orbital

component and an additional peak at low binding energy attributed to LMM Auger peak is found for Ni/LSCF. Besides the two peaks associated $2p_{3/2}$ orbital component of Co^{2+} species (at 780.2 and 785.0 eV), the formation of Co-Ni alloy might be deduced for Ni-LSCF by the peak located at 778.9 eV [201]. The $2p_{1/2}$ and $2p_{3/2}$ orbital component can be seen for both for both catalysts in the XPS spectra of Fe 2p region (***Figure 2.6 (c)***), exhibiting peaks at 721.5 ($2p_{1/2}$) and 711.1 eV ($2p_{3/2}$) for Ni/LSCF and 722.9 ($2p_{1/2}$) and 711.0 ($2p_{3/2}$) eV for Ni-LSCF that correspond to the existence of Fe^{3+} species. In addition, a L3VV Auger peak placed at 703.3 eV is shown for Ni/LSCF catalysts, whereas the peak located at lowest temperature into Ni-LSCF spectra (709.2 eV) has been associated to the formation of Fe-Ni alloy [202]. Therefore, the partial insertion of Ni into LSCF structure promoted through sol-gel favours the formation of CoNi and FeNi alloys at the surface of Ni/LSCF catalyst. The presence of these alloys can play an important role in the catalytic activity of this material.

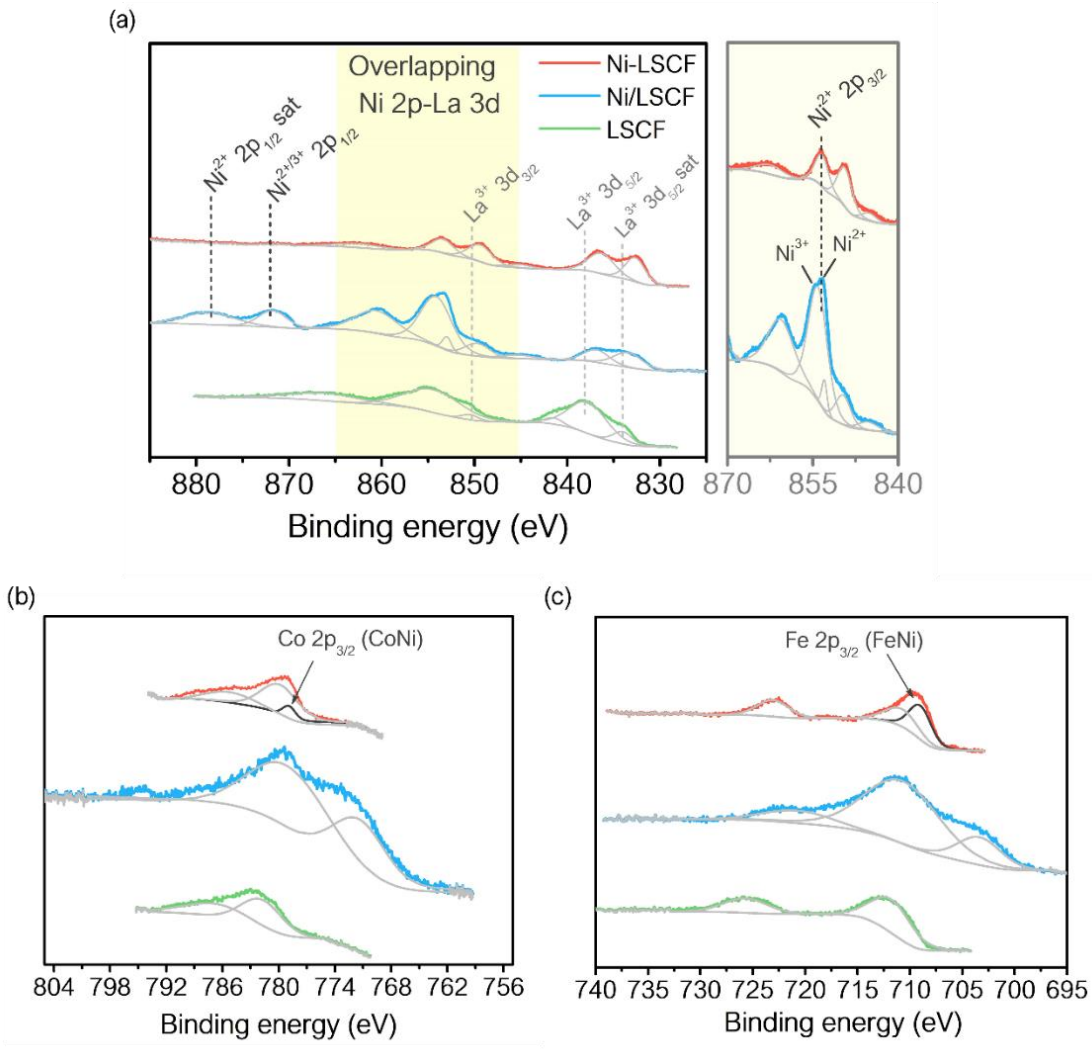

Figure 2.6. XPS of the synthesized La-based materials: (a) La 3d – Ni 2p, (b) Co 2p and (c) Fe 2p regions

The chemical surface composition of the different materials, calculated from the XPS spectra, are reported in ***Table 2.5*** and compared to the stoichiometric bulk composition in brackets. Comparing with the bulk, slightly lower Zr and higher Sm surface content is noticeable for CZS (***Table 2.5 (a)***). Similar surface composition was found comparing with bulk for the CY-based materials (***Table 2.5 (b)***). As expected from H_2-TPR results, higher Ce^{3+} content at the surface was found for CZS (9.4%) in comparison with CY support (3.8%), since the incorporation of Y^{3+} into CeO_2 structure may reduce the formation of Ce^{3+} as it has been above discussed. Regarding the bare LSCF mixed oxide (***Table 2.5 (c)***), in order to remove the Ni interference, only the region areas associated to La $3d_{5/2}$ components (from 845 to 830 eV) were considered to calculate the La surface content. A different surface composition compared to the bulk was detected for the bare LSCF mixed oxide. Higher amount of La is found at the surface compared to the bulk, consistent with the presence of La_2O_3 phase prior observed by XRD result for LSCF oxide.

Relating to the impregnated materials, an increase of Ni content at the surface compared to the nominal bulk was observed (85.8 %At. *vs* 23.1 %At. for Ni/CZS and 43.4 %At. *vs* 21.5 %At. for Ni/CY). Thus, higher Ni/(total Ce ions) surface ratio has been found for Ni/CZS (8.8) with respect to Ni/CY (4.1). Since the surfaces of impregnated materials are highly covered by Ni, no Ce^{3+} species at the surface are observed for Ni/CZS, while a decrease of Ce^{3+} is evidenced Ni/CY (1.2%) with respect to the corresponding bare supports. Concerning LSCF impregnated catalyst, Ni/LSCF, higher Ni content at the surface compared to the bulk is also discerned. Additionally, a noteworthy decrease of La and Sr content compared to the bulk composition and to the bare support surface composition can be detected, which could suggest that the NiO phase is mainly located over the La or/and Sr cations in this catalyst. The rather decrease in La content (8.2 %At.) compared to the bare support (34.9 %At.) verifies the formation of the second perovskite phase based on $LaNiO_3$, according to previous characterization results.

A fairly lower Ni surface content is evidenced for the sol-gel solids comparing with the bulk composition (11.4 %At. vs 23.1 %At. for Ni-CZS and 9.1 %At. *vs* 21.5 %At. for Ni-CY, not estimated for Ni-LSCF) and with the surface composition of the impregnated materials. Once again, it is highlighted that Ni addition by sol-gel method encourages Ni^{2+} insertion into the oxide structures. Regarding the Ni/total Ce ions ratio, same Ni content at the surface has been found for Ni-CZS and Ni-CY (0.20). A larger amount of Ce^{3+} ions at the surface was noticed for the Ce- based sol-gel materials with respect to the impregnated ones, as Ni insertion promotes the reduction of Ce^{4+} to Ce^{3+} along with formation of oxygen

vacancies. The Ni surface content is not reported for the LSCF-based sol-gel material, Ni-LSCF, since no noticeable peaks into the Ni $2p_{1/2}$ region has been appreciated (see ***Figure 2.6 (a)***). Similar to Ni/LSCF, the La content shown at the surface for Ni-LSCF (29.5 %At.) is lower than that displayed for the bare support (34.9 %At.) indicating that Ni insertion facilitates La introduction into the LSCF structure. Thereby, the formation of La_2O_3 phase is less favored through sol-gel method and, it elucidates its non-detection by XRD analysis for Ni-LSCF. Moreover, an increase of the Sr surface content is clearly found for this material (30.0 %At.), compared to the bulk composition (16.5 %At.) and to the corresponding bare LSCF mixed oxide (21.2 %At.) and impregnated materials (5.4 %At.), Ni/LSCF. Owing to its basic character, this high Sr content displayed for Ni-LSCF could favor the water adsorption at the surface of this material under steam reforming conditions. Moreover, the lower Co and Fe content is displayed for Ni-LSCF compared to the impregnated Ni/LSCF might be due to the CoNi and FeNi alloy observed at the surface for the former catalyst.

(a)	*Ce (%)*	*Zr (%)*	*Sm (%)*	*Ni (%)*	*Ni/total Ce ions*	*% Ce^{3+}*
CZS	63.0 [63.0]	29.6 [33.0]	7.4 [4.0]	-	-	9.4
Ni/CZS	9.7 [48.5]	4.5 [25.4]	- [3.1]	85.8 [23.1]	8.8	-
Ni-CZS	59.1 [48.5]	29.5 [25.4]	- [3.1]	11.4 [23.1]	0.2	5.9

(b)	*Ce (%)*	*Y (%)*	*Ni (%)*	*Ni/total Ce ions*	*% Ce^{3+}*
CY	48.2 [50.0]	51.8 [50.0]	-	-	3.8
Ni/CY	10.6 [39.2]	32.2 [39.2]	43.4 [21.5]	4.1	1.2
Ni-CY	46.1 [39.2]	44.8 [39.2]	9.1 [21.5]	0.2	5.5

(c)	*La (%)*	*Sr (%)*	*Co (%)*	*Fe (%)*	Ni (%)
LSCF	34.9 [30.0]	17.3 [20.0]	17.5 [10.0]	30.4 [40.0]	-
Ni/LSCF	8.2 [25.0]	5.4 [16.5]	21.4 [8.3]	40.8 [33.0]	24.2 [17.3]
Ni-LSCF	29.5 [25.0]	30.0 [16.5]	19.7 [8.3]	20.8 [33.0]	-

Table 2.5. Chemical surface composition calculated by XPS and bulk composition in brackets for (a) CZS-, (b) CY- and (c) LSCF-based materials

In the literature, oxygen surface species have been commonly studied for materials with high oxygen mobility and/or oxygen storage capacity, since the lattice oxygen species at the surface could avoid coke deposition by generating oxycarbonate species which might react with deposited carbon to produce CO_2/CO [203,204]. Therefore, information about the role of these species in C-H cleavage and coke formation on the surface can be deduced.

Accordingly, ***Figure 2.7*** shows the O 1s region for the investigated materials. By curve fitting analysis, peaks located around 529-528 eV and 530-532 eV can be distinguished for all solids. Whereas the peak at lower binding energy (BE) is generally associated to the lattice oxygen species, the latter is connected to the surface or adsorbed one [126,134,205]. No noticeable differences in the shape and binding energy has been found between the bare CZS mixed oxide and the corresponding sol-gel material (Ni-CZS), an additional peak can be detected at lower binding energy for the equivalent impregnated one (Ni/CZS) (***Figure 2.7 (a)***). This additional peak around 526-527 eV has been associated to monoxygen species in the literature [206]. No modification in the shape and binding energy between the bare CY mixed oxide and its corresponding Ni-containing materials has been found (***Figure 2.7 (b)***). Regarding LSCF-based materials (***Figure 2.7 (c)***), an additional peak located at higher BE (534-533 eV), identified as adsorbed water [134,163], was found for bare LSCF mixed oxide and it remained in the corresponding impregnated catalyst, Ni/LSCF. Additionally, a shift to lower binding energies can be evidenced for both Ni-containing materials (Ni/LSCF and Ni-LSCF), being more pronounced for the sol-gel material, compared to the bare LSCF mixed oxide. Sutthiumporn *et al.* [163] investigated the role of lattice oxygen on C-H bond activation over a series of $La_{0.8}Sr_{0.2}Ni_{0.8}M_{0.2}O_{3-\delta}$ perovskites (M= Bi, Co, Cr, Cu and Fe) under dry reforming of methane. In this work, a relation between the shift to lower BE into the O 1s region in XPS and the catalytic performance of the different perovskite were found. The lower the BE, the weaker the interaction between O^{2-} species and A/B-cations, then, higher is the lattice oxygen mobility. The enhancement in oxygen mobility improved catalytic activity. Taking that into account, the shift to lower BE detected in the Ni containing materials may be related to the enhancement of the lattice oxygen mobility in the LSCF support by the Ni addition. Thereby, high removable oxygen species are attained by the Ni addition for LSCF-based materials. This fact is in concordance with H_2-TPR analysis, in which the shift to lower reduction temperature observed for Ni/LSCF and Ni-LSCF compared to the bare LSCF indicates that oxygen species can be more easily removed in presence of Ni species.

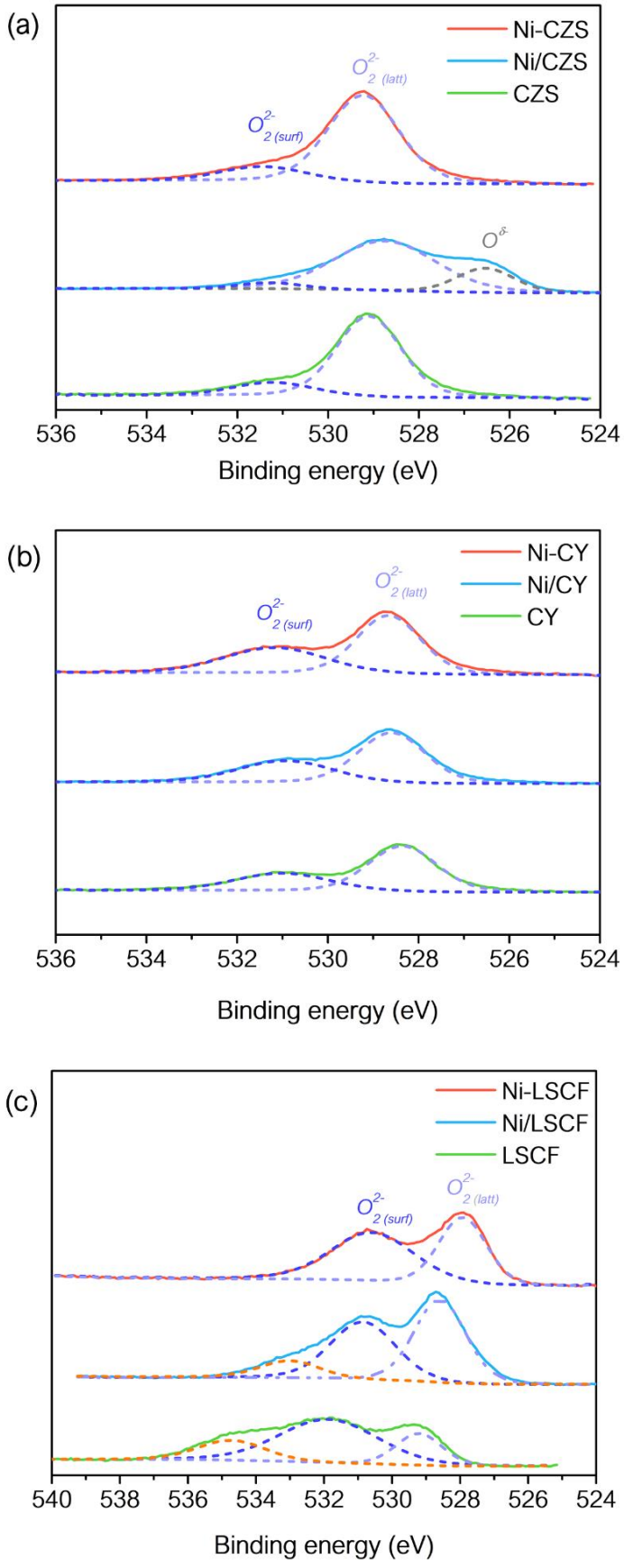

Figure 2.7. XPS of the synthesized materials. O 1s region for (a) CZS-, (b) CY- and (c) LSCF- based materials

2.5.5. H_2 chemisorption and Temperature Programmed Desorption (H_2-TPD)

The H_2 chemisorption and temperature programmed desorption is widely used to determine the metallic surface of the active phase. In addition to H_2 chemisorption, adsorbed hydrogen species with different H-metal and eventually H-mixed oxide interaction could be distinguished by H_2-TPD profiles, providing information about the different kinds of metal sites or other hydrogen adsorption sites generated at the surface.

Figure 2.8 shows the H_2-TPD profiles of the investigated materials. Concerning the Ce-based materials (***Figure 2.8 (a)***), some differences in the TPD profile shapes areappreciated between CZS- and CY-based materials. A peak located around 120-140 ºC,ascribed to hydrogen species weakly adsorbed over the active metal sites, are found for both, CZS- and CY-based materials, whereas an additional desorption peak at high temperatures, around 200 ºC, is also discerned for CY-based ones. This high temperature peaks have been linked to hydrogen species strongly adsorbed over the active metal [207]. The broad desorption peak attained at temperatures above 300 ºC could be associated to hydrogen on the mixed oxide surface caused by hydrogen spillover phenomena from the Ni metal site to the mixed oxides surface. As it has been shown in the H_2-TPR profiles, the presence of Co species partially reduced under reduction conditions at 600 ºC is extremely probable for La-based oxides (see ***Figure 2.4 (c)***). Therefore, in order to determine the desorption peaks as consequence of the hydrogen-Co^0 interactions, the H_2-TPD profile of the bare support as well as the Ni containing LSCF solids are presented in ***Figure 2.8 (b)***. Hence, two main peaks, one located at 124 ºC and the other at 386 ºC, have been evidenced for the bare LSCF. Gonzalez Tejuca *et al.* [208] found desorption peaks at 72 ºC and above 200 ºC during H_2-TPD carried out over $LaCoO_3$ solid reduced at 500 ºC. These peaks were respectively attributed to a weakly and a strongly adsorbed H species on reduced cobalt. Thus, the two desorption peaks observed for LSCF have been related to different H-Co^0 interaction and proved the partial reduction of cobalt during the reduction conditions at 600 ºC. Similar H_2-TPD profile have been found for Ni- and RuNi- containing catalysts. A slight increase in intensity of the peak at higher temperature for Ni/LSCF suggested the promotion of Co reduction by the presence of Ni. This enhancement has been also observed by H_2-TPR analysis, where an increase in the H_2 consumption is observed in the region I, linked to the reduction of Co and Ni species, for Ni/LSCF catalyst (***Figure 2.4 (c)***). By contrary, this peak became less intense for the sol-gel Ni-LSCF compared to the bare support and the impregnated Ni/LSCF. This decrease is in

accordance with the lower Co content found for Ni-LSCF than Ni/LSCF by XPS (*Table 2.5 (c)*). Moreover, the reduction of Co species might be less favoured in the case of Ni-LSCF catalyst due to the CoNi alloy formed at the surface of Ni-LSCF. An increase in the intensity of both peaks, at low and high temperature, by the addition of Ru over Ni/LSCF was detected, standing out that the presence of Ru facilitates the reduction of Co and Ni species as observed by H_2-TPR analysis. Thereby, a higher amount of reduced Co is achieved for RuNi/LSCF compared to Ni/LSCF.

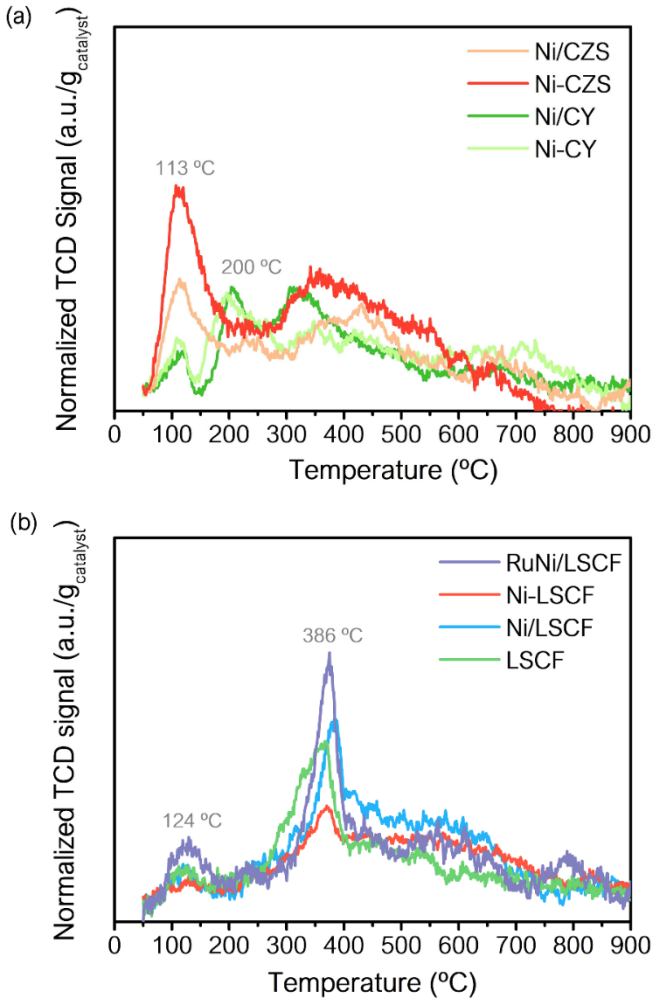

Figure 2.8. H_2-TPD profiles of the synthesized materials: (a) Ce-based systems (CZS and CY) and (c) LSCF-based systems

The metallic nickel surface obtained after reduction pre-treatment at 600ºC has been determined considering the total mmol H_2 desorbed related to the peak at around 120- 200 ºC (H-metal interaction) for Ce-based oxides and around 124 – 386 ºC for La-based oxides by H_2-TPD. Considering that it is complex to distinguish between Ni^0 and Co^0 within the La-based materials, a general metallic surface was calculated. As Co and Ni

shown similar exposed surface per atom (6.59 $Å^2$ for Co and 6.51 $Å^2$ for Ni), this metallic surface has been estimated using the Ni exposed surface, since this metal is prevailing in the catalysts. Similarly, the Ni exposed surface has been used for the calculation of metallic surface for RuNi/LSCF catalyst. Thus, the amount of desorbed hydrogen along with the metallic surface are listed in ***Table 2.6*** for the prepared catalysts.

Concerning CZS-based materials, sol-gel Ni-CZS catalyst led to higher metallic nickel surface (1.7 $m^2 \cdot g^{-1}$) than the impregnated Ni/CZS catalyst (0.9 $m^2 \cdot g^{-1}$). This higher value might be related to the higher SSA displayed for Ni-CZS (22 $m^2 \cdot g^{-1}$) compared to Ni/CZS (15 $m^2 \cdot g^{-1}$). Additionally, the low metallic nickel surface attained for Ni/CZS might suggest a strong deactivation by sintering process during the reduction pre-treatment due to the high Ni content exposed at the surface of this material estimated by XPS (***Table 2.5 (a)***). The opposite tendency is followed by the CY-based materials, in which the impregnated Ni/CY material displayed the highest metallic nickel surface (2.2 $m^2 \cdot g^{-1}$), pointing out that Ni dispersion is more favoured by Ni impregnation on CY than CZS support. The low Ni surface showed for Ni-CY (1.0 $m^2 \cdot g^{-1}$) compared to Ni/CY (2.2 $m^2 \cdot g^{-1}$) can be also associated to the lower SSA (12 $m^2 \cdot g^{-1}$) than Ni/CY (22 $m^2 \cdot g^{-1}$). In brief, the metallic nickel surface decreased in the following order among the Ce-based catalysts: Ni/CY (2.2 $m^2 \cdot g^{-1}$) > Ni-CZS (1.7 $m^2 \cdot g^{-1}$) > Ni-CY (1.0 $m^2 \cdot g^{-1}$) = Ni/CZS (0.9 $m^2 \cdot g^{-1}$). Within the La-based oxides, rather lower metallic surface is attained for Ni-LSCF (0.5 $m^2 \cdot g^{-1}$) compared to the impregnated Ni/LSCF (1.9 $m^2 \cdot g^{-1}$). This low metallic surface might be associated to the fact that Ni is well integrated into the LSCF structure and to the formation of CoNi and FeNi alloys observed by XPS for Ni-LSCF catalyst. Eventually, the highest metallic surface among the La-oxide materials is attained by the addition of Ru over Ni/LSCF, leading to a metallic surface of 2.1 $m^2 \cdot g^{-1}$. These metallic surface values are no comparable with those estimated for Ce-based materials, since in the latter the metallic surface is fully associated to metallic Ni, whereas a general surface including metallic Ni and Co is reported for La-based materials. Generally, rather low metallic surface is attained for all prepared catalysts, caused by the low SSA of the supports and the Ni sintering due to the high reduction temperature used for the reduction (600 ºC).

It should be highlighted that few data can be found in the literature of tar reforming about the use of H_2-TPD technique for estimating metallic surface, making a bit more complex the understanding of the obtained results.

	H₂-TPD	
	μmol $H_2/g_{catalyst}$	S_{Ni}^0 $(m^2 \cdot g^{-1})$¥
Ni/CZS	11.2	0.9
Ni-CZS	22.8	1.7
Ni/CY	28.6	2.2
Ni-CY	13.1	1.0
	μmol $H_2/g_{catalyst}$ $(x10^{-2})$	$S_{metallic}$ $(m^2 \cdot g^{-1})$¥
Ni/LSCF	24.2	1.9
Ni-LSCF	5.9	0.5
RuNi/LSCF	26.5	2.1

¥ Estimated by equation 12 (*Annex, section D*)

Table 2.6. Quantitative analysis of metallic Ni surface of the synthesized catalysts

2.6. Conclusions

Six nickel-based catalysts using three different supports (CZS, CY and LSCF) were synthesized by two preparations methods, *wet impregnation* (Ni/CZS, Ni/CY and Ni/LSCF) and *one step sol-gel* (Ni-CZS, Ni-CY and Ni-LSCF). In this chapter, the influence of the synthesis pathway on the support physicochemical properties has been investigated by several characterization techniques, such as N_2 physisorption, XRD, H_2-TPRXPS and H_2-chemisorption and TPD.

Firstly, an improvement in the textural properties (SSA and V_{pore}) by the sol-gel method has been observed for Ni-CZS and Ni-LSCF catalysts compared to the bare supports, whereas this enhancement was not noticeable for sol-gel Ni-CY catalyst. By comparing with their corresponding bare supports, an enhancement was also attained by impregnation method for Ni/LSCF catalyst, while similar textural properties were attained for Ni/CZS and Ni/CY catalysts. Among all the catalytic systems, Ni/CY and Ni-CZS led to the best textural properties with the highest SSA (22 $m^2 \cdot g^{-1}$). No modification in crystalline structures and similar support particle sizes due to the preparation method has been found within the Ce-based supports and their equivalents Ni containing materials. Among Ce-based oxides, a fluorite-type structure was attained for CZS mixed oxide, whereas the existence of a fluorite- and pyrochlore-type structure was found for CY mixed oxide. Concerning the NiO particle size, opposite behaviour along these two families of materials. Smaller NiO particle size was reached by impregnation method for CY (Ni/CY) compared to the sol-gel ones, while the sol-gel method generated the smaller NiO particles into CZS based solids (Ni-CZS). Within the catalytic systems, the smallest NiO particles size was achieved for Ni/CY catalyst (8 nm). As regard to La-based materials, a predominant perovskite structure with orthorhombic symmetry along with a secondary phase related to the cubic La_2O_3 phase were identified for LSCF mixed oxide. The formation of $LaNiO_3$ phase

through NiO impregnation has been evidenced by XRD, H_2-TPR and XPS results for Ni/LSCF, whereas the insertion of La into LSCF structure promoted by Ni addition through sol-gel method has been also verified by XRD and XPS for Ni-LSCF. Moreover, the addition of Ru over Ni/LSCF does not lead to significant modification in the physicochemical properties compared to the corresponding Ni/LSCF catalyst. Generally, the lower support lattice parameter, the stronger NiO-support interaction elucidated by the H_2-TPR profiles and the lower Ni content detected at the surface by XPS for the sol-gel catalysts highlighted the presence of $Ni^{2+/3+}$ species partially inserted into the mixed oxide structures in these catalysts. The noticeable increase in the support reducibility for the three sol-gel catalysts compared to bare supports and impregnated catalysts highlights that the existence of inserted Ni ions promotes the reduction of the supports. The metallic Ni surface is strongly influence by the preparation method for each family of material. The sol-gel method produced a better metallic surface for CZS materials, while the higher metallic surface within CY- and LSCF-based materials was attained by impregnation. Once again, Ni/CY showed the highest metallic Ni surface (2.2 $m^2 \cdot g^{-1}$) among all catalytic systems. Therefore, Ni/CY can postulate as a promising catalytic material for tar abatement since displayed the best physicochemical properties within all the synthesized materials.

A summary of the effect of the Ni addition pathway on the physicochemical properties of the supports is reported in *Table 2.7.* Generally, similar influence on the support properties caused by the impregnated and one step sol-gel methods have been evidenced. Thus, the effect of Ni addition pathway and the effect of the support structure on reforming reaction of toluene and phenol as tar model compounds will be investigated in the subsequent chapter (Chapter 3).

	Addition pathway	SSA	$a_{support}$	Support reducibility	$S_{metallic}$
CZS	Impregnation	↔	↔	↑	↓
	Sol-gel	↑	↓↓	↑↑	↑
CY	Impregnation	↔	↔	↑	↑↑
	Sol-gel	↓	↓	↑	↓
LSCF	Impregnation	↑	↔	↑	↑↑
	Sol-gel	↑	↓	↑↑	↓

↑ Increase ↓ Decrease ↔ Similar

Table 2.7. Effect of the Ni addition pathway on the physicochemical properties of the different supports.

CHAPTER 3

PRE-TREATMENT CONDITIONS AND CATALYTIC TESTS: POWDERED SYSTEMS

Abstract

Catalytic steam reforming of tars has been considered as one of the most promising and attractive method for post-treatment of syngas produced by biomass gasification process. Great advantage of this strategy is that high-quality syngas can be achieved by producing useful gas compounds such as H_2, CH_4 or CO from tar conversion at relatively low temperature.

In this chapter, the general aspects of steam reforming reactions and the different reaction conditions reported in the literature for tar removal over Ni-based catalysts are discussed. Afterwards, the catalytic performances of the six prepared catalysts in tar removal using phenol and toluene as model tar compound are discussed. Parameters such as reaction temperature and pre-treatment conditions are studied in order to mimic real biomass gasification conditions and to elucidate their effect on the catalytic behaviour.

3.1. Introduction

The chemistry involved in catalytic tar decomposition is a complex mix of hydrocarbon decomposition (*Equations 4.1-4.4*) and equilibrium reactions (*Equations 4.5-4.9*) [209]. The products distribution of these catalytic reactions is a result of the competition among them, and it is closely connected to reaction conditions (temperature, pressure, steam/carbon ratio, inlet gas composition etc…). In the literature, the principal mechanism of the steam reforming of tar on the metal sites of catalysts is linked to the hydrocarbon dehydrogenation, generating carbon deposits at the surfaces. This deposited carbon can further react with steam to produce additional CO and preserve the catalytic activity. The resulting CO can also react with the excess of steam through water gas shift reaction producing H_2 and CO_2 [35]. Furthermore, the formation of carbon deposits on the catalyst surface through unwanted site reactions, as tar decomposition (thermal cracking) or Boudouard reaction, can simultaneously occur. This undesirable effect is usually enhanced by molecular weight and aromaticity of the tar molecules [210].

Many researchers studied tar abatement by catalytic steam reforming. Owing to the complexity of real tar mixtures, most of the studies have chosen different model tar molecules such as benzene [73], toluene [61,99,211] or naphthalene [64,86] to well understand the catalytic performance and elucidate the mechanisms. Jess [212] investigated the mechanism and the kinetics of thermal reactions of aromatic hydrocarbons using naphthalene, toluene and benzene as model molecules. He indicated that the thermal decomposition of aromatic hydrocarbons leads to the formation of benzene as intermediate. Michel *et al*. [89] showed a positive effect of a pre-treatment of olivine by water on the activity of Ni/olivine catalyst in steam reforming of α-methylnaphthalene. The enhancement was noticeable by the tar conversion, becoming 75% compared to 30% for the non pre-treated catalyst. They linked the improvement to a water storage which is released during the steam reforming reaction, causing higher CO and H_2 production. Among model compounds, toluene has been selected in literature as the tar model compound par excellence in order to well understand the efficiency of tar removal of many catalytic formulations, since it is one of the most abundant compounds in the syngas produced by biomass gasification and because it presents a stable aromatic structure [25,213]. Therefore, mechanistic studies, effect of reaction temperature, steam/carbon ratio and catalytic support for diverse catalysts have been widely reported for this model tar molecule.

(i) Hydrocarbon decomposition reactions:

$C_nH_m + nH_2O \rightarrow nCO + (n + {}^1/_2\, m)H_2$	$\Delta_r H°_{298K} \gg 0$	Steam reforming	*Reaction 3.1*
$C_nH_m + nCO_2 \rightarrow 2nCO + {}^1/_2\, mH_2$	$\Delta_r H°_{298K} \gg 0$	Dry reforming	*Reaction 3.2*
$C_nH_m \rightarrow C_xH_y + C_{(n-x)}H_{(m-y)}$	$\Delta_r H°_{298K} \gg 0$	Thermal cracking	*Reaction 3.3*
$C_nH_m \rightarrow nC^* + {}^1/_2\, m\, H_2$	$\Delta_r H°_{298K} > 0$	Carbon formation	*Reaction 3.4*

(i) Equilibrium reactions:

$CO + H_2O \leftrightarrow CO_2 + H_2$	$-41\ kJ \cdot mol^{-1}$	Water gas shift	*Reaction 3.5*
$CO + 3H_2 \leftrightarrow CH_4 + H_2O$	$-223\ kJ \cdot mol^{-1}$	CO methanation	*Reaction3.6*
$C^* + 2H_2 \leftrightarrow CH_4$	$-87\ kJ \cdot mol^{-1}$	Hydrogenation	*Reaction 3.7*
$2CO \leftrightarrow C^* + CO_2$	$-172\ kJ \cdot mol^{-1}$	Boudouard	*Reaction 3.8*

Standard reaction enthalpies values ($\Delta_r H°_{298K}$)

The mechanism of steam reforming of toluene over $La_{0.8}Sr_{0.2}Ni_{0.8}Fe_{0.2}O_3$ (LSNF) catalysts has been investigated by Oemar *et al*. [127], who stand out the important role of oxygen species in this reaction. Based on the characterization results over reduced LSNF catalysts, they concluded that water activation occurs on La_2O_3 or SrO to produce H_2, whereas toluene decomposes on the metal sites (Ni/Fe) to generate H_2 and adsorbed C_2 species as intermediate products. The C_2 species can react with the adsorbed oxygen species either from or with species issued from the water activation or lattice oxygen, to form adsorbed aldehyde species. These adsorbed aldehydes decompose into adsorbed CO and H_2 or react with another adsorbed oxygen species to form adsorbed CO_2. The final step is the desorption of the adsorbed CO, H_2 and CO_2. Simell *et al.* [209] studied the toluene decomposition reactions over dolomite, nickel catalyst, alumina and SiC in different gas atmosphere at 900 ºC under 2.0 and 5 MPa of pressure. They found that hydrocracking was the predominant reaction over SiC and alumina, whereas with dolomite and nickel catalyst the steam and dry reforming reactions took place at high rate.

The influence of several parameters in steam reforming of toluene, as reaction temperature, molar steam/carbon in the tar ratio (S/C) and catalysts, has been extensively studied. Zhao *et al*. [214] investigated, through thermodynamic simulations, the effect of temperature and S/C on the product distribution. The calculations indicate that, at reaction temperature from 750-900 ºC, a S/C molar ratio of 2.0 was favourable operation conditions for steam reforming of toluene in order to attain optimal hydrogen yield. Zhang *et al.* [215] used Ni/olivine catalysts, doped with CeO_2, for toluene reforming experiments at temperatures from 700 to 830 ºC with a S/C ratio of 5.0. An enhancement of toluene conversion and coke resistance by NiO/olivine doped with CeO_2 was noticeable at low temperature (700 ºC) compared to non-doped catalyst. Srinakruang *et al.* [216] investigated the sulphur and coke resistance for steam reforming of tar (toluene and naphthalene) over Ni/dolomite catalyst at reaction temperature of 730-850 ºC. An increase of toluene conversion has been evidenced by rising reaction temperature and almost no influence on catalytic activity by the presence of sulphur at 800-850 ºC was found.

Most of the studies discussed before were performed on a laboratory scale, introducing only toluene and water as reagents, since it allows a better understanding of the reaction process. Nevertheless, operating conditions on an industrial scale is significantly different. For instance, in a biomass gasification process, tar reforming reactions occur within the raw syngas composed of H_2, CO_2, CO, CH_4, H_2O, ashes, particles, tars etc… A study of the reforming of toluene or other tar model molecules in syngas atmosphere was hardly found. Oh *et al*. [217] conducted toluene reforming in syngas using different reaction temperatures (400-800 ºC) and a S/C ratio of 25 over a CaNiRu/Al_2O_3 catalyst with a loading of 1 %wt. Ca, 20 %wt. Ni and 0.6 %wt. Ru. The addition of toluene in the feed along with the raw syngas caused a modification in the catalytic activity toward CO_x methanation and WGS reactions, leading to differences in the produced syngas composition compared to reaction in raw syngas without tars. They observed that methanation reaction is inhibited at low temperatures (below 500 ºC). This suppression was associated to the preferred adsorption of toluene at the mesopores whose large size blocks the adsorption of smaller molecules such as, CO or CH_4. At temperatures above 500 ºC, the adsorbed toluene species reacted and the adsorption of CO, CH_4 and CO_2 in syngas were favoured, promoting the CO_x methanation and WGS reactions. The influence of a particular raw gas composition (1.5 vol% H_2, 2.1 vol% CO, 1.5 vol% CO_2 and 0.3 vol% CH_4 balanced with Ar) on catalytic activity for tests conducted in steam reforming of toluene and 1-methylnaphthalene at 800 ºC with a S/C ratio of 2.4 over Ni/CZ catalyst has been also revealed by Lacmaz *et al.* [218]. The introduction of the

raw gas caused a decrease in total tar conversion, due to the partial consumption of H_2O in methane steam reforming reaction. Similarly, methane dry reforming was predominant reaction than tar dry reforming in raw gas atmosphere. Moreover, the higher contribution of structural carbon in presence of raw gas mixture (HC + H_2 + CO + CO_2 + CH_4 + H_2O) compared to steam reforming of model tar compound (HC+H_2O) was attributed to the presence of CO, H_2 and CH_4 that could facilitate the formation of carbon nanotubes (CNTs) and carbon nanofibers (CNFs).

As it can be noted in the literature, tar reforming has been generally carried out at temperatures above 650 ºC, since tar reforming is significantly kinetically limited at low temperatures [209,217,219]. Currently, it has been reported complete tar conversion at reaction temperatures above 650 ºC for nickel-based materials and olivine-supported catalysts [217,219]. Consequently, these kinds of catalytic systems have been used in an in-bed configuration as primary catalysts for tars abatement at industrial scale in order to improve the efficiency of the overall process and decrease the costs. However, metal-supported catalysts as primary catalysts are prone to undergo fast catalytic deactivation. Then, a tar removal strategy at low temperatures and using metal supported catalysts as secondary catalysts are desired in order to increase the energy efficiency of the overall process. Considering the outlet temperature of syngas produced during gasification process (≈ 500-600 ºC) and the reaction temperatures of the subsequent process, as Fischer-Tropsch (250-400 ºC), an efficient tar removal approach at temperature range from 400-600 ºC is highly required [47,217]. Thereby, some researchers have performed steam reforming of toluene at temperatures below 600 ºC. Jousiunkas *et al.* [220] investigated the steam reforming of toluene over Ni catalysts obtained from hydrotalcite precursors in a temperature range from 400-750 ºC with a S/C ratio of 1.5 and GHSV of 20000 h^{-1}. Toluene conversions of 60 and 65% have been reached at 500 and 550 ºC, respectively, for a catalyst with 10 wt% Ni loading. They observed that total toluene conversion was attained at temperatures above 650 ºC and that the catalytic efficiency decreased with high Ni loadings, in good agreement with other studies [88,219]. Liu *et al*. [221] explored steam reforming of toluene over 10 %wt Ni/activated carbon catalysts at different reaction temperatures (500-700 ºC) with a S/C ratio and LHSV equal to 2.0 and 0.87 h^{-1}, respectively. Their results show the lowest catalytic activity at 500 ºC. At this temperature the carbon conversion went from 45 to 24% along the reaction time. An improvement in toluene conversion was observed at 550 ºC with an initial toluene conversion of 90%. Nevertheless, a fast deactivation was observed with a depletion in the conversion. Besides that, better catalytic performance was found for Ni/AC catalyst at 600

ºC, reaching a complete toluene conversion, compared to two conventional catalysts, Ni/Al_2O_3 (69%) and Ni/olivine (37%).

Several researches suggest differences in steam reforming mechanism of hydrocarbons and oxygenates, highlighting the faster deactivation *via* carbon formation caused by the latter. Czernik *et al*. [210] remarked that oxygenated compounds such as, furans and phenols, showed a greater tendency to coke formation due to their thermal instability. Artxete *et al*. [70] evidenced also a higher carbon formation through steam reforming of oxygenated compounds (furfural, anisol and phenol) compared to hydrocarbons (toluene, indene and methylnaphathalene). This tendency to carbon formation highlights the low thermal stability of oxygenated compounds, resulting in thermal decomposition as well as cracking reactions on the catalyst surface. In addition, an enhancement of reverse WGS reaction was also found during steam reforming of the oxygenate compounds (phenol, furfural and anisole) and underlines that these oxygenates compounds displace the thermodynamic equilibrium to the endothermic route. Among all oxygenated compounds, phenol displayed the lowest conversion. It has been reported that decomposition of phenol over Ni-based catalysts is harder than other tar model compounds. For instance, Wang *et al.* [222] estimated the adsorption pathway and the potential energy surface for decomposition of phenol, among other model tars, on Ni (111) surface. In their study, they showed that phenol decomposition is an endothermic process and generates products with higher energies and lower stability compared to the other oxygenated compounds, like furfural, whose decompositions are exothermic. The endothermicity of phenol decomposition compared to the other compounds suggested that phenol decomposition may be harder. Similarly, M. Koike *et al.* [223] estimated the reaction order with respect to toluene and phenol for Ni/Mg/Al catalyst. Whereas a reaction order close to zero was found for toluene, a strongly negative reaction order with respect to phenol was obtained. Therefore, these results suggested a strong phenol adsorption and/or a high coverage of its derivatives. Contrary to toluene, a limited number of studies have been focused on steam reforming of phenol as tar model molecule [80,224–226]. Peng *et al.* [226] conducted steam reforming of phenol over Fe/Ni-catalysts at different reaction temperatures (600 – 750 ºC) and S/C ratios (0.3 - 13.3). They found that 700 ºC was the optimal reaction temperature and no significant improvement in phenol conversion by increasing the S/C ratio from 1.3 to 13.3 was observed. Constantinou *et al.* [80] compared three natural catalysts (calcite, dolomite and olivine) in steam reforming of phenol in the range of temperature of 650-800 ºC. At 800 ºC, dolomite displayed the best catalytic activity in terms of phenol conversion (35%) and hydrogen selectivity compared

to olivine (27%), whereas at low temperature (650 ºC) olivine led to the more active material with a conversion of 29% compared to 20% for dolomite. They also studied the steam reforming of phenol with a S/C ratio of 1.3, in a low temperature range (350-550 ºC), over Rh-based catalysts deposited on different Ce-Zr mixed oxides and compared to a conventional Ni-based material. A enhancement in phenol conversion was observed at temperature range of 350-450 ºC for 0.5 wt%Rh-based catalysts compared to 44 wt% Ni-based one [224].

To date, steam reforming seems to be an attractive alternative to enhance the global efficiency of the biomass gasification process. In many researches works, different kinds of tar molecules have been investigated in steam reforming in order to well understand the catalytic reaction process. Plenty operational conditions, configurations and catalysts dealing with steam reforming of toluene as model molecule have been reported. Fewer studies are related to other tar molecules, such as phenol.

3.2. Partial objectives

The effect of Ni addition pathway and support structure on the catalytic performance of the prepared catalysts in tar reforming reaction has been evaluated. Toluene and phenol were the model tar compounds. The catalytic tests were carried out in realistic ex-biomass gasification syngas composition and under isothermal conditions at two reaction temperatures (400 and 550 ºC). As prior shown in the introduction, these reaction temperatures are low for catalytic tar abatement.

The results of these catalytic tests allowed the selection of the best catalysts for being further studied at pilot plant scale. As well, in order to conduct an in-situ reduction pretreatment under the raw product gases at pilot plant scale, the influence of a reduction pretreatment under syngas on catalytic efficiency in tar removal has been also evaluated over the selected catalysts.

3.3. Experimental set-up and procedure

3.3.1. Choice of tar model molecules and inlet gas composition

As it has been already mentioned in *Chapter 1*, the objective of this work is the implementation of a catalytic system working under real gasification conditions in a pilot plant scale. Hence, the tar model molecules, as well as the operating conditions of catalytic steam reforming at laboratory scale were chosen based on the tar distribution, syngas composition and temperature measured at the outlet of the gasifier in Offenburg. Thus, the raw syngas composition produced under real biomass gasification conditions varied in the

intervals listed in ***Table 3.1*** and a similar gas composition was selected in consequence for conducting the catalytic test at laboratory scale.

	CH_4 (%vol)	H_2 (%vol)	CO_2 (%vol)	CO (%vol)	H_2O (%vol)	
Pilot plant	1-2	14-16	10-12	20-25	10	N_2 balance
Laboratory	2	16	12	20	10	N_2 balance

Table 3.1. Raw syngas composition range produced at pilot plant scale and the syngas composition chosen for catalytic test at laboratory scale.

The tar content at different operational conditions of the gasifier and the raw syngas composition is also shown in ***Figure 3.1.*** In good agreement with literature, toluene was the majority tar among all molecules, followed by naphthalene. This explains why toluene is one of the model molecules under study. As some kinetic studies reported differences in reaction mechanism between hydrocarbon and oxygenated compounds over Ni surface, in this work phenol was also studied in order to investigate the efficiency of the catalysts in the reforming of these oxygenated compounds.

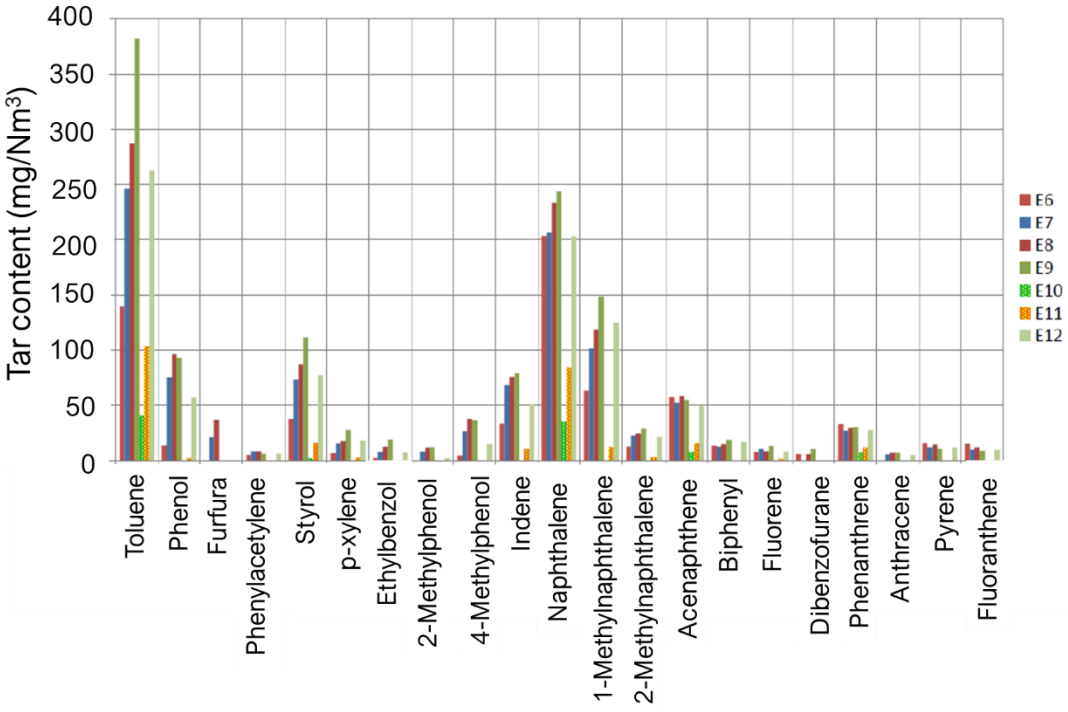

Figure 3.1. Tar distribution in raw syngas at different operating conditions at the outlet of gasifier on real biomass pilot plant from University of Offenburg

The feed composition of the gaseous components along with the two model tar molecules chosen are presented in ***Table 3.2***. As the tar molecules were injected one-by-

one, a higher inlet tar content than that attained at pilot plant scale were used, keeping the constant the inlet constant ratio (lab/pilot) at around 40 (*Table 3.2*).

Gaseous Component	Gas Flow ($Nml \cdot min^{-1}$)
CH_4	2.8
H_2	22.2
CO_2	16.7
CO	27.8
H_2O	13.9
N_2	55.6
Total gas flow	139

		Lab scale	Pilot plant	Inlet content ratio
Model tar molecules		*Inlet content ($g \cdot Nm^{-3}$)*	*Inlet content ($g \cdot Nm^{-3}$)*	*Lab/pilot*
Phenol	0.14	4.0	0.090	44
Toluene	0.64	13.4	0.350	40

Table 3.2. Inlet gas flows of the gaseous components and the model tar molecules

Eventually, the reaction temperature was chosen based on the temperature of the raw syngas resulting from biomass gasification at pilot plant, which was around 500 ºC. Thus, reaction temperatures of 400 and 550 ºC were used during the catalytic steam reforming at laboratory scale.

3.3.2. Catalytic performances

The catalytic tests were performed at atmospheric pressure in a fixed bed down-flow quartz reactor with 5.0 mm of internal diameter in a home-made experimental set-up coupled to an on-line gas chromatograph Agilent 6890N fitted with a TCD (*Scheme 3.1*.) The reactor was heated with a programmable tubular oven and the reaction temperature were followed *in situ* by a thermocouple placed at the centre of the catalytic bed. The flow of the reactants in gas phase was managed by calibrated mass flow controllers and the distilled water was injected at the inlet of the reactor by means of calibrated micro-pump. Afterwards, the product gases were analyzed on-line and the product liquids were recorded using cooled traps.

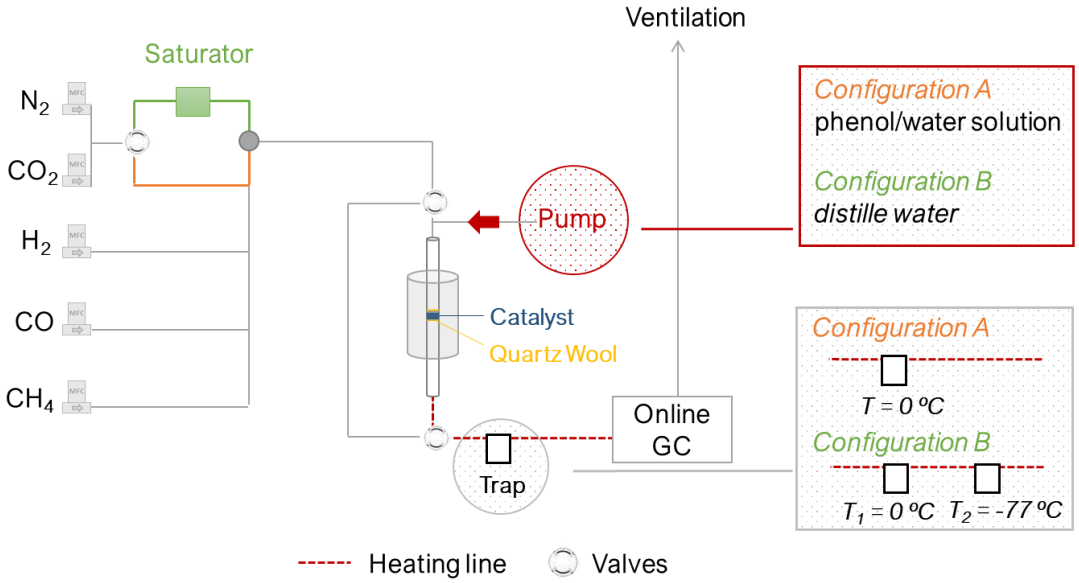

Scheme 3.1. Experimental set-up at laboratory scale. *Configuration A* and *B* for phenol and toluene reforming, respectively.

3.3.2.1. Catalytic test without tar model molecules

Firstly, catalytic tests without tars at the inlet were performed to evaluate the catalytic activity toward water gas shift (WGS) and CO_x methanation reactions. The catalytic tests were carried out in 350-600 ºC range of temperature using the gaseous feed (except tars) reported in ***Table 3.2***. The water was introduced using a total liquid flow of

10.4 µL·min^{-1}. The total gas flow rate was fixed at 139 NmL·min^{-1} and the catalyst loading into the reactor was 23.0 mg ($WHVS_{gas}$ = 370 h^{-1}, *Equation 3.1*), leading to around 2.3 mg of Ni° in the reactor.

$$WHSV_{gas}(h^{-1}) = \frac{Total\ gas\ mass\ flow\ (g{\cdot}h^{-1})}{Mass\ of\ catalyst\ (g)} \qquad \textit{Equation 3.1}$$

Afterwards, the catalytic efficiency at different temperature in steam reforming of tar has been studied, using the same gaseous feed composition (***Table 3.2***), total gas flow (139 NmL·min^{-1}) and catalysts loading (23 mg) than that used for the catalytic test without tar. As observed in ***Table 3.2.,*** the fraction of tars introduced are rather smaller compared to those of gas phase, therefore, the variation of the total flow rate and the decrease of the fraction of the other components can be neglected. In order to investigate the effect of temperature in tar reforming, the catalytic tests have been carried out under isothermal conditions at

400 ºC and/or 550 ºC for 6 h, using a fresh catalytic bed for each reaction temperature.

Reduction pre-treatment in two different atmospheres were performed: (i) H_2/N_2 mixture and (ii) syngas atmosphere

3.3.2.2. Phenol reforming

An aqueous phenol solution with a molar concentration of 0.56 M (1.0 mol%) was injected at the inlet of the reactor by means of calibrated micro-pump employing a total liquid flow of 10.4 μL·min^{-1} (corresponding gas flow in ***Table 3.2***) (*Scheme 3.1. Configuration A*). Then, the corresponding steam was supplied into the reactor, using the gaseous phase as a carrier. The steam-carbon molar ratio S/C_{tar}, calculated by considering only the moles of carbon in the tar molecule, was 16.5. The tar weight hourly space velocity was 14 h^{-1} and has been determined using the following equation:

$$WHSV_{tar,Ni^0}(h^{-1}) = \frac{Total\ tar\ mass\ flow\ \ (g \cdot h^{-1})}{Mass\ of\ Ni^0\ (g)} \qquad \textit{Equation 3.2}$$

The gaseous feed and products were analyzed online by gas chromatography. The liquid products were condensed by a trap cooled at 0 ºC (*Scheme 3.1. Configuration A*) and afterwards, weighed and analyzed offline *via* gas chromatography equipped with a flame ionization detector (FID) and using a non-polar CP-Sil-5CB Agilent column.

3.3.2.3. Toluene reforming

Toluene was fed into the reactor by passing a CO_2-N_2 flow of 73 NmL min^{-1} through a saturator at -20 ºC (*Scheme 3.1. Configuration B*). In this case, the reaction was carried out operating with a $WHSV_{tar,Ni}{}^0$ of 26 h^{-1}, and a S/C_{tar} ratio of 7.7.

The gaseous phase was analyzed online, as mentioned above, while the condensable products were recovered with two traps (*Scheme 3.1. Configuration B*). The first one was in a water-ice bath (0 ºC) and aimed to collect most of the outlet water as well as traces of tars. The second one was placed in an acetone-dry ice bath (-77 ºC) condensed the rest of water not trapped by the first one, as well as the non-converted toluene and other derivatives. As the miscibility of toluene with water is low, before the analysis, an amount of 60 ml of ethanol was added to the liquid phases collected in each trap in order to obtain a homogeneous solution. Afterwards, these liquid phases have been weighed and analyzed offline.

Reaction blanks were conducted for both model tar molecules in order to evaluate the efficiency of the cooled trap system. An efficiency closes to 100% was found for both model molecules. To sum-up, the main operating conditions of tar reforming are listed in

Table 3.3. for both model molecules. As expected, the use of a constant inlet tar content ratio (lab/pilot) (*see* ***Table 3.2.***) lead to differences in $WHSV_{tar,Ni}^{0}$.

	$WHSV_{gas}$ (h^{-1})	$WHSV_{tar,Ni}^{0}$ (h^{-1})	S/C_{tar}
Phenol	370	14	16.5
Toluene	370	26	7.7

Table 3.3. Summary of catalytic test conditions at laboratory scale for both model tar molecules

The catalytic performance can be described based on the average tar conversion (X_{tar}) and, for toluene reforming, average benzene selectivity ($S_{benzene}$). These average values are determined over the whole duration of the experiments (6 h) and calculated by *Equations 3.3 and 3.4* respectively. Moreover, as nickel-based catalysts are well known for their strong deactivation by coke deposition and in order to evaluate the resistance to coke formation, the selectivity to carbon deposits (S_{coke}) was estimated by TGA analysis of catalyst after test, using *Equation 3.5*. The variation of the outlet molar flow rate (F_i) of compound i (H_2, CO, CO_2 or CH_4) *versus* time on stream was also plotted for each configuration. They are calculated from the online gas analyses and are based on the inlet flow of N_2 as internal standard.

$$X_{tar} = \frac{n_{C\,tar,in} - n_{C\,tar,out}}{n_{C\,tar,in}} \qquad \textit{Equation 3.3}$$

$$S_{benzene} = \frac{n_{C,benzene,out}}{n_{C\,tar,in}\,.\,Xtar} \qquad \textit{Equation 3.4}$$

$$S_{coke}(\%) = \frac{mol\ deposited\ coke\ (TGA)}{n_{C\,tar,in}\,.\,Xtar} \qquad \textit{Equation 3.5}$$

Where "*n*" represents the mole of carbon in the tar molecule feed ('in') or collected in the trap during the experiments ('out').

A reproducibility study was carried out in order to determine if the configuration of the experimental set-up used for each molecule leads to accurate results. Therefore, three catalytic tests using same conditions (inlet tar content, gas composition, temperature and mass of catalyst) for each tar molecule were conducted for a given catalyst. An acceptable reproducibility has been found and the detailed results are presented and discussed in *Appendix* at the end of the chapter.

In the following sections, the catalytic results in reaction without tar model molecules along with phenol and toluene reforming are presented for the prepared

catalysts, prior reduced under H_2/N_2 atmosphere. Additionally, the main results of the catalytic reducibility under simulated syngas atmosphere also shown for all catalysts. Taking into account both, the catalytic performance and the ability to be reduced under syngas, three catalytic systems were selected to be further tested in real operating conditions at large scale. The impact of the syngas pretreatment on the physicochemical properties of these selected catalysts, as well as on their catalytic efficiency in tar reforming are detailed and discussed.

3.4. Catalytic test on powdered catalysts

3.4.1. Reduction pre-treatment under H_2/N_2 atmosphere

Before tar reforming reactions all the catalysts were treated under a reducing mixture of 40 mol%H_2/N_2 with a total gas flow of 77 NmL·min^{-1} at 600 ºC for 2 h using a heating ramp of 2 ºC·min^{-1}. These conditions have been chosen based on the H_2-TPR profiles of the synthesized catalysts (*Chapter 2, section 2.5.3.*).

3.4.1.1. Catalytic tests without tar model molecule

Figure 3.2. shows the change of the partial molar flow of each gas compound, compared to the inlet one (dotted lines), versus reaction temperature for the six Ni-based catalysts after reduction under hydrogen. The simultaneous consumption of CO and production of CO_2 and CH_4 highlights that water gas shift (*Reaction 3.5*) and CO methanation (*Reaction 3.6*) reactions are the main reactions that occur in parallel. As expected, for all catalysts, a low catalytic activity can be observed at reaction temperatures below 450 ºC and above 550 ºC, since both reactions are thermodynamically favoured and kinetically limited at low temperature [227]. Some differences in catalytic activity toward WGS/CO methanation reactions were found among the catalytic families (CZS, CY and LSCF). A rather lower catalytic activity in CO methanation was noticeable for LSCF-based materials compared to CZS-based and CY-based ones.

Several studies reported that the reactivity to WGS or CO methanation for a given catalysts depends on several factors such as metal loading, metal particle size, active phase dispersion, metal-support interaction and support composition [228–230]. For instance, the support reducibility has an important influence on WGS reaction. Reducible supports might easier provide oxygen/hydroxyl species to the metal phase than non-reducible ones [230,231]. It has been reported that the better catalytic performance for WGS than for CO methanation is correlated to the density of active hydroxyl species that can react in WGS reaction to form intermediates. For instance, Hwang *et al.* [227] showed

that potassium-modified Ni catalysts exhibited high catalytic activity to WGS than to CO methanation, associated to an enhancement of the density of active OH species by the presence of potassium. An enhancement of water adsorption by the presence of alkaline earth metals, such as Sr, into perovskite materials has been shown and associated to its basic character [211]. Thus, the presence of Sr in LSCF materials might increase the content of active OH species at the surface due to its basic character and, the WGS reaction could be highly favoured compared to CO methanation for these types of catalytic systems, in line with the literature.

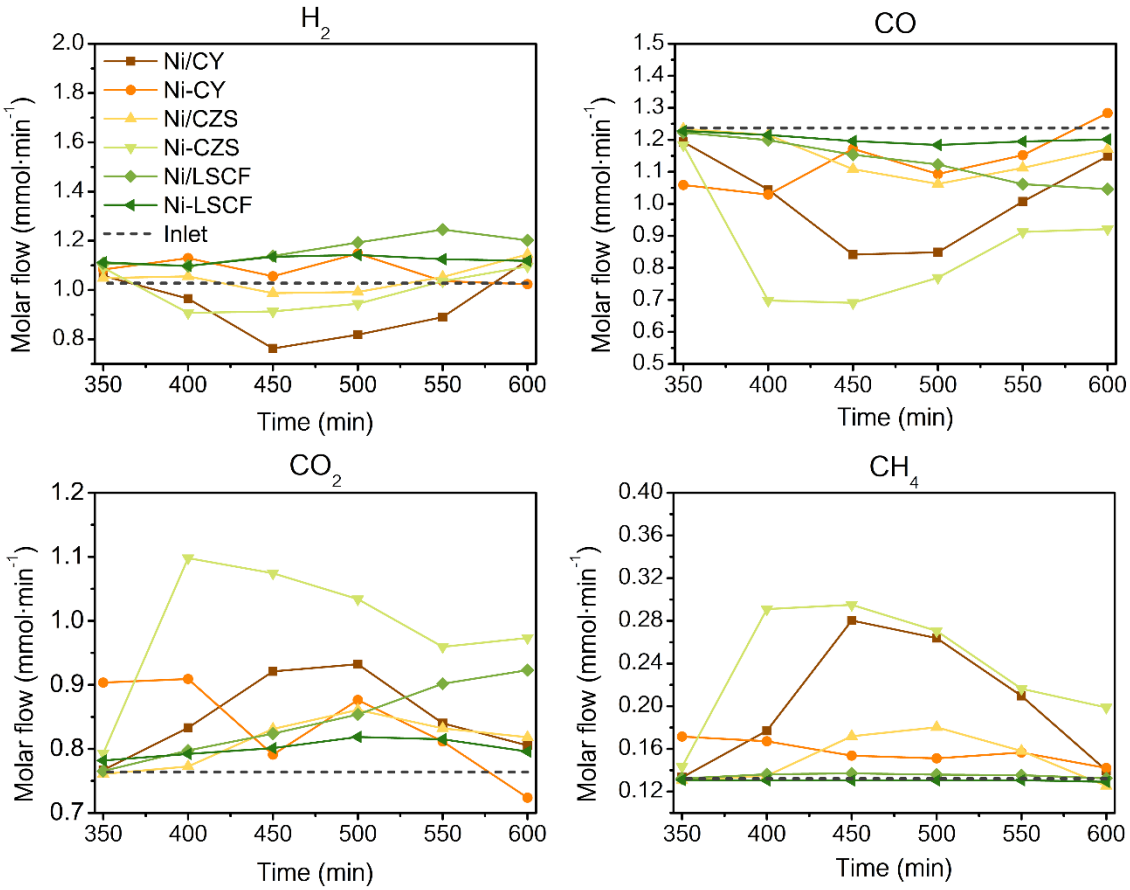

Figure 3.2. Partial molar flows at the outlet of the reactor vs temperature during catalytic test without tar model molecules in 350-600ºC temperature range over the Ni-based catalysts ($WHSV_{gas}$ = 370 h^{-1})

3.4.1.2. Phenol reforming.

The steam reforming of phenol is described by *Reaction 3.9*:

$$C_6H_5OH + 5H_2O \rightarrow 6CO + 8H_2 \qquad \textit{Reaction 3.9}$$

As it has been found in the prior section, other parallels equilibrium reactions such as WGS, CO_x methanation and/or carbon formation by phenol decomposition or Boudouard reactions can simultaneously occur.

The variations of partial molar flow of each gas component, compared to the inlet one (dotted line), versus time-on-stream are plotted in ***Figure 3.3 and 3.4*** for 400 and 550 ºC, respectively. Additionally, the average phenol conversion is listed in ***Table 3.4*** for the six Ni catalysts in phenol reforming at 400 and 550 ºC. As it is well known, nickel-based catalysts undergo strong deactivation by coke deposition. Thus, in order to evaluate the deactivation by carbon deposition, the selectivity to carbon has been estimated by TGA analysis (see *Equation 3.*5) and reported along with the average phenol conversion in ***Table 3.4.*** The TGA curves are presented in the characterization of the spent catalysts (***Figure 3.12***), where the nature and morphology of these carbon deposits are discussed in deep. Generally, a similar trend of the partial flows can be seen for the different catalysts. At first, CO flow decreases while an increase in H_2, CO_2 and CH_4 flows are detected (***Figure 3.3 and 3.4***). The consumption of CO is associated to WGS reaction, producing CO_2 and H_2 (*Reaction 3.5*). As prior discussed, Ni-based catalyst have been reported as active catalysts for CO_x methanation within the literature [105,146,232]. Therefore, the CO and CO_2 can simultaneously react with H_2 through CO_x methanation (*Reaction 3.6*), producing in the overall pathway H_2, CO_2 and CH_4, as it can be appreciated in the outlet partial flows. It should be underlined that the difficulty in the integration of the peak and the low response factor associated to H_2 in the GC analysis lead to an inaccurate measurement of the modifications of this gas flow. Due to the endothermal nature of reforming reaction and limited kinetic at low reactions temperatures, an enhancement in the catalytic efficiency with an increase of reaction temperature has been expected. Thereby, higher phenol conversions (***Table 3.4***) along with strong decreases of CO and increases of CO_2 and CH_4 partial molar flows at 550 ºC (***Figure 3.4***) compared to 400 ºC (***Figure 3.3***) have been evidenced for the six catalysts. Moreover, the selectivity to carbon is notably higher at low reaction temperature, might be due to the coke formation are thermodynamically limited at higher temperatures and/or reactions such as reforming or carbon gasification are more favoured at 550 ºC than at 400 ºC. Generally, similar tendency in the catalytic behavior has been followed into each catalytic family (CZS, CY and LSCF) at both reaction temperatures.

Regarding CZS-based materials, different performances are evidenced through the gas phase variation at the outlet of the reactor for reaction temperature of 400 ºC.

Whereas slight changes of the molar flows compared to the inlet ones were detected for the sol-gel catalyst in phenol reforming at 400 ºC, accounting for a slight catalytic activity, no modification of the flows, thus no catalytic activity, was observed for the impregnated one (*Figure 3.3 insets*). However, at 550 °C, both catalysts exhibit comparable initial outlet flows, far from the inlet ones (*Figure 3.4*). Whereas the outlet partial flows lean to the inlet ones after 120 min of test for Ni/CZS catalyst, stable behavior is obtained for Ni-CZS catalyst. This conduct is in concordance with the higher carbon selectivity found at 550 ºC for the Ni/CZS catalyst (24%) compared to Ni-CZS one (6%). Thus, the Ni/CZS catalyst undergoes to a strong deactivation process that might mainly be associated to its low resistance to coke formation. Similar average phenol conversion is attained at 400ºC for both, Ni/CZS (44%) and Ni-CZS (40%) catalysts, whereas a lower average phenol conversion is displayed at 550 ºC for Ni/CZS (64%) compared to Ni-CZS (85%) (*Table 3.4*). Even though both catalysts display similar average conversion at low temperature (400 ºC), the negligible catalytic activity found in the gas phase for Ni/CZS evidenced its lower catalytic activity compared to Ni-CZS catalyst. This catalytic activity increases at high temperature (550 ºC) for Ni/CZS with an increase in average phenol conversion, however, displays lower catalytic activity and stability when compared with Ni-CZS catalyst. Thereby, Ni-CZS catalyst lead to the best performance in term of stability and average phenol conversion within CZS-based catalysts.

Regarding CY-based materials, the tendency of the gas phase at low temperature is similar for both catalysts (*Figure 3.3*). A decrease in partial molar flow of CO along with an increase of H_2 and CO_2 evidenced the catalytic activity toward WGS for both catalysts. The additional CH_4 production observed for Ni/CY catalyst highlights, as well, the activity toward CO methanation displayed for this material. The stability seems to be comparable in both materials at low temperature. At high temperature, catalytic activity toward CO methanation and WGS reaction is found for both materials, exhibiting Ni/CY catalyst higher catalytic activity than Ni-CY (*Figure 3.4*). In term of stability, whereas a stable gas phase composition is perceived for Ni-CY catalyst over whole interval of time, the trend of the outlet gas flows to reach the inlet values after 130 min of test for Ni/CY reveals the strong deactivation suffered by this catalyst. Ni/CY shows higher average phenol conversion values than Ni-CY at both reaction temperatures (*Table 3.4*), following the same tendency as already seen in gas phase. At low temperature, average value of 69% with a carbon selectivity of 9% is displayed for Ni/CY catalysts, while lower average conversion (48%) and carbon selectivity (3%) is shown for Ni-CY catalyst. An increase in reaction temperature leads to an increase the average phenol conversion for Ni/CY catalysts,

reaching 89%, while the average conversion does not increase much for Ni/CY catalysts (59%). A slightly lower carbon selectivity is exhibited at high temperature for Ni/CY (5%) than for Ni-CY (10%). Accordingly, the sol-gel catalyst Ni-CY shows better catalytic stability than Ni/CY whereas a higher catalytic activity is exhibited for the latter catalyst. As previously observed for CZS-based materials, the addition of Ni through one step sol-gel synthesis provides a high catalytic stability. However, there is an opposite behavior in terms of catalytic activity for CY- compared to CZS-based materials, impregnated catalysts (Ni/CY) being more active than the sol-gel one (Ni-CY). Concerning LSCF-based materials, the catalytic activity was comparable for both catalysts, Ni/LSCF and Ni-LSCF, at 400 and 550 ºC. The modification of the gas phase composition with time is similar for both materials, at 400 and 550 ºC. At low temperature, catalytic activity toward WGS and CO methanation can be discerned for Ni-LSCF catalyst, whereas the no production of CH_4 detected for Ni/LSCF catalysts reveals its low activity toward CO_x methanation (***Figure 3.3***). At high temperature, catalytic activity toward WGS reaction is prevailing for both Ni-containing catalysts (***Figure 3.4***). Generally, stable partial molar flows along the reaction time is found for both reaction temperatures. The effect of Ru addition over Ni/LSCF has been also evaluated in phenol reforming at 550 ºC. Similar outlet partial molar flows are obtained for RuNi/LSCF and Ni/LSCF catalysts. Thus, from the gas phase, no noticeable enhancement in apparent catalytic activity can be evidenced for the addition of Ru. The average phenol conversion values achieved at both reaction temperatures for the three catalytic systems are also comparable. At low temperature, average phenol conversion of 36% and 32% are displayed for Ni/LSCF and Ni-LSCF catalysts, respectively. An increase in catalytic activity is evidenced at high temperature, achieving similar toluene conversion of 85% for Ni/LSCF and 90% for Ni-LSCF catalysts. A low resistance to coke formation was found for Ni/LSCF which displays carbon selectivities of 20 and 15% at 400 and 550 ºC, respectively. It should be pointed out that the composition of the gas phase kept stable along the all reaction time at both reaction temperatures for this catalyst, despite the high carbon selectivity attained, accounting for an apparent stable catalytic activity. Much lower values in terms of carbon selectivities are found for Ni-LSCF, 6% at 400 ºC and 9% at 550 ºC. According to the gas phase modifications, the addition of Ru does not enhance the catalytic activity in terms of average phenol conversion and resistance to coke formation. The average phenol conversion attained for RuNi/LSCF at 550 °C is 76%, close to the unpromoted Ni/LSCF catalyst (85%), and the carbon selectivity showed is similar (16%). The comparable catalytic activity and stability found among the LSCF-based materials,

suggests that the catalytic efficiency in phenol reforming might not be directly connected or affected by the Ni addition pathway within the LSCF-based materials.

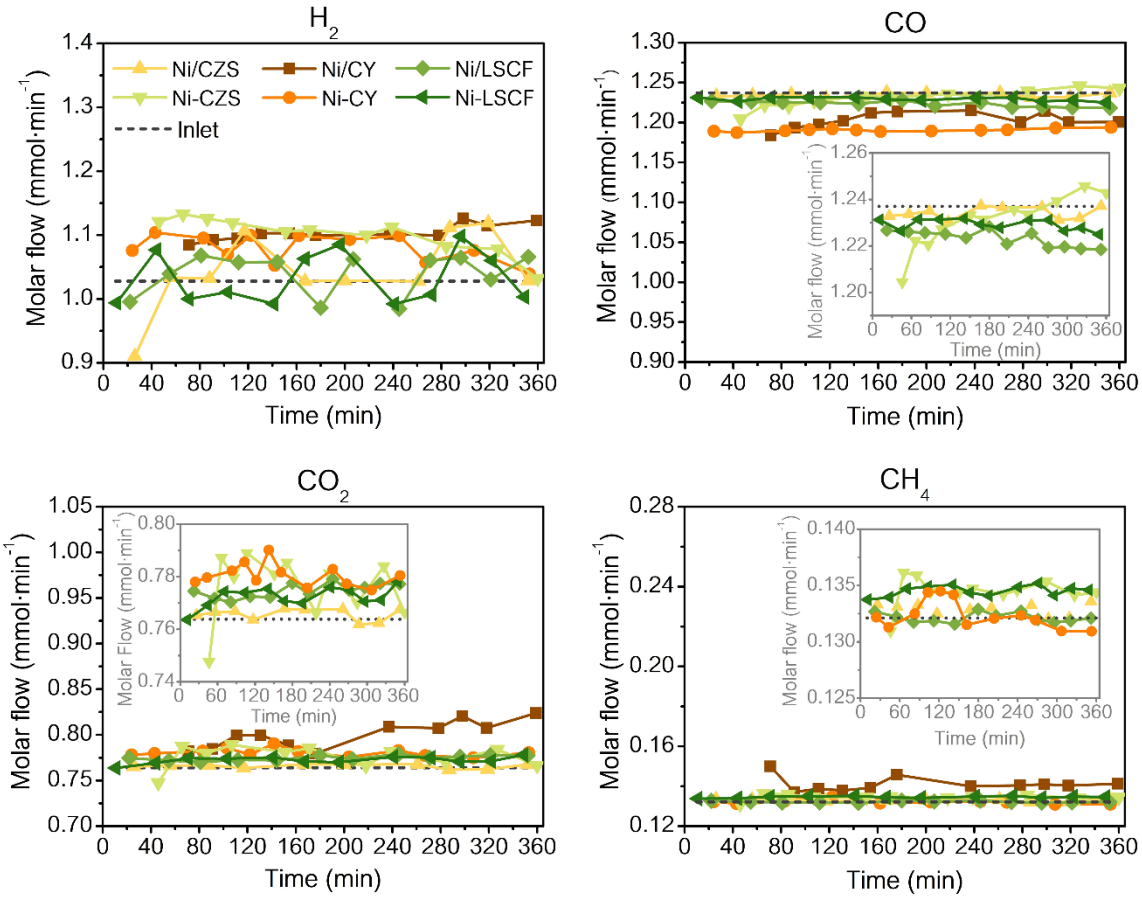

Figure 3.3. Partial molar flows at the outlet of the reactor vs time on stream during steam reforming of phenol at 400 ºC over the Ni-based catalysts ($WHSV_{gas}$ = 370 h^{-1}; $WHSV_{tar,Ni}^{0}$ = 14 h^{-1} and S/C_{tar} =16.5)

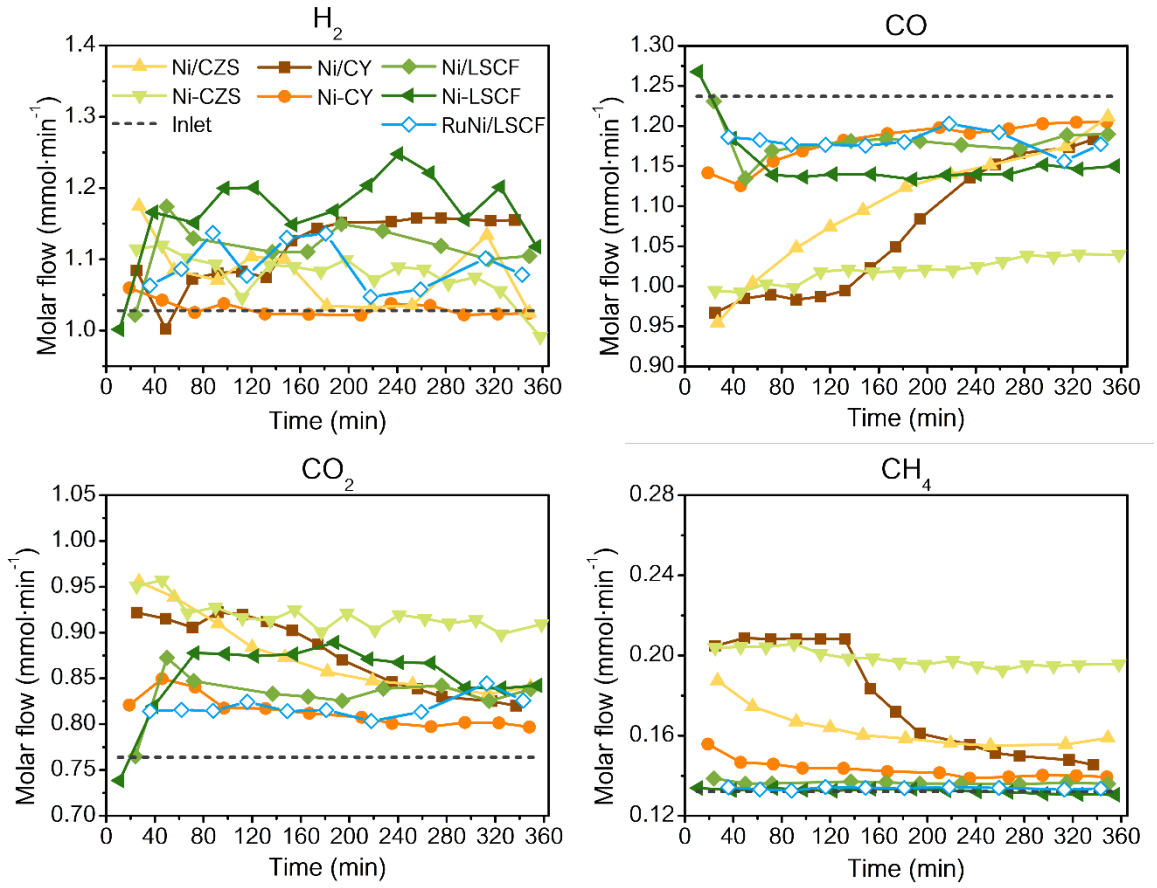

Figure 3.4. Partial molar flows at the outlet of the reactor vs time on stream during steam reforming of phenol at 550 ºC over the Ni-based catalysts ($WHSV_{gas}$ = 370 h^{-1}; $WHSV_{tar,Ni}^{0}$ = 14 h^{-1} and S/C_{tar} =16.5)

Temperature (°C)	400		550	
	X_{phenol} (%)	S_{coke} (%)	X_{phenol} (%)	S_{coke} (%)
Ni/CZS	44	2	64	24
Ni-CZS	40	15	85	6
Ni/CY	69	9	89	5
Ni-CY	48	3	59	10
Ni/LSCF	36	20	85	15
Ni-LSCF	32	6	90	9
RuNi/LSCF	-	-	76	16

Table 3.4. Average phenol conversion and selectivity to carbon for the six Ni-based catalysts in phenol reforming at reaction temperatures of 400 and 550 ºC.

In order to determine a tendency in the catalytic activity in phenol reforming among the six Ni-based catalysts, the catalytic activity at high temperature, the catalytic activity at low temperature as well as the stability observed in the gas phase were taken into account as first, second and third criteria, respectively. Therefore, considering the catalytic

activity at high temperature, two groups of catalysts can be distinguished, one with average phenol conversion around 90% (Ni-CZS, Ni/CY, Ni/LSCF and Ni-LSCF) and another around 60% (Ni/CZS and Ni-CY). The catalytic activity displayed at low temperature clearly evidenced that Ni/CY led to the best catalytic activity among the catalysts, whereas not deep differences can be discerned for the rest. Lastly, taking into account the stability of the gas phase composition, Ni-CZS and Ni-CY show the highest catalytic stability among the first and second group of catalysts, respectively. Thus, the catalytic activity of the six investigated catalysts can be classified as follows: Ni/CY > Ni-CZS > Ni-LSCF ~ Ni/LSCF > Ni-CY > Ni/CZS.

3.4.1.3. Toluene reforming.

In the present work, toluene reforming over the synthesized catalysts was performed at 550 ºC, as better catalytic performance and resistance to coke formation have been previosly found for phenol reforming at this reaction temperature. The steam reforming of toluene could proceed as follow:

$$C_7H_8 + 7H_2O \rightarrow 7CO + 11H_2 \qquad \textit{Reaction 3.10}$$

Besides toluene reforming, hydrogenation of toluene can simultaneously take place (*Reaction 3.11*) along with other parallels equilibrium reactions like WGS, CO_x methanation and/or carbon formation through thermal decomposition of toluene or Boudouard reactions. Therefore, the modifications observed in the partial molar flows should not been only linked to the catalytic activity in toluene reforming, since catalytic activity or deactivation process could be also related to these parallel reactions.

$$C_7H_8 + H_2 \rightarrow C_6H_6 + CH_4 \qquad \textit{Reaction 3.11}$$

The partial molar flow of each gas component in function of time on stream during toluene reforming has been plotted in ***Figure 3.5***. In addition, the average toluene conversion, selectivity to benzene and carbon can be also found in ***Table 3.5***. Generally, same tendencies than the ones observed for phenol reforming were detected in the outlet gas flows, where CO consumption leads to H_2, CO_2 and CH_4 production via CO_x methanation and WGS processes.

Concerning CZS systems, similar catalytic behavior than in phenol reforming is perceived. Whereas Ni/CZS catalyst partial flows of all gaseous components quickly tend to the inlet molar flows due to catalytic deactivation, stable partial flows and far from the inlet flows were obtained for Ni-CZS one (***Figure 3.5***). The impregnated catalyst Ni/CZS

displays lower activity in term of average toluene conversion (39%) and higher selectivity to coke formation (20%) with respect to its equivalent sol-gel Ni-CZS ($X_{toluene}$ of 52% and S_{coke} of 9%) (***Table 3.5***). A negligible benzene selectivity as by-product is obtained for Ni-CZS (< 2%) in comparison with the impregnated Ni/CZS (7%) catalyst. Within the CZS-based systems, once again, better activity with higher stability in tar abatement is exhibited for Ni-CZS than for Ni/CZS.

Regarding the CY materials, the variation in the partial molar flows of the gaseous component highlights higher catalytic activity and lower stability for Ni/CY catalyst than for Ni-CY catalyst (***Figure 3.5***). The tendency of outlet partial flows to rapidly go back to the inlet ones for Ni/CY catalyst points out the strong deactivation underwent by this material. On the contrary, more stable partial molar flows are shown for the sol-gel Ni-CY catalyst. An average toluene conversion of 47% was calculated for the sol-gel Ni-CY catalyst, with a high selectivity to carbon deposit (31%), while the impregnated Ni/CY material displayed a complete toluene conversion (100%) and good resistance to coke formation (S_{coke} of 7%). Besides, low benzene selectivity was found for both catalysts (2-3%). It should be stressed that a higher tar removal efficiency is found for Ni/CY catalysts in toluene reforming compared to phenol reforming, in spite of a lower S/C_{tar} ratio in toluene reforming (7.7 compared to 16.5) (see ***Table 3.3***).

Concerning LSCF-based materials, the partial molar flows variation indicates a higher catalytic activity toward WGS reaction for Ni-LSCF compared to Ni/LSCF (***Figure 4.5***). Both catalysts exhibit stable partial flows along the whole interval of time. As already observed in phenol reforming, the addition of Ru on Ni/LSCF result in comparable catalytic activity and stability, as concern to the gas phase variation. Slightly higher average toluene conversion (65%) and resistance to coke formation (S_{coke} of 7%) is displayed for Ni-LSCF than for Ni/LSCF catalysts ($X_{toluene}$ of 54% and S_{coke} of 16%). A low selectivity to benzene is attained for both catalysts (2% for Ni-LSCF and 4 % for Ni/LSCF). Additionally, the presence of Ru in Ni/LSCF results in an enhancement in terms of toluene conversion and a decrease in the selectivity to coke. Therefore, the toluene conversion becomes 82% for RuNi/LSCF (54% for Ni/LSCF) and the selectivity to carbon decrease from 16% to to 8% with the addition of ruthenium.

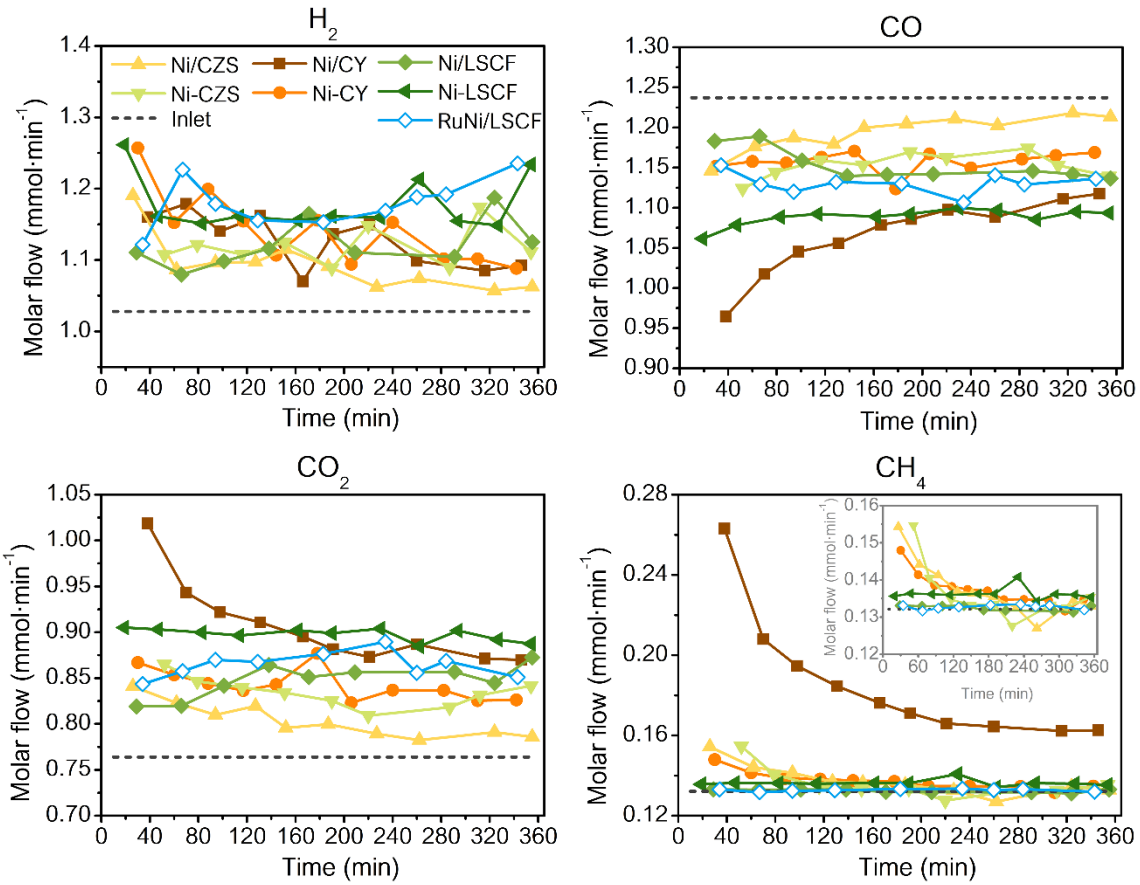

Figure 3.5. Partial molar flows at the outlet of the reactor vs time on stream during steam reforming of toluene at 550 ºC over the Ni-based catalysts ($WHSV_{gas}$ = 370 h^{-1}; $WHSV_{tar}$ = 26 h^{-1} and S/C_{tar} =7.7)

	$X_{toluene}$ (%)	$S_{benzene}$ (%)	S_{coke} (%)
Ni/CZS	39	7	20
Ni-CZS	52	2	9
Ni/CY	100	< 2	7
Ni-CY	47	3	31
Ni/LSCF	54	4	16
Ni-LSCF	65	2	7
RuNi/LSCF	82	< 2	8

Table 3.5. Average toluene conversion, selectivity to benzene and carbon for the six Ni-based catalysts under toluene reforming at 550 ºC.

As it could be expected, a lower tar conversion was found for most of the prepared catalysts during toluene reforming compared to phenol, since the reaction conditions were harder (lower S/C_{tar} ratio) for toluene reforming (see ***Table 3.3***). Despite the hard reaction conditions, a higher tar conversion has been evidenced for Ni/CY and RuNi/LSCF in toluene (100% for Ni/CY and 82% for RuNi/LSCF) compared to phenol reforming (89% for

Ni/CY and 76% for RuNi/LSCF). As it has been reported in literature, the decomposition of phenol over Ni-based catalysts is harder than other tar model compounds, leading to a decrease in term of catalytic activity in some cases [70,222,223]. Consequently, the lower tar efficiency in phenol reforming compared to toluene one found for Ni/CY catalyst could be due to possible differences in reaction mechanism pathway between both model molecules. The different effect of Ru addition observed between the two model molecules suggests that the improvement in terms of tar conversion by the presence of this noble metal becomes more noticeable at low S/C_{tar} ratio. Additionally, similar carbon selectivities have been measured for both model molecules, regardless the S/C_{tar} used. This fact might be connected to the lower thermal stability of oxygenates compounds compared to hydrocarbons reported in literature [62,233,234]. The low thermal stability enhances undesired processes as thermal decomposition and/or cracking over the support, leading to carbon deposition. In this line, the higher amount of deposited coke from oxygen containing reactants has been also reported in other papers. For example, Artetxe *et al.* [70] showed stronger carbon deposition over Ni/Al_2O_3 catalyst in the case of oxygenate molecules as phenol, furfural and anisole. Koike *et al.* [223] observed a larger amount of deposited coke from phenol reforming compared to toluene and benzene reforming. They proposed that this could be related to a blockage of the water activation due to the high coverage of phenol derivative species on Ni surface. As a consequence, phenol decomposition might be able to produce high amount of carbon deposits at the catalytic surface even in presence of high-water content.

Despite the differences in tar conversion between both tar model molecules due to the different reaction conditions used, a similar tendency in catalytic activity and stability is appreciated among the six investigated catalysts. Once again, among the six catalysts, Ni/CY leads to the best catalytic activity, whereas Ni/CZS shows the worst catalytic performance. Considering the average toluene conversion and the catalytic activity and stability evidenced in the gas phase, Ni-LSCF catalyst exhibits better activity than Ni-CZS, Ni-CY and Ni/LSCF catalysts. Since the stability and activity of the gas phase are close for the three latter catalysts, the selectivity to coke was considered in order to discriminate among them. Therefore, the catalytic activity in toluene reforming among the six catalysts decreases as follow: Ni/CY > Ni-LSCF > Ni-CZS > Ni/LSCF > Ni-CY > Ni/CZS.

Generally, Ni/CY, Ni-LSCF and Ni-CZS catalysts showed the best catalytic efficiency in catalytic tar reforming as well as the lowest carbon selectivities.

3.4.1.4. Discussion: characterization and catalytic test results

In this section, the results of catalytic activity displayed for the prepared catalysts will be correlated with the physicochemical properties shown and discussed in *Chapter 2*. Due to the differences in crystalline structure and elemental composition presented for the Ce- and La-based materials, the correlation between these main groups of catalysts will be conducted separately.

In the literature, the metal particle size of reforming catalysts has been considered a parameter with a significant role in the catalytic performance. For instance, Gai *et al.* [235] investigated the phenol decomposition over hydrochar-supported Fe and observed that the catalysts synthesized by one-pot hydrothermal carbonization method displayed smaller particle size and better catalytic performance than those prepared by impregnation method. Likewise, Wu *et al.* [236] studied the effect of Ni precursor in steam reforming of glycerol for Ni/Al_2O_3 catalysts and they found that the Ni/Al_2O_3 catalyst with small particle size provided the highest H_2 yield. Accordingly, the better catalytic activity found for Ni-CZS (1.9 $m^2 \cdot g^{-1}$) and Ni/CY (2.2 $m^2 \cdot g^{-1}$) compared to their equivalent catalysts, Ni/CZS (0.9 $m^2 \cdot g^{-1}$) and Ni-CY (1.0 $m^2 \cdot g^{-1}$) can be correlated to the higher metallic Ni surface displayed for the formers. In terms of catalytic stability, general improvement of the catalytic stability has been clearly detected for the catalysts prepared through one step sol-gel (Ni-CZS and Ni-CY) compared to their equivalent impregnated ones (Ni/CZS and Ni/CY). The enhancement in catalytic stability might be associated to the incorporation of Ni^{2+} into the mixed oxide structured promoted by one step sol-gel synthesis as being identified by XRD and H_2-TPR analysis in *Chapter 2.* Similarly, Ocampo *et al.* [146] observed that the presence of partial Ni^{2+} species into CZ mixed oxide induced by sol-gel method provided higher catalytic stability than the catalyst obtained through wetness impregnation. Therefore, the Ni insertion in the sol-gel catalysts, may favor the oxygen vacancies formation and promote the carbon gasification process, improving consequently the catalytic activity. This is supported by DFT studies about Ni-Ce systems, which emphasize the improvement of oxygen vacancies formation by mean of Ni^{2+} insertion into the CeO_2 structure [237–239]. In their study, Ye *et al*. [237] proposed the substitutional and interstitial Ni insertion in CeO_2 structure as the two possibilities (*Reactions 3.12 and 3.13*) and estimated the required energy for both. They concluded that the former Ni insertion, associated to the oxygen vacancies formation, is energetically favored. The existence of oxygen vacancies might be important if the pathway of steam reforming process proposed in the literature is taken into consideration. In this general mechanism,

the C-H or C-C bond is cracked over the metal surface to generate carbon deposits (C*) and H_2. Later, these surface carbon species react with the hydroxyl groups produced from water dissociation (OH*), which is carried out on the support to generate CO [70,223]. In this sense, other studies have also evidenced the promotion of water activation caused by the simultaneous coexistence of oxygen vacancies and nickel ions positively charged [240,241].

$$NiO \rightarrow Ni_{Ce}^{"} + V_O^{\cdot\cdot} + O_O^x \qquad E = 5.00\ eV \qquad \textit{Reaction 3.12.}$$

$$2NiO \rightarrow Ni_{Ce}^{"} + Ni_i^{\cdot\cdot} + 2O_O^x \qquad E = 9.46\ eV \qquad \textit{Reaction 3.13}$$

, where $Ni_{Ce}^{"}$ is Ni^{2+} atom place at Ce^{4+} atom with two negative charges, $V_O^{\cdot\cdot}$ is oxygen vacancy double positively charged, $Ni_i^{\cdot\cdot}$ is interstitial Ni^{2+} cations double positively charge and O_O^x is an oxygen atom at oxygen site into the lattice (neutral)

Other researches have been stressed that coke deposition during steam reforming reactions is structural sensitive [242–244]. Thus, larger Ni particles with more terrace sites could lead to more severe coke formation and propagation, while small Ni particles could inhibit this coke formation by increasing the corner and step sites fraction. Accordingly, lower selectivity to carbon showed by sol-gel CZS catalyst, Ni-CZS, than its equivalent catalyst, Ni/CZS, can be associated to: (i) higher S_{Ni}^0 and (ii) the promotion of carbon gasification as consequence of the inserted Ni^{2+} into CZS oxide. Additionally, the higher support reducibility displayed for Ni-CZS (89%) with respect its equivalent Ni/CZS (49%) due to the presence of inserted Ni^{2+} species into CZS oxide could also elucidate these differences. A high content of Ce^{3+} species should provide more oxygenates species such as reactive -O and/or -OH species, at the surface through steam activation and dissociation. Afterwards, these oxygen species can react with the carbonaceous species produced at the surface by tar decomposition, enhancing the carbon gasification and consequently the catalytic activity and stability. This fact is supported by the stable partial flows and the lower carbon selectivity performed by Ni-CZS compared to Ni/CZS during tar reforming reactions, outstanding that the deactivation process by surface deposited coke is reduced. As expected, the sol-gel catalyst, Ni-CY, exhibits higher selectivity to carbon than the impregnated one Ni/CY. This behavior is well linked to the no favorable Ni^{2+} insertion into CY mixed oxide structure as well as the larger NiO particle size and lower S_{Ni}^0 found for Ni-CY material compared to its equivalent Ni/CY. Among the Ce-based catalysts (CZS and CY), the impregnated Ni/CY shows the highest metallic Ni surfaces,

resulting in the best catalytic activity, whereas the sol-gel Ni-CZS catalyst presents the best catalytic stability due to the inserted Ni^{2+} species.

Within LSCF-based catalysts, Ni/LSCF displayed higher metallic surface (Ni°+Co°), 1.5 $m^2 \cdot g^{-1}$, than Ni-LSCF, 0.5 $m^2 \cdot g^{-1}$. However, similar catalytic performances in term of stability and average tar conversion were obtained for both catalysts, being the prone to carbon formation the main difference found between these two catalysts. As it can be seen from the selectivity to carbon, Ni/LSCF is more susceptible to carbon formation compared to Ni-LSCF catalysts. The similar catalytic behavior can be associated to the fact that the active phase, Ni, forms part of a perovskite structure in both catalysts, as evidenced the XRD and XPS studies shown in *Chapter 2.* The slightly better catalytic efficiency found for Ni-LSCF material in toluene reforming compared to Ni/LSCF could be connected to the Ni-Co and Ni-Fe alloy formation observed at the surface of this material by XPS (*Chapter 2, section 2.5.4*). The addition of a second transition metal, such as Co or Fe, to Ni-based catalysts has been highlighted as an option in order to improve their catalytic efficiency and resistance to coke deposition [189]. For instance, a significant improvement in coke resistance during dry reforming of methane over Co-Ni/TiO_2 catalysts due to the formation of Ni-Co alloy at the catalyst surfaces has been evidenced by Aiwa *et al.* [245]. Besides, the effect of Fe-Ni alloy formation has been also studied. Perovskite catalysts containing both Ni-Fe has been intensively investigated. Oemar *et al.* [185] studied the effect of Fe addition to $LaNiO_3$ perovskite in steam reforming of toluene and higher stability and activity was observed for Fe-added catalyst due to its stronger resistance to coke formation and metal sintering process displayed by Ni-Fe bimetallic particles. Yan *et al.* [61] found that the addition of Fe to Ni supported over activated carbon (Ni/AC) prevents the aggregation of nickel particles and reduces the amount of carbon deposit during steam reforming of toluene at 600 ºC compared to bare Ni/AC. Therefore, the formation of Ni-Co and Ni-Fe alloy at the surface of the catalysts induced by sol-gel method might cause an enhancement in term of catalytic efficiency for Ni-LSCF compared to Ni/LSCF. In addition, it could explain the low selectivity to carbon shown for the sol-gel Ni-LSCF catalysts. Likewise, several studies have been pointed out the positive effect of Sr in reforming reactions due to its basicity. Catalyst surface basicity is known to inhibit coke formation in dry reforming of methane [246] and steam reforming of n-heptane [247]. Zhuang *et al*. [247] observed that the addition of basic metal oxide over CeO_2 enhanced the water adsorption and carbon gasification on the catalyst surface in steam reforming of n-heptane. Sekine *et al.* [135] compared impregnated Ni/Sr/$LaAlO_3$ catalysts and Ni/$La_{0.7}Sr_{0.3}AlO_{3-\delta}$ in steam reforming of toluene. A lower amount of carbon deposition for

$Ni/La_{0.7}Sr_{0.3}AlO_{3-\delta}$ was found. This better resistance to coke formation was associated to an enhancement of the lattice oxygen mobility at the surface by substituting La with Sr into the perovskite structure. The role of lattice oxygen species has been also remarked to be crucial in steam reforming reactions. Indeed, Oemar *et al*. [127] carried out kinetic and mechanistic studies of steam reforming of toluene over $La_{0.8}Sr_{0.2}Ni_{0.8}Fe_{0.2}O_{3-\delta}$ perovskite materials. They pointed out the important role of adsorbed oxygen species, lattice oxygen species and/or redox properties of some metals such as Ce or Fe to react with CH_x species generated at the surface by tar decomposition. According to literature, the high resistance to coke deposition displayed by Ni-LSCF compared to Ni/LSCF might be linked to: (i) the higher Sr content at the surface evidenced by XPS for NI-LSCF, that can promote water adsorption and, thus, carbon gasification and/or (ii) lattice oxygen species with higher mobility found for Ni-LSCF catalysts by means of the shift to lower BE of O 1s spectra (presented in *Chapter 2, Section 2.5.4*). This higher Sr content at the surface could also explain the higher catalytic activity as toward WGS reaction exhibited by Ni-LSCF compared to Ni/LSCF catalyst (see ***Figure 3.4-3.5***). Besides that, it has been reported that iron can form stables carbide species at the surface during tar reforming [223,248]. Consequently, the larger Fe content detected at the surface for Ni/LSCF than for Ni-LSCF could lead to the formation of high amount of stable carbides at the surface. This fact along with the low Sr content at the surface observed for Ni/LSCF catalysts could clarify its prone to coke formation. Eventually, as similar textural and structural properties have been observed for Ni/LSCF and RuNi/LSCF catalysts, the increase in average toluene reforming and the decrease in carbon selectivity evidenced for RuNi/LSCF can be mainly associated to the presence of Ru. At high S/C_{tar} ratio the improvement by addition of Ru was not noticeable. In fact, a decrease in catalytic activity in terms of phenol conversion and resistance to carbon deposits was shown for RuNi/LSCF related to Ni/LSCF catalyst.

As a summary, an enhancement in the catalytic performances and in resistance to coke formation are attained by the Ni addition through sol-gel compared to the impregnation method within the CZS- and LSCF-based materials. Thus, a better catalytic activity and stability as well as a higher resistance to coke formation was attained for Ni-CZS catalyst compared to Ni/CZS. This improvement has been mainly related to the high Ni surface and the presence of Ni^{2+} inserted into CZS structure. Generally, similar catalytic activity and stability has been shown for Ni/LSCF and Ni-LSCF, but the sol-gel catalyst resulted in a high resistance to coke formation, linked to the formation of Co-Ni and Fe-Ni alloys promoted by sol-gel method and its high Sr content at the surface. At contrary, the addition through wetness impregnation (Ni/CY) led to the better catalytic activity with

higher resistance to coke formation into CY-based materials associated to the high metallic Ni surface. While the insertion of Ni^{2+} species into CY through sol-gel method (Ni-CY) led to a better the catalytic stability under steam reforming of tars. Therefore, influence of the Ni addition pathway on the catalytic activity and stability has been discerned for both reactions, phenol and toluene reforming.

Concerning the effect of the catalytic support on the catalytic activity, among the impregnated catalysts the catalytic activity can be correlated to the metallic surface. The catalytic activity as well as the metallic surface decrease as follow: Ni/CY (2.2 $m^2 \cdot g^{-1}$) > Ni/LSCF (1.5 $m^2 \cdot g^{-1}$) > Ni/CZS (0.9 $m^2 \cdot g^{-1}$). Therefore, through impregnation method, CY mixed oxides favored the Ni dispersion compared to LSCF and CZS, leading to the best catalytic activity. The highest catalytic stability among the impregnated catalysts was obtained for Ni/LSCF in both tar reforming reactions (see ***Figure 3.4*** for phenol and ***Figure 3.5*** for toluene). This could be related to the presence of Ni as part of $LaNiO_3$ structure. The formation of this perovskite structure could inhibit the Ni sintering, since the strong Ni-La_2O_3 interaction can delay the NiO reduction. No correlation between the catalytic activity and the metallic surface is attained among the sol-gel catalysts. Among them, the catalytic activity decreases as follow: Ni-LSCF (0.5 $m^2 \cdot g^{-1}$) = Ni-CZS (1.9 $m^2 \cdot g^{-1}$) > Ni-CY (1.0 $m^2 \cdot g^{-1}$). In this case, the better catalytic performance showed by Ni-LSCF and Ni-CZS compared to Ni-CY might be related to the limited Ni insertion of Ni observed for CY mixed oxide, thus the "absence" of a Ni^0/Ni^{2+} mixture into the catalytic system can explain the low catalytic activity displayed compared to the other supports (LSCF and CZS). The different tendencies observed into the impregnated and sol-gel catalysts highlights, once again, the influence of the Ni addition method on the catalytic activity.

3.4.2. Reduction pre-treatment under syngas atmosphere

Taking into account that the aim of this work is the final application of the best catalysts in a gasification pilot plant (pre-industrial scale), the *in situ* reduction under real syngas composition of the catalysts is crucial. Thereby, the influence of a pre-treatment under syngas on the catalysts reducibility and coke formation has been investigated for the six Ni-based catalysts of this study.

Accordingly, the catalysts were pre-treated under the selected gas composition of ex-biomass syngas (***Table 3.2***) without tars, at 500 ºC for 1 h using a heating ramp of 5 ºC·min^{-1} with a total gas flow of 139 NmL·min^{-1}. In order to avoid condensation, the distilled water was introduced from 100 ºC of temperature using a liquid flow of 10.4

$\mu L \cdot min^{-1}$ (gas flow reported in ***Table 3.2***). The gaseous feed and products were followed by online by gas chromatography, in order to follow modifications of the gas phase due to catalytic performance by the possible presence of Ni^0 species generated.

3.4.2.1. Influence of pre-treatment on NiO reducibility and carbon deposition

The variation of the partial molar flow of each gas component compared to the inlet one *versus* time on stream is plotted in ***Figure 3.6*** for the six catalysts. A noticeable modification of the outlet partial molar flows is detected from reaction temperatures above 360 ºC for the six catalysts. The catalytic activity displayed can be associated to the *in situ* formation of the active phase (Ni^0) by reduction of NiO species under these conditions. As expected, water gas shift and CO methanation reactions occurs simultaneously. The significant CH_4 production and the low H_2 production suggest that the catalytic activity to CO methanation prevailed for all the catalysts under these conditions. This fact is remarkable for Ni/LSCF material, since its catalytic activity toward CO methanation has been almost negligible in catalytic test without tar under H_2/N_2 reduction pre-treatment (*section 3.4.1.1.*, ***Figure 3.2***). Moreover, a tendency similar to what was found previously in tar reforming can be deduced considering the variation on the gas phase flows. The catalytic activity of WGS and CO methanation reactions follows the order: Ni/CY > Ni/LSCF > Ni-CZS ~ Ni-CY > Ni/CZS > Ni-LSCF.

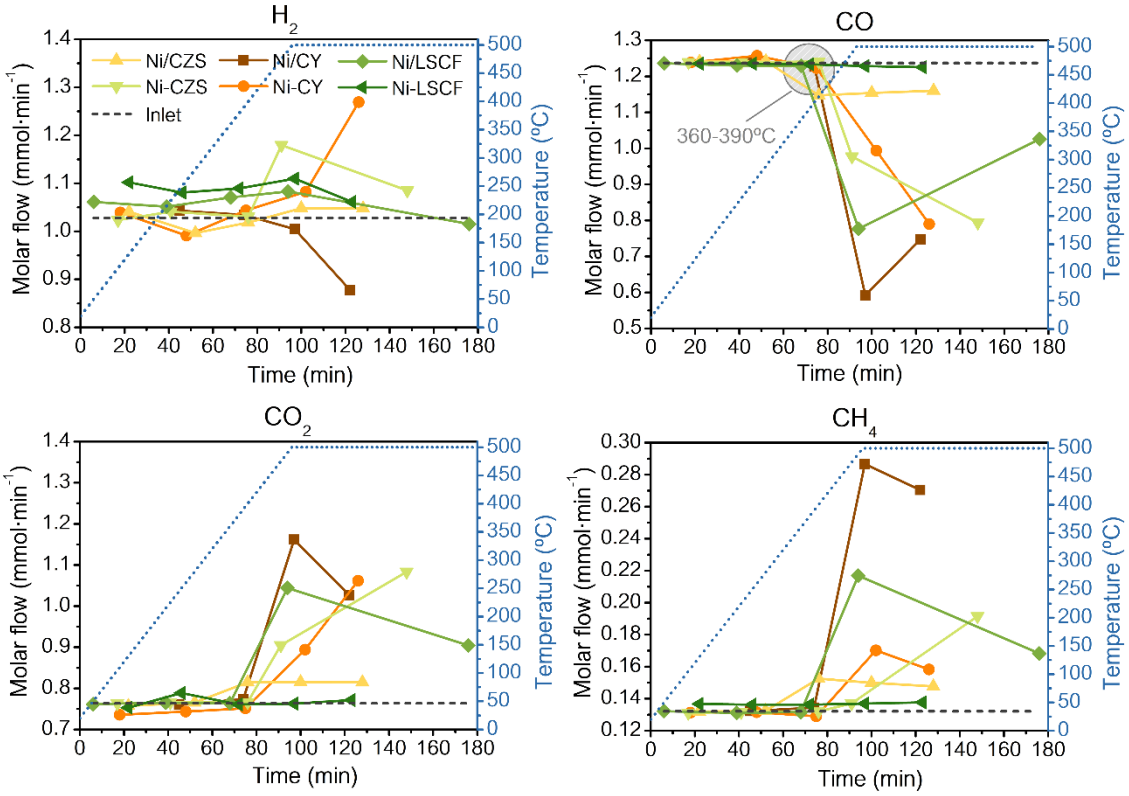

Figure 3.6. Partial molar flows at the outlet of the reactor vs time on stream during reduction pre-treatment under syngas atmosphere over the six Ni-based catalysts

H_2-TPR analysis have been performed on the catalysts pre-treated in syngas, in order to determine if complete NiO reduction was achieved through these pre-treatment conditions. The H_2-TPR profiles of the pre-treated samples are displayed ***Figure 3.7***. A main peak located at temperatures around 600 ºC is evidenced for all the materials except for Ni-LSCF (***Figure 3.7 (a)***) and it is associated to the CH_4 formation by reaction of H_2 and deposited carbon at the surface ($C + 2H_2 \rightarrow CH_4$). This deposited carbon is generated by the catalytic activity, mainly toward CO_x methanation, displayed by metallic Ni^0 and it is another proof of the formation of Ni^0 under these conditions. Besides that, less intense peaks can be also detected in the temperature range between 100-500 ºC (***Figure 3.7 (a), inset***). These peaks might be linked to the reduction of NiO to Ni^0 process indicating no complete reduction of NiO species to Ni^0 under syngas atmosphere. The contrast in the reduction temperature of these NiO species among the catalysts highlights the existence of different Ni-support interactions as it has been discussed in *Chapter 2* (*section 2.5.3*). The persistence of NiO was also observed by Kim *et al.* [249] during reduction pretreatment performed under syngas mixture at 500 ºC for 1 h. Moreover, they investigated the effect of pretreatment condition in the catalytic activity of CO removal by WGS and CO methanation reactions. They found that C-O bond was weakened by NiO

species, and the surface carbonaceous intermediate provided by NiO was easily hydrogenated to generate methane. Thereby, NiO behaved as a promoter and favored the CO methanation. Accordingly, the presence of NiO could explained the higher catalytic activity toward CO methanation compared to WGS found under this pretreatment conditions for the catalysts studied. Concerning Ni-LSCF catalyst, the weak modification in the gas phase flows along the reduction pretreatment (***Figure 3.6***) is in good agreement with the absence of the peak associated to the CH_4 formation in its corresponding H_2-TPR profile (***Figure 3.7 (a)***). Thus, the absence of catalytic activity underlines that the reduction of NiO to Ni^0 under these conditions for this material becomes harder, probably owing to the strong Ni-support interaction induced by the Ni-Co and Ni-Fe alloy formation detected at the surface for Ni-LSCF (*Chapter 2, section 2.5.4*). Additionally, the pre-treated Ni-LSCF catalyst displayed similar H_2-TPR profile and H_2 consumption (7.1 mmol/g catalyst) than the fresh one (7.5 mmol/g catalyst) ***(Figure 3.7 (b)***), evidencing that the reduction pre-treatment under syngas was not efficient to deeply reduce NiO.

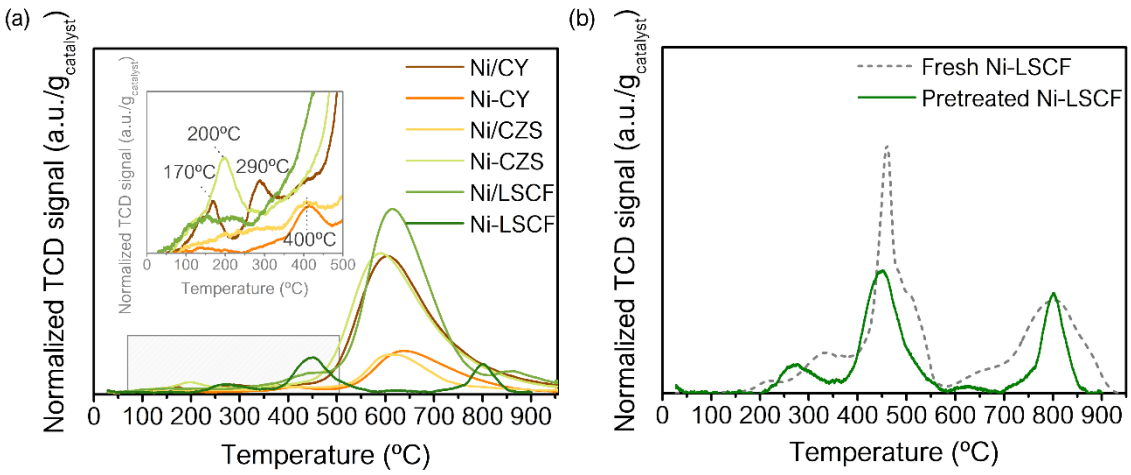

Figure 3.7. H_2-TPR profiles of catalysts pretreated under syngas atmosphere

In addition, the H_2 consumption associated to the reduction peaks at temperatures below 500 ºC and the NiO reducibility achieved during the pre-treatment have been listed in ***Table 3.6.*** The NiO reducibility has been estimated assuming that the H_2 consumption of the peaks at temperatures below 500 ºC are mainly due to NiO reduction. A H_2 consumption required to completely reduce NiO to Ni^0 assuming a theoretical Ni loading of 10 wt% (1.70 mmol H_2/g) has been considered to the calculation of NiO reducibility. As it can be seen, NiO reducibilities close to 100% is attained for most of the catalysts.

The main peak detected in H_2-TPR of the pretreated samples has been associated to CH_4 formed from the carbon deposited generated by Ni^0 species. Thus, TGA analysis of the pretreated samples were conducted to quantify the amount of deposited carbon and characterize its nature and structure. The mass of deposited carbon normalized by the mass of fresh catalyst in $g_C.g^{-1}_{f\text{-}catalyst}$, along with the oxidation temperature are listed in ***Table 3.6***. The deposited carbon follows same tendency than the catalytic activity deduced from the variation of the molar flows (***Figure 3.6***): Ni/CY (0.11 $g_C.g^{-1}_{f\text{-}catalyst}$) > Ni/LSCF (0.10 $g_C.g^{-1}_{f\text{-}catalyst}$) > Ni-CZS (0.09 $g_C.g^{-1}_{f\text{-}catalyst}$) > Ni-CY (0.04 $g_C.g^{-1}_{f\text{-}catalyst}$) > Ni/CZS (0.01 $g_C.g^{-1}_{f\text{-}catalyst}$) > Ni-LSCF (~0.0 $g_C.g^{-1}_{f\text{-}catalyst}$). Oxidation temperature around 500 ºC is evidenced for all catalysts, indicating the formation of filamentous carbon during the pretreatment.

	mmol H_2/g_{cata}*	NiO reducibility (%)	$T_{oxidation}$ (ºC)	$g_{coke}/g_{f\text{-}catalyst}$±
Ni/CZS	0.08	97	500	0.01
Ni-CZS	0.35	79	500	0.09
Ni/CY	0.23	86	500	0.11
Ni-CY	0.05	95	450	0.04
Ni/LSCF	0.09	95	480	0.10
Ni-LSCF	-	-	530	< 0.01

*H_2 consumption from H_2-TPR of pre-treated catalysts

±Calculated by TGA

Table 3.6. H_2 consumption, NiO reducibility, oxidation temperature ($T_{oxidation}$)and amount of deposited carbon for catalysts pretreated under syngas atmosphere

Furthermore, in order to determine the type of morphology of the carbonaceous species formed on the surface during the pre-treatment, SEM images of Ni/LSCF after treatment under syngas atmosphere are displayed in ***Figure 3.8.*** The orange zones in ***Figure 3.8 (a)*** correspond to the surface areas in which the carbonaceous species are highly concentrated. The distribution of these carbonaceous species over the surface is clearly heterogeneous. These species mainly display a filamentous morphology, such as carbon nanotubes or filaments (***Figure 3.8 (b)***) according to the oxidation temperature prior observed by TGA analysis. Two growth mechanisms of these carbon species have been widely reported in literature for Ni-based catalysts: base- and tip-growth. The metal particles remain anchored to the catalyst surface in the former, whereas the particles lifts off the catalytic surface and it is observed in the top of the carbon nanotubes in the latter [250]. The difference of growth mechanism is often associated to the metal-support interaction. Thus, a weak metal-support interaction facilitates the tip-growth mechanism, while a strong interaction leads to base-growth. Thereby, the presence of metallic nickel

particles in the top of the carbonaceous filaments evidenced by chemical contrast mode in SEM (***Figure 3.8 (c)***) suggests that tip-growth mechanism seems to be promoted during the pre-treatment under syngas atmosphere. Several studies highlighted that this kind of growth mechanism caused by pre-treatments in absence of H_2, such as CH_4/O_2, or *in situ* under reaction conditions, improves the catalytic activity due to an enhancement of the metallic nickel dispersion [251,252]. However, the decrease in catalytic activity associated to the loss of Ni-support interaction by detachment of Ni from the catalytic surface has been also reported by other researches [218].

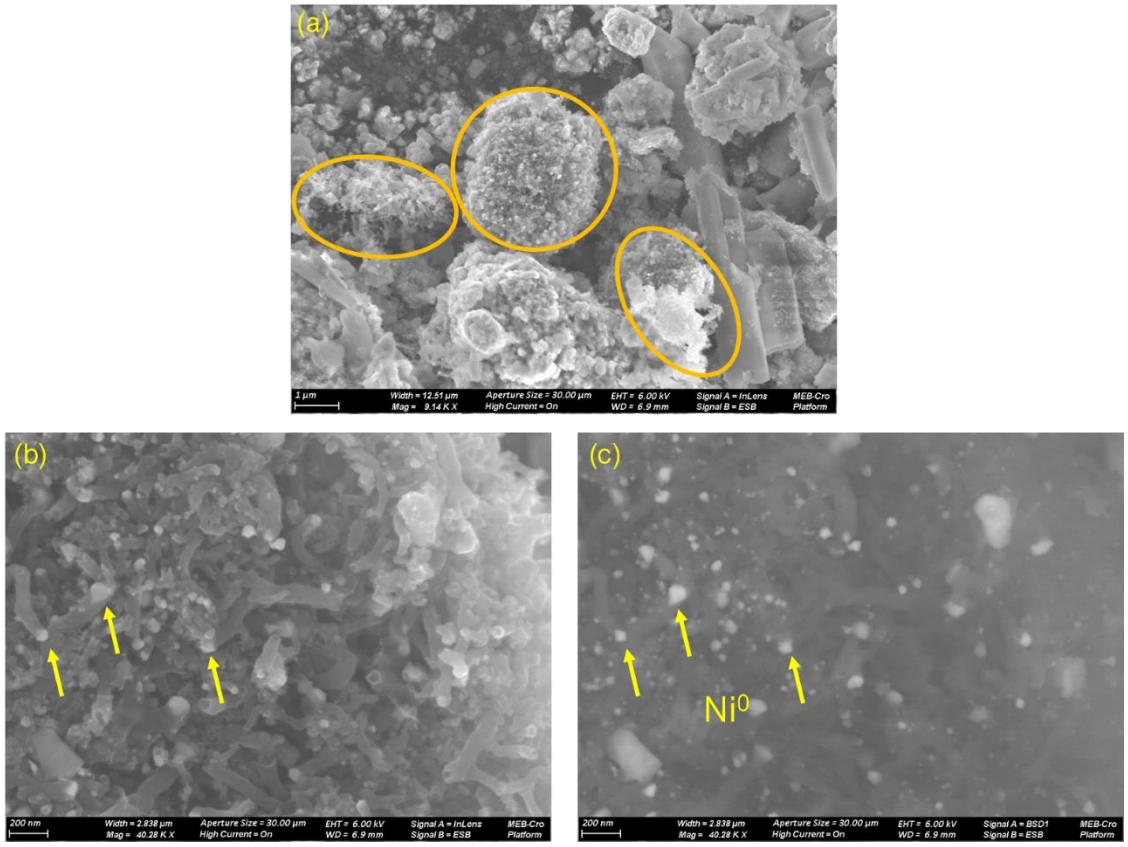

Figure 3.8. SEM images of reduced Ni/LSCF under syngas atmosphere

As discussed in prior sections, the metallic surface is a key parameter in reforming reactions. Therefore, in order to elucidate the influence of the treatment under syngas on the metallic surface, H_2-TPD analysis were conducted for Ni/CY, Ni/LSFC and RuNi/LSCF catalysts. It should be underlined that Ni^0 surface area is evaluated for Ni/CY, whereas a general metallic surface, including Ni^0+Co^0, is measured for Ni/LSCF and RuNi/LSCF catalysts. The resultant H_2-TPD profiles of the pretreated catalysts have been plotted in ***Figure 3. 9.***. Peaks of hydrogen desorption at temperature range of 100-200 ºC have been observed for the three catalysts (***Figure 3.9, inset***), previously attributed to H_2 species weakly adsorbed on the active metal. An additional small desorption peak at temperatures

around 300 ºC was noticeable for Ni/CY catalyst, highlighting the existence of different H-metal interactions. The changes in the distribution of H adsorbed have been ascribed to: (i) changes in the surface morphology of the crystallites (adsorption on different reticular planes) that could occur with change in dispersion and/or (ii) different coordination of H adsorbed atoms with the surface, being the bridge bonding and adsorption on top of metal atom more prevalent on the smaller particles [253]. The bridge bonding and on top adsorption evidenced lower strength than H adsorbed species in higher coordination [253]. Consequently, the peak desorption at lower temperatures (100-200 ºC) may be due to a H species adsorbed on smaller particles. The much lower intensity of these peaks that those found in the H_2-TPD profile under H_2/N_2 pretreatment (shown in *Chapter 2, section 2.5.5*) may underline a decrease of small particles content at the surface due to either sintering or blockage of Ni surface by coke deposition process. The peak found at 300 ºC for Ni/CY could be identified as H adsorbed over a different surface morphology of the Ni crystals and/or H-adsorbed on larger particles. Eventually, the peaks detected at temperatures above 500 ºC for Ni/LSCF and RuNi/LSCF might be linked to desorbed CH_x species generated by hydrogenation of surface carbonaceous species. The high desorption temperatures of these species have been associated in literature to the hydrogenation of iron carbides ($Fe_{2.5}C$) or graphitic films [254]. Thus, the poor resistance to coke deposition due to the possible stabilization of iron carbide at the surface of Ni/LSCF based catalyst has been evidenced.

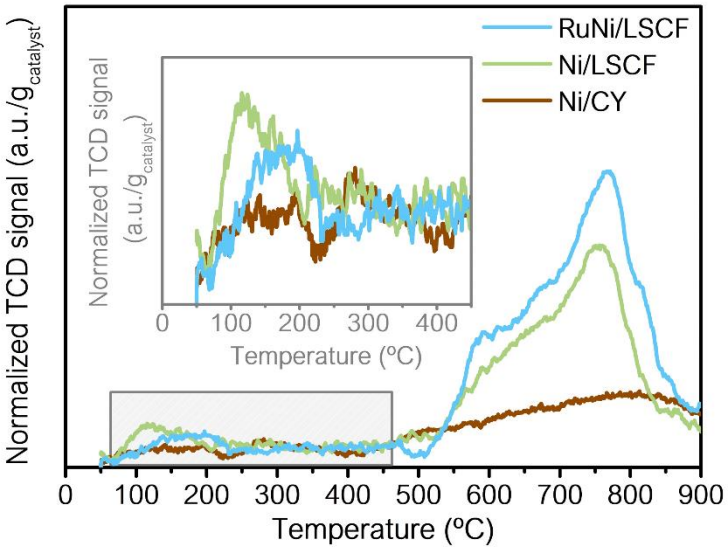

Figure 3.9. H_2-TPD profile of selected catalysts (Ni/CY, Ni/LSCF and RuNi/LSCF) prior reduced under syngas atmosphere

The catalytic results after reduction pre-treatment under H_2/N_2 atmosphere indicated that Ni/CY and Ni-LSCF catalysts were the best catalytic systems in terms of average tar conversion and resistance to coke deposition. However, as mentioned in this section, reduction under syngas is difficult for Ni-LSCF catalyst and the low NiO reduction could derive in a low catalytic activity after activation under syngas. Its impregnated equivalent, the Ni/LSCF catalyst, evidenced a similar tar conversion but with greater carbon selectivity. This poor resistance to coke deposition has been improved for this catalyst by adding Ru (RuNi/LSCF). Accordingly, in the following section the effect of the pretreatment conditions on the catalytic efficiency in tar removal has been investigated for these three catalysts (Ni/CY, Ni/LSCF and RuNi/LSCF).

3.4.2.2. Toluene reforming: Ni/CY, Ni/LSCF and RuNi/LSCF. Effect of pre-treatment under syngas.

Toluene reforming has been performed over the selected catalysts after reduction pre-treatment under syngas. The same reaction conditions than those in pre-treatment under H_2/N_2 atmosphere were used (described in *section 3.3.2.3*).

The average toluene conversion and benzene selectivity are presented ***Table 3.7*** together with the coke deposits normalized by the mass of fresh catalyst ($g_{coke}/g_{f\text{-}catalyst}$) for the reduced catalysts under both atmospheres. In addition, ***Figure 3.10.*** compares the variation in the partial molar flows of the gaseous compounds along reaction time for the selected catalysts under H_2/N_2 (solid lines) and syngas (dot lines) atmosphere. Partial molar flows not far from the inlet one was noticed for pre-treated Ni/CY under syngas, whereas significant changes are observed in the partial molar flows for Ni/LSCF and RuNi/LSCF catalysts. Comparing with the H_2 pre-treatment, the syngas pretreatment lead to a noticeable decrease in catalytic activity toward WGS and CO_x methanation for Ni/CY. An increase of H_2 and CO_2 flows accompanied by a decrease of CO one is displayed for Ni/LSCF under syngas pre-treatment. Indeed, comparing the partial molar flows obtained for this catalyst pre-treated under both atmospheres, it seems that pre-treatment under syngas leads to higher catalytic activity to WGS reaction compared to H_2/N_2 pre-treatment. Similarly, RuNi/LSCF catalyst also displayed activity to WGS reaction after pre-treatment under syngas. Nevertheless, as it can be appreciated by the modifications in the gas phase, its catalytic efficiency toward WGS was lower than that reached under H_2/N_2 pre-treatment. Generally, the pre-treatment under syngas atmosphere has a negative effect on tar removal efficiency. No catalytic activity toward toluene reforming has been evidenced for Ni/CY and Ni/LSCF catalysts, whereas toluene conversion reached 19%

value for RuNi/LSCF, compared to 82% obtained with the same catalyst after reduction under H_2/N_2 mixture.

Likewise, Du *et al.* [255] evidenced a lower toluene conversion accompanied by an increase in catalytic activity toward WGS reaction for those Ni-based catalysts pyrolyzed at higher temperatures. They informed that these behaviours were connected to the less available catalytic sites owing to a decrease in the Ni dispersion due to high pyrolysis temperature. Besides, they also investigated the metal size dependence in steam reforming of toluene. A decrease in turnover frequency (TOF, $mol_{toluene} \cdot mol_{surface\ Ni}^{-1} \cdot s^{-1}$) with larger Ni crystalline size led to the conclusion that toluene reforming is structural sensitive. As, theoretically, the fraction of corners or steps decreases with respect to the terrace when metal size is larger, toluene steam reforming should be favoured on the corner and steps sizes. Considering the latter, DFT studies of toluene decomposition on flat or stepped Ni (111) surface were carried out in order to prove the structural sensitivity of this reaction. They showed that the activation energies barrier was lower for all decomposition steps on stepped Ni (111) surface, except the ring-opening that was more favoured on flat Ni (111) surface. According to this study and the effect of pre-treatment under syngas previously discussed, the no catalytic activity in term of toluene reforming showed for the pre-treated catalysts under these conditions might be due to:

(i) No complete reduction of NiO species to Ni^0 was achieved (***Table 3.6***)

(ii) Detachment of metallic Ni from the surface caused by formation of filamentous carbon species through tip-growth mechanism during the pre-treatment under syngas (lose of metal-support interaction) (***Figure 3.8***)

(iii) Less active sites available owing to the presence of CO chemisorbed during the pre-treatment, inhibiting toluene adsorption.

(iv) The decrease in metallic surface attained by pre-treatment under syngas result in a lower fraction of corner/steps Ni sites. Then, toluene reforming could be disfavoured in accordance with Du *et al.* study [255].

Thus, Ni/CY catalyst underwent a strong deactivation under syngas pre-treatment, as indicate the higher amount of coke deposits (***Table 3.7***) and the decrease in the metallic Ni surface compared to samples pre-treated under H_2/N_2. The syngas pre-treatment improved the catalytic activity toward WGS reaction for Ni/LSCF catalyst compared to the pre-treatment under H_2/N_2 mixture, prevailing over toluene reforming. Similar to Ni/CY, the pre-treatment under syngas also lead to high amount of coke deposits for Ni/LSCF catalyst. Concerning RuNi/LSCF, similar catalytic activity toward WGS reaction is

displayed under both pre-treatments, whereas a severe decrease in catalytic activity to toluene reforming caused by the pre-treatment under syngas is clearly noticed (*Table 3.7*). It should be stressed that the amount of coke deposits achieved for RuNi/LSCF catalysts are similar in both pre-treatments, outstanding that the resistance to coke formation is improved by the presence of Ru. In general, the syngas pre-treatment resulted in a decrease in catalytic efficiency in tar abatement for the three catalysts under study.

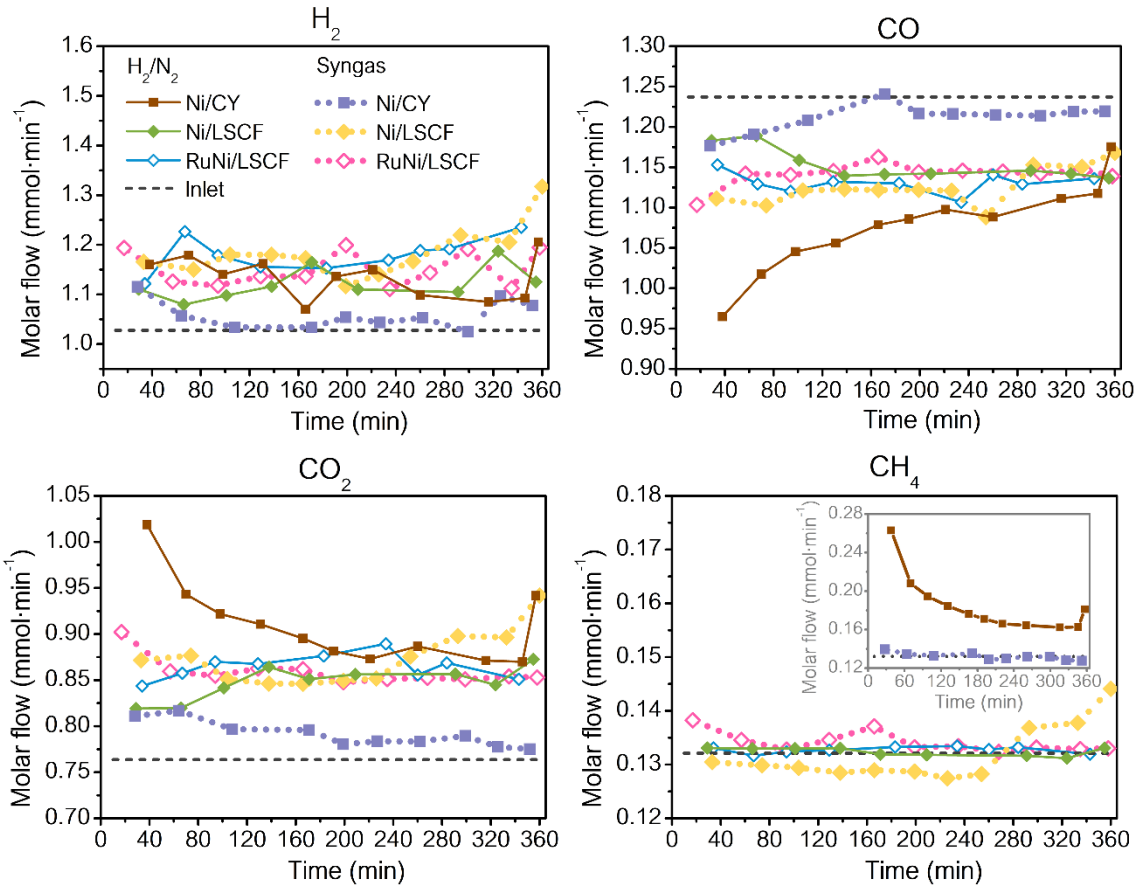

Figure 3.10. Partial molar flows at the outlet of the reactor vs time on stream during toluene reforming at 550 ºC over Ni/CY, Ni/LSCF and RuNi/LSCF catalysts ($WHSV_{gas}$ = 370 h^{-1}; $WHSV_{tar}$= 26 h^{-1} and S/C_{tar}=7.7). Solid and dot lines: pretreatment under H_2/N_2 and syngas respectively.

	Pre-treatment	$X_{toluene}$ (%)	$S_{benzene}$ (%)	$g_{coke}/g_{f\text{-}catalyst}$ ±
Ni/CY	H_2/N_2	100	< 2	1.1
Ni/LSCF	H_2/N_2	54	4	1.3
RuNi/LSCF	H_2/N_2	82	< 2	1.0
Ni/CY	Syngas	4	67	2.1
Ni/LSCF	Syngas	0	-	2.1
RuNi/LSCF	Syngas	19	10	0.9

Table 3.7. Average toluene conversion, selectivity to benzene and deposited carbon attained during toluene reforming at 550 ºC under both reduction pretreatments.

3.5. Characterization of spent catalysts

In order to investigate the modifications in the structural properties of the catalysts after steam reforming reactions, XRD analysis were conducted on the spent catalysts. In this section the discussion will be focused on the influence of the reaction temperature (400 or 550 ºC), the tar model molecule (phenol or toluene) and the reduction pre-treatment conditions (H_2 or syngas) on the structural properties of the previous selected catalysts (Ni/CY, Ni/LSCF and RuNi/LSCF). The analysis of the rest of the catalytic systems has been also done, the results are reported in *Appendix*, at the end of the chapter.

Figure 3.11. shows the diffractograms of the fresh and used catalysts after steam reforming reactions for 6 h. Regardless the reaction conditions, the crystalline structure of the support remained for all spent catalysts. Generally, peaks associated to Ni (111) and to Ni (200) at 2θ~44º and 52º, respectively, have been discerned in all materials after reaction. Moreover, a less intense diffraction peak related to NiO (200) placed at 2θ~43º was also detected. The presence of NiO phase could be a consequence of oxidation of Ni mainly with steam or with the oxygen of the catalytic support during the reforming reactions [223,256]. As it can be noticed, the intensity of this phase is higher for catalysts post toluene reforming pre-treated in syngas, probably due to the no complete reduction of NiO to Ni^0 under this pre-treatment conditions (see *section 3.4.2.1*). Additionally, a peak at 2θ~26º highlighted the presence of significant amount of graphitic carbon over the spent catalysts. These peaks were more intense after toluene reforming than after phenol reforming, probably due to the higher inlet tar content used for toluene compared to phenol (see ***Table 3.2***). As expected, the pre-treatment under syngas leads to the highest amount of graphitic carbon, in line with the results obtained by TGA reported in ***Table 3.7.***

The support and nickel particle size has been as well estimated by Scherrer equation and listed in ***Table 3.8*** for the spent catalysts. In general, similar support particle size than the fresh catalysts have been attained for the spent catalysts. Regarding to the Ni particle size, whereas a slightly smaller particle size is observed for Ni/CY by increasing the reaction temperature in phenol reforming, the opposite was found for Ni/LSCF. The slightly decrease in the Ni particle size at high temperature for NiO could be attributed to the partial oxidation of Ni to NiO according to Koike *et al.* [223]. Meanwhile, the larger Ni particle size displayed for Ni/LSCF at high reaction temperature should be caused by sintering [234]. A rather smaller Ni particle size was noticeable after toluene reforming compared to phenol reforming for Ni/CY (11 nm for toluene vs 20 nm for phenol) and Ni/LSCF (9 nm for toluene vs 15 nm for phenol) catalysts. Thereby, larger Ni particles due

to sintering process was favoured through phenol reforming conditions compared to that for toluene (see ***Table 3.3***). At contrary, the slightly larger Ni particle size showed for RuNi/LSCF catalysts in toluene (20 nm) compared to phenol (14 nm) reforming underlined that sintering was highly promoted for this catalyst during toluene reforming. Despite the larger Ni particle size, better catalytic performance and resistance to coke formation was displayed for RuNi/LSCF material during toluene reforming with respect to its equivalent Ni/LSCF (see ***Table 3.5,*** *section 3.4.1.3*) This improvement might be associated to the enhancement of carbon gasification by the presence of Ru in Ni/LSCF. Eventually, an increase in the Ni particle size has been also discerned for Ni/CY post toluene reforming pre-treated in syngas compared to the pre-treated in H_2 atmosphere. This increase in the particle size could be a reason of the deactivation observed for reduced Ni/CY during toluene reforming under syngas atmosphere (***Figure 3.10***). Whereas same Ni particles size (9 nm) was evidenced for reduced Ni/LSCF catalyst in both pre-treatment conditions, a smaller Ni particle size was observed for pre-treated RuNi/LSCF under syngas than H_2 atmosphere (10 nm vs. 20).

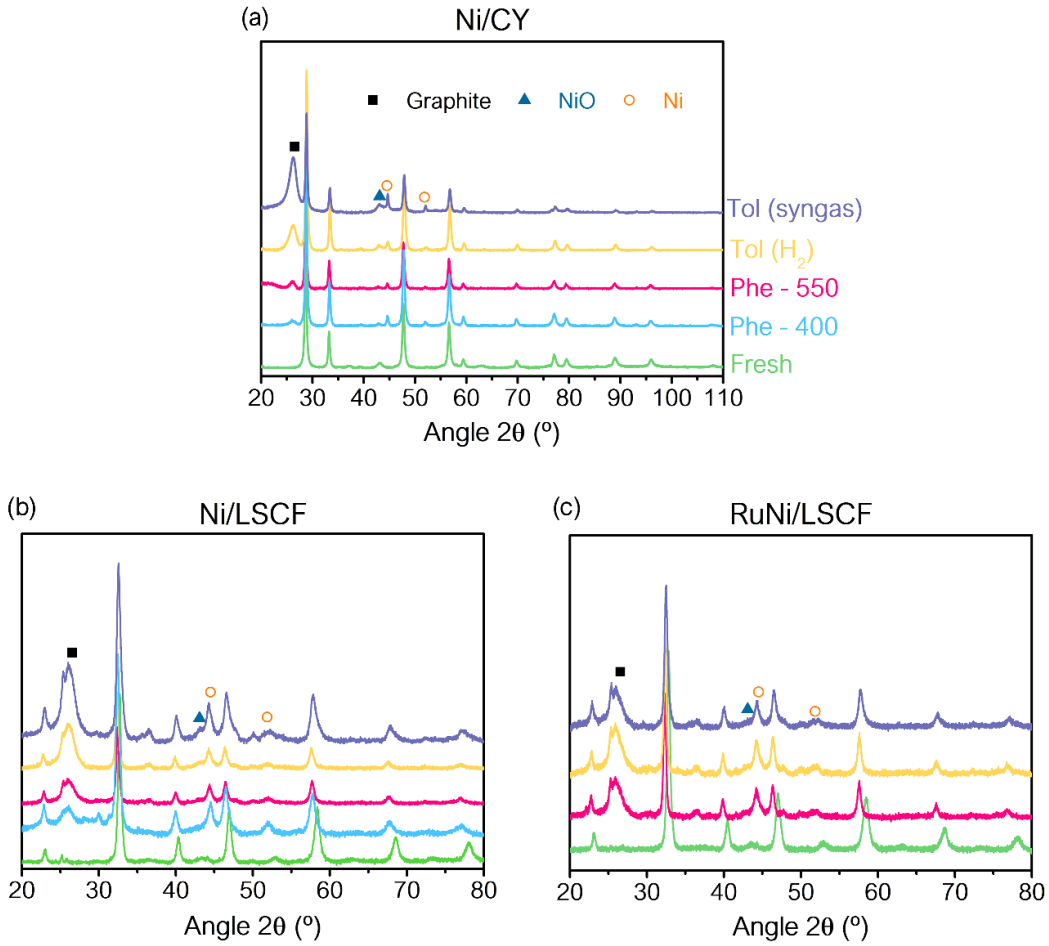

Figure 3.11. Diffractograms of the selected materials (fresh and post steam reforming reaction): (a) Ni/CY, (b) Ni/LSCF and (c) RuNi/LSCF catalysts

	Ni/CY		Ni/LSCF		RuNi/LSCF	
Reaction conditions	*Support*	*Ni^0*	*Support*	*Ni^0*	*Support*	*Ni^0*
Fresh	*23*	-	*17*	-	*14*	-
Phe400	22	23	15	12	-	-
Phe550	20	20	18	15	18	14
Tol(H_2) - 550	14	11	19	9	18	20
Tol(syngas)	20	21	12	9	13	10

Table 3.8. Support and nickel particle sizes of selected catalysts post steam reforming reactions.

In order to evaluate the deactivation by carbon deposition, the selectivity to carbon deposit has been estimated by TGA analysis and already discussed in the section of catalytic results (***Table 3.4-3.5***). In addition to the surface carbon selectivity, the type and morphology of these surface carbonaceous species can, as well, affect both catalytic activity and stability. In literature, mainly two types of carbonaceous deposits can be formed over Ni surface: (i) amorphous carbon, and (ii) structural and graphitic carbon, comprising carbon nanotubes (CNTs) and/or carbon nanofibers (CNFs). The formation of amorphous carbon over the surface could be easily remove by oxidizers in the reaction feed, such as CO_2 or H_2O, or oxygen species from the catalytic support lattice. Nevertheless, structural carbon is mainly generated on the metal active site and might lead to detachment of metal particle from catalytic support surface. Considering previous reports, the amorphous carbon is easily oxidized at temperature below 500 ºC due to its highly instability [175,223,257]. However, oxidation temperatures above 500 ºC have been attributed to structural and/or graphitic carbon which are quite stable and oxidizes at higher temperatures [218,257]. Thus, in order to elucidate the kind of carbonaceous species formed after the reforming reactions, the TGA curves normalized by the mass of catalyst has been plotted for the three selected catalysts post-test in ***Figure 3.12.***

The careful analysis shows one peak around 600 ºC for all catalysts after phenol and toluene reforming at reaction temperature of 550 ºC associated to graphitic or structural carbon. Meanwhile, peak centered at 500 ºC has been showed for Ni/CY (***Figure 3.12 (a)***) and Ni/LSCF (***Figure 3.12 (b)***) post phenol reforming at reaction temperature of 400 ºC, revealing the presence of more amorphous carbon. These results are in concordance with the intensity of the peak associated to graphite (2θ~26º) displayed in XRD analysis for the spent catalysts (***Figure 3.11***), attaining the lowest intensity for phenol reforming at 400 ºC. The formation of mainly structural or graphitic carbon deposits could be promoted by presence of some gaseous components in the inlet

syngas mixture such as CH_4, H_2 and CO, according to Łamacz *et al.* [218]. They observed a more significant contribution of the structural carbon when the steam reforming of toluene was conducted in the presence of the syngas mixture containing H_2, CO, CO_2 and CH_4. This high contribution was attributed to CO and CH_4 components, which are typical precursors for CNTs and CNFs formation by Catalytic Chemical Vapor Deposition. Moreover, they underlined that H_2 could also promote CNTs formation and influences their shape and structure.

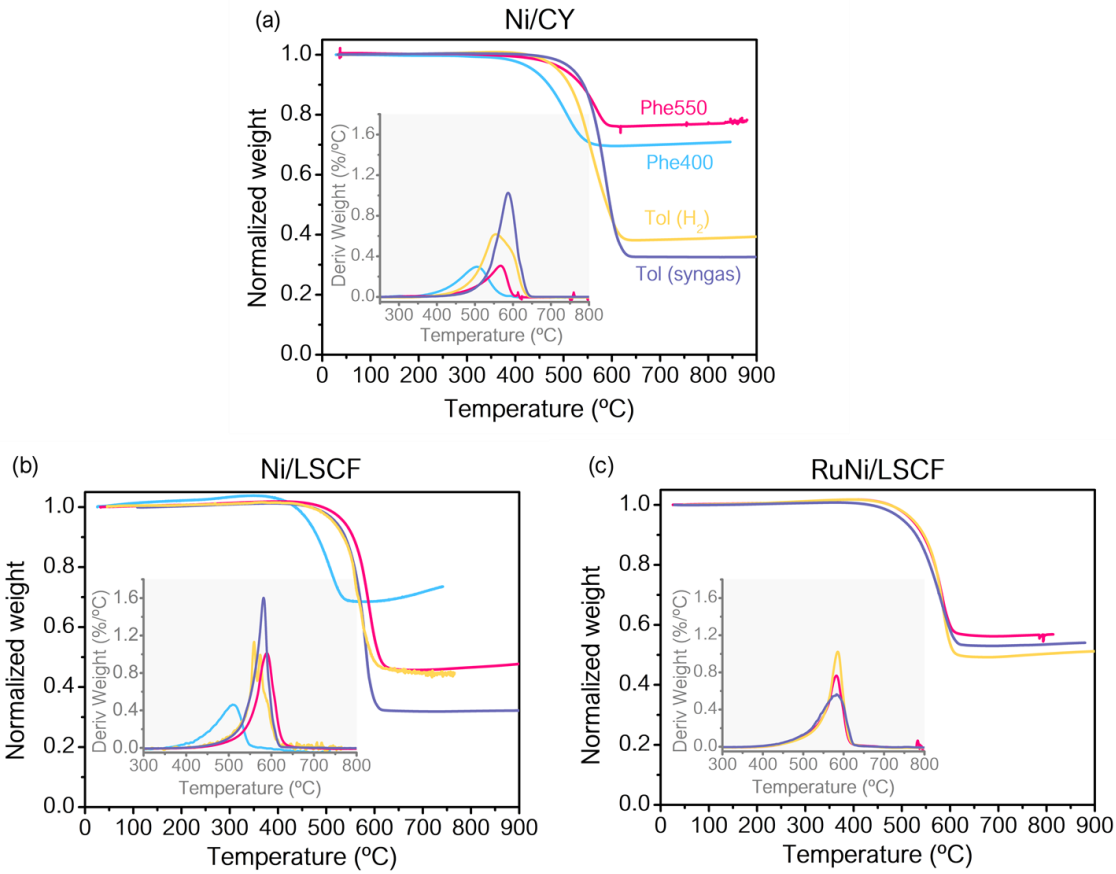

Figure 3.12. TGA analysis of the selected catalysts post steam reforming reactions: (a) Ni/CY, (b) Ni/LSCF and (c) RuNi/LSCF catalysts. *Color code*: phenol reforming at 400 ºC (blue) and at 550 ºC (pink), toluene reforming at 550 ºC - H_2 (yellow) and - syngas (purple)

The morphology of the carbonaceous species has been also verified by microscopy for spent Ni/LSCF catalyst in the different catalytic steam reforming reactions (***Figure 3.13***). The filamentous carbons were the main morphology detected in all reaction conditions in concordance with the previous TGA results. The tip-growth mechanism was as well noticeable by the chemical contrast mode (***Figures 3.13 (b), (d), (f), (h)***), even for the

reduced samples under H_2/N_2 mixture, underlined that this growth mechanism was also favoured during reforming reaction conditions.

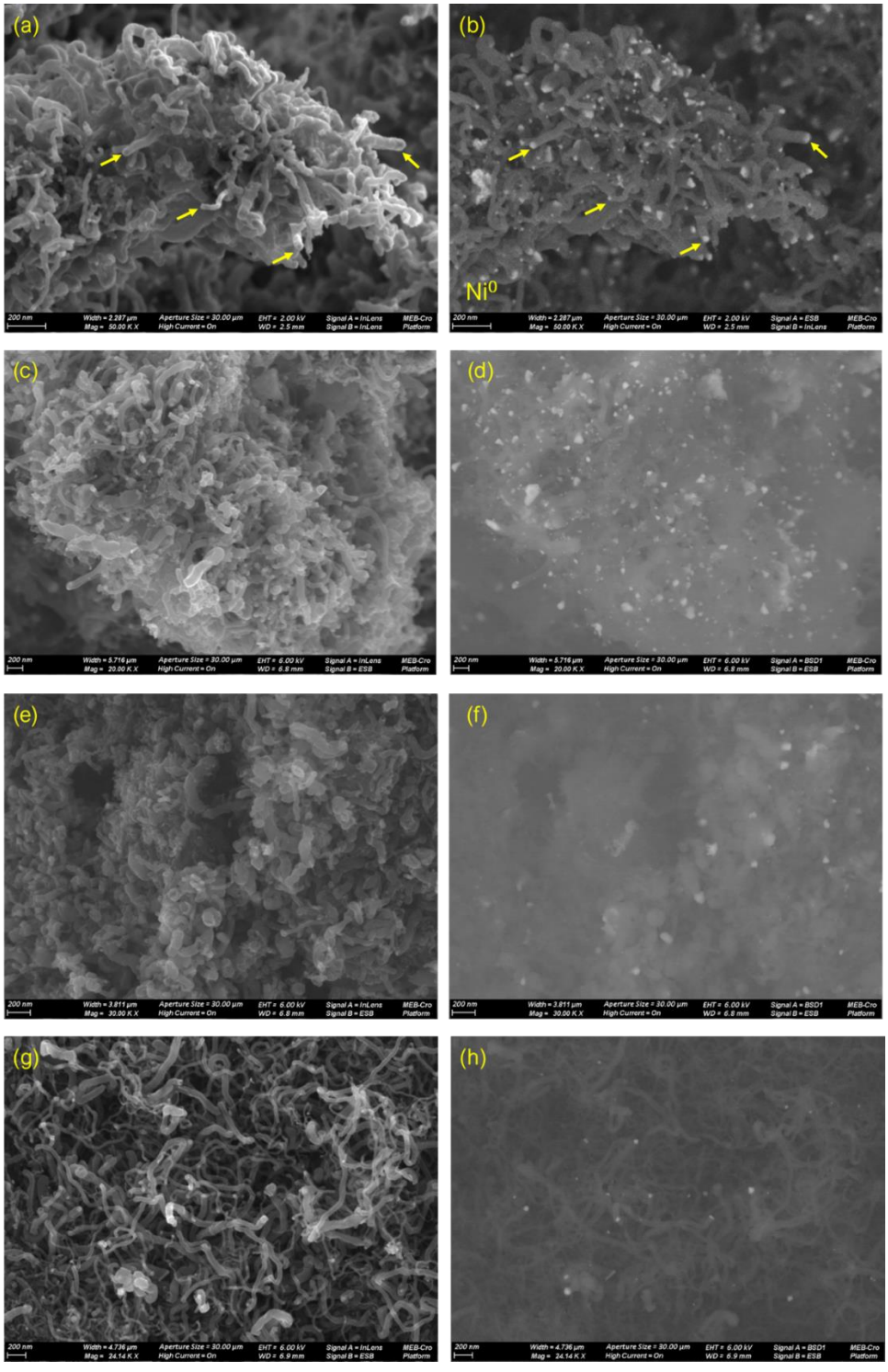

Figure 3.13. SEM images of Ni/LSCF catalysts after 6 h steam reforming of ***(a-b)*** phenol T400, ***(c-d)*** phenol T550, ***(e-f)*** toluene (H_2) T550 and ***(g-h)*** toluene (syngas) T550

3.6. Literature comparison

A comparison of the catalytic activity in terms of tar conversion between the studied catalysts and other catalytic systems reported in literature is presented in this section.

Table 3.9 shows the comparison between the catalytic activity in steam reforming of phenol for the selected catalysts of the present work and other catalysts reported in literature. As presented in the introduction, a limited number of researches investigated the steam reforming of tar using phenol as tar model molecule. Generally, softer reaction conditions such as lower time on stream, higher temperature compared to our conditions have been found for reaching phenol conversions around 80%. Nevertheless, greater tar space velocity has been used within these studies. It should be as well stressed that studies about steam reforming of phenol under simulated syngas composition has not been reported. By comparing with literature, the catalytic results attained in the present work points out the high catalytic activity displayed for our catalysts. An average phenol conversion similar to that obtained in literature (80-90%) using more severe reaction conditions, under simulated syngas atmosphere and at much lower temperatures, have been achieved.

Catalyst	Gas composition	Metal loading (wt%)	Time (h)	T (ºC)	S/C$_{tar}$	WHSV$_{tar,metal}$ (h^{-1})	Phenol conversion (%)
In the present work							
Ni/CY	*Simulated syngas*	*10 (Ni)*	*6*	*550*	*16.5*	*14*	*89*
Ni/LSCF							*85*
RuNi/LSCF		*10 (Ni) 1 (Ru)*					*79*
In literature							
Ni/K-La-ZrO_2 [258]	H_2O	3.5 (Ni)	22	700	20	51	85
Ni/Ce-ZrO_2 [258]							80
Ni/Al/Mg [223]	H_2O	12 (Ni)	1.2	600	1.9	94	60
Rh/$Ce_{0.14}Zr_{0.81}Mg_{0.05}O_2$ [224]	H_2O	0.5 (Rh)	-	550	11	188	80

Table 3.9. Comparison of catalytic activity in steam reforming of phenol conducted by the studied catalysts and other catalysts from the literature

Table 3.10. evidences the comparison of catalytic activity in steam reforming of toluene for the investigated catalysts in the present work and different catalysts studied in the literature. As it can be seen in *Table 3.10,* some studies reported the efficiency in steam reforming of toluene at similar reaction temperatures and lower S/C than those used in the present work [88,221,259,260], exhibiting toluene conversions around 70-80%. However,

most of these researches performed the catalytic activity at lower tar space velocity and/or shorter reaction times. Additionally, they do not consider a simulated syngas atmosphere to conduct the steam reforming of toluene. The influence of a simulated syngas composition on the catalytic performance in toluene reforming has been just reported by two different works [217,218]. Both of them required harder reactions conditions (higher temperature, higher S/C, lower tar space velocity and/or the used of novel metals) than the reactions conditions conducted in the present studied to reach toluene conversion of 90%. As shown this literature comparison, catalytic systems with high catalytic efficiency on tar abatement, reaching average toluene conversion up to 100% under simulated industrial biomass gasification conditions has been obtained in the present work.

Catalyst	Gas composition	Metal loading (wt%)	Time (h)	T (ºC)	S/C_{tar}	$WHSV_{tar,metal}$ (h^{-1})	Toluene conversion (%)
In the present work							
Ni/CY	*Simulated syngas**	*10 (Ni)*	*6*	*550*	*7.7*	*26*	*100*
Ni/LSCF							*54*
RuNi/LSCF		*10 (Ni) 1 (Ru)*					*82*
In literature							
Ni/olivine [88]	H_2O	3.9 (Ni)	7	560	2.3	11	29
Ni/AC [221]	H_2O	10 (Ni)	3	550	2.0	7.5	~70
Fe-Ni/Pal‡ [259]	H_2O	8 (Ni) 3 (Fe)	2	550	1.0	21	~80
Ni/CZ [218]	H_2O	9.1 (Ni)	2	550	2.4	0.97	~75
	*Simulated syngas**		5	800			93
CaNiRu/Al_2O_3 [217]	*Simulated syngas**	20 (Ni) 0.6 (Ru) 3 (Ca)	-	500	25	-	~22
				600			~90
Ni/$La_{0.7}Sr_{0.3}AlO_{3-\delta}$ [260]	H_2O	5 (Ni)	-	600	14	8	73

*Mixture of H_2O, CO, CO_2, H_2 and CH_4
‡Palygorskite (Pal) - (65.5 wt% SiO_2, 5.4 wt% Al_2O_3, 14.0 wt% MgO and 3.2 wt% Fe_2O_3)

Table 3.10. Comparison of catalytic activity in steam reforming of toluene conducted by the studied catalysts and other catalysts from the literature

3.7. Conclusions

The influence of the support and the Ni addition pathway on catalytic efficiency catalysts in terms of tar reforming has been investigated for the six synthesized catalysts. Phenol and toluene have been selected as tar model molecules. The catalytic steam reforming reactions has been carried out at relatively low temperature (400ºC/550ºC) and

using a simulated syngas composition based on the product gas composition measured at the outlet of the pilot gasifier in Offenburg. In addition, the effect of reducing pre-treatment under two different atmospheres (H_2/N_2 mixture or syngas) on the catalytic performance in steam reforming of toluene were described.

The study of the effect of reaction temperature (400 ºC or 550º C) in steam reforming of phenol revealed an increase of phenol conversion and a decrease in carbon selectivity at high reaction temperature. Thus, the use of high reaction temperature facilitates the carbon gasification and the catalytic activity toward steam reforming reaction. The lower S/C operated in steam reforming of toluene compared to phenol resulted in a slight decrease of the catalytic activity in the former reaction in term of tar conversion. The differences in reaction mechanism or reactivity over Ni surface between both molecules has been also underlined in this work. Thereby, the similar carbon selectivity observed in toluene and phenol reforming for some catalysts pointed out that phenol is thermally less stable in comparison with toluene, and easily underwent to thermal decomposition and/or cracking, producing higher amount of carbon deposits, as described in other researches. Despites these differences between the two model molecules, same catalytic performance has been obtained for the three families of catalysts (CZS-, CY- and LSCF-based materials) under both reaction conditions. Whereas the sol-gel Ni-CZS and Ni-LSCF catalysts displayed better catalytic activity and lower carbon selectivity than its impregnated corresponding catalyst (Ni/CZS and Ni/LSCF), the opposite catalytic behaviour was detected for CY-based materials. The better catalytic activity of Ni-CZS and Ni/CY with respect to their corresponding Ni/CZS and Ni-CY catalysts were attributed to their higher metallic Ni^0 surface. The better catalytic performance shown for the sol-gel Ni-LSCF catalyst than the impregnated Ni/LSCF catalyst has been associated to the Ni-Co and Ni-Fe alloy formation and the higher Sr content detected at the surface by XPS analysis in the former material. Moreover, the addition of Ru over Ni/LSCF led to a negative effect in tar conversion for phenol reforming compared to the bare Ni/LSCF, while an improvement in the catalytic conduct were detected in toluene reforming. As concern to the catalytic stability, sol-gel catalysts displayed higher stability than the impregnated ones within the Ce-based materials, whereas similar stability was attained for both Ni containing LSCF materials. Generally, the catalytic activity in term of catalytic stability and average tar conversion decrease for both tar model molecules as follow: Ni/CY > Ni-LSCF > Ni/LSCF ~Ni-CZS > Ni-CY > Ni-CZS, being Ni/CY and Ni-LSCF the best catalysts in tar conversion and resistance to coke formation.

Additionally, the partial reduction of NiO to Ni^0 was feasible for all the materials through the reduction pre-treatment under syngas atmosphere, except for Ni-LSCF. Carbonaceous filaments species with tip-growth mechanism and a decrease in the metallic nickel surface has been showed in the surface of the catalysts as consequence of the catalytic activity caused by formation of Ni^0 during the pre-treatment in syngas. Considering the catalytic activity attained after reduction pre-treatment under H_2/N_2 and the reducibility of the catalysts obtained through the pre-treatment under syngas, three catalysts (Ni/CY, Ni/LSCF and RuNi/LSCF) were chosen for the succeeding structuration of the catalysts and final implementation in the pilot plant. A drastic decrease in the catalytic activity toward toluene reforming reaction has been evidenced for samples pre-treated under syngas, for the three selected catalysts.

The characterization of the spent catalysts highlighted no modification in the crystalline structure of the catalysts during the steam reforming reactions. A higher Ni particle size was attained for spent catalysts post phenol reforming compared to toluene reforming at reaction temperature of 550 ºC caused by the higher S/C ratio. In addition, the presence of mostly structural and graphitic carbon was evidenced by XRD, TGA and SEM for all catalysts and it has been mainly associated to the use of a simulated syngas composition. Lastly, the comparison with other catalysts and steam reforming reaction conditions allows to conclude that catalysts with high catalytic efficiency in tar removal have been developed during this work.

Appendix of chapter 3

(i) Reproducibility tests and conditions of liquid phase analysis

○ *Phenol reforming*

The variation of the partial molar flows of the gaseous compounds compared to the inlet ones versus time on stream during three similar catalytic tests in phenol and toluene reforming at 550 ºC for Ni/LSCF is plotted in ***Figure 3.14*** and ***Figure 3.15,*** respectively. In addition, the average tar conversion (X_{tar}) and the selectivity to benzene/carbon deposit ($S_{benzene/coke}$) are listed for phenol and toluene reforming in ***Table 3.11***. and ***Table 3.12***, respectively.

As it can be seen, same phenol conversion (90%) and carbon selectivity (14%) was reached for test 2 and 3, whereas a lower value in terms of conversion (73%) and higher carbon selectivity (25%) has been attained during test 1 (***Table 3.11***). This fact is in good agreement with the variation observed in the partial molar flows of the gas phase (***Figure 3.14***). A stable value of the different partial molar flows with similar tendency along time were attained for test 2 and 3, whereas the tend to the inlet molar flows for test 1 remarked the lower catalytic activity obtained during this test. Thus, the low activity achieved during catalytic test 1 could be associated to an experimental issue caused by a lower temperature due to a wrong catalyst place into the reactor and/or the introduction of higher phenol flow due to pressure problem in the micropump.

Within the three tests in toluene reforming, similar toluene conversion (35-40%), benzene selectivity (6%) and carbon selectivity (19-21%) has been found for test 2 and 3 (***Table 3.12***), which is in concordance with the gas phase variation on the reaction time (***Figure 3.15***). Meanwhile, rather high values in term of toluene conversion (77%) and carbon selectivity (63%), as well as an unusual conduct in the partial molar flows in the gas phase was displayed during the test 1. The high toluene conversion and carbon selectivity attained suggest that there was probably an increase in the pressure drop during test 1.

Moreover, the analysis of the liquid phases recollected during test 3 for both tar molecules were analysed using split and spitless injection mode in GC leading to slightly different values in phenol and toluene conversion. Generally, only a small part of vapor is injected into the column through the split injection mode while nearly all the evaporated sample is injected by using the spitless mode. The former mode is rather used for analysing concentrated samples in order to avoid saturated peaks. However, the use of split mode

for quantifying compounds in low concentration can lead to selective injection of one product compare to another in link with the boiling point of these compounds. Therefore, no precise results can be obtained from the analysis of diluted samples by split injection mode. In this work, the tar content (no converted tar) present in the liquid phase recollected after test is rather low and the analysis using spitless injection mode should give more reliable results.

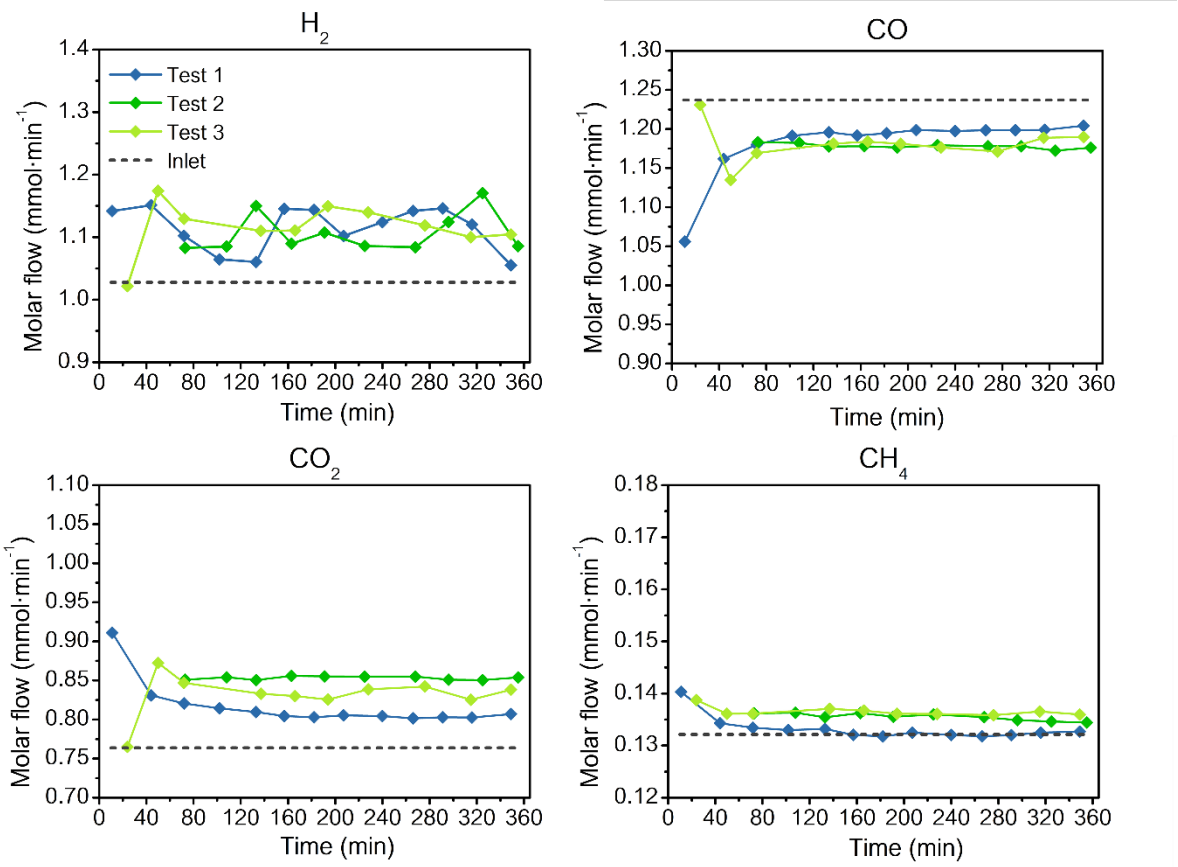

Figure 3.14. Partial molar flows at the outlet of the reactor vs time on stream during the phenol reforming at 550 ºC over Ni/LSCF ($WHSV_{gas}$ = 370 h^{-1}; $WHSV_{tar}$= 14 h^{-1} and S/C_{tar}=16.5). Reproducibility test

	X_{phenol} (%)	S_{coke} (%)
Test 1	73	25
Test 2	90	14
Test 3	90	14
Test 3	85	15

Split	Splitless

Table 3.11. Average phenol conversions and selectivity to carbon during phenol reforming at 550 ºC for Ni/LSCF: split and spitless GC mode. Reproducibility test

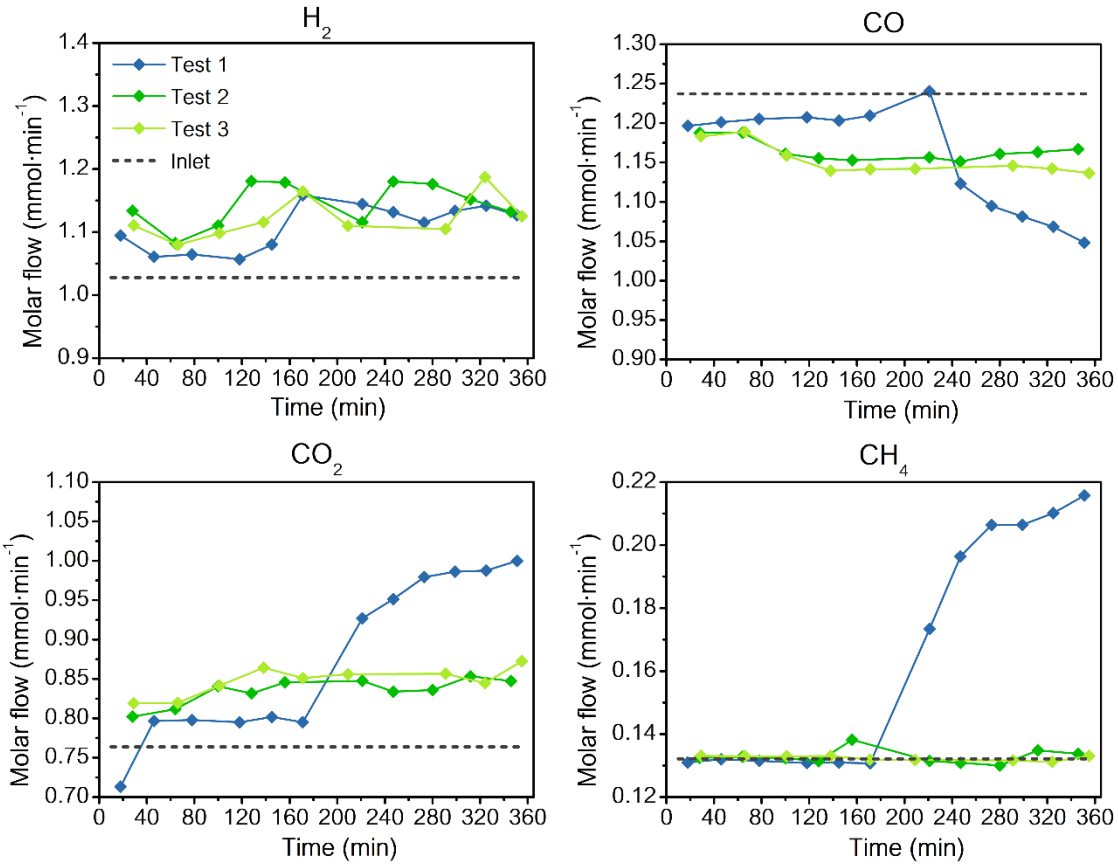

Figure 3.15. Partial molar flows at the outlet of the reactor vs time on stream during toluene reforming at 550 ºC over Ni/LSCF catalyst ($WHSV_{gas}$ = 370 h^{-1}; $WHSV_{tar}$= 26 h^{-1} and S/C_{tar}=7.7). Reproducibility test

	$X_{toluene}$ (%)	$S_{benzene}$ (%)	S_{coke} (%)
Test 1	77	2	63
Test 2	35	6	19
Test 3	40	6	21
Test 3	54	4	16

Split	Splitless

Table 3.12. Average toluene conversion, selectivity to benzene and carbon during toluene reforming at 550 ºC for Ni/LSCF catalyst: split and spitless GC mode. Reproducibility test

(ii) Characterization of spent catalysts

- *XRD analysis*

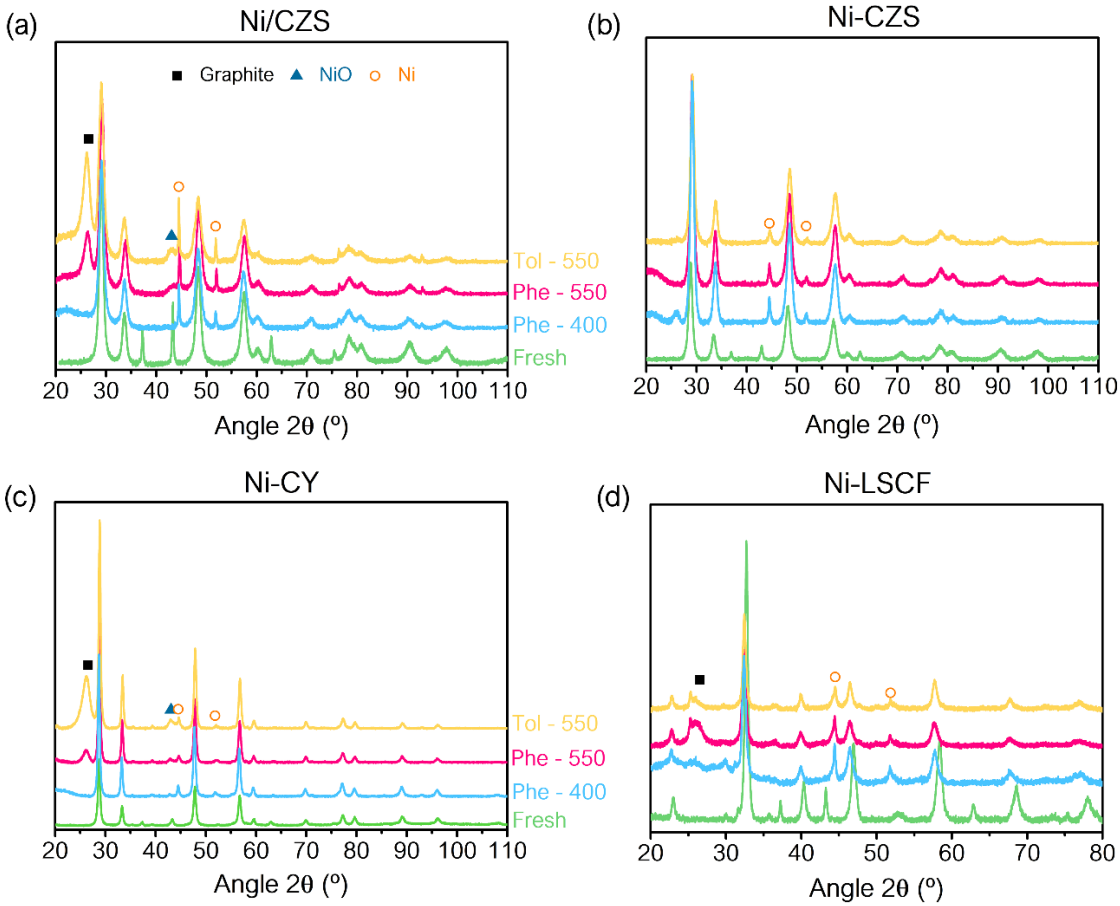

Figure 3.16. Diffractograms of catalytic systems (fresh and post steam reforming reactions): (a) Ni/CZS, (b) Ni-CZS, (c) Ni-CY and (d) Ni-LSCF

- *TGA analysis*

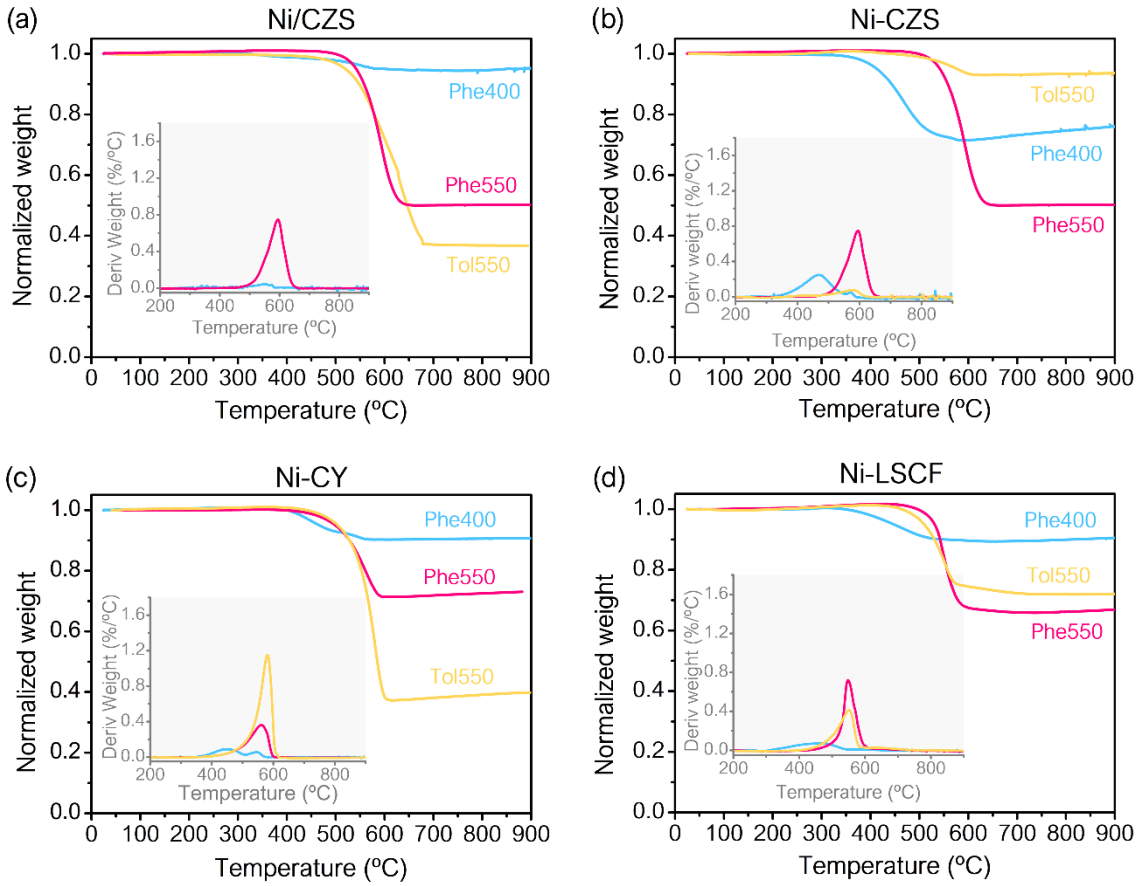

Figure 3.17. TGA analysis of the catalytic systems post steam reforming reactions: (a) Ni/CZS, (b) Ni-CZS, (c) Ni-CY and (d) Ni-LSCF catalysts

CHAPTER 4

OPTIMIZATION OF CATALYTIC STRUCTURATION OVER SiC-BASED EXTRUDATES AND CATALYTIC TESTS

Abstract

The use of metal-supported catalysts in an in-bed configuration as a primary catalyst is limited by the catalytic deactivation, specially by coke deposition. Pellets, rings or monolithic structures are required for its use as a secondary catalyst in a downstream reactor in order to diminish operational problems such as pressure drops.

In the present chapter, the optimization of the catalytic structuration over SiC extrudates is presented in order to select the optimal conditions for the preparation at large scale. The influence of some parameters such as, solution concentration, solvent or SiC shape on the catalytic deposition is investigated. The characterization results of the final structured catalysts are shown. Additionally, the catalytic results obtained in toluene reforming are discussed and, afterwards, compared to those obtained for the powders. The influence of the preparation at large scale using the optimal conditions chosen for the catalytic structuration is also exposed.

4.1. Introduction

As aforementioned in *General Introduction* (Chapter 1), the use of structured catalysts improves the limitations displayed by the traditional fixed-bed catalytic reactors, playing a crucial role in the optimization and intensification of industrial processes [261]. In order to provide an adequate design of these structured catalysts, many parameters such as the type of substrate, the structure (shape and size) and the preparation method must be taken into consideration. Catalytic substrate geometries such as metal-gauzes, extrudates, foams and parallel longitudinal channel monoliths have been studied for the preparation of structured catalysts [262–265]. Concerning the type of catalytic substrate, the structured catalysts have been classified in two main categories: (i) ceramic and (ii) metallic-based substrates. The ceramic-based substrates provide high surface/volume ratios, low heat expansion coefficients, high resistance to oxidation and to high temperatures and excellent durability [262]. Among them, cordierite is the most extensively used as a ceramic substrate due to its high refractoriness, good mechanical strength and open porosity. Some of their limitations are associated to the wall thickness for a correct extraction (100 μm) and the low thermal conductivity, causing a non-homogeneous thermal profile [266]. Generally, these type of substrates are cheaper than metallic ones and normally provide better adhesion of the catalytic phase [267,268].The metallic–based substrates show higher thermal conductivity and smaller wall thickness (25 – 50 μm), favouring the heat and mass transfer, compared to the ceramic ones [266,267]. For that reason, the use of these last materials in strong exothermic reactions becomes relevant [262]. The Fe-Cr-Al alloy-based steel (Fecralloy® steel) has been reported as a promising metallic substrate, since the formation of a Al_2O_3 layer at the surface provides high resistance to high temperatures and corrosion and, besides, enhances the catalytic coating adherence [268–270].

Accordingly, the effect of the type of substrate or its geometry has been widely investigated for several researchers in different catalytic reactions. For instance, Brussino *et al.* [262] studied the ethylene production over NiO structured on three ceramic substrates: alumina foam, cordierite monolith and alumina-silica paper. They also investigated the influence of the geometry surface area of metallic monoliths (Fecralloy®) by the structuration of Ni/Al_2O_3 catalyst [269]. Three kinds of foam substrates based on Al_2O_3, β-SiC and aluminium for carbon dioxide methanation reaction at low temperature have been used by Frey *et al.* [265]. Santos *et al.* [267] showed the catalytic performance

in VOC abatement of coated metallic (Fecralloy®) and ceramic (cordierite) monoliths with a manganese-based oxide mineral, called cryptomenale.

Other catalytic substrates that are currently receiving special attention are the porous β-SiC materials [271]. Silicon carbide shows excellent thermal stability, high mechanical strength, great resistance to oxidation and corrosion, a low thermal expansion and high thermal conductivity [272,273]. The low specific surface (0.1 – 1 $m^2 \cdot g^{-1}$) area characteristic of this material was one of the main limitations for its use in heterogeneous catalysis fields. However, in the 1980s Ledoux *et al.* [274] developed a single gas-solid method, called shape memory synthesis (SMS), to manufacture a medium specific surface β-SiC (10 – 40 $m^2 \cdot g^{-1}$) and tailored pore distribution with pore volume up to 1 $cm^3 \cdot g^{-1}$, which made this material useful for catalytic support/substrate applications. These SiC based materials can be found into diverse shapes as extrudates, spheres, monoliths, open cell foams and can be as well chemically modified by addition of promoters (Al_2O_3, TiO_2, ZrO_2, metals…)[271]. Despite that, few articles using β-SiC as a catalytic substrate for preparation of structured catalysts have been reported in the open literature. Most of these works have been focused on the impregnation of cobalt, as active phase, over SiC extrudates or foams for an application in Fischer-Tropsch synthesis [272,275–277]. The application of β-SiC as catalytic substrate in exothermic reactions, as carbon dioxide methanation, has been reported by some researchers [278,279].

In addition to the nature and shape of the catalytic substrate, a good control of the preparation of the structured catalysts is crucial for attaining the satisfactory catalysts distribution, high adherence and accessible active sites. Avila *et al.* [268] reported two preparation methods for ceramic monoliths, one labelled as coated-type resulting from washcoating method and another named incorporated-type. In the former type, the catalyst phase is dispersed exclusively in the external wall of the substrate, whereas in the latter type the catalyst is distributed in the external wall as well as within the substrate. Whereas for metallic substrates, the most developed and popular preparation method is the washcoating [280–282]. The preparation of the coated structured catalysts can be carried out by dipping the catalytic substrate into a slurry or by *in situ* synthesis using a precursor solution [268]. The coating from a slurry is highly developed and studied in the literature. In this coating procedure, a homogeneous and stable colloidal suspension of the catalyst is used. For this method, adequate rheological and compositional properties (solid content and particles size, pH, zeta potential, addition of surfactants and stabiliser, etc.) should be considered in order to control the catalytic deposition and achieve a uniform dispersion [268,281].

Generally, the preparation of structured catalysts from slurry involves dipping the catalytic substrate into the slurry, blowing with an inert gas to remove the excess of liquid, drying and calcining [268,280,283]. In the *in situ* synthesis procedure, the catalysts are directly prepared onto the catalytic substrate by the deposition of a precursor solution [268,278,284]. A stronger anchoring of the catalysts is provided by this method compared to the coating from slurry, but it is a considerably more complex procedure. The use of a solution, precursor of the final catalytic phase, could lead to the formation of non-desired crystalline structure by reaction with the substrate during the thermal treatment [268]. Many studies have reported the effect of the slurry properties on the washcoating of ceramic and metallic substrates. However, few studies reported the effect of the properties of the precursor solution in the *in situ* synthesis of the catalysts over the catalytic substrate. As regards to this, the work carried out by Frey *et al.* [278] should be stressed. They evaluated different parameters in the preparation of SiC open cell foams coated with Ni/ceria-zirconia (CZ) catalyst and evaluated their activity in carbon dioxide methanation. Among these parameters, they studied the use of two solution concentrations for the precursor solution of CZ, reaching an enhancement of the catalytic anchoring by using a diluted precursor concentration. Additionally to the coating procedure, many studies have been carried out on diverse pre-treatment methods to improve the textural properties at the surface of the catalytic substrate and, thereby, enhance the catalytic anchoring [278,282,285]. For instance, M. González-Castaño *et al.* [282] displayed a thermal pre-treatment of metallic micromonoliths (Fecralloy®) (900 ºC for 22 h, under air) in order to generate an oxidized surface layer of α-Al_2O_3. This alumina layer increases the surface roughness, favours the adhesion and the chemical anchoring of the catalyst. Others pre-treatments, as anodisation of aluminium substrates, were also performed to generate this advantageous alumina layer [283,286]. M. Frey *et al.* [278] studied the deposition of Ni/CZ catalysts over different catalytic substrates based on β-SiC-, Al_2O_3- and Al- based foams. Whereas a good anchoring was achieved for the two former types of foam without any pre-treatment, an optimized acidic pre-treatment was required for the latter to improve the anchoring of the catalyst. They also reported that a thermal pre-treatment of β-SiC foams (900 ºC – 2 h, under air) resulted in the formation of SiO_2-SiO_xC_y washcoat layer, improving the anchoring of the deposited active phase [279].

4.2. Partial objectives

Up to now, six different Ni based catalysts have been synthesized by wetness impregnation (Ni/CZS, Ni/CY and Ni/LSCF) and one step sol-gel (Ni-CZS, Ni-CY and Ni-

LSCF) and characterized through several characterization techniques (*Chapter 3*). Afterwards, a catalytic screening in phenol and toluene conversion, along with the study of reducibility ability under syngas atmosphere, allowed the choice of three catalysts for their structuration to be finally tested at pilot plant scale (*Chapter 5*). The selected catalysts were Ni/CY, Ni/LSCF and RuNi/LSCF.

In the present chapter, the optimization of the catalytic deposition over β-SiC based extrudates is studied by using a precursor solution for the coating procedure. As reported in literature, the characteristics of the final structured catalysts depend of many variables as the properties of the catalytic substrate, the slurry or precursor solution properties and the coating procedure conditions. Accordingly, the evaluation of the following parameters in the catalytic deposition and anchoring has been performed:

- β-SiC extrudates shape
- Precursor solution concentration (0.30 – 0.60 M)
- Effect of scale-up; from 1 mL for one extrudate to batch of 1 L of extrudates
- Pre-treatment conditions

In our research group, the use of propionic acid as a solvent to prepare the precursor solution has been widely employed for conducting the catalytic structuration on different kinds of substrates such as, SiC, Al and Al_2O_3 foams [207,278,279]. Owing to the high chemical affinity, the solution of the gel obtained by the pseudo sol-gel synthesis method (mixed propionates) is highly favoured by the use of this solvent. However, its corrosive properties, its flammability and its toxicity are some of the drawbacks for the use of this solvent at large scale. Therefore, in addition to propionic acid, the use of water as solvent has been investigated in the presented work.

Before the evaluation of this parameters in the catalytic deposition, the characterization results of the bare SiC extrudates shapes and the powder formed from the propionic- and water-based solution are presented and discussed. Afterwards, the effect of the SiC shape and the solution precursor concentration on the deposition, performed individually for each extrudate shapes is investigated. In order to determine the accuracy of the deposited mass attained, a comparison between the coating conducted individually and in batch of several extrudates is presented. Besides, the effect of the solvent, the pre-treatment as well as the use of other catalytic support on the deposition are evaluated and discussed.

Afterwards, in order to determine the adequate β-SiC shape and preparation conditions for the catalytic structuration at large scale, the selected catalysts in Chapter 3 were structured, characterized and tested in toluene reforming at laboratory scale. These catalytic results were compared to those obtained for the systems in powder to evaluate the influence of the structuration in the catalytic activity. Lastly, the structuration of the three catalysts at large scale, using the optimal conditions, has been conducted for being subsequently tested at pilot plant scale.

4.3. Experimental procedure

4.3.1. Shape of extrudates

In the present work, three β-SiC based extrudates with different shapes (rings and pellets) and dimensions, have been used as catalytic substrate. The samples were supplied by SICAT company. The main characteristics of the three SiC based extrudates such as dimensions, packed density or number of extrudates per apparent litre of fresh extrudate are listed in ***Table 4.1.*** All extrudates shown a high metallurgical purity and the average elemental composition associated to this purity provided by SICAT is shown in ***Table 4.2.***

Shape		$\emptyset_{ext}$ (mm)*	$\emptyset_{in}$ (mm)*	Length (mm)	Packed density ($g \cdot L^{-1}$)	Nº extrudates/L	Nomenclature
Pellet		5	-	3	811	8.4×10^3	PSiC
Ring	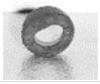	5	3	3	484	9.6×10^3	RSiC 5/3
Ring		8	5	5	499	2.7×10^3	RSiC 8/5

**External (ext) and internal (in) diameters*

Table 4.1. Main characteristics of the β-SiC-based extrudates

	Fe	Al	Ca	Na	K	S
Composition (ppm)	3.0×10^3	1.0×10^3	4.0×10^2	80	1.0×10^2	50

Table 4.2. Elemental composition of β-SiC-based extrudates (provided by SICAT)

4.3.2. Structuration of the catalysts

4.3.2.1. Support precursor solutions

The preparation of the support precursor solution used for the coating was based on the pseudo sol-gel synthesis already described in *Chapter 3.* Thereby, the corresponding

starting salts for CY and LSCF supports were dissolved individually in propionic acid (0.12 mol·L^{-1}) in order to form the metallic propionates. The mixture of the individual solutions underwent a heat under reflux during 2 h in order to generate the mixed propionates. Afterwards, the excess of solvent was removed by distillation resulting in a formation of a resin/gel through oligomerization. Lastly, the resin/gel was re-dissolved in a given quantity of solvent in order to achieve the aimed cationic concentration of precursor solution (***Figure 4.1.***). Propionic acid and water were used as a solvent, and two different solutions with 0.30 and 0.60 mol total cations·$L_{solvent}^{-1}$ range of concentration were prepared.

To check the accuracy of the precursor solutions, a given volume of the resulting solutions was calcined using the same conditions than those used for the prepared supports from the resin/gel calcination (800 ºC for 6 h, heating ramp of 2 ºC/min). The formed solids from the solutions were characterized by N_2 physisorption, XRD and H_2-TPR. The operating conditions of the characterization techniques used are reported in *Annex.*

Figure 4.1. Preparation of the support precursor solution by pseudo sol-gel method

4.3.2.2. Coating procedure

In the present work, the aimed deposited mass of catalyst has been chosen based on the typical values reported in literature for catalytic structuration at large scale. Thus, the aimed mass of catalyst chosen for the tests at pilot plant scale was 60 $g_{catalyst}$ per liter of apparent volume of fresh extrudates ($L_{extrudate}$). In order to make comparisons, same mass composition as in catalysts in powder was used (10 wt% Ni^0). Therefore, the desired amount of catalytic support and Ni^0 were 54 $g_{support}/L_{extrudates}$ and 6 $g_{Ni}{}^0/L_{extrudates}$, respectively.

The coating procedure of the extrudates is shown in ***Scheme 4.1.*** The β-SiC-based extrudates with different morphologies were coated with support (CY or LSCF) by dipping them into the prepared support precursor solution for 2 min. Subsequently, the excess of solution was removed by flushing air. The extrudates were then dried at 100 ºC for 3 h.

Lastly, the extrudates were calcined under air atmosphere using the same temperature program than the powdered supports (800 ºC for 6 h, heating ramp of 2 ºC·min^{-1}). In order to evaluate the stability and anchoring of the deposited support at the surface of the extrudates, the resulting CY/SiC- and LSCF/SiC-extrudates were exposed to ultrasound for 5 min. The whole procedure of impregnation was replicated until attaining approximately the desired amount of deposited support (54 $g_{support}/L_{extrudates}$).

The impregnation of the active phase (Ni) was carried out by following the same coating procedure prior discussed (***Scheme 4.1***). Thus, the resulting CY/SiC- and LSCF/SiC-extrudates were dipped into an ethanolic solution of nickel nitrate hexahydrate using two concentration solutions: 0.13 and 0.26 M. Afterwards, the samples were dried at 100 ºC for 3 h and, then, calcined under air at 500 ºC for 6 h using a heating ramp of 5ºC min^{-1}. The process was repeated until a Ni^0 loading approximately the same than in the powdered systems (10%wt Ni^0, corresponding to 6 $g_{Ni}{}^0/L_{extrudates}$) is reached, leading to Ni/CY/SiC- and Ni/LSCF/SiC-extrudates. Additionally, the impregnation of Ru over Ni/LSCF/SiC-extrudate has been performed using an ethanolic solution of ruthenium acetylacetonate (0.050 M). It should be stressed that the coating procedure of both the support and the active phase, were performed using: (i) individual dipping of the extrudates or (ii) batches of 20-30 extrudates.

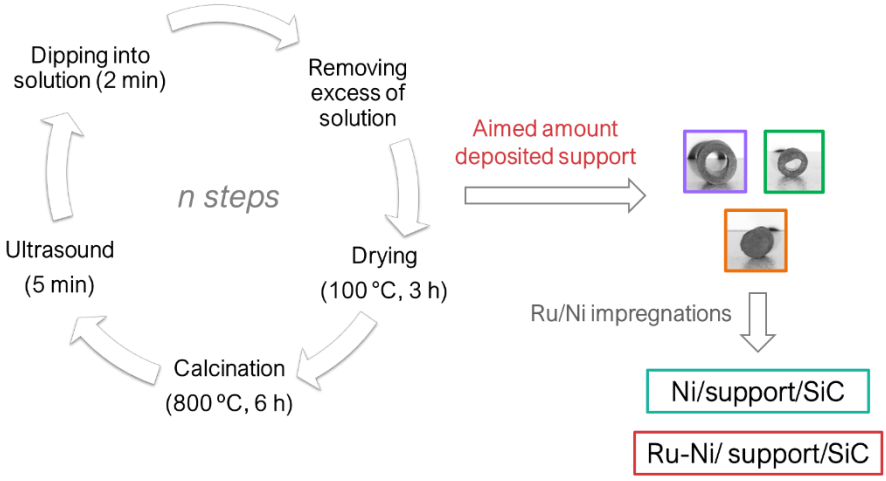

Scheme 4.1. Extrudates coating procedure

In the present chapter, mass uptake of the support (or of nickel) was defined as cumulative mass of deposited support (or Ni) normalized per liter of apparent volume of fresh extrudates($g/L_{extrudate}$), being 54 $g_{support}/L_{extrudate}$ and 6 $g_{Ni}{}^0/L_{extrudate}$ the targets. Additionally, the different parameters such as, support (or Ni) solution concentration, type of solvent, individual or batch deposition have been investigated for Ni/LSCF/SiC-

extrudates. The optimized parameters were subsequently used for the preparation of Ni/CY/SiC-extrudates. The target contents and the variation of the parameters are summarized in ***Table 4.3.*** Eventually, the prepared structured catalysts have also been characterized by means of different characterization techniques such as BET, XRD, H_2-TPR, H_2-TPD and TGA.

	Parameters			
	Precursor concentration (M)	*Solvent*	*$[Ni(NO_3)_2]$ (M)*	*Coating*
PSiC	0.30	Prop	0.26	Batch
RSiC 5/3	0.30	Prop	0.26	Batch
RSiC 8/5	0.30	Prop	0.26	Ind/batch
	0.60	Prop	0.13/0.26	Batch

Table 4.3. Summary of the studied parameters on the preparation of Ni/LSCF/SiC-extrudates

4.3.3. Catalytic performances: structured catalysts

Toluene has been selected as the tar model molecule to determine the catalytic efficiency in tar removal of the structured catalysts. As for the powdered catalysts, the catalytic tests were performed at atmospheric pressure in a fixed-bed down-flow quartz reactor with 5.0 mm of internal diameter, leading to a catalytic bed with a height around 1 cm. As described in *Chapter 3*, the tests were conducted under isothermal reaction temperature at 550 ºC for 6h with a S/C_{tar} ratio of 7.7 (see ***Table 3.3***).

Before the test, the structured catalysts were crushed into small pieces and the same Ni^0 loading than that used in *Chapter 3* for the powders (2.3 mg Ni^0) was kept constant in all tests. A homogeneous Ni loading on the extrudate was assumedy. All the samples were previously reduced under syngas atmosphere (defined in *Chapter 3*). The variation of the outlet partial molar flow rate (F_i) of compound i *versus* time on stream along with the average model tar conversion (X_{tar}), average benzene selectivity ($S_{benzene}$) are also informed for structured catalysts. In order to compare structured and powdered catalysts, the $WHSV_{tar,Ni^0}$ prior defined in *Chapter 3* has been as well reported in this chapter for the structured catalysts.

4.4. Support precursor solutions and bare SiC extrudates: characterization

4.4.1. Bare SiC extrudates

The adsorption-desorption isotherms and the pore size distribution of the bare β-SiC-based extrudates provided by SICAT are presented in ***Figure 4.2*** for the different shapes. The three samples show a type IV isotherm with a H3 type loop linked to macroporous and mesoporous materials [272,287]. No significative differences are observed in the pore size distribution among the three shapes (***Figure 4.2, inset***). A pore size distribution located at 25 nm for RSiC 5/3 and 32 nm for RSiC 8/5 and PSiC is displayed, outstanding the mesoporosity of the three β-SiC-based extrudates. The textural properties of these extrudates are also listed in ***Table 4.4.*** In accordance with the values reported in literature, the specific surface area (SSA) varies from 27-32 $m^2.g^{-1}$ among the three shapes [271,272]. Moreover, a high contribution of macropores is exhibited by the Hg porosimetry analysis, supplied by SICAT. A slightly higher mesopore volume is attained by Hg porosimetry (0.17 $cm^3 \cdot g^{-1}$) than that obtained by N_2 physisorption (0.14 $cm^3 \cdot g^{-1}$) for both RSiC 8/5 and PSiC.

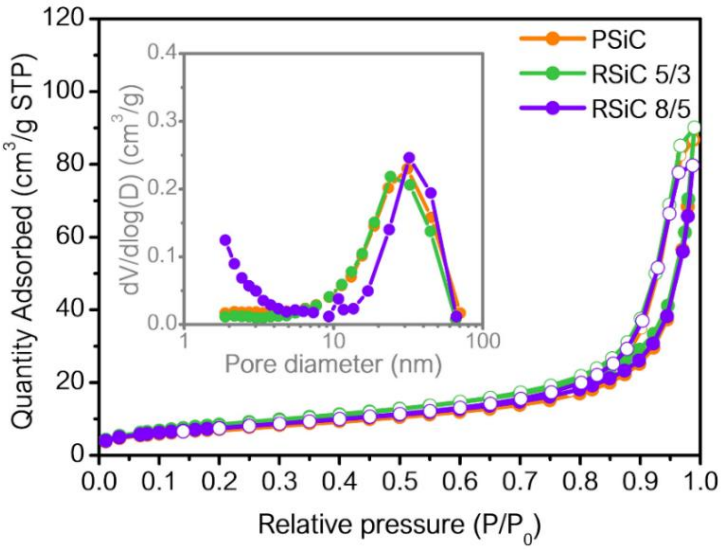

Figure 4.2. Adsorption-desorption isotherms and pore size distributions of β-SiC-based extrudates with different shapes

	N_2 physisorption*		Hg porosimetry±		
	SSA ($m^2 \cdot g^{-1}$)	V_{pore} ($cm^3 \cdot g^{-1}$)	V_{pore} ($cm^3 \cdot g^{-1}$)		
			6-50 nm	6-100 nm	< 5 μm
PSiC	27	0.14	0.17	0.25	0.51
RSiC 5/3	32	0.14	-	-	-
RSiC 8/5	28	0.13	0.17	0.26	0.53

*Measured using conditions and equipment described in Chapter 2

±Data from SiCat

Table 4.4. Textural properties of the β-SiC-based extrudates with different shapes

The X-ray diffractogram of RSiC 8/5 is shown in ***Figure 4.3*** Two crystalline phases can be distinguished: hexagonal α-SiC and face-centered cubic phase ascribed to β-SiC (JPCD 00-101-0995) as the main phase, in line with other results reported [271]. Thus, main intense diffraction peaks placed at 2θ = 36º, 41º, 60º and 72º are associated to the (111), (200), (220) and (311) reticular planes of β-SiC phase, whereas the small diffraction peaks placed at 2θ = 33.5º is allocated to the (111) reticular plane of α-SiC phase. Nguyen *et al.* [129] linked the formation of this latter crystalline phase to the presence of stacking faults along the (111) easy growth direction of the material.

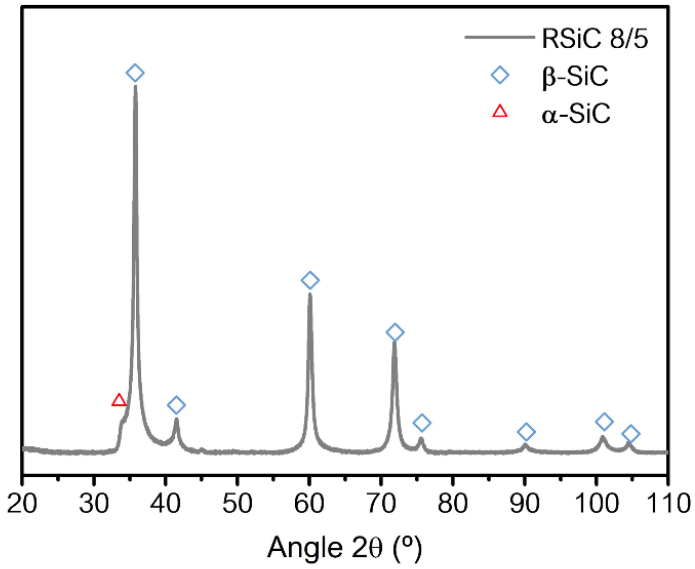

Figure 4.3. Diffractogram of β-SiC-based extrudate (RSiC 8/5 shape)

In order to evaluate the mass uptake due to SiC oxidation, TGA analysis under atmosphere air at high temperature (up to 900 ºC, 5 ºC·min^{-1}) was carried out. Thereby, the mass uptake (g) normalized by literfresh extrudate ($L_{extrudate}$) versus temperature is shown in ***Figure 4.4*** for RSiC 8/5 during two different analyses. In both analyses, a stable mass is achieved in 250-550/600 ºC temperature range. At temperatures above 550-600 ºC, the mass uptake increases with temperature, reaching 17.5 g/$L_{extrudate}$ and 12 g/$L_{extrudate}$ for

analysis 1 and 2, respectively. This mass rise has been widely attributed to the formation of a mixture of SiO_2 and SiO_xC_y by SiC oxidation process [271,272,288]. In addition, a different behavior in the oxidation process is observed when comparing the two TGA curves, even if samples from the same batch were used for both analyses. In analysis 2 the increase of mass begins at higher temperature (600 ºC) compared to analysis 1 (550 ºC) and, besides, the final mass uptake reached due to oxidation effect is lower. This fact suggests differences toward resistance to oxidation or initial oxidation state even when come from the same batch and shape. No plateau is attained at high temperatures for any analysis, meaning that β-SiC oxidation might continue at higher temperatures.

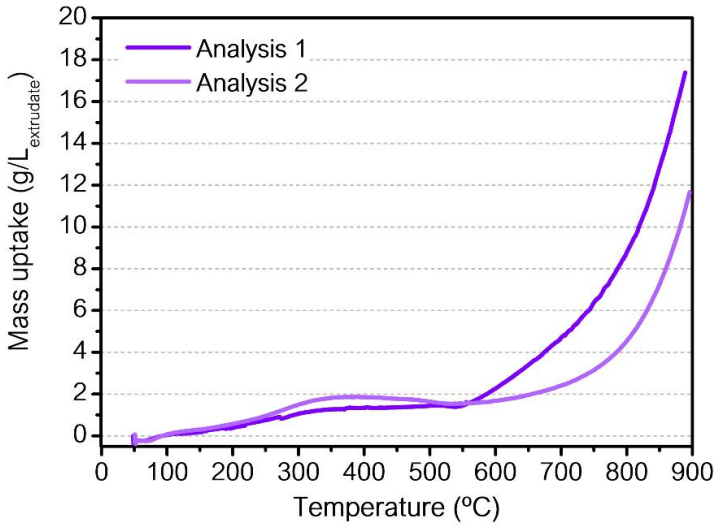

Figure 4.4. Mass uptake due to SiC oxidation for RSiC 8/5

4.4.2. Support precursor solutions

The characterization of the supports (CY and LSCF) resulting from the calcination of the precursor solutions (prop or water) has been carried out in order to evaluate the possible modifications in their physicochemical properties due to the step of gel/resin dissolution. In this section, the textural, structural and reducibility properties of these supports are compared to the corresponding supports obtained by calcination of the prepared resin/gel (SG).

Figure 4.5 exhibits the adsorption-desorption isotherm and the pore distribution of the supports from the calcination of gel (SG) and solutions (prop and water). Similar type of isotherm and hysteresis is observed for the gel (SG) and solutions (prop and water) supports in both, LSCF- and CY-based materials. Within the LSCF supports (***Figure 4.5 (a)***), a type IV isotherm with a H1 type loop is found, characteristic of mesoporous materials [287]. A homogeneous pore distribution in the range of 14 – 100 nm is attained for the three supports, centered at 70 nm for SG-LSCF and around 45 nm for prop-LSCF and for water-

LSCF supports (***Figure 4.5 (b)***). This highlights the presence of meso- and macroporosity, with a predominance of mesoporosity, in the LSCF support from solutions (water- and prop-LSCF) compared to the SG-LSCF. Within the two LSCF supports from propionic acid or water as solvent, the use of the water leads to the lowest porous material. A type IV isotherm with a H1 type loop is as well evidenced for CY supports (***Figure 4.5 (c)***). The smaller hysteresis loop for water-CY compared to SG-CY underlines, once again, the loss of porosity due to the dissolution of the gel. Both curves of pore distribution were in the range 8-90 nm, around 50 nm and 30 nm for SG- and water-CY respectively

The textural properties such as, the specific surface area (SSA) and the pore volume (V_{pore}) of the different supports are listed in ***Table 4.5.*** No modification in the SSA is detected for the LSCF supports (9-8 $m^2 \cdot g^{-1}$), whereas a decrease in the pore volume is noticeable for prop-LSCF and water-LSCF compared with the SG-LSCF. Within the CY supports, the SSA becomes 13 for water-CY from 22 $m^2 \cdot g^{-1}$ for SG-CY. The pore volume decreases also from 0.14 for CY-SG to 0.07 $cm^3 \cdot g^{-1}$ for water-SG, as result of the gel dissolution. Despite the negative effect of the dissolution of the gel on the textural properties, the tendency between LSCF and CY supports is similar. Thereby, as observed between the SG-supports (LSCF and CY), water-CY shows higher SSA (13 $m^2 \cdot g^{-1}$) and pore volume (0.07 $cm^3 \cdot g^{-1}$) than the equivalent water-LSCF solid, SSA and V_{pore} of 8 $m^2 \cdot g^{-1}$ and 0.02 $cm^3 \cdot g^{-1}$, respectively.

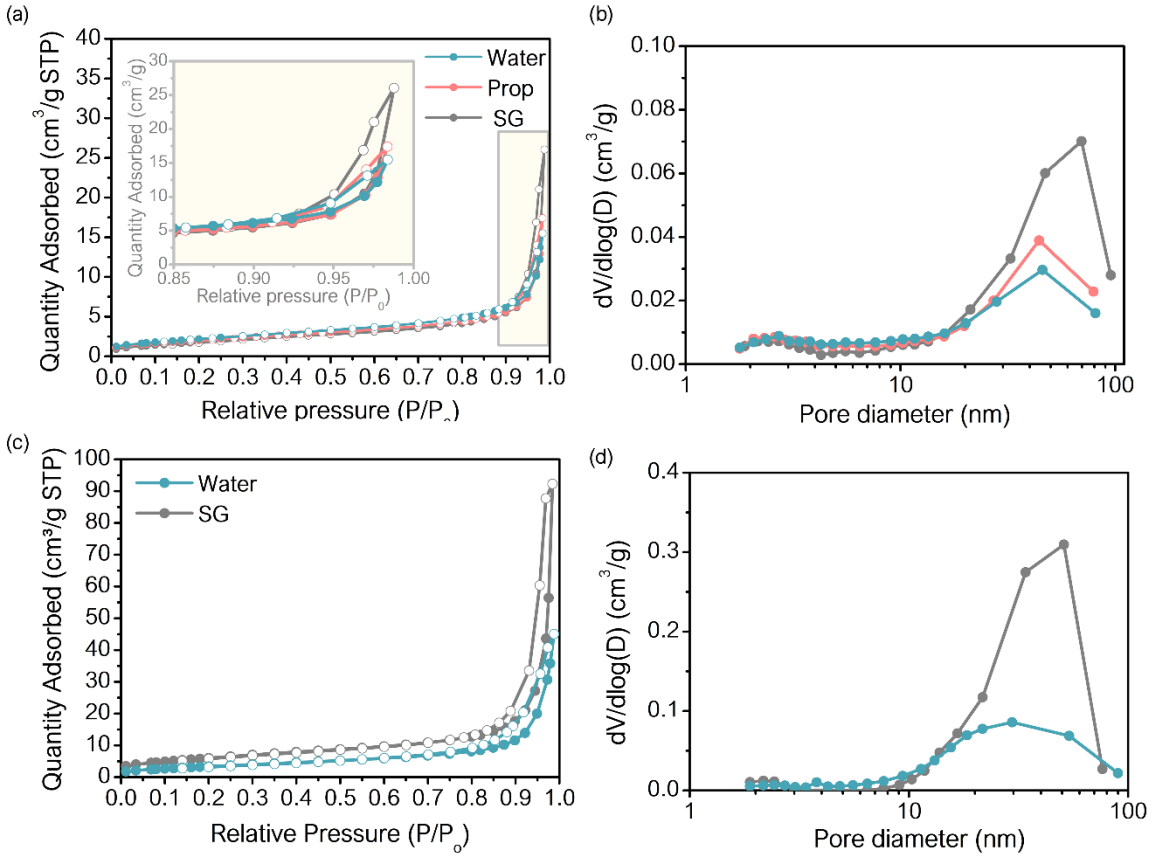

Figure 4.5 Adsorption-desorption isotherm and pore sized distribution according to the BHJ method of selected support obtained by gel (SG) and solution (prop or water) calcination: (a-b) LSCF and (c-d) CY supports

	SSA ($m^2 \cdot g^{-1}$)	V_{pore} ($cm^3 \cdot g^{-1}$)	$d_{support}$ (nm)	$a_{support}$ (Å)	Support reducibility (%)
SG – LSCF	9	0.04	17	3.872	29
prop – LSCF	8	0.03	17	3.858	29
water – LSCF	8	0.02	18	3.840	31
SG – CY	22	0.14	21	5.387	13
water – CY	13	0.07	18	5.377	14

Table 4.5. Textural and structural properties of the LSCF and CY supports from gel (SG) and solutions (prop or water).

The diffractogram of the different supports obtained from gel (SG) or solution (prop and water) are plotted in ***Figure 4.6.*** Additionally, the crystalline particle size of the supports ($d_{support}$) determined by Scherrer equation, as well as support lattice parameter ($a_{support}$), assuming a cubic structure (as described in *Annex*), are listed in ***Table 4.5***.

The same crystalline phases are predominant for the SG- and prop- or water-supports, for both LSCF (***Figure 4.6 (a)***) and CY mixed oxides (***Figure 4.6 (b)***). Besides that,

some additional crystalline phases, less intense, can be also observed in the diffractograms of the supports prepared from the solutions. Regarding LSCF supports, the perovskite structure with orthorhombic symmetry ($La_{0.7}Sr_{0.3}Fe_{0.7}Co_{0.3}O_{3-\delta}$, JPCD 01-089-1268) is still formed from the solutions obtained by dissolution of the gel, being the main crystalline structure (***Figure 4.6 (a)***). Additionally, less intense reflected peaks, associated to lanthanum oxide (La_2O_3, JPCD 01-083-1344), are detected for the prop- and water-LSCF supports. Other perovskite phase(s) with hexagonal symmetry ($La_{0.85}Sr_{0.15}CoO_{3-\delta}$, JPCD 01-153-3518) can be also discerned for prop- and water-LSCF supports (***Figure 4.6 (a), inset***). Moreover, a shift to higher diffraction angle as well as a lower support lattice parameter (***Table 4.5***) is clearly noticeable for the diffraction peaks of prop- and water-LSCF compared to SG-LSCF support. This is consistent with the decrease of La and Sr content in these supports as result of the second perovskite structure formed. Similar to LSCF supports, an additional crystalline phase less intense associated to yttrium oxide (Y_2O_3, JPCD 00-043-0661) is detected for water-CY, besides the main cubic fluorite phase ($Ce_2Y_2O_7$, JPCD 00-009-0286) (***Figure 4.6 (b)***). A shift in the diffractogram peaks along with a decrease in the lattice parameter (***Table 4.5***) are again noticeable for water-CY compared to SG-CY, probably caused by the no complete insertion of yttrium cations into the mixed oxide structure (***Figure 4.6 (b), inset***). Thereby, the formation of these secondary crystalline phases in both supports could suggest a possible hydrolysis of the oligomers forming the gel, due to the dissolution step. Similar support particle sizes are displayed for both supports, LSCF (17 – 18 nm) and CY (18 – 21 nm).

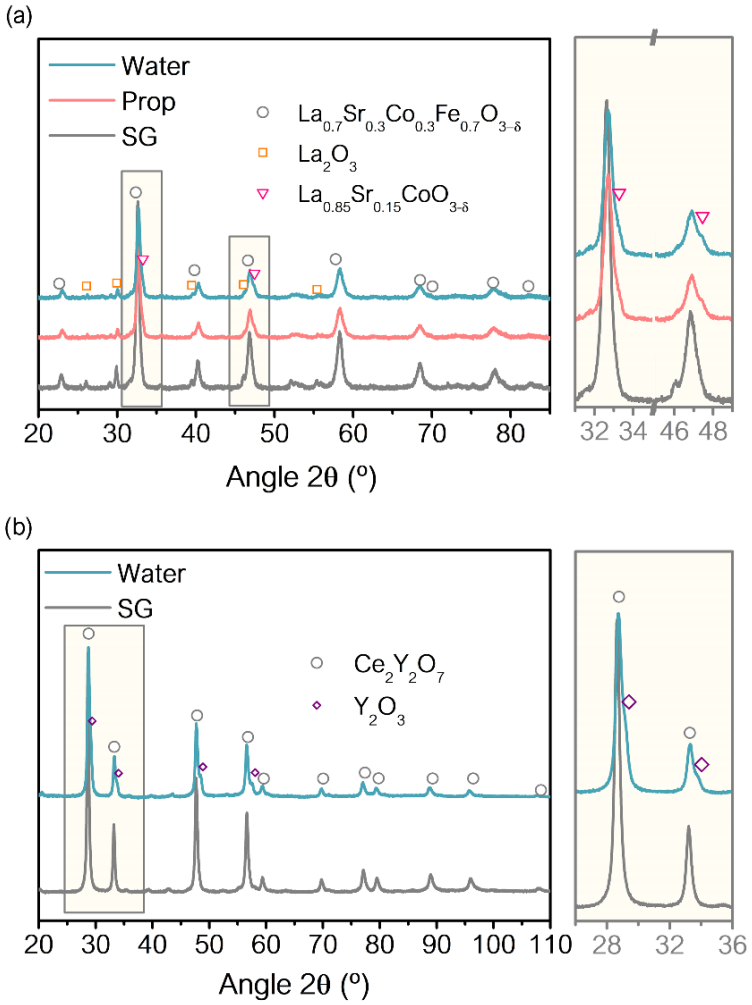

Figure 4.6. Diffractograms of selected support obtained by gel (SG) and solution (prop or water) calcination: (a) LSCF- and (b) CY supports

The H_2-TPR profiles of the different supports are presented in ***Figure 4.7.*** A slight modification of the H_2-TPR profile due to the dissolution step is revealed within the LSCF-based supports (***Figure 4.7 (a)***). Two reduction regions are clearly distinguished for all supports. As it has already discussed in *Chapter 2,* the first region at temperatures below 500 ºC (*region I*) is mainly associated to the reduction process of Co^{3+} cations, whereas the region at high temperature, above 500 ºC, (*region II*) is linked to the reduction of Fe^{3+} species [183]. Regarding the shape of the former region (*region* I), some additional reduction peaks appear for prop-LSCF and water-LSCF supports. The presence of another perovskite structure ($La_{0.85}Sr_{0.15}CoO_{3-\delta}$) detected by XRD for prop-LSCF and water-LSCF supports (***Figure 4.7 (a), inset***) could explain these additional reduction peaks. Regarding the high temperature region (*region II*), in contrast with SG-LSCF, two reduction peaks are discerned for the prop-LSCF and water-LSCF supports around 600 and 875 ºC for prop-LSCF and around 850 and 950 ºC for water-LSCF. These peaks might be associated to the

reduction of $Fe^{4+/3+}$ cations into $Fe^{3+/2+}$ species [289]. However, due to the complexity of the reduction process of this type of materials, it is rather complicated to well denote the different reduction processes that may occur. Relating to CY supports, same H_2-TPR profile is found for both SG-CY and water-CY supports (***Figure 4.7 (b)***). A single reduction peak, located at slightly higher temperature for water-CY (625 ºC) than for SG-CY (606 ºC), ascribed to the reduction of Ce^{4+} to Ce^{3+} species from the bulk, is exposed [167]. This shift to high temperature could be caused by the no complete insertion of Y^{3+} species into the CY structure for this support, as it has been shown by XRD (***Figure 4.6 (b), insert***).

The support reducibility was estimated (***Table 4.5***) considering the same assumptions than those already described in *Chapter 2.* Values of support reducibility of 29-31% and 13-14% are attained for LSCF- and CY-based supports, respectively, with no influence of the dissolution of the gel.

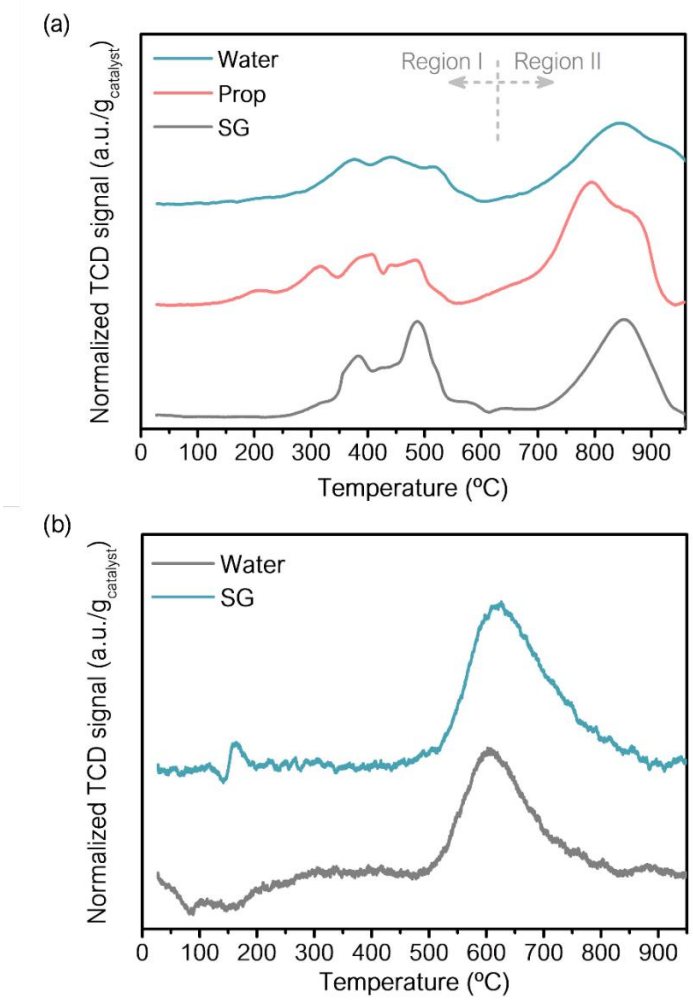

Figure 4.7. H_2-TPR profile of selected supports obtained by gel (SG) and solution (prop or water) calcination: (a) LSCF- and (b) CY supports

4.5. Optimization of catalytic structuration

4.5.1. β-SiC oxidation

In order to reach the aimed amount of deposited catalyst, the extrudates should undergo successive impregnation followed by calcination process at high temperature (800 ºC, ***Scheme 4.1***). As presented in ***Figure 4.4.***, β-SiC-based extrudates are susceptible to be oxidized at temperatures above 550-600 ºC. Thus, the mass uptake due to β-SiC oxidation must be considered in order to well follow the amount of deposited catalyst during the β-SiC coating procedure. Accordingly, the mass uptake ($g/L_{extrudate}$) through successive calcination steps under air is shown in ***Figure 4.8.*** for the three different shapes, using the temperature program described in experimental section for the support's deposition. Since the β-SiC oxidation seems to be non-uniform (see ***Figure 4.4***), a batch of 20 extrudates was used for this study, in order to determine an average oxidation degree of the β-SiC extrudates. As it can be seen in ***Figure 4.8***, the mass uptake rises with the number of calcination steps, attaining a final mass uptake after four calcination steps of 39 $g/L_{extrudate}$ for PSiC, of 29 $g/L_{extrudate}$ for RSiC 5/3 and of 24 $g/L_{extrudate}$ for RSiC 8/5. These mass uptakes are mainly due to the first calcination and increase slowly for the following calcination steps. Among the different β-SiC extrudates shapes, similar oxidation behaviour is followed for RSiC 5/3 and RSiC 8/5 whereas PSiC suffers higher oxidation degree. These differences on β-SiC oxidation could be related to different factors such as the impurity levels of each sample [290].

SEM micrographs of the fresh and calcined β-SiC- based extrudates are shown in ***Figure 4.9 (a)*** and ***(b)***, respectively. No huge modification of the particle morphology is discerned between the two extrudates. A typical morphology of well crystallized beta silicon carbide particles is observed [271]. A high amount of carbon nanofibers residues is visible at the surface of the calcined extrudate, caused by the synthesis process of the extrudates. No presence of SiO_2-SiO_xC_y layer at the surface due to calcination was detected. In order to further characterize the SiO_2-SiO_xC_y layer formed during the oxidation process, the use of other characterization techniques such as TEM or XPS would have been needed.

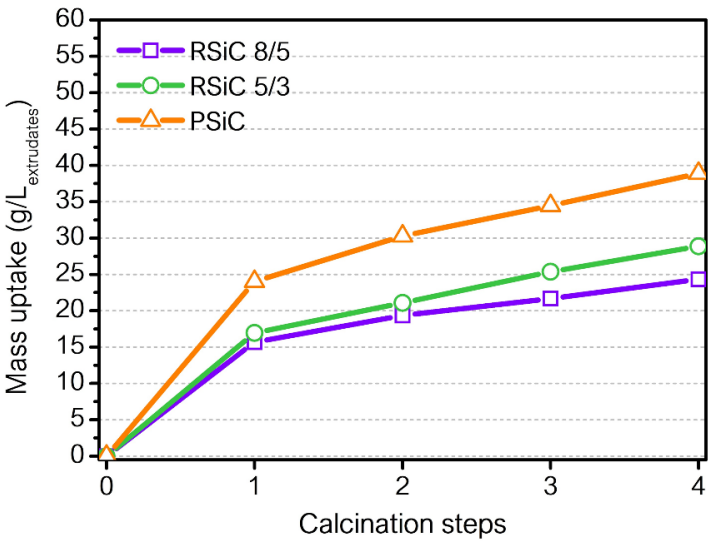

Figure 4.8. Mass uptake due to β-SiC oxidation through successive calcination steps at 800 ºC for 6 h (heating ramp of 2 ºC·min^{-1})

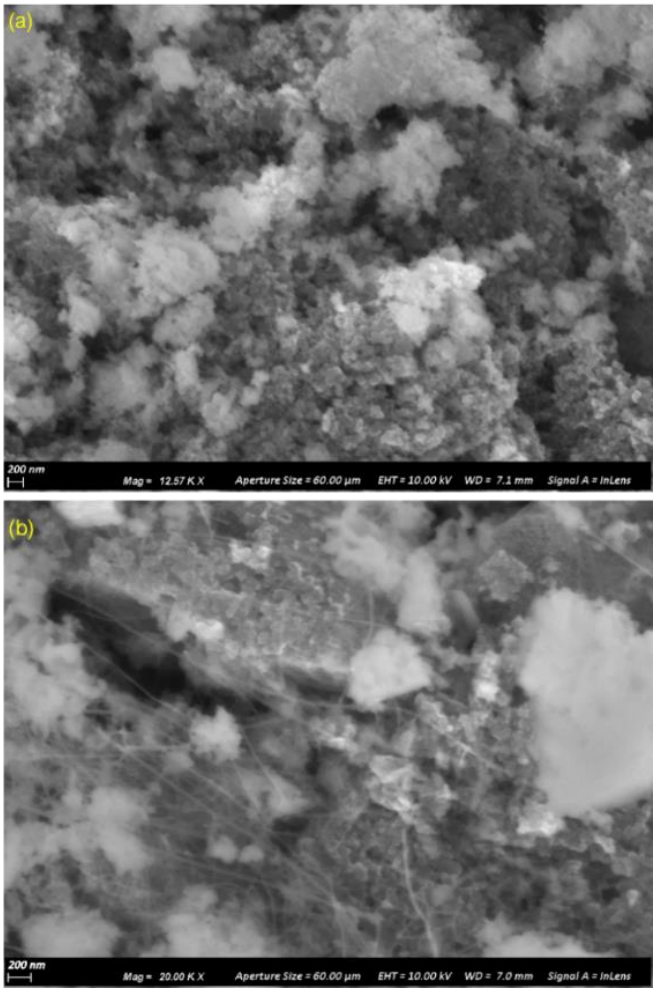

Figure 4.9. SEM images of (a) fresh and (b) calcined β-SiC extrudate (RSiC 8/5 shape)

The mass uptake due to the oxidation of the extrudates was subtracted from the total mass uptake measured after the coating steps to evaluate the mass uptake caused by the support deposition.

4.5.2. Extrudate shape

In order to evaluate the possible differences in the coating due to the shape of the β-SiC extrudates, the mass of LSCF and its anchoring at the surface were followed along consecutive coating steps for the three shapes. A LSCF precursor solution of concentration of 0.60 M in total cations in propionic acid was used. The coating procedure was carried out on individual extrudates (not by batch) and repeated for 10 to 20 extrudates. Average values are discussed in this section. The results can be seen in ***Figure 4.10***. The mass of LSCF deposited ($g/L_{extrudate}$) after successive coating steps as well as the target mass for the three extrudate shapes are shown in ***Figure 4.10 (a)***. A linear increase of mass of deposited LSCF is evidenced for all shapes after the first coating step (***Figure 4.10 (a)***). The mass of LSCF deposited per coating step is higher for the first coating and becomes stable with the following steps. Different behaviour is noticeable for the three shapes, the lowest amount of LSCF is achived for RSiC 5/3 shape, whereas PSiC displayed the highest amount of LSCF. After the first coating step, a mass uptake of 43, 35 and 62 $g/L_{extrudate}$ was found for RSiC 8/5, RSiC 5/3 and PSiC, respectively, whereas a constant mass uptake per step of 23 $g/L_{extrudate}$ for RSiC 8/5 and 16 $g/L_{extrudate}$ for RSiC 5/3 and 26 $g/L_{extrudate}$ for PSiC was obtained for the following coating steps.A differences in the air flow used during the removal of the impregnated solution could explain the different deposited mass attained for the shapes. Nevertheless, an explanation is difficult to be given as similar physicochemical properties were found for the three shapes. Two coating steps are needed to reach the target for RSiC (69 $g/L_{extrudate}$ for RSiC 8/5 and 53 $g/L_{extrudate}$ for RSiC 5/3), whereas only one step is enough to attain the target amount for PSiC (62 $g/L_{extrudate}$). The anchoring of the deposited LSCF at the surface was also evaluated after each coating steps for the three shapes. The mass uptake of LSCF (in $g/L_{extrudate}$) achieved before and after ultrasound (US) is displayed for the 1st and 4th coating steps in ***Figure 4.10 (b).*** In order to give an idea about the working mass precision, the raw mass of deposited LSCF before and after US is as well listed in ***Table 4.6*** for the three shapes after 1st and 4th coating steps, together with the average mass of individual fresh extrudates. Regardless the shape, the amount of LSCF remains after US test after one and four coating steps. This fact might suggest a strong anchoring for all samples. However, as it can be seen ***Table 4.6,*** the working mass range is

small (~0.1 mg and the detection of a possible loss of mass could be limited by the balance precision.

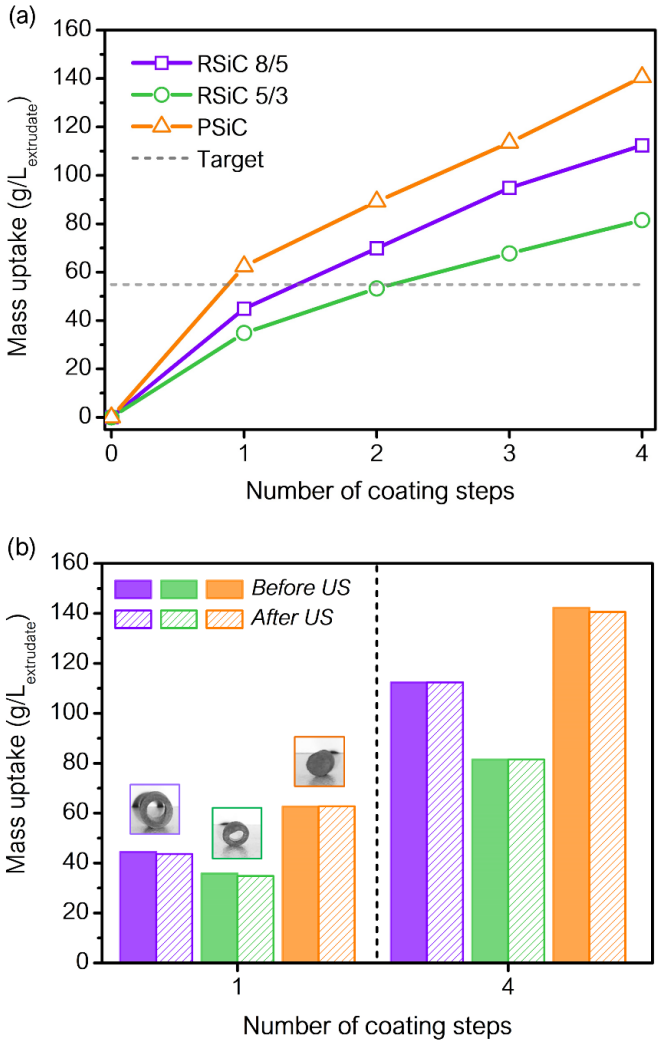

Figure 4.10. Influence of β-SiC based extrudate shapes on: (a) mass uptake of LSCFand (b) anchoring of the LSCF phase after successive coating steps

		1st coating step		4th coating step	
	Mass of individual extrudate (mg)	*Raw mass of deposited LSCF (mg)*			
		Before US	*After US*	*Before US*	*After US*
PSiC	98.2	7.3	7.2	18.3	18.0
RSiC 5/3	43.5	3.4	3.3	8.9	8.9
RSiC 8/5	159.0	14.2	13.5	38.8	38.4

Table 4.6. Comparison of raw mass of deposited LSCF before/after ultrasound (US) test for 1st and 4th coating steps

The modification of the textural properties after several coating steps was examined by N_2 physisorption, for RSiC 8/5. ***Figure 4.11*** exhibits the modification of the specific surface area (SSA) and of the pore volume (V_{pore}) after different coating steps. As expected, the variation of the mass of deposited LSCF (presented in ***Figure 4.10 (a)***) upon coating step is almost symmetric to the variation of both SSA and V_{pore}. They undergo a dramatic decrease after the first coating step and are less affected by the following steps. The highest porous availability prevailing in the fresh extrudate, leads to a higher amount of LSCF deposition during the 1st coating step. Consequently, after one coating step, the strong decrease observed for SSA and V_{pore} should be connected to the high mass of deposited LSCF and the β-SiC oxidation (***Figure 4.11***). This can also explain the lower mass of deposited LSCF found for the subsequent coatings, that might be caused by the loss of mesoporosity during the 1st coating step. Moreover, the quasi stable SSA and V_{pore} values shown for steps 2 to 4 suggest that the low amount of LSCF deposited in these steps could be related more to chemical interaction with the first LSCF layer formed than to physical steps of pore filling by the impregnation solution.

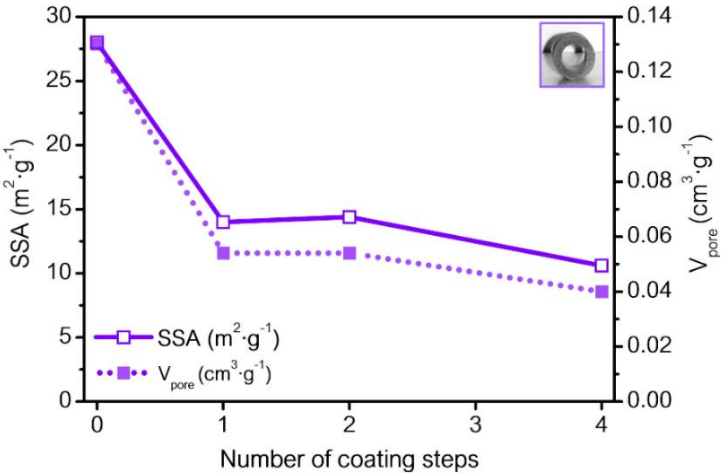

Figure 4.11. Variation of the SSA and V_{pore} upon coating steps for RSiC 8/5

In order to characterize the crystalline phase of the deposited LSCF mixed oxide, XRD analysis was conducted for RSiC 8/5. The diffractograms of RSiC 8/5 after one and four coating steps are presented in ***Figure 4.12.*** A main crystalline phase of face-centered cubic β-SiC (JPCD 00-101-0995) is detected in both extrudates. Some additional diffraction peaks of much less intensity ascribed to La_2O_3 phase (JPCD 01-083-1344) are noticeable after four coating steps. The presence of this phase as the most intense one instead of LSCF structure underlines the modification of the crystalline phase through the dissolution of the gel. As previously discussed, the dissolution of the gel could provoke the hydrolysis of the

mixed propionate formed during the pseudo sol-gel route and, thus, modify the crystalline structure of the deposited mixed oxide. No phase related to La_2O_3 was found after one coating step since the amount of LSCF deposited is under the detection limit of the apparatus.

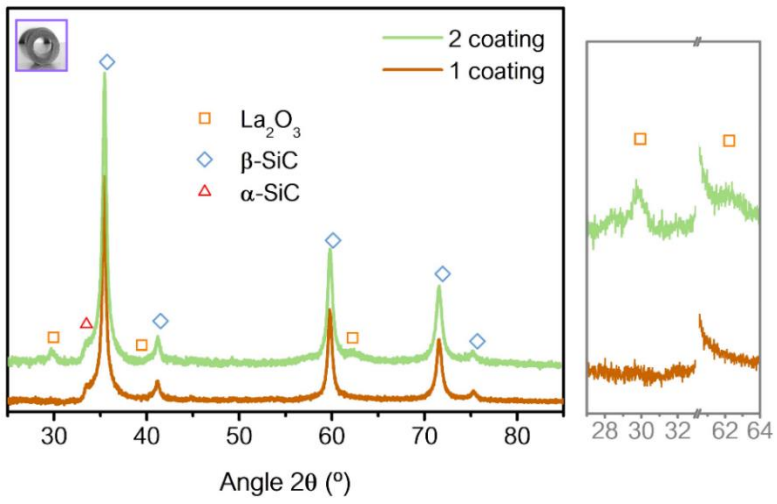

Figure 4.12. Diffractogram of RSiC 8/5 after one and four coating steps of LSCF

4.5.3. Support (LSCF) precursor solution concentration: 0.60 vs 0.30 M in total cations

As presented in the introduction, some researchers have studied the influence of the concentration of the precursor solution to well-optimized and control the catalytic structuration. In the present work, the influence of the support precursor solution concentration on the mass of deposited LSCF and the anchoring strength after consecutive coating steps were also investigated for the three extrudate shapes. Two LSCF precursor solutions of concentration 0.60 M and 0.30 M in total cations in propionic acid were used. The coating procedure was conducted individually for each extrudate shapes. The mass uptake of LSCF ($g/L_{extrudate}$) deposited after two coating steps by dipping in 0.60 and 0.30 M solutions are displayed in ***Figure 4.13*** for RSiC 8/5. As expected, the deposited mass observed for 0.30 M solution is lower. Once again, the deposited mass per step is higher after the first step. Afterwards, a mass uptake per step of 25 $g/L_{extrudate}$ for 0.60 M and 10 $g/L_{extrudate}$ for 0.30 M was observed, being proportional to the solution concentration. While the target is overpassed after the 2nd coating step through the 0.60 M solution, a mass of deposited LSCF lower that the target is obtained for the 0.30 M solution. Similar to the dipping in 0.60 M solution (see ***Figure 4.10 (b)***), no significative loss of mass was observed for extrudates dipped in 0.30 M solution after the ultrasound test, outstanding the strong

chemical anchoring. However, as the coating performance was individual, the no detection of this loss due to the small amount of LSCF deposited cannot be rejected. These anchoring results can be found at the end of this chapter in *Appendix (**Figure 4.33**)*, together with the corresponding coating performance of the other two β-SiC-based shapes (RSiC 5/3 and PSiC), for which the same study was conducted (***Figure 4.34***).

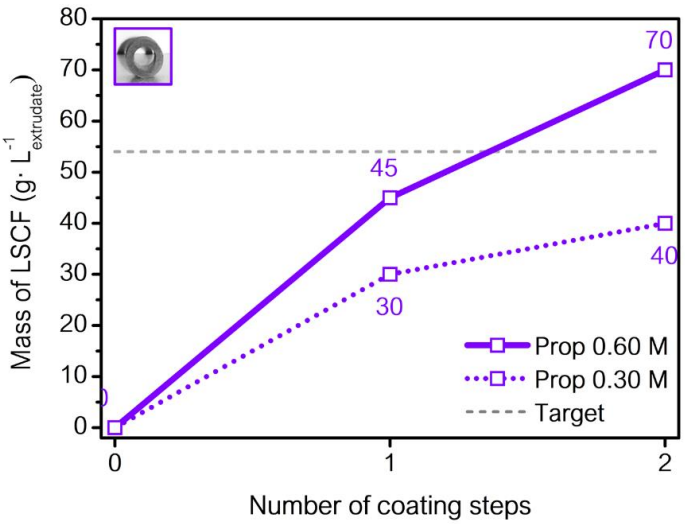

Figure 4.13. Effect of support precursor concentration (0.60 – 0.30 M) on the mass uptake of LSCF mixed oxide

The SEM images of coated extrudates using 0.60 and 0.30 M solutions are presented in ***Figure 4.14.*** All the images were conducted by using the chemical contrast mode. As it was also verified by EDX analysis, the clearer zones are ascribed to the deposited perovskite phase (LSCF) and the darker ones are mainly associated to SiC. ***Figure 4.14 (a)*** and ***(b)*** show the surface of coated SiC after the first coating using 0.60 M and 0.30 M, respectively. An agglomeration of LSCF can be clearly seen for both solutions concentrations, being larger for the concentrated solution (0.60 M). Thereby, the formation of segregated LSCF over the surface is accentuated for the concentrated solution. The presence of bare SiC after the first coating step with 0.30 M solution indicates that one step is not enough to reach the complete coverage of the surface. After the second coating (***Figure 4.14 (c)***), besides LSCF agglomeration, a LSCF phase highly dispersed is discerned in some zones (***Figure 4.14 (d)***). This disperse phase was not evidenced after the 1st coating step. Additionally, all elements of the LSCF phase (La, Sr, co and Fe) are detected by EDX analysis over the entire surface after the second coating step. Therefore, a good dispersion and large coverage of LSCF can be achieved by two coating steps with 0.30 M solution.

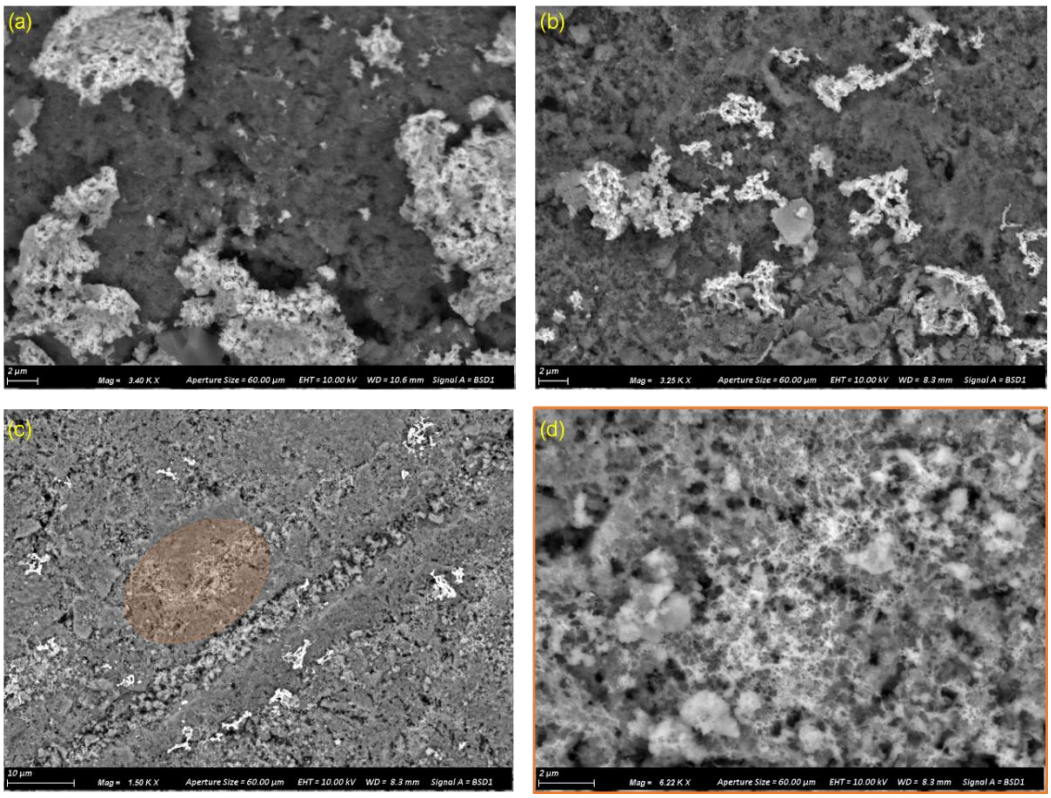

Figure 4.14. SEM images of β-SiC extrudates after (a) 1st coating - 0.60 M solution; (b) 1st coating - 0.30 M and (c-d) 2nd coating – 0.30 M

4.5.4. Scale up effect: individual vs batch

Up to now, all the results of coating presented were obtained from individual extrudate coating. As aforementioned, the small working mass (see ***Table 4.6***) could lead to big error in the measurement of the deposited mass.Thus, and as the main aim of this work is the preparation of batches at large scale to be tested in a pilot plant conditions, the coating of batches of about 20-30 extrudates was conducted and compared to the individual procedure. The corresponding results are shown in ***Figure 4.15***. *and* ***Table 4.7***. Similar mass uptakes after the first coating step are attained for both procedures, whereas a slightly high mass, closer to the target, is deposited after the second coating step for the batch procedure. This difference might come from the imprecisions on the mass measured in the individual procedure: order range ~0.1 -1.0 mg, compared to an order range ~10 – 100 mg for batch (***Table 4.6***). Thereby, the batch coating performance should decrease the error in the measurement and result in more accurate values. The anchoring strength was also evaluated for the batch procedure. The mass uptakes of LSCF before and after ultrasound (US) test are shown in ***Figure 4.15 (b)*** for the two consecutive coating steps. No significant loss of mass is observed after any coating step. Consequently, the formation of a strong chemical anchoring can be concluded with accuracy.

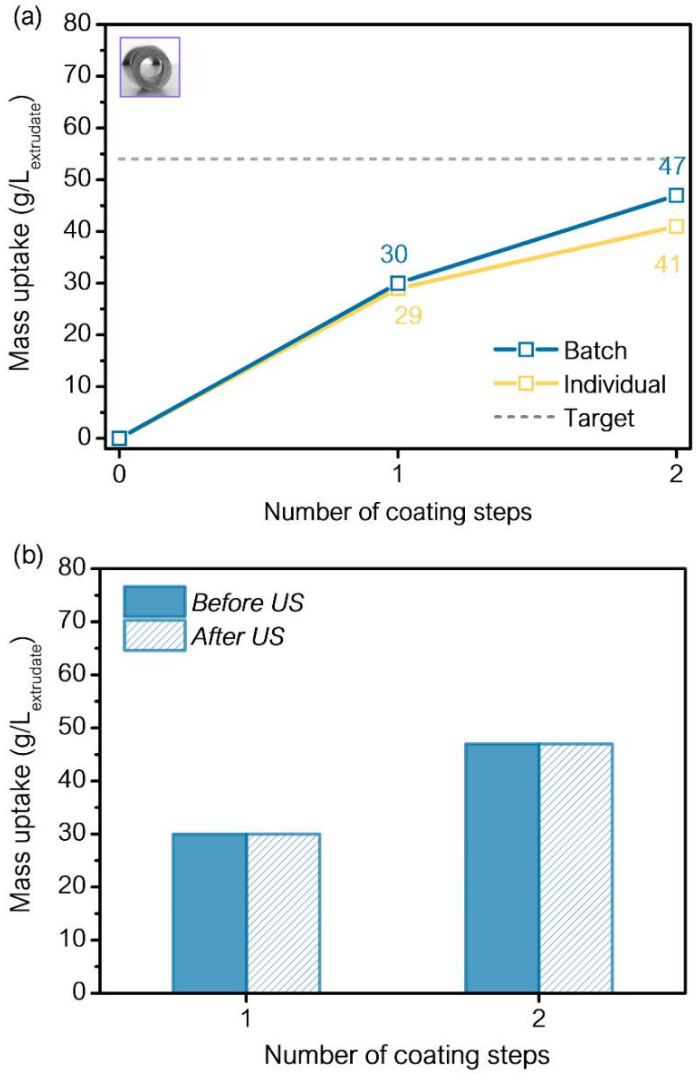

Figure 4.15. Effect of coating performance (individual – batch) on (a) the mass uptake of LSCF and (b) anchoring of the LSCF phase after successive coating steps

	Mass of extrudate (mg)		*Raw mass of deposited LSCF (mg)*			
			1st coating step		*2nd coating step*	
	Ind	*Batch*	*Ind*	*Batch*	*Ind*	*Batch*
PSiC	83.9	818.9	4.7	48.6	6.6	73.4
RSiC 5/3	43.6	429.6	3.0	33.0	5.9	49.6
RSiC 8/5	164.2	3093.8	9.8	183.3	13.6	291.2

Table 4.7. Individual and batch mass of fresh extrudates and deposited LSCF mixed oxide

4.5.5. Solvent: propionic acid vs water

In this work the solution of the gel using water as a neutral and non-toxic solvent was performed and its effect on the catalytic structuration was evaluated. A water-based precursor solution with a concentration of 0.62 M in total cations has been used. The mass

of deposited LSCF along two consecutive coating steps by dipping in water and propionic based precursor solutions are presented in ***Figure 4.16.*** for RSiC 8/5. Similar to propionic acid solution, a higher mass uptake per coating step is detected for water solution after first coating than after second one. The use of water-based solution evidenced a total deposited mass (60 g/$L_{extrudate}$) closer to the target (54 g/$L_{extrudate}$). Generally, the use of water solution led to slightly lower amount of deposited LSCF than that attained for propionic acid in both coating steps. This fact might be related to the high hydrophobicity displayed by fresh SiC based materials, as reported by Socha *et al*. [291]. Onve again, no loss of mass is observed after ultrasound test (data shown in *Appendix,* ***Figure 4.35***). Thus, water does not provoke meaningful modification of the anchoring strength of the deposited LSCF phase.

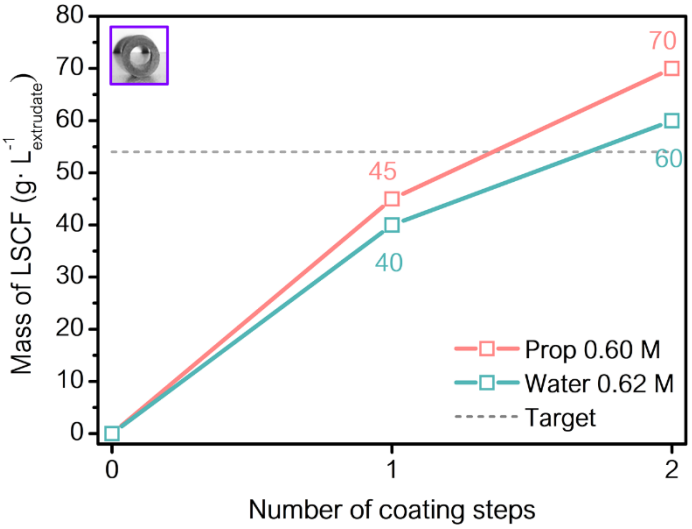

Figure 4.16. Effect of solvent (water – propionic acid) on the mass uptake of LSCF mixed oxide

4.5.6. Thermal pretreatment

As it has been reported in literature, a thermal pre-treatment of SiC-based extrudate lead to the growth of the SiO_2-SiO_xC_y layer that might promote the catalytic deposition. Additionally, Socha *et al.* [291] showed an enhancement in the hydrophilic character of SiC surface through oxidation process caused by the formation of SiO_2 at the surface, which is more hydrophilic than bare SiC. Accordingly, an effect of a thermal pre-treatment on the structuration of the catalytic support has been investigated for the three β-SiC shapes. Previously to the support coating, the β-SiC-based extrudes were calcined, once (1C-SiC) and twice (2C-SiC), at 800 ºC for 6 h under air atmosphere in order to form the SiO_2-SiO_xC_y surface layer. In order to determine the influence of the oxidized layer on the hydrophobic

character of SiC, the coating procedure were conducted by using a water-based solution of LSCF support with a concentration of 0.62 M.

The results of the mass uptake of LSCF after several coating steps over fresh and pre-treated β-SiC-based extrudates are shown in ***Figure 4.17.*** for RSiC 8/5 shape. A negative effect on the deposited amount of LSCF is evidenced owing to the thermal pre-treatment of the β-SiC-based extrudates. A decrease in the deposited mass of LSCF is clearly denoted for the pre-treated β-SiC-based extrudates after one coating step, reaching the lowest amount the pre-calcined SiC by twice. After second impregnation, the masses of LSCF measured are similar for fresh and 1C-SiC and slightly lower for 2C-SiC. Therefore, in line with Socha *et al.* [291] results, the formation of SiO_2-SiO_xC_y produced through this thermal pre-treatment hardly decreases the hydrophobic character of the SiC surface. They showed that a great SiO_2 content at the SiC surface, achieved under aggressive oxidation conditions (using H_2O_2), was required to improve the hidrophilicity of these materials. Hence, the decrease in mass of deposited LSCF for pre-treated β-SiC based extrudates might be mainly attributed to the loss of mesoporosity and SSA caused by sintering process during the thermal pre-treatment. Similar behaviour has been observed for the other two extrudate shapes (RSiC 5/3 and PSiC) and the corresponding results are shown in *Appendix* (*Figure 4.36*).

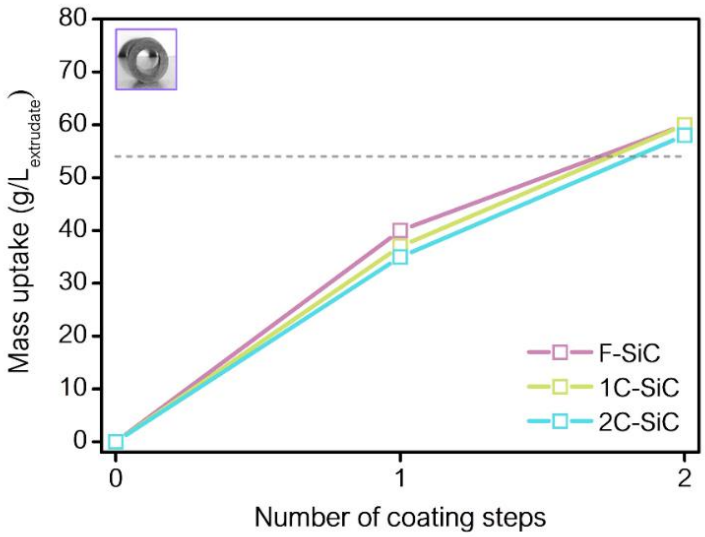

Figure 4.17. Effect of thermal pre-treatment on the mass uptake of LSCF mixed oxide after successive coating steps

4.5.7. $Ni(NO_3)_2$ solution concentration (0.13 - 0.26 M)

The influence of $Ni(NO_3)_2$ precursor solution concentration on the active phase impregnation was investigated on water-LSCF extrudates after two coatings. The impregnations of nickel were carried out by dipping batch of extrudates into $Ni(NO_3)_2$ solution of two different concentrations, 0.13 M ($Ni_{0.13}/LSCF_{water}$/RSiC 8/5)and 0.26 M ($Ni_{0.26}/LSCF_{water}$/RSiC 8/5). After each coating step the extrudates were calcined at 500 ºC. The mass uptake of NiO were followed and, then converted in mass uptake of Ni^0. The results of the deposited mass of nickel (Ni^0) are plotted in ***Figure 4.18*** for RSiC 8/5. Logically, a lower mass of Ni is deposited per coating step for a solution at 0.13 M. Per step, 1.6 $g/L_{extrudate}$ and 3.4 $g/L_{extrudate}$ were impregnated for 0.13 M and 0.26 M concentration, respectively. Thus, the deposited mass along the coating steps exhibits a linear tendency and is proportional to the precursor solution concentration. After three coating steps, a deposited mass (4.9 $g/L_{extrudate}$) lower than the target (6 $g/L_{extrudate}$) is obtained with a 0.13 M solution, while the target is slightly overpassed (6.8 $g/L_{extrudate}$) after two coating steps with a 0.26 M solution. Regardless the $Ni(NO_3)_2$ concentration, no mass loss is noticeable after the ultrasound test. Thus, a stable deposited Ni phase is obtained (***Figure 4.18. (b)***).

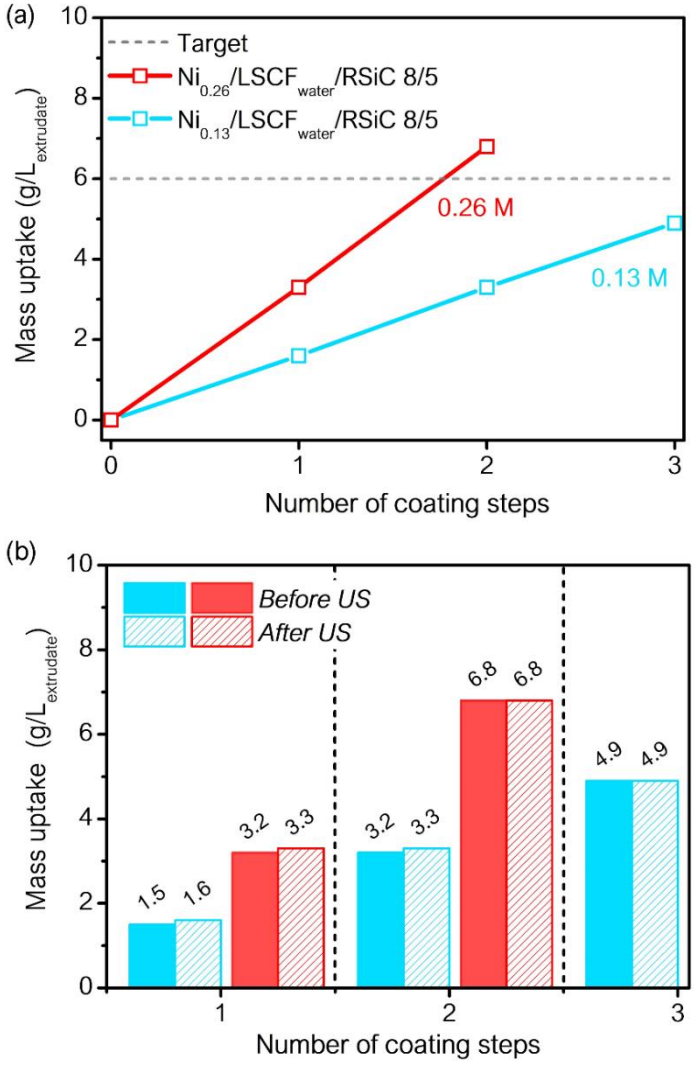

Figure 4.18. Effect of $Ni(NO_3)_2$ solution concentration (0.13 – 0.26 M) on (a) the mass uptake of Ni^0 and (b) the anchoring strength for $LSCF_{water}$/RSiC 8/5 after successive coating steps

XRD and H_2-TPD analysis were performed for $Ni_{0.13}/LSCF_{water}$/RSiC 8/5 and $Ni_{0.26}/LSCF_{water}$/RSiC 85. The diffractograms of both $Ni_{0.13}$- and $Ni_{0.26}/LSCF_{water}$/RSiC 8/5 are presented in ***Figure 4.19.*** A main crystalline phase related to SiC phase (JPCD 00-101-0995) is detected in both diffractograms. Moreover, less intense diffraction peaks at 2θ ~ 37º, 44º and 63º related to (111), (200) and (220) reticular planes of face-centered cubic structure of NiO (JCPDS 03-065-2901) are evidenced. This NiO phase is more intense for $Ni_{0.26}/LSCF_{water}$/RSiC 8/5 than for $Ni_{0.13}/LSCF_{water}$/RSiC 8/5, in accordance with the higher mass deposited. A small diffraction peak associated to La_2O_3 phase (JPC 01-083-1344) is as well appreciated (***Figure 4.19, inset***), being less intense for $Ni_{0.26}/LSCF_{water}$/RSiC 8/5. The NiO particle size has been roughly calculated by using

Scherrer equation for both structured catalysts based on the peak at the low intensity peak at 44° and are listed in ***Table 4.8.*** Due to the low intensity of NiO, the big error in the estimation of these values must be considered. Regardless the concentration solution, similar NiO particle size is displayed, around 21-23 nm.

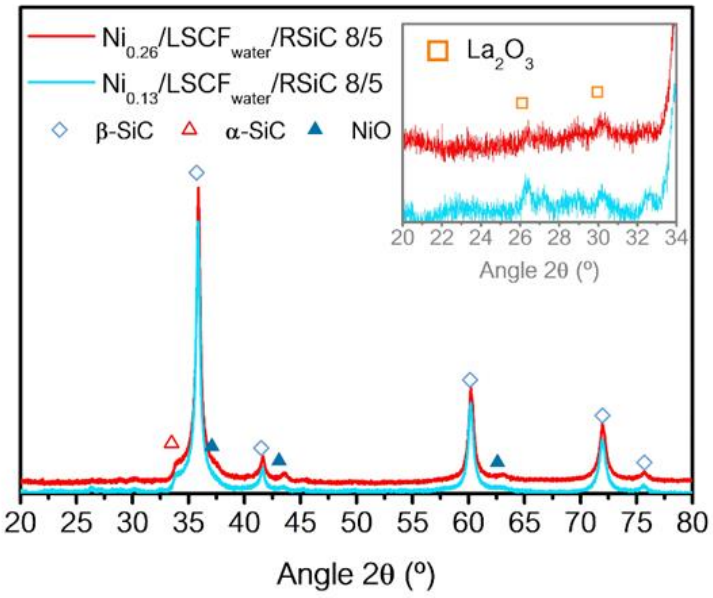

Figure 4.19. Diffractogram of $Ni_{0.13\text{-}0.26}/LSCF_{water}/RSiC$ 8/5 catalysts

	d_{NiO} (nm)	H_2 desorbed ($\mu mol \cdot g^{-1}$)	S_{Ni}^0 ($m^2 \cdot g^{-1}$)
$Ni_{0.13}/LSCF_{water}/RSiC$ 8/5	23	15	1.2
$Ni_{0.26}/LSCF_{water}/RSiC$ 8/5	21	14	1.1

Table 4.8. NiO particle size, H_2 desorbed and metallic Ni surface for $Ni_{0.13\text{-}0.26}/LSCF_{water}/RSiC$ 8/5 catalysts

The H_2-TPD analysis was performed by using the experimental conditions described in *Annex*. The H_2-TPD profiles of both structured catalysts are shown in ***Figure 4.20.*** Two main peaks, one at low temperature (160 ºC), ascribed to the desorption of chemisorbed H on the Ni/Co metal sites [292], and other at higher temperature (750 ºC) can be distinguished. The peak at high temperature might be related either to the desorption of chemisorbed hydrogen on Ni^0 species with strong Ni-LSCF-SiO_2-SiO_xC_y interaction or to hydrogen chemisorbed on Co partially reduced with strong Co-SiC interaction. No huge difference in the intensity of the low temperature peak is observed between the two structured catalysts, standing out that the $Ni(NO_3)_2$ concentration solution does not have

strong influence on the metallic surface. The quantity of desorbed H_2 related to the first peak is reported in ***Table 4.8.*** together with the corresponding metallic Ni surface areas, assuming that H_2 chemisorbed exclusively on Ni^0 species. Both structured catalysts show close metallic Ni surface area, which is consistent with the similar NiO crystallites sizes found by XRD as metal loading between both samples are comparable.

According to these results, no significative modifications were observed by the use of $Ni(NO_3)_2$ solution with different concentrations.

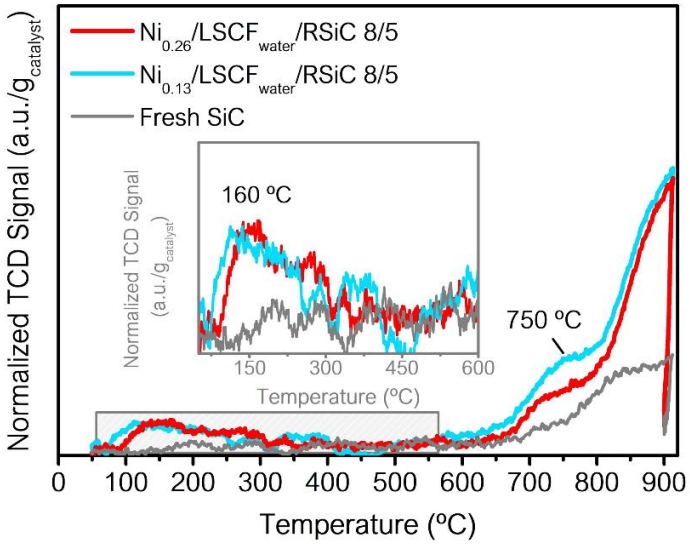

Figure 4.20. H_2-TPD profiles of $Ni_{0.13\text{-}0.26}/LSCF_{water}$/RSiC 8/5 catalysts

4.5.8. Catalytic support: CY mixed oxide

The deposition of CY mixed oxide over the three extrudates shapes has been performed to verify that the structuration follows the same tendency than that found for LSCF mixed oxide. A water-based precursor solution with a concentration of 0.60 M in total cations was used for the deposition of CY mixed oxide. The mass uptake of CY per successive coating steps is presented in ***Figure 4.21.*** No differences attributed to the shape of the extrudates can be noticeable. As presented for LSCF, the deposited mass per coating step is higher for the first coating than for the second one. After the second coating, the deposited mass achieved is still lower than the target for RSiC 8/5 and RSiC 5/3, whereas it is significantly higher for PSiC. Generally, a lower amount of CY is deposited compared to that attained for LSCF in the same conditions (water solution, 0.62 M; see ***Figure 4.16***). Concerning the anchoring strength of CY, no noteworthy loss of mass was detected after the ultrasound test.

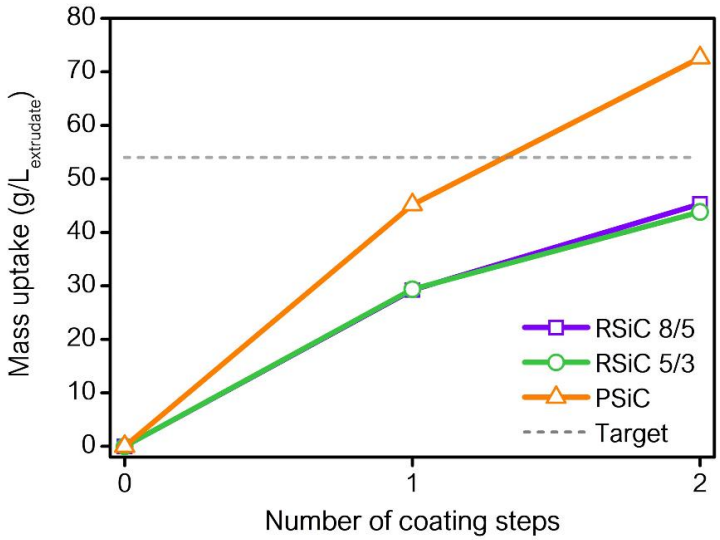

Figure 4.21. Effect of β-SiC extrudate shapes on the mass uptake of CY mixed oxide

4.6. Choice of parameters for catalytic structuration and list of structured catalyst prepared at small scale

Table 4.9 shows a summary of the different parameters that has been chosen in the present work to prepare the final structured catalysts. Regarding LSCF-based structured catalysts, the SEM images (***Figure 4.14***) show a better LSCF dispersion for the diluted propionic acid-based precursor solution (0.30 M) compared to the concentrated one (0.60 M). The use of water as a solvent led to a more accurate deposited mass (closer to the target) than the propionic acid-based solution (***Figure 4.16***). Accordingly, in order to evaluate the influence of solvent/concentration in tar removal efficiency, the diluted propionic acid (0.30 M) and the concentrated water-based (0.62 M) precursor solution has been used for the preparation and characterization of the final structured catalysts. Eventually, the addition of Ru to Ni/LSCF-based structured catalyst was also carried out over the structured catalyst, obtained by dipping batch of extrudate into water-based precursor solution (Ni/$LSCF_{water}$/RSiC 8/5). Concerning the CY-based structured catalysts, a water-based precursor solution with a concentration of 0.60 M in total cation was used for the deposition of the catalytic support for all β-SiCextrudate shapes.

As previously presented, two coating steps are needed to attain the aimed amount of deposited support in most of the cases. Additionally, no enhancement in the deposited mass by the thermal pre-treatment has been detected (see ***Figure 4.17***). Thereby, in the present work, the coating of the catalytic supports (LSCF and CY) were always conducted by performing two successive coating steps over fresh β-SiC-based extrudates. The impregnation of active phase (Ni) were carried out using the $Ni(NO_3)_2$ solution with a

concentration of 0.26 M in all cases. At small scale, all coating steps were performed using batches of 20-30 extrudates.

	Solvent	Precursor concentration ($M_{total\ cations}$)	*[$Ni(NO_3)_2$] (M)*	*Nomenclature*
LSCF/PSiC	prop	0.30	0.26	$Ni/LSCF_{prop}/PSiC$
LSCF/RSiC 5/3	prop	0.30	0.26	$Ni/LSCF_{prop}/RSiC\ 5/3$
LSCF/RSiC 8/5	prop	0.30	0.26	$Ni/LSCF_{prop}/RSiC\ 8/5$
LSCF/RSiC 8/5	water	0.62	0.26	$Ni/LSCF_{water}/RSiC\ 8/5$
LSCF/RSiC 8/5	water	0.62	0.26	*$RuNi/LSCF_{water}/RSiC\ 8/5$*
CY/PSiC	water	0.60	0.26	Ni/CY/PSiC
CY/RSiC 5/3				Ni/CY/RSiC 5/3
CY/RSiC 8/5				Ni/CY/RSiC 8/5

Table 4.9. Summary of the chosen parameters for the catalytic structuration at small scale

The final composition of the structured catalysts prepared at small scale is given in *Table 4.10.* Globally, the deposition results are consistent with what obtained from the optimization study.

	$m_{support}/V_{ext}$ ($g/L_{extrudate}$)	$m_{Ni}{}^0/V_{ext}$ ($g/L_{extrudate}$)	$m_{Ni/Ru}{}^0/m_{cat}$ (%)
Target	54	6	10
$Ni/LSCF_{prop}/PSiC$	72	9.5	12
$Ni/LSCF_{prop}/RSiC\ 5/3$	56	7.5	12
$Ni/LSCF_{prop}/RSiC\ 8/5$	47	7.2	13
$Ni_{0.26}/LSCF_{water}/RSiC\ 8/5$	78	6.7	8
$Ru\text{-}Ni_{0.26}/LSCF_{water}/RSiC\ 8/5$	68	4.0 (Ni^0) 0.5 (Ru^0)	5 (Ni^0) 0.7(Ru^0)
$Ni/CY_{water}/PSiC$	71	6.5	8
$Ni/CY_{water}/RSiC\ 5/3$	43	7.0	13
$Ni/CY_{water}/RSiC\ 8/5$	45	7.7	15

Table 4.10. Final composition of the different batches obtained at small scale using the chosen parameters

4.7. Characterization of structured catalysts

The influence of the solvent (prop- or water) and concentration (0.30-0.60 M) of the LSCF-precursor solution as well as the effect of $Ni(NO_3)_2$ solution concentration (0.13-0.26 M) on the the Ni-support-substrate interaction and catalytic support reducibility

were studied by H_2-TPR analysis of the LSCF-based structured catalysts. As well, the effect of the catalytic support and the shape of SiC extrudates on the reducibility properties were investigated for CY-based structured catalysts.

The corresponding H_2-TPR profiles for the bare catalytic support deposited over RSiC 8/5 (LSCF/RSiC 8/5 and CY/RSiC 8/5) and the (Ru-)Ni containing structured catalysts ((Ru-)Ni/$LSCF_{prop-water}$/SiC and Ni/CY_{water}/SiC) are plotted in ***Figure 4.22 and 4.23,*** respectively. In order to identify the possible existence of Ni species in closer contact with SiC surface, a H_2-TPR of Ni over bare SiC (Ni/SiC), without deposited catalytic support (LSCF or CY), was also performed. As well, the catalytic support reducibilities of the bare support and Ni-containing structured catalysts are listed in ***Table 4.11*** and ***Table 4.12***, respectively. These support reducibilities were estimated considering the assumptions reported in *Annex* and β-SiC as no reducible phase. Then, the H_2 consumption was associated to the reducible species present in the deposited catalyst (active phase + catalytic support).

Regarding the bare LSCF deposited on RSiC 8/5 ($LSCF_{prop-water}$/RSiC 8/5), differences in the shape of reduction profile and the H_2-consumption are noticeable compared to the powdered supports (***Figure 4.22 (a)***). However, similarly to the powders, two reduction regions can be distinguished for the $LSCF_{prop-water}$/RSiC materials. These regions are shifted to higher temperature than the corresponding powdered LSCF owing to the strong LSCF-SiC interaction accomplished after the LSCF deposition. In line with the LSCF powder results, a H_2-TPR profile located at higher temperature is as well achieved by the use of water than propionic acid as solvent for $LSCF_{prop-water}$/RSiC 8/5 materials. The first zone is located at 400 - 700 ºC temperature range, centered at 550 ºC for $LSCF_{prop}$/RSiC 8/5 and 620 ºC for $LSCF_{water}$/RSiC 8/5, whereas the second zone consists in a main reduction peak at temperature of 830ºC for both $LSCF_{prop-water}$/RSiC 8/5.. A reduction peak around 620 ºC ascribed to Co species that strongly interact with SiC to form cobalt silicate has been reported by Díaz *et al.* for a series of catalysts based on Co/modified β-SiC-based extrudates [272]. Thereby, the peak located at low temperature in LSCF/RSiC 8/5 could be attributed to the reduction of Co silicate formed during the coating procedure. The simpler reduction profile of this first region observed for $LSCF_{prop-water}$/RSiC 8/5 materials compared to the powder supports might be a consequence of a modification in the LSCF phase caused by its deposition on SiCThis fact could be in concordance with the XRD results shown in ***Figure 4.12***. Additionally, the H_2 consumption, reported in ***Table 4.11***, is around three time lower for the $LSCF_{prop-water}$/RSiC 8/5 (1.4 $mmol \cdot g^{-1}$) than for the powders (4.2-4.4 $mmol \cdot g^{-1}$).

This decrease could be caused by: (i) a reduction less favoured due to the strong LSCF-SiC interaction and/or (ii) the structuration process which leads to the formation of different crystalline phases which display lower reducibility than the LSCF one. As expected, the support reducibility decreases from 29-31% for prop-LSCF and water-LSCF powders to 10% for both $LSCF_{prop\text{-}water}$/RSiC 8/5 materials. Briefly, the use of water as solvent result in a reduction profile moved to high temperature, whereas same support reducibility is evidenced for both, regardless the solvent/concentration. A slightly different reduction profile is exhibited for bare CY_{water}/RSiC 8/5 material compared to the equivalent powdered CY oxide (***Figure 4.22 (b)***). Mainly, two reduction peaks placed at 690 and 800ºC along with a small shoulder at low temperature (~500 ºC) can be discerned for CY_{water}/RSiC 8/5 material, while a reduction profile centered at 615 ºC is showed for powdered CY oxide. These additional peaks found for CY_{water}/RSiC 8/5 suggests the formation of two different phases as consequence of the CY deposition. The reduction peak placed at 690 ºC could be associated to the reduction of Ce^{4+} to Ce^{3+} species associated to the $Ce_2Y_2O_7$ phase. As consequences of the strong CY-SiC interaction, this peak is shifted to higher temperature compared to that found in powdered CY oxide (615 ºC). Besides, the peak located at the highest temperature (800 ºC) and the small shoulder at lowest one (500 ºC) are close to reduction temperatures ascribed in literature to the surface (510 ºC) and bulk reduction (850 ºC) of pure CeO_2 phase [293]. Therefore, and as expected from the XRD of water-CY in powder (***Figure 4.6 (b)***), a mixture of single (CeO_2-Y_2O_3) and mixed oxide ($Ce_2Y_2O_7$) are generated during the coating procedure for CY/RSiC 8/5 materials. In addition, the support reducibility increases from 14% to 89% for CY_{water}/RSiC 8/5 caused by the no complete insertion of Y^{3+} species into CeO_2 (***Table 4.11***).

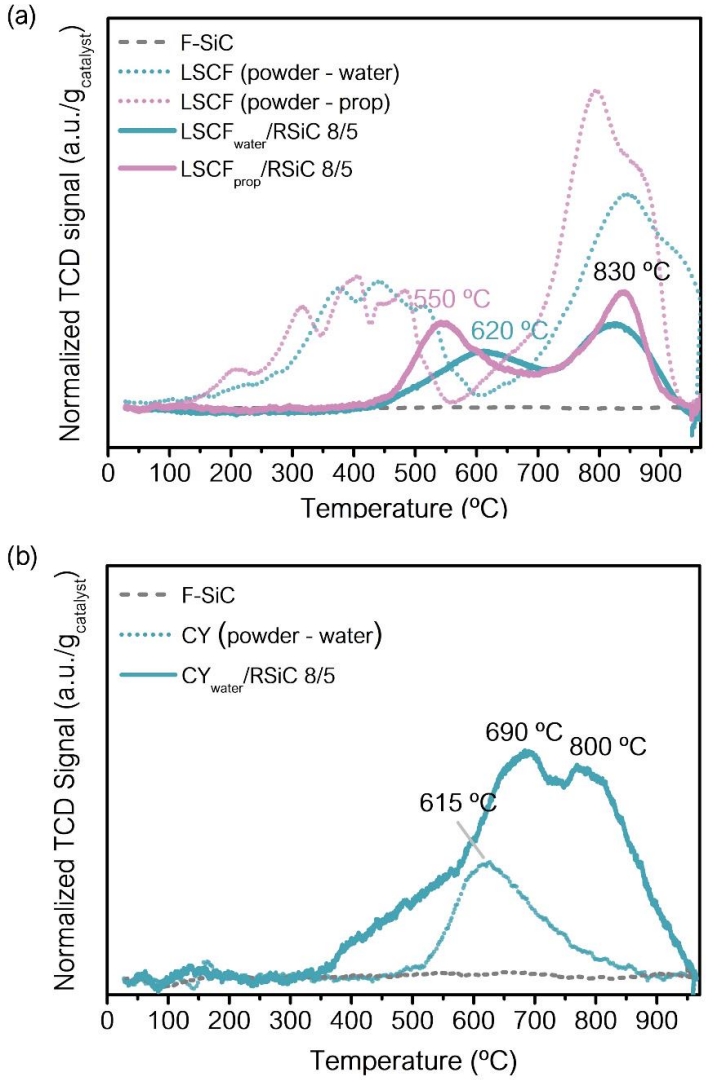

Figure 4.22. H_2-TPR profile of (a) bare LSCF and (b) CY deposited on RSiC 8/5 ($LSCF_{prop-water}$/RSiC 8/5 and CY/RSiC 8/5)

	H_2 consumption (mmol·g^{-1})	Reducibility (%)
Prop -LSCF (powder)	4.2	29
Water-LSCF (powder)	4.4	31
$LSCF_{prop}$/RSiC 8/5	1.4	10
$LSCF_{water}$/RSiC 8/5	1.4	10
Water-CY (powder)	0.2	14
CY/RSiC 8/5	1.5	86

Table 4.11. H_2 consumption and catalytic support reducibility of the catalytic supports deposited over RSiC 8/5

Additionally, the H_2-TPR profiles of the prepared (Ru-)Ni-containing structured catalysts ((Ru-)Ni/$LSCF_{prop-water}$/RSiC 8/5) along with Ni/SiC and $LSCF_{water}$/RSiC 8/5 profiles

are shown in ***Figure 4.23 (a)*** for RSiC 8/5 shape. Three different reduction peaks located at temperatures ~480 ºC, 620 ºC and > 700 ºC can be noticed for Ni/SiC catalyst. The reduction peaks at lowest temperature has been widely linked to the reduction of free NiO species [292–296], whereas the two reduction peaks at higher temperature are controversial. Clause *et al.* [297] also observed two reduction peaks at 620 and 820 ºC for a Ni/SiO_2 catalysts and they were associated to the thermal decomposition products of layered Ni(II) silicates. Similar reduction temperatures (~400 ºC, ~560 ºC and >700 ºC) were observed by He *et al.* [294] in a series of Ni/SiO_2 catalysts with different Ni loading. They attributed the peak located at 400 and 560 ºC to the reduction of NiO to Ni^0 species with negligible interaction and strong interaction with the support, respectively. Meanwhile, the peak at temperature above 700 ºC was ascribed to the reduction of nickel silicates. These peak at highest (>700 ºC) temperature has been also labelled to nickel silicate reduction by other work [295]. Accordingly, the reduction peak observed at 620 ºC might be associated to the reduction of NiO species with strong NiO-SiO_xC_y-SiC interaction and the peak at highest temperature to the reduction of nickel silicates. A simple scheme in order to clarify the H_2-TPR result for Ni/SiC is shown in ***Scheme 4.2. (a)***. As expected, two reduction regions are also found for the Ni-containing structured catalysts. In the first region (300-700ºC), two new reduction peaks at 410 and 500 ºC caused by the addition of Ni can be appreciated in comparison with the bare LSCF/RSiC materials. Besides that, the reduction profile shape in this region seems similar to that exhibited for Ni/SiC. Consequently, these peaks located at 410 and 500 ºC could be related to the reduction of NiO species with weak and strong interaction with SiO_xC_y-SiC substrate. Generally, a shift to lower reduction temperature compared to Ni/SiC due to the coverage of SiC surface with the catalytic support (LSCF) is noteworthy. This fact suggests that previous deposition of LSCF support on SiC may avoid the closer interaction NiO-SiO_xC_y-SiC by formation of NiO-LSCF-SiO_xC_y-SiC and facilitate the reduction of these species (***Scheme 4.2 (b)***). One reduction peak at 830 ºC is observed in the second reduction region and it could be mainly ascribed to the reduction of Fe species. However, even if the formation of nickel silicates might be limited by the deposited LSCF, the presence of these species in small amount cannot be completely rejected. Similarly, a move to higher temperature is attained, associated with larger H_2 consumption, for $Ni/LSCF_{water}$/RSiC 8/5 than for $Ni/LSCF_{prop}$/RSiC 8/5 due to the use of water as solvent. Moreover, similar profile is achieved for RuNi/LSCFwater/RSiC 8/5 compared to $Ni/LSCF_{water}$/RSiC 8/5 with an additional reduction peak at low temperature (215 ºC) ascribed to the reduction of RuO_2 to Ru^0. Concerning CY-based structured catalysts, the H_2-TPR profiles of Ni containing structured

catalysts (Ni/CY/SiC) are presented in ***Figure 4.23 (b)*** for the three β-SiC-based extrudate shapes. The H_2-TPR profile of Ni/SiC and CY_{water}/RSiC 8/5 are also shown. Similar reduction profile shape than that observed for Ni/SiC sample with a first reduction region also present for LSCF-based structured catalysts (***Figure 4.23 (a)***) is accomplished for all Ni/CY/SiC catalysts. Thus, as prior mentioned, the peak at 410ºC is related to free NiO reduction, whereas the peak at 610 ºC is linked to the reduction of NiO species with strong NiO-SiO_2-SiO_xC_y interaction. The broader reduction peak located at temperature around 800 ºC is associated to the bulk reduction of CeO_2 species. It should be stressed that the peak associated to NiO reduction with strong NiO-SiO_2-SiO_xC_y interaction is located at higher temperature (610 ºC) for Ni/CY_{water}/RSiC 8/5 than the equivalent peak displayed for Ni/$LSCF_{water}$/RSiC 8/5 catalyst (500 ºC). This fact might be associated to the lower amount of CY support deposited compared to the LSCF one (see ***Table 4.10***), resulting in stronger NiO-SiO_2-SiO_xC_y interaction due to lower support coverage of the extrudate. Generally, no significant differences in the reduction profile are noticeable among the Ni/CY/SiC.

Regarding to the support reducibility (***Table 4.12***), the Ni/SiC displays a support reducibility higher than 100% caused by the hydrogen spillover effect from Ni metallic sites to the SiO_2-SiO_xC_y sites, according to Frey *et al.* [265]. No noticeable spillover effect is detected for the Ni/LSCF/RSiC 8/5 materials attained support reducibilities lower than 100%. This fact highlights once again that the presence of LSCF avoid the NiO-SiO_2-SiO_xC_y interaction, thus, inhibiting the spillover effect. Among the Ni containing materials, higher support reducibility is reached for Ni/$LSCF_{water}$/RSiC 8/5 (38%) than for Ni/$LSCF_{prop}$/RSiC 8/5 (20%). The addition of Ru does not enhance the support reducibility for RuNi/$LSCF_{water}$/RSiC 8/5 (40%). A support reducibility higher than 100% is attained for Ni/CY_{water}/PSiC and Ni/CY_{water}/RSiC 5/3 catalysts, indicating the possible spillover from metallic Ni sites to SiC in these structured catalysts. A support reducibility of 94% is evidenced for Ni/CY_{water}/RSiC 8/5.

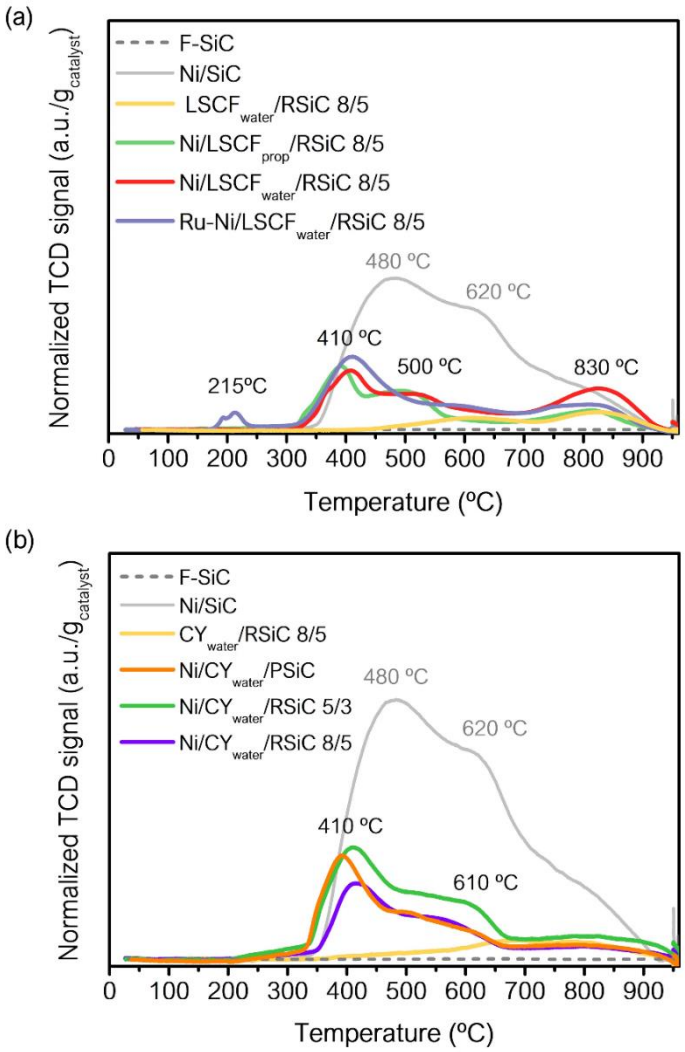

Figure 4.23. H_2-TPR profile of Ni-containing structured catalysts: (a) LSCF-based catalysts ((Ru-)Ni/$LSCF_{prop-water}$/RSiC 8/5) and (b) CY-based catalysts (Ni/CY_{water}/SiC)

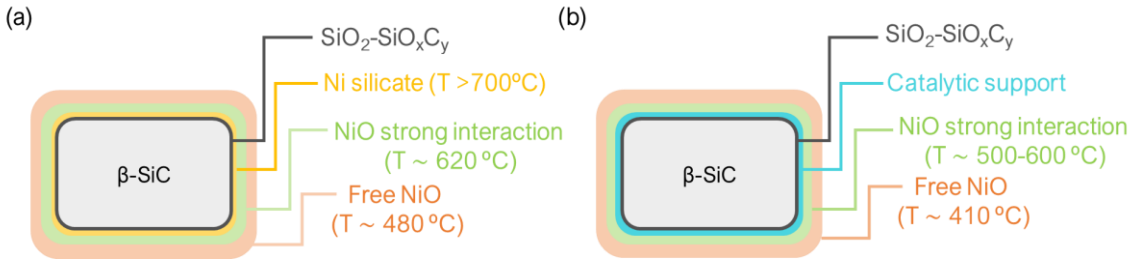

Scheme 4.2. Different NiO-β-SiC interaction generated (a) Ni deposited on bare β-SiC (Ni/SiC) and (b) Ni deposited on catalytic support (LSCF-CY)/β-SiC (adapted from ref. [294]).

	H_2 consumption (mmol·g^{-1})	Reducibility (%)
Ni/SiC	12.4	>> 100
$LSCF_{water}$/RSiC 8/5	1.4	10
$Ni/LSCF_{prop}$/RSiC 8/5	3.1	20
$Ni_{0.26}/LSCF_{water}$/RSiC 8/5	4.6	38
$Ru\text{-}Ni_{0.26}/LSCF_{water}$/RSiC 8/5	4.9	40
CY/RSiC 8/5	1.5	86
Ni/CY_{water}/PSiC	3.6	186
Ni/CY_{water}/RSiC 5/3	4.3	239
Ni/CY_{water}/RSiC 8/5	2.6	94

Table 4.12. H_2 consumption and catalytic support reducibility of the prepared structured catalysts

4.8. Catalytic tests: toluene reforming

4.8.1. Influence of studied parameters for the structuration and shape of β-SiC-based extrudates

In order to select the coating parameters and the type of extrudate for the subsequent catalytic scale-up, the effect of β-SiC-based shape on catalytic efficiency in toluene reforming has been investigated for the series of $Ni/LSCF_{prop}$/SiC and Ni/CY_{water}/SiC catalysts. As well, the catalytic activity of $Ni/LSCF_{water}$/RSiC 8/5 catalyst was also evaluated and compared to its equivalent $Ni/LSCF_{prop}$/RSiC 8/5 to elucidate the influence of the precursor solution solvent in the catalytic performance.

Similar to the powdered catalysts, the evolutions in the partial flows has been also followed during the pre-treatment under syngas atmosphere for the structured catalysts in order to verify that they are reducible under these stablished conditions.

4.8.1.1. Reduction pretreatment under syngas atmosphere

The evolutions in the partial flow of CO along the time during the pre-treatment conditions are presented in ***Figure 4.24.*** for both series, LSCF- and CY-based structured catalysts. The modifications of the other gas components were deeply discussed in *Chapter 3 for the catalysts in powder.* Among the LSCF-based structured catalysts, a noticeable decrease in the partial molar flow of CO at temperatures around 300 ºC for $Ni/LSCF_{prop}$/RSiC 8/5 and, 400 ºC for $Ni/LSCF_{prop}$/RSiC 5/3 and $Ni/LSCF_{prop}$/PSiC can be observed (***Figure 4.24 (a)***). The higher temperature displayed for $Ni/LSCF_{prop}$/RSiC 5/3 and $Ni/LSCF_{prop}$/PSiC than the $Ni/LSCF_{prop}$/RSiC 8/5 could be caused by differences in

NiO-LSCF-SiC interacions. Then, a stronger NiO-LSCF-SiC interaction might be expected for RSiC 5/3 and PSiC than for RSiC 8/5 shape. Decrease in the CO partial flow is also discerned for Ni/$LSCF_{water}$/RSiC 8/5 from temperature close than the equivalent Ni/$LSCF_{prop}$/RSiC 8/5, outstanding the no influence of the solvent in the reducibility of the catalysts under these conditions. As well, decrease in the CO partial molar flow along time are detected for the CY-based structured catalysts (***Figure 4.24 (b)***). These modifications from temperatures of 280, 320 and 395 ºC for Ni/CY_{water}/RSiC 5/3, Ni/CY_{water}/RSiC 8/5 and Ni/CY_{water}/PSiC, respectively, indicate, once again, the differences in Ni-CY-SiC interaction displayed for the different shapes. As it is noteworthy, different tendencies regarding the shape are found for CY-based materials compared to LSCF one. Whereas the RSiC 8/5 shape is easier to reduce among Ni/$LSCF_{prop}$/SiC catalysts, the RSiC 5/3 displayed the lower temperature among the Ni/CY_{water}/SiC catalysts. However, other factors as the use of different solvent or the influence of the catalytic support must be considered to explain the different tendencies found among CY- and LSCF-structured catalysts. Moreover, the variation of the CO partial flow becomes noticeable at slightly higher temperature for Ni/CY_{water}/RSiC 8/5 (320 ºC) than for Ni/$LSCF_{water}$/RSiC 8/5 (300 ºC). This fact is in accordance with the shift to higher temperature of the reduction peak associated to NiO species with stronger NiO-SiO_2-SiO_xC_y for Ni/CY_{water}/RSiC 8/5 compared to Ni/$LSCF_{water}$/RSiC 8/5, prior observed by H_2-TPR analysis.

Generally, these modifications in the CO partial flow highlights that the reduction of NiO to Ni^0 are successful under these conditions for both LSCF- and CY- structured catalysts.

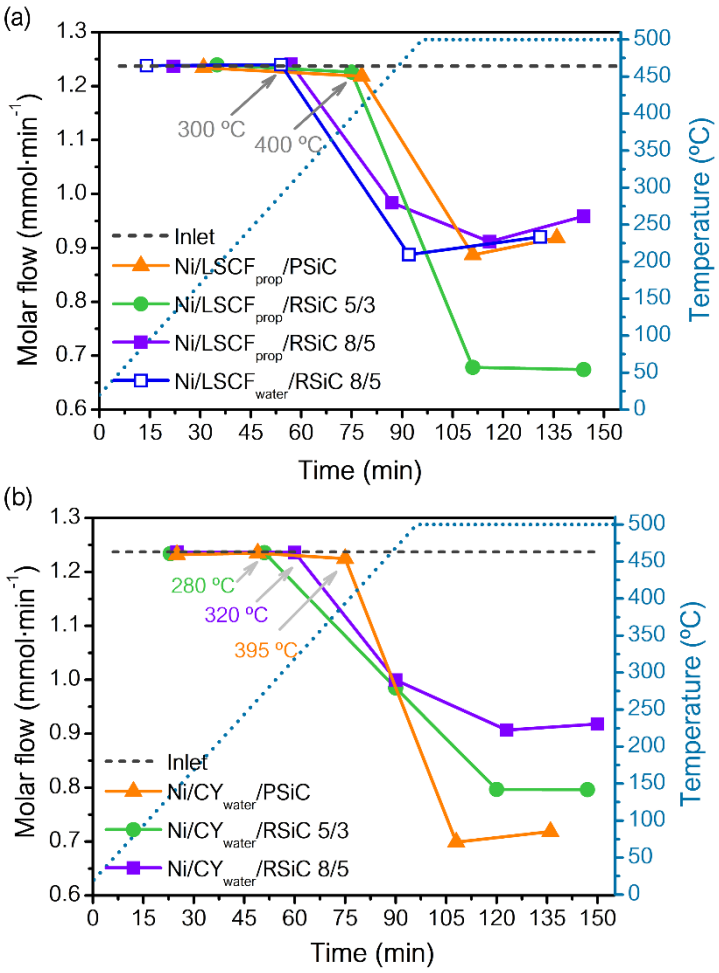

Figure 4.24. Partial molar flow of CO at the outlet of the reactor vs time on stream during the pre-treatment conditions under syngas atmosphere for (a) LSCF- and (b) CY-based structured catalysts

4.8.1.2. Catalytic performance. Toluene reforming

The variation of the partial molar flow of each gas component versus the time on stream during toluene reforming is shown in ***Figure 4.25*** for LSCF-based structured catalysts. The operating conditions such as mass of catalyst and of Ni^0 into the reactor, together with the average toluene conversion, selectivity to benzene and carbon can be as well found in ***Table 4.13*** for LSCF- and CY-based materials. Similar behavior in the partial gas flows was attained for CY-based structured catalysts (see *Appendix, see* ***Figure 4.37*** at the end of the chapter) and are similar to that shown for the powdered catalysts in *Chapter 3.* Likewise, the CO consumption lead to H_2, CO_2 and CH_4 production via CO_x methanation and WGS and processes. Whereas no significative variations are evidenced in the partial molar flows or toluene conversion among the different Ni/LSCF/SiC catalysts, some differences in carbon selectivity are found (***Table 4.13***). Similar toluene conversions

are reached and varied from 21 to 29% among all Ni/LSCF/SiC catalysts, with a benzene selectivity of 5% attained for RSiC 8/5, and negligible for RSiC 5/3 and PSiC (< 2%). Thereby, the main differences in the catalytic performance of the three type of extrudates are associated to the amount of coke deposits. Indeed, the selectivity to coke decreased as follows: Ni/LSCF$_{prop}$/PSiC (16%) > Ni/LSCF$_{prop}$/RSiC 5/3 (11%) > Ni/LSCF$_{prop}$/PSiC (5%). Thus, the RSiC 8/5 leads to the best catalytic performance in term of resistance to coke deposition within the Ni/LSCF$_{prop}$/SiC catalysts. Besides that, similar toluene conversion with a noticeable increase in carbon selectivity is found for Ni/LSCF$_{water}$/RSiC 8/5 with respect to Ni/LSCF$_{prop}$/RSiC 8/5. Due to the use of water, the carbon selectivity becomes 16% from 5% in the case of the use of propionic acid, with a toluene conversion of 22%. Similar to Ni/LSCF/SiC materials, no significative changes in toluene conversion are noticeable for Ni/CY$_{water}$/SiC catalysts. However, a slightly different tendency concerning the effect of shape of β-SiC extrudates in the catalytic performance is detected. Within these catalysts, Ni/CY$_{water}$/RSiC 5/3 shows the best resistance to coke formation (6%), followed by Ni/CY$_{water}$/RSiC 8/5 with carbon selectivity of 10%.

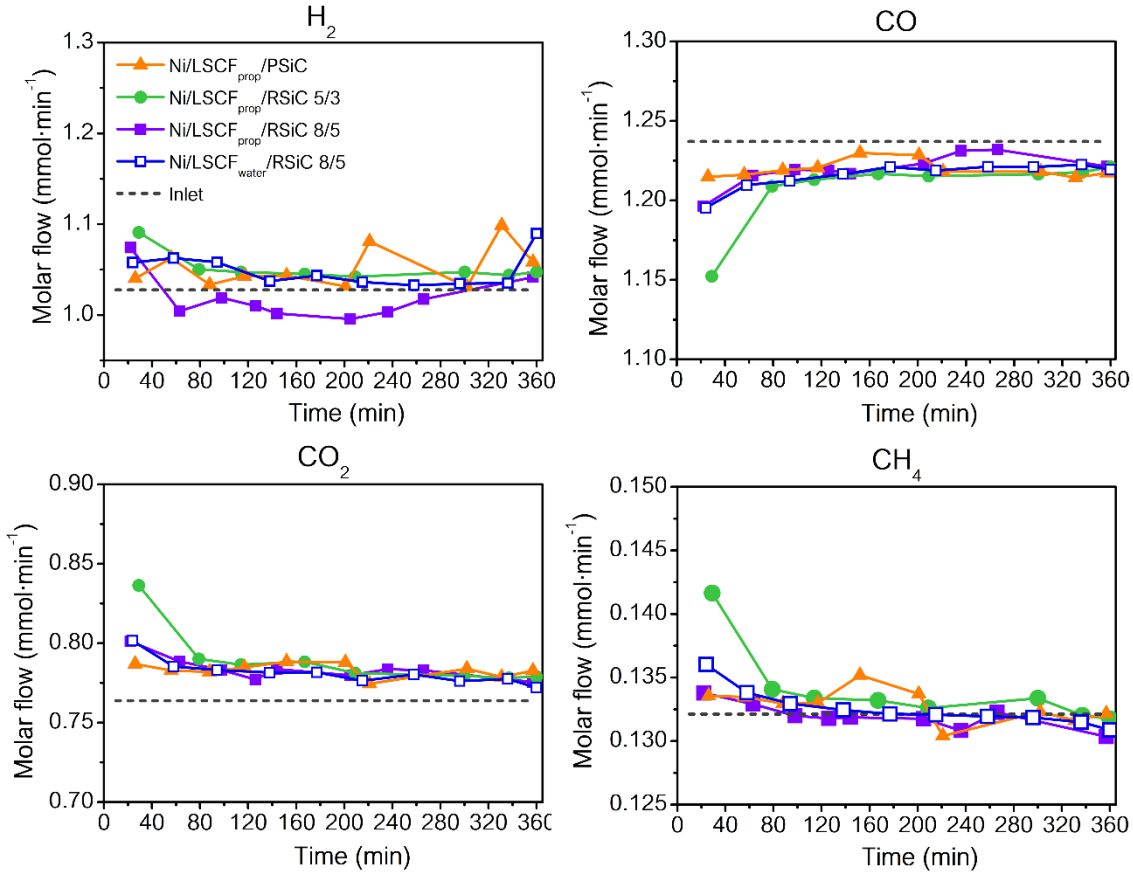

Figure 4.25. Partial molar flows at the outlet of the reactor vs time on stream during steam reforming of toluene at 550 ºC over LSCF-based structured catalysts (Ni/LSCF/SiC) (S/C$_{tar}$= 7.7)

	m_{cata} (mg)	m_{Ni^0} (mg)	$X_{toluene}$ (%)	$S_{benzene}$ (%)	S_{coke} (%)
$Ni/LSCF_{prop}/PSiC$	20	2.4	21	< 2	16
$Ni/LSCF_{prop}/RSiC$ 5/3	20	2.4	25	< 2	11
$Ni/LSCF_{prop}/RSiC$ 8/5	17	2.2	29	5	5
$Ni/LSCF_{water}/RSiC$ 8/5	32	2.5	22	7	16
$Ni/CY_{water}/PSiC$	27	2.2	13	13	~ 0
$Ni/CY_{water}/RSiC$ 5/3	17	2.2	28	5	6
$Ni/CY_{water}/RSiC$ 8/5	16	2.4	19	8	10

Table 4.13. Experimental conditions (mass of catalysts/Ni^0 into the reactor) along with average toluene conversion, selectivity to benzene and carbon for the prepared structured catalysts under steam reforming of toluene at 550 ºC

A deep characterization of the different structured catalysts would be required in order to better understand and discuss about the catalytic performance of these structured materials. As prior remarked, the aim of these catalytic tests was the choice of the coating conditions and of the β-SiC extrudate shape with best catalytic performance for the subsequent catalytic scale up and tests at pilot plant conditions. Structured vs powdered catalysts

4.8.2. Structured vs powdered catalysts

The effect of the catalytic structuration in the reduction pre-treatment and catalytic activity in toluene reforming has been compared to the catalytic activity in powder for the three chosen catalysts using RSiC 8/5 shape shape ($Ni/LSCF_{water}/RSiC$ 8/5, $RuNi/LSCF_{water}/RSiC$ 8/5 and $Ni/CY_{water}/RSiC$ 8/5).

4.8.2.1. Reduction pretreatment under syngas atmosphere

Figure 4.26 shows the variation of the outlet partial molar flow of CO with time found during the reduction pre-treatment under syngas. Generally, a modification of the partial flow can be observed at lower temperature for the structured catalysts compared to the catalysts in powder. Catalytic activity is noticeable from temperatures around 290 ºC for $Ni/LSCF_{water}/RSiC$ 8/5 and 320ºC for $Ni/CY_{water}/RSiC$ 8/5 whereas temperatures around 360-390ºC need to be reached for the equivalent catalytic powders. Concerning Ru containing catalysts, differences in the partial molar flow are noticeable at lower temperatures for $RuNi/LSCF_{water}/RSiC$ 8/5 (145 ºC) compared to the RuNi/LSCF powder catalyst (295 ºC). Therefore, a promotion of the reduction *in situ* of NiO and RuO_2 due to the catalytic structuration can be clearly appreciated. A synergic effect of both, the

presence of ruthenium and the structuration, are remarkable, leading to a catalyst able to display catalytic activity at the lowest temperature. Despite that, the structured catalysts require more time on stream to shows same or higher catalytic activity than the catalysts in powder. For instance, a lower CO conversion was found for RuNi/LSCF$_{water}$/RSiC 8/5 than for RuNi/LSCF after around 80 min on stream. As well, Ni/CY$_{water}$/RSiC 8/5 catalysts needs more time on stream to reach same partial flow values than the corresponding Ni/CY powder catalyst. As shown by the H_2-TPR results, the presence of NiO species hard to reduce due to the strong NiO-SiO_2-SiO_xC_y interaction accomplished through the structuration might be the reason of these differences in catalytic activity between structured and catalysts in powder.

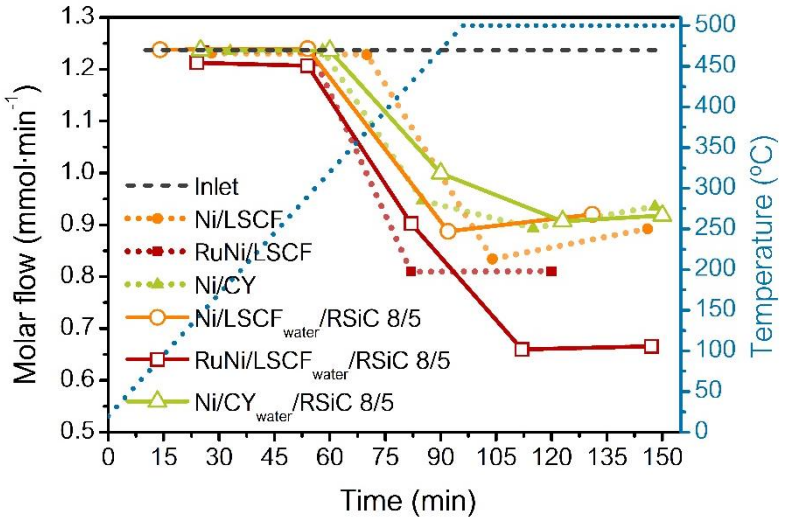

Figure 4.26. Partial molar flow of CO at the outlet of the reactor vs time on stream during the pre-treatment conditions under syngas atmosphere for selected structured and powdered catalysts

4.8.2.2. Catalytic performance. Toluene reforming

The variation of the outlet partial molar flows of the gas components along time on stream is shown in ***Figure 4.27.*** In addition, the operating conditions such as mass of catalyst/Ni^0 and $WHSV_{tar}$, and the average toluene conversion, the benzene selectivity and the amount of coke normalized by the mass of Ni^0 are listed in ***Table 4.14.*** for the structured and powdered catalysts. As it can be observed, the mass of Ni^0 and $WHSV_{tar,Ni^0}$ have been kept constant.

Differences in toluene conversion as well as in the gas phase composition are detected between the structured and powdered catalysts. The effect of the structuration in the catalytic performance can be observed in the variation of the partial molar flows of the

gas components (***Figure 4.27***). A decrease in catalytic activity toward WGS reaction for Ni/LSCF$_{water}$/RSiC 8/5 catalyst compared to Ni/LSCF is clearly denoted by the low H_2 and CO_2 production attained. This fact along with the higher toluene conversion shows for the former catalysts (22%) compared to the latter (almost no conversion) highlights that the structuration of Ni/LSCF enhances the catalytic activity toward toluene reforming reaction (***Table 4.14***). Additionally, the quantity of deposited coke decreases drastically for the structured catalysts from 21 g_{coke}/g_{Ni}^0 to 5 g_{coke}/g_{Ni}^0. Concerning Ru containing materials, the CO methanation reaction prevailed for the RuNi/LSCF$_{water}$/RSiC 8/5 catalyst, while its equivalent RuNi/LSCF displays a high catalytic activity toward WGS reaction (***Figure 4.27***). In this case, the RuNi/LSCFwater/RSiC 8/5 shows higher toluene conversion (55%) but also higher amount of carbon deposits (16 g_{coke}/g_{Ni}^0) than the RuNi/LSCF catalysts with toluene conversion and carbon deposits of 19% and 10 g_{coke}/g_{Ni}^0, respectively. As widely reported in literature, the selectivity toward CO methanation or WGS reactions could be associated to different parameters such as the particle size, the catalytic support and the reaction conditions [229]. Thereby, these differences in selectivity toward CO methanation and WGS reaction between RuNi/LSCF$_{water}$/RSiC 8/5 and RuNi/LSCF might be linked with a change in the metal particle sizes and/or a change in the catalytic support structure owing to the catalytic structuration. Similar tendencies in the outlet partial molar flows for Ni/CY$_{water}$/RSiC 8/5 catalyst were found compared to Ni/CY, whereas an increase in toluene conversion associated to the catalytic structuration is discerned for Ni/CY$_{water}$/RSiC 8/5 (19%) compared to Ni/CY (4%). A lower amount of coke deposit is observed for Ni/CY$_{water}$/RSiC 8/5 (7 g_{coke}/g_{Ni}^0) in comparison with Ni/CY (21 g_{coke}/g_{Ni}^0). In general, an improvement in the catalytic activity toward toluene reforming is attained for the structured catalysts with respect to the powdered ones. This enhancement of catalytic activity toward toluene reforming reaction displayed for the structured catalysts can be related to the strong NiO-SiO_2-SiO_xC_y interaction accomplished through the catalytic structuration. As it has been reported within literature, a strong metal support interaction limits the migration of metal Ni particles on the support and inhibited the growth of Ni nanoparticles [295]. Furthermore, the base-growth mechanism of the filamentous carbon deposits is more favoured than the tip-growth mechanism through a strong Ni-support interaction (discussed in *Chapter 3*) [250]. Accordingly, the strong NiO-SiO_2-SiO_xC_y interaction displayed for the structured catalysts may decrease or inhibit:

(i) the sintering process that could occur under the pre-treatment conditions

(ii) the detachment of Ni particles from the support-substrate due to the formation of filaments carbon species *via* the tip-growth mechanism caused by the pre-treatment conditions.

Lastly, among the structured catalysts, RuNi/LSCF$_{water}$/RSiC 8/5 leads to the best catalytic activity in terms of toluene conversion (55%). Meanwhile, similar toluene conversion and tendencies in the gas phase partial outlet molar flows are evidenced for Ni/CY$_{water}$/RSiC 8/5 (19% of toluene conversion) and Ni/LSCF$_{water}$/RSiC 8/5 (22%). Nevertheless, higher amount of catalyst is introduced for the latter catalysts in the reactor (***Table 4.14***), indicating that Ni/CY$_{water}$/RSiC 8/5 may display higher catalytic activity compared to Ni/LSCFwater/RSiC 8/5. Accordingly, the catalytic activity in toluene reforming among the structured catalysts decrease as follow: RuNi/LSCF$_{water}$/RSiC 8/5 > Ni/CY$_{water}$/RSiC 8/5 > Ni/LSCF$_{water}$/RSiC 8/5.

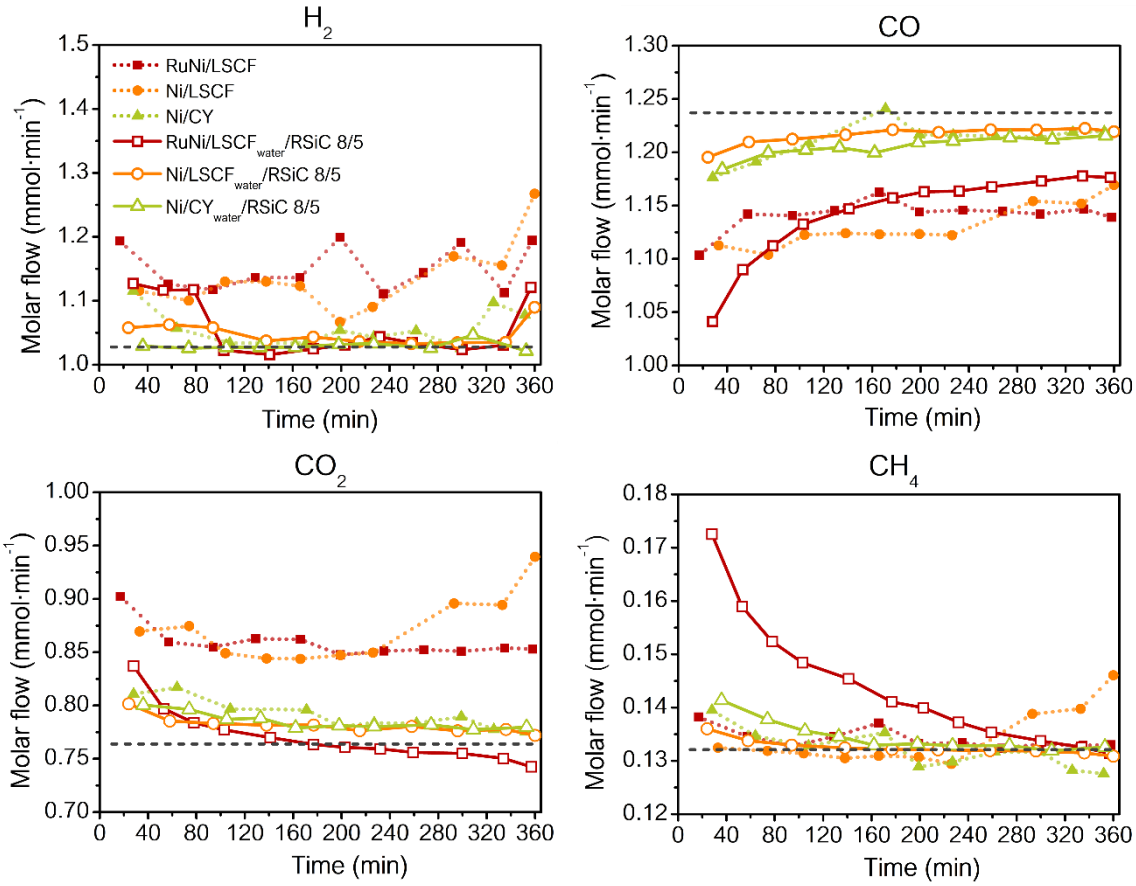

Figure 4.27. Partial molar flows at the outlet of the reactor vs time on stream (min) during steam reforming of toluene at 550 ºC over selected structured and powdered catalysts (S/C_{tar}= 7.7)

	m_{cata} (mg)	m_{Ni}^0 (mg)	$WHSV_{gas}$ (h^{-1})	$WHSV_{tar,Ni}^0$ (h^{-1})	$X_{toluene}$ (%)	$S_{benzene}$ (%)	g_{coke}/g_{Ni}^0
$Ni/LSCF_{water}/RSiC$ 8/5	32	2.5	270	24	22	7	5
$RuNi/LSCF_{water}/RSiC$ 8/5	42	2.1	203	28	55	4	16
$Ni/CY_{water}/RSiC$ 8/5	16	2.4	526	25	19	8	7
Ni/LSCF	23	2.3	370	26	0	-	21
RuNi/LSCF					19	10	10
Ni/CY					4	67	21

Table 4.14. Experimental conditions (mass of catalysts/Ni^0 into the reactor and $WHSV_{gas/tar}$) along with average toluene conversion, selectivity to benzene and carbon for the selected structured and powdered catalysts under steam reforming of toluene at 550 ºC

4.9. Characterization of spent structured catalysts

Similar to the powdered catalysts, the type and the morphology of the carbonaceous deposits have been also characterized by TGA and SEM analysis for the spent structured catalysts. Thus, the TGA curves normalized by the initial mass of structured catalysts (catalyst + SiC) have been plotted for the spent Ni/LSCF/SiC catalysts in ***Figure 4.28.*** An oxidation temperature close to 600 ºC was found for all catalysts, regardless the extrudate shape and the type of solvent used for the deposition of LSCF support. This oxidation temperature has been associated to the formation of structural and/or graphitic carbon deposits on the catalytic surface and it is in concordance with the results attained for the powdered catalysts (shown in *Chapter 3*). The TGA analysis obtained for $Ni/CY_{water}/SiC$ are presented in *Appendix (**Figure 4.38***) since no significative modifications were observed.

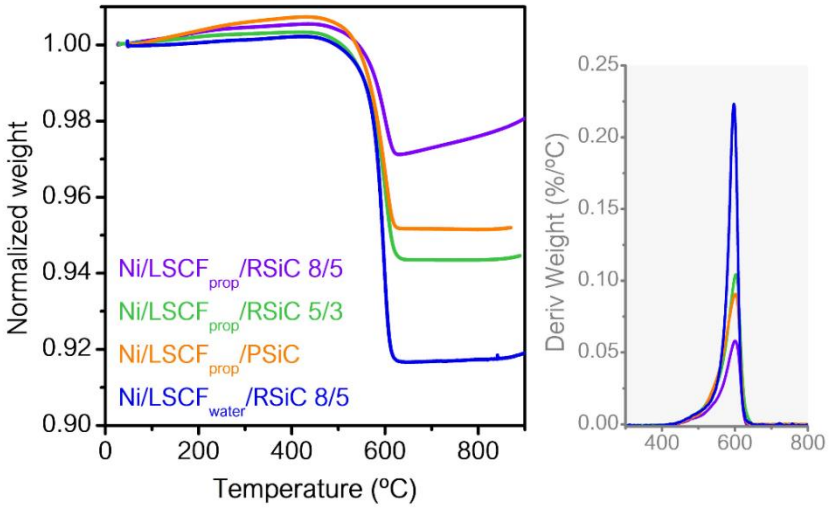

Figure 4.28. TGA analysis of the LSCF-based structured catalysts post steam reforming of toluene at 550 ºC

SEM images of the spent Ni/LSCF$_{prop}$/RSiC 8/5 and Ni/LSCF$_{prop}$/RSiC 5/3 catalysts are presented in ***Figure 4.29.*** and ***Figure 4.30,*** respectively. A heterogeneous morphology can be appreciated on the catalytic surface of Ni/LSCF$_{prop}$/RSiC 8/5 (***Figure 4.29***). In order to elucidate the differences in composition among the diverse morphologies found, EDX analysis were carried out in the remarked zones in red. The results of the elemental analysis composition (*Appendix,* ***Figure 4.39***) of each zone lead to: (1) mainly bare SiC; (2) presence of Ni over SiC, (3) presence of Ni + Fe (LSCF) over SiC and (4) presence of Ni + La,Fe (LSCF) over SiC. The detection of nickel on SiC is consistent with the existence of NiO with strong interaction with β-SiC substrate, according to H_2-TPR results. As expected, mainly filamentous carbons are formed under the reaction conditions on the catalytic surface (***Figure 4.30 (a) and (c)***). In order to verify the type of carbon growth mechanism on the structured catalysts, a comparison between the images (a) – (c) and their equivalents using the chemical contrast mode (b) – (d) were also carried out. No noticeable clear zones related to Ni particles size on the top of the filamentous carbon are discerned in image (b) compared to image (a), whereas several clear zones are found for image (d) by comparing to image (c). These results can suggest that both type of growth mechanism might be displayed on the structured catalysts and it can be associated with the presence of NiO species with different NiO-support-SiC interaction evidenced by H_2-TPR analysis.

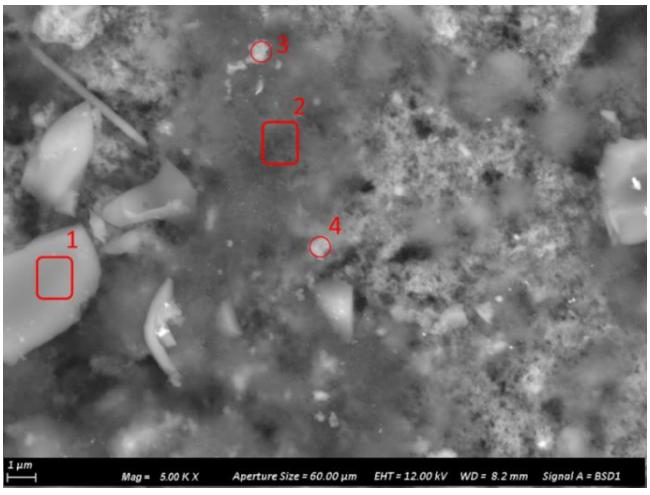

Figure 4.29. SEM images of Ni/LSCF$_{prop}$/RSiC 8/5 catalyst post steam reforming of toluene at 550 ºC

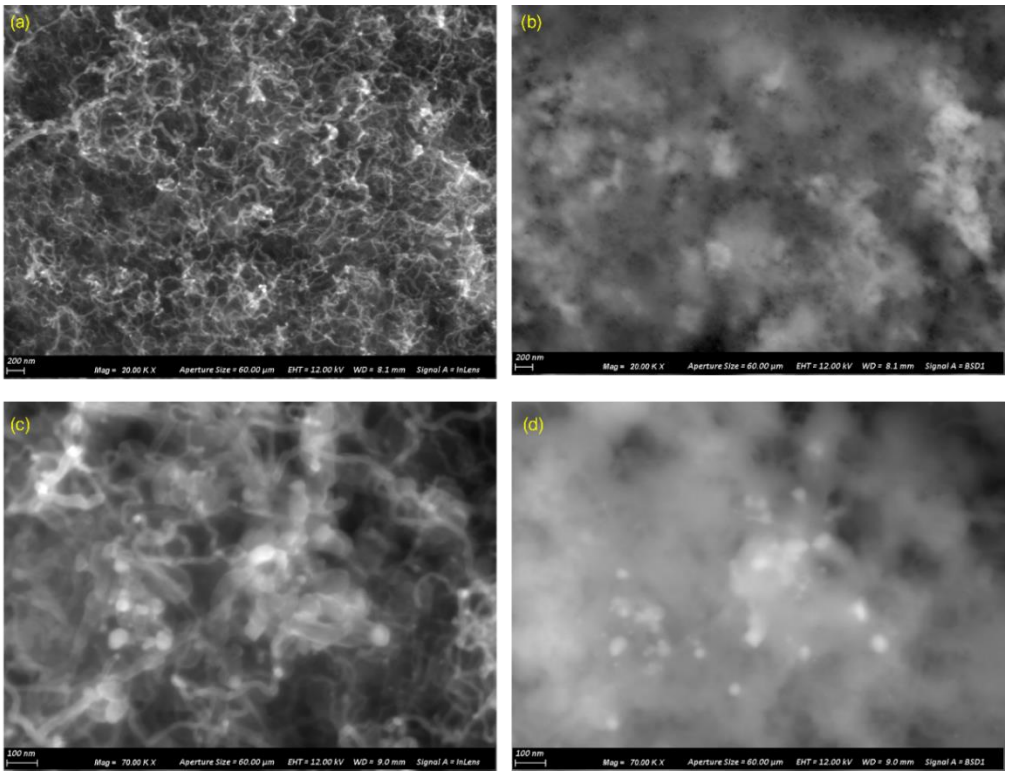

Figure 4.30. SEM images of Ni/LSCF$_{prop}$/RSiC 5/3 catalysts post steam reforming of toluene at 550 ºC

The SiC shape and the conditions of the catalytic structuration for the preparation of the catalysts at large scale have been selected based on the catalytic results presented in *section 4.8.1* for the structured catalysts. The selection of the SiC shape is a controversial point, since RSiC 8/5 leads to the best performance among Ni/LSCF$_{prop}$/SiC catalysts, while the RSiC 5/3 is the best within the Ni/CY$_{water}$/SiC ones. As presented in *Chapter 3,* the Ni/LSCF displays the worst catalytic performance among the three catalysts under study (Ni/LSCF, RuNi/LSCF and Ni/CY). This fact could be also deduced from the catalytic results attained for Ni/LSCF$_{water}$/RSiC 8/5 and Ni/CY$_{water}$/RSiC 8/5. Therefore, the choice of the extrudate shape was based on the results reached for Ni/LSCF$_{prop}$/SiC catalysts to decrease as much as possible the loss of activity of this catalyst by the structuration process. Then, RSiC 8/5 shape was selected as catalytic substrate for the structuration of catalysts at large scale. Additionally, this shape supplies more open area than the RSiC 5/3, therefore, operational drawbacks related to pressure drop due to the accumulation of particles and ashes into the catalytic bed at pilot plant scale might be diminished. Regarding the solvent, similar catalytic results were attained for both, propionic acid and water. Consequently, due to its low less toxicity and corrosive character, water was chosen as a solvent for the preparation of one liter of support precursor solution at large scale.

4.10. Scale – up of the selected structured catalysts

Before testing at pilot plant scale, the effect of the scale up in the catalytic structuration has been investigated for the chosen coating conditions.

Thus, four batches of 1.2 L of RSiC 8/5 extrudates has been prepared through two coating steps using the water-based support precursor solution with a concentration of 0.62 - 0.60 M. Afterwards, the impregnation of the active phase was performed using an ethanolic based solution with a $Ni(NO_3)_2$ concentration of 0.26 M. The mass of LSCF and CY supports obtained after consecutive coating steps are shown in ***Figure 4.31.*** As well, the main characteristic of the prepared batches at large scale compared to these obtained at small one is listed in ***Table 4.15.***

Small differences in the mass deposition can be appreciated among the different batches at large and small scale for (Ru)Ni/LSCF/RSiC 8/5 catalyst (***Figure 4.31 (a)***), whereas same tendency is followed for the prepared batches at large and small scale for the Ni/CY/RSiC 8/5 catalyst (***Figure 4.31 (b)***). As prior mentioned in the introduction, many parameters influence in the final coated structured catalysts. Among these parameters, the modification of the air velocity during blowing the excess of solution out could alter the coating load result [268]. This could be one of the causes of the differences in the mass uptake among the prepared batches of Ni/LSCF/RSiC 8/5, being also noticeable at small scale. Despite the complexities, two prepared batches at large scale led to similar mass of deposited LSCF per volume of extrudate ($m_{support}/V_{extr}$) (~80 $g \cdot L^{-1}$), whereas one of them led to a slightly lower value (70 $g \cdot L^{-1}$) (***Table 4.15***). As prior noticed at small scale, a lower mass of deposited support per volume of extrudate is as well attained at large scale for Ni/CY/RSiC 8/5 catalyst (44 $g \cdot L^{-1}$) compared to Ni/LSCF/RSiC 8/5 (***Table 4.15***) Generally, the scale up led to similar mass of the deposited supports than that found at small scale and far from the target (54 $g \cdot L^{-1}$), highlighting that the coating procedure is reproducible. Regarding the amount of deposited Ni^0 per extrudate volume (m_{Ni}^0/V_{extr}), values close to the target (6 $g \cdot L^{-1}$) were accomplished in most of the cases.

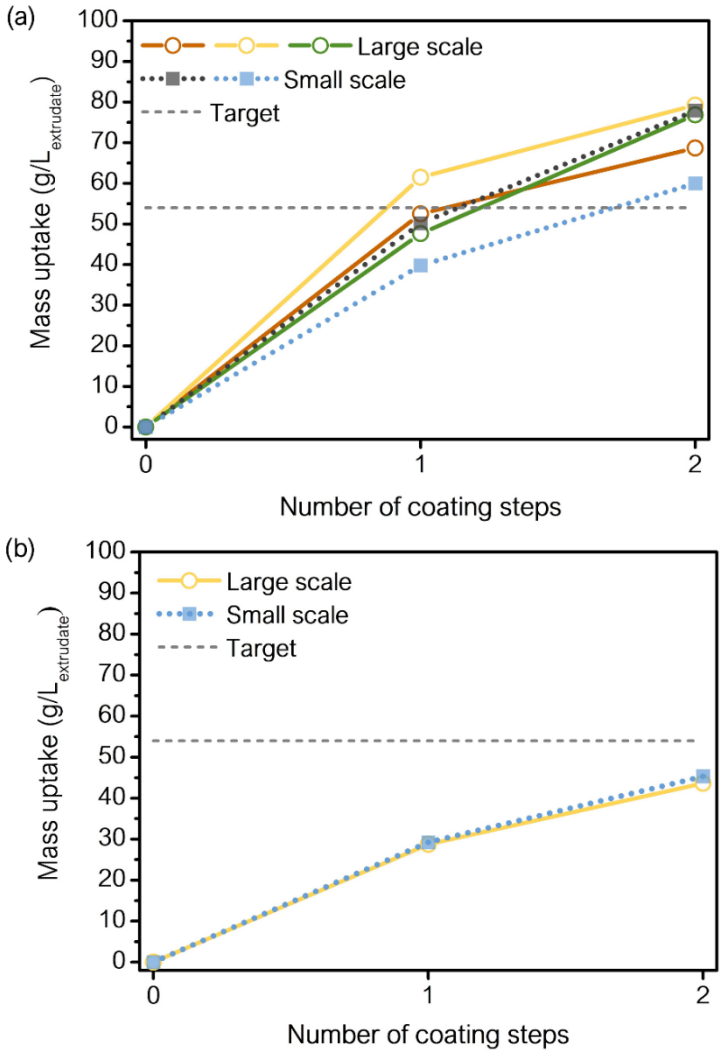

Figure 4.31. Effect of scale up on the mass uptake of LSCF mixed oxide after successive coating steps

	$m_{support}/V_{ext}$ $(g \cdot L^{-1})^{\pm}$	m_{Ni}^0/V_{ext} $(g \cdot L^{-1})^{\pm}$	m_{Ni}^0/m_{cat} (%)	m_{Ru}^0/m_{cat} (%)
Ni/LSCF/RSiC 8/5 – lab	78	7	8	-
Ni/LSCF/RSiC 8/5	79	5	6	-
RuNi/LSCF/RSiC 8/5-1	69	4	5	1
RuNi/LSCF/RSiC 8/5-2	77	6	8	0.5
Ni/CY/RSiC 8/5 – lab	45	7	15	-
Ni/CY/RSiC 8/5	44	6	12	-

Table 4.15. Properties of the structured catalysts - effect of catalytic scale up.

The reducibility of batches prepared at large scale has been also studied by H_2-TPR in order to determine modifications in the deposited phases associated to the scale up. The H_2-TPR profiles of catalysts prepared at large and small scale are plotted in ***Figure 4.32*** for

Ni/LSCF/RSiC materials. In addition, the H_2 consumption and the support reducibility are presented in ***Table 4.16.*** Similarly, two reduction regions with a new peak at low temperature (~290 ºC) are noticeable for the prepared Ni/LSCF/RSiC 8/5 at large scale (***Figure 4.32 (a)***). In comparison with the small batch, the first reduction region is shifted to higher temperature whereas the second is clearly moved to lower temperature for the Ni/LSCF/RSiC 8/5 at large scale. The additional reduction peak might be linked with the reduction of NiO to $Ni^{\delta+}$ species with weak NiO-support-SiC interaction. Besides, an increase in intensity of the reduction peak place at 410 ºC together with the decrease of the peak located at 500 ºC is noticeable for Ni/LSCF/RSiC 8/5 at large scale compared to the small one. Therefore, the catalytic scale up results in a different NiO-LSCF-SiC interaction, favouring a weaker NiO-SiC interaction compared to the small one. This fact could lead to a different catalytic behaviour between the catalysts prepared at large and small scale. Regardless the preparation scale, similar support reducibilities, around 40%, are observed for both Ni/LSCF/RSiC 8/5 catalysts (***Table 4.16***). Similarly, NiO species with weaker NiO-SiC interaction were found for Ni/CY/SiC catalyst at large than at small scale and their corresponding H_2-TPR profiles are shown in *Appendix* (***Figure 4.40***).

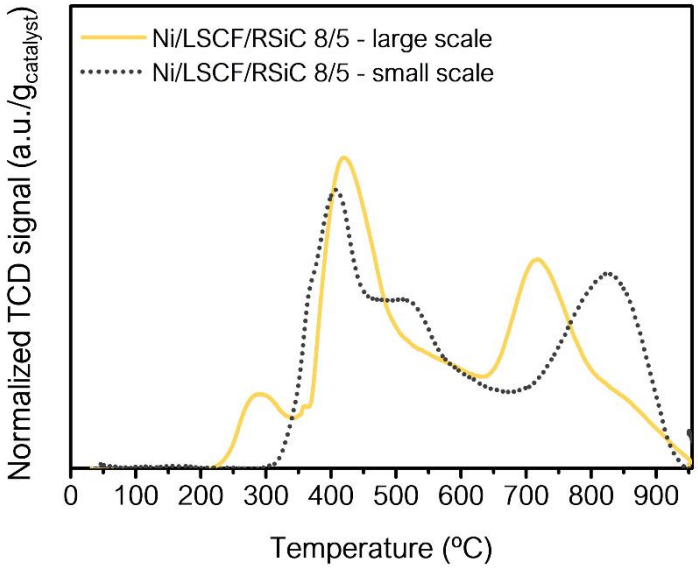

Figure 4.32. H_2-TPR profile of Ni/LSCF/RSiC 8/5. Effect of the catalytic scale up

	H_2 consumption (mmol·g^{-1})	Support reducibility (%)
Ni/LSCF/RSiC 8/5 – lab	4.6	38
Ni/LSCF/RSiC 8/5 - scale up	4.8	40

Table 4.16. H_2 consumption and support reducibility of Ni/LSCF/RSiC 8/5 catalysts. Effect of the catalytic scale up

4.11. Conclusions

In the present chapter, the optimization of the catalytic structuration over β-SiC-based extrudates with different shape as catalytic substrate has been carried out. The resulting structured catalysts were characterized and tested in toluene reforming at laboratory scale. The effect of the catalytic scale up was evaluated for the final application at pilot plant scale.

The characterization of the bare SiC extrudates showed similar textural or structural properties, regardless the shape. Regarding the dissolution of the gel, modifications in the textural and structural properties of the catalytic supports were noticeable. Similar SSA with a lower V_{pore} for prop/water-LSCF oxides than SG-LSCF oxide were noticed, whereas a decrease in both, SSA and V_{pore} were achieved for water-CY compared to SG-CY oxide. In addition, the modification of the crystalline structure was clearly evidenced by the formation of additional crystalline phases and the decrease in the support lattice parameters for both, prop/water-LSCF- and water-CY-based oxides, compared to their equivalent SG ones. As results, the formation of La_2O_3 with an additional perovskite phase was displayed for prop/water-LSCF oxides and a phase associated to Y_2O_3 oxide was showed for water-CY oxide. No significative changes in the H_2-TPR profile or in support reducibility were detected.

Concerning the optimization of the catalytic structuration, no significative changes in the support mass uptake associated to the β-SiC extrudate shape were noteworthy. A lower amount of deposited mass of support was attained using low propionic acid-based precursor solution concentration (0.30 M instead of 0.60 M), as well as, using water-based instead of propionic acid-based solution with similar concentration (0.60 M). At least, two coating steps were needed to reach deposited mass close to the target, regardless the concentration or solvent used. Generally, no loss of mass was appreciated, revealing the strong chemical affinity accomplished between the catalytic support and the catalytic substrate. In addition, no enhancement in the mass of the deposited support per coating step was achieved by the thermal pre-treatment, as consequence of the loss of porosity. Lastly, concerning the impregnation of the active phase, three coating steps were required for reached the target by using $Ni(NO_3)_2$ concentration of 0.13 M, whereas two were enough in the case of 0.26 M. Similar NiO particle size and metallic Ni surface were attained by XRD and H_2-TPR for the structured catalysts impregnated with both concentrations. Thereby, no significative influence of $Ni(NO_3)_2$ concentration on the nature of deposited NiO phase was attained.

The H_2-TPR profiles of the β-SiC supported with the catalytic supports (LSCF and CY) highlighted changes in the structural properties of these oxides due to the structuration were achieved, leading to a modification in their reduction profiles and reducibility. In comparison with the catalytic supports in powder, a decrease in the support reducibility was attained for $LSCF_{prop}$/RSiC 8/5, and $LSCF_{water}$/RSiC 8/5, while an increase was noticeable for CY_{water}/RSiC 8/5 material. Regarding the Ni containing structured catalysts, the H_2-TPR results pointed out that the presence of a catalytic support deposited over β-SiC surface decrease the strength of the NiO-SiC interaction and could avoid the formation of nickel silicate.

Concerning to the catalytic performance, all kind of extrudates were able to be reduced under syngas atmosphere, as evidenced by the variations in the outlet partial molar flow of CO. The efficiency in toluene reforming evidenced similar catalytic activity in term of toluene conversion (~20-30%) and stable gas phase among the different structured catalysts. Despite that, differences in the carbon selectivity were attained for the different shapes and preparation method. Thus, RSiC 8/5 shape, Ni/$LSCF_{prop}$/RSiC 8/5, lead to the lowest carbon selectivity (5%) whereas the PSiC, Ni/$LSCF_{prop}$/PSiC, showed the highest value (16%). Based on the differences in carbon selectivity attained for Ni/$LSCF_{prop}$/SiC materials, the RSiC 8/5 shape was the shape chosen for the structuration at large scale. Additionally, the use of water as a solvent provoked a clear increase in carbon selectivity for Ni/$LSCF_{water}$/RSiC 8/5 (16%) compared to Ni/$LSCF_{prop}$/RSiC 8/5 (5%). However, the water as solvent has been selected for the structuration at large scale, owing to its as solvent compared to propionic acid.

Additionally, a general enhancement in the catalytic activity toward toluene conversion with a decrease in the carbon deposition have been reached for the structured catalysts compared to their equivalent powdered ones. This improvement has been associated to the strong NiO-SiC interaction accomplished by the catalytic structuration. The toluene conversion, the gas phase modifications and the reaction conditions displayed for the selected structured catalysts allowed to clarify the tendency in catalytic activity among them. Accordingly, the catalytic activity decreased as follow: RuNi/$LSCF_{water}$/RSiC 8/5 > Ni/CY_{water}/RSiC 8/5 > Ni/$LSCF_{water}$/RSiC 8/5. Similar to the powdered catalysts, structural/graphitic carbon deposits have been found for the spent structured catalysts. Moreover, the partial inhibition of the tip-growth mechanism of the filamentous carbon as consequence of the strong NiO-SiC interaction was verified by the SEM images.

Lastly, similar mass of the deposited supports than that found at small scale and far from the target (54 $g \cdot L^{-1}$) were obtained for the catalytic scale up of (Ru)Ni/LSCF/RSiC 8/5 and Ni/CY/RSiC 8/5 materials. Thereby, the coating procedure used was reproducible, but does not allow to master a precise control of the deposited mass. Regarding the amount of deposited Ni^0 per extrudate volume (m_{Ni}^0/V_{extr}), values close to the target (6 $g \cdot L^{-1}$) were accomplished in most of the cases. Furthermore, modifications in Ni-support-SiC interaction as consequence of the catalytic scale-up were clearly noticeable by H_2-TPR. These modifications could vary the catalytic performance of the prepared catalysts at large scale compared to that obtained at small scale preparation.

Appendix of chapter 4

(i) Optimization of catalytic structuration

- *Support (LSCF) precursor solution concentration: 0.60 vs 0.30 M in total cations*

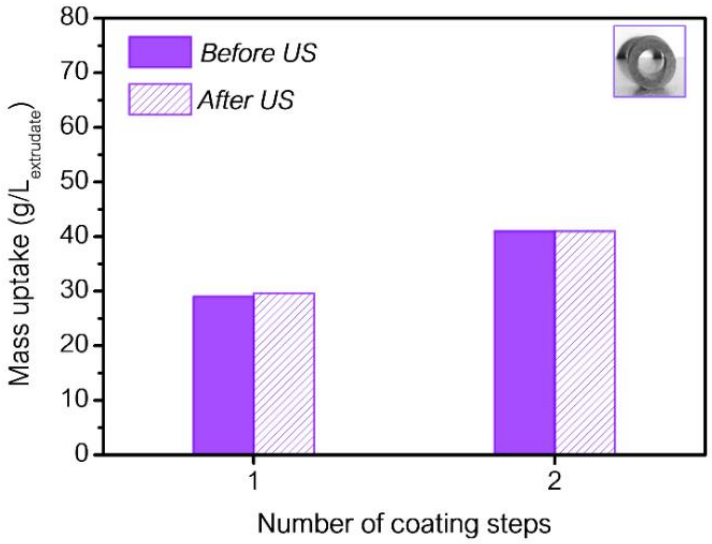

Figure 4.33. Evaluation of the anchoring of LSCF phase using 0.30 M solution for RSiC 8/5

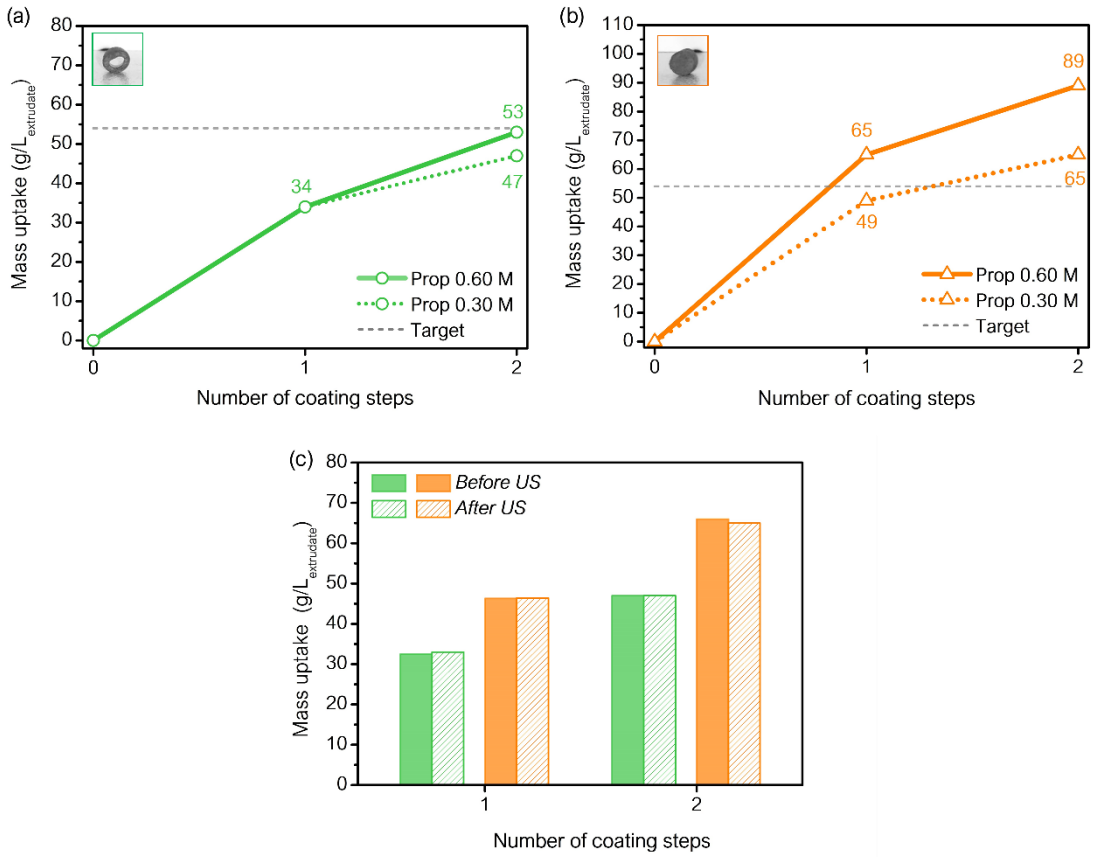

Figure 4.34. Effect of support precursor concentration (0.60 – 0.30 M) on the mass uptake LSCF mixed oxide for (a) RSiC 5/3 and (b) PSiC shapes and (c) evaluation of the anchoring of LSCF phase using 0.30 M solution

- *Solvent: propionic acid vs water*

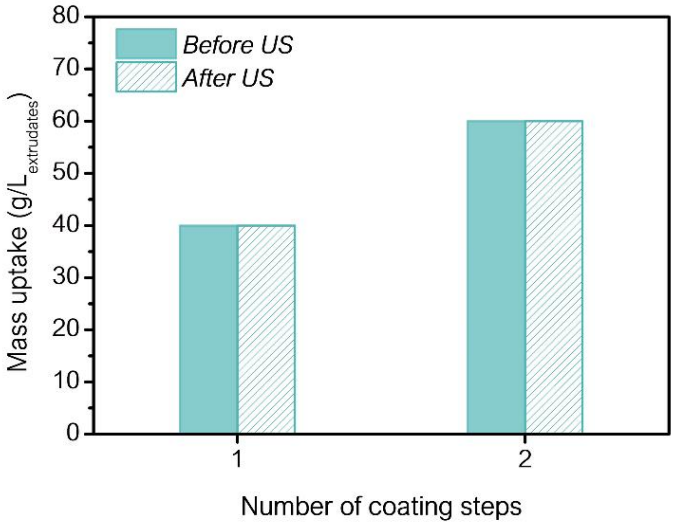

Figure 4.35. Effect of solvent (water) in the anchoring of the LSCF phase after successive coating steps

- *Thermal pretreatment*

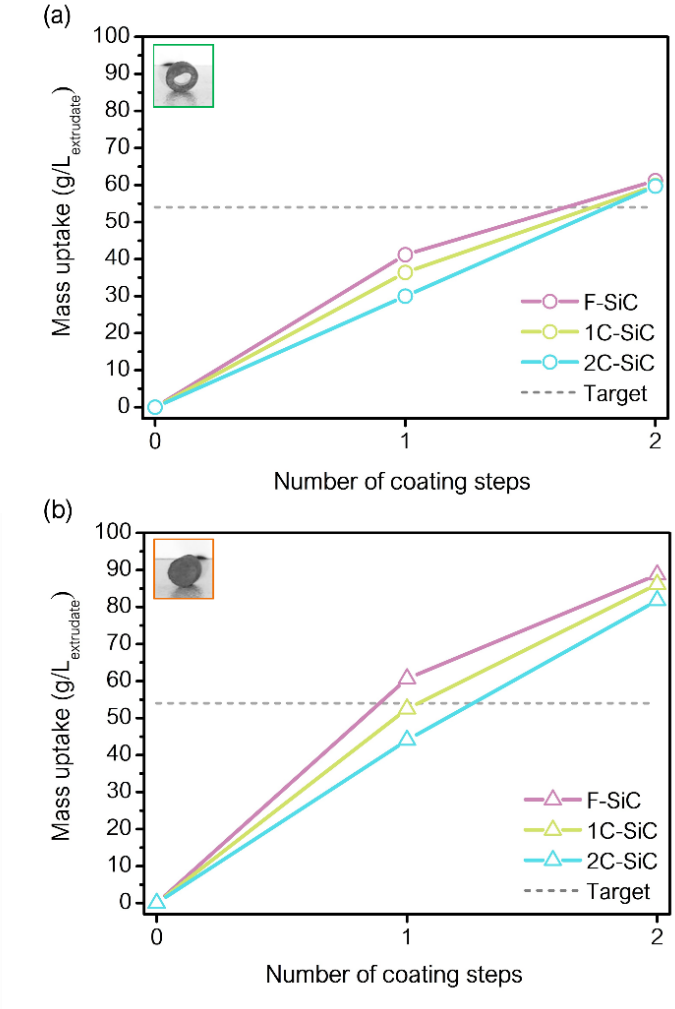

Figure 4.36. Effect of thermal pre-treatment on the mass uptake of LSCF mixed oxide after consecutive coating steps for RSiC 5/3 and PSiC shape

(ii) Catalytic test: toluene reforming

- *Influence of shape of β-SiC-based extrudates: Ni/CY$_{water}$/SiC catalysts*

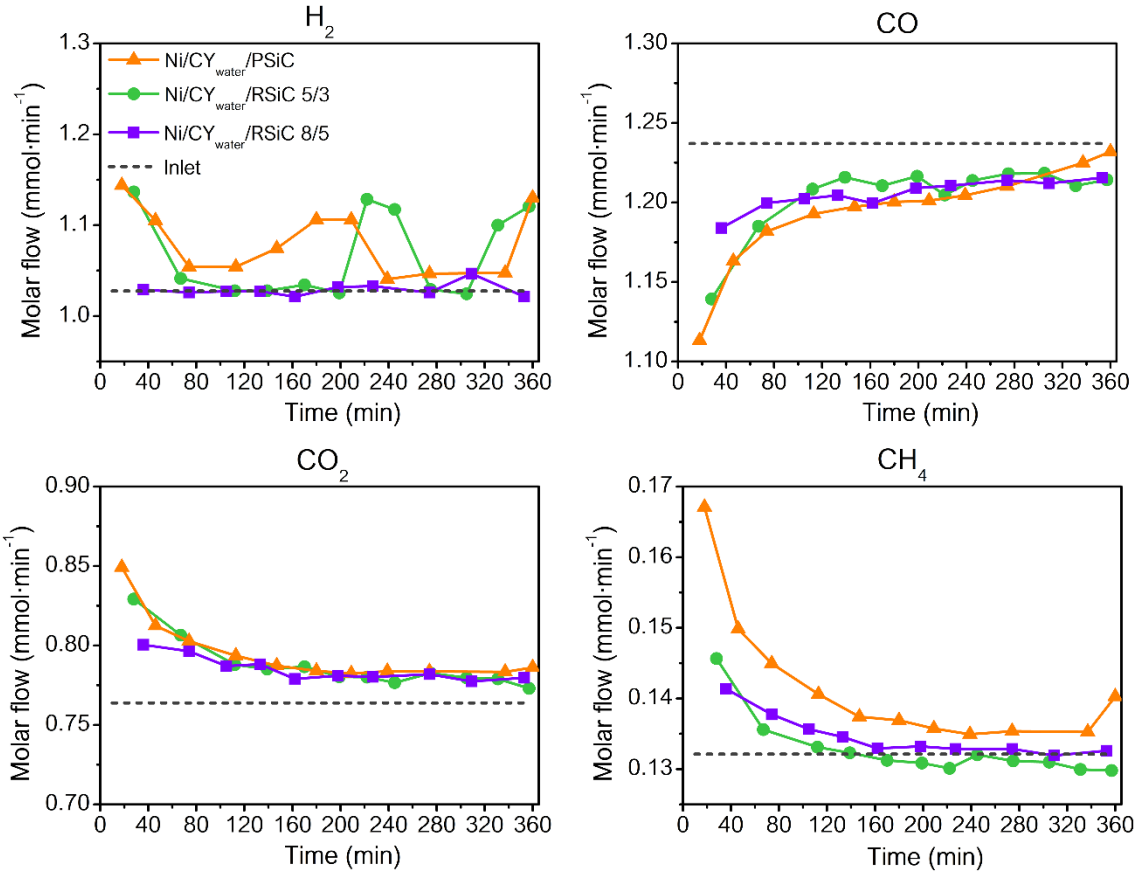

Figure 4.37. Partial molar flows at the outlet of the reactor vs time on stream during steam reforming of toluene at 550 ºC over CY-based structured catalysts (Ni/CY$_{water}$/SiC) (S/C$_{tar}$= 7.7)

- *Characterization of spent structured catalysts*

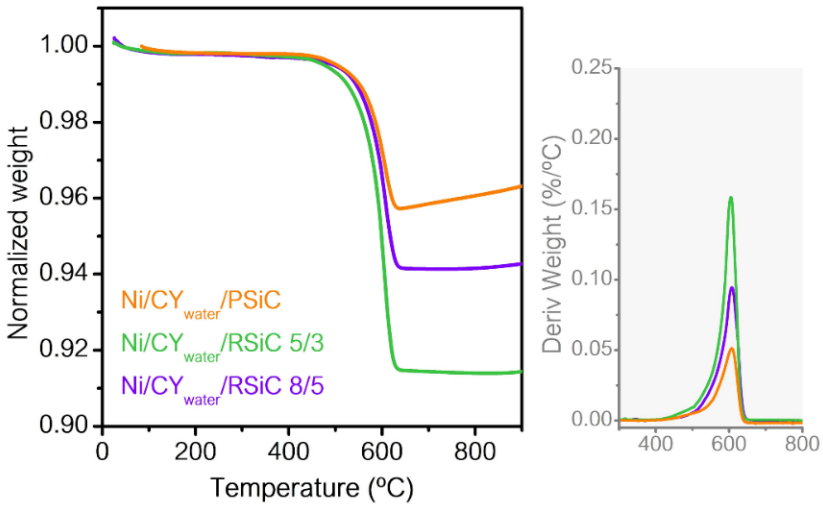

Figure 4.38. TGA analysis of the CY-based structured catalysts post steam reforming of toluene at 550 ºC

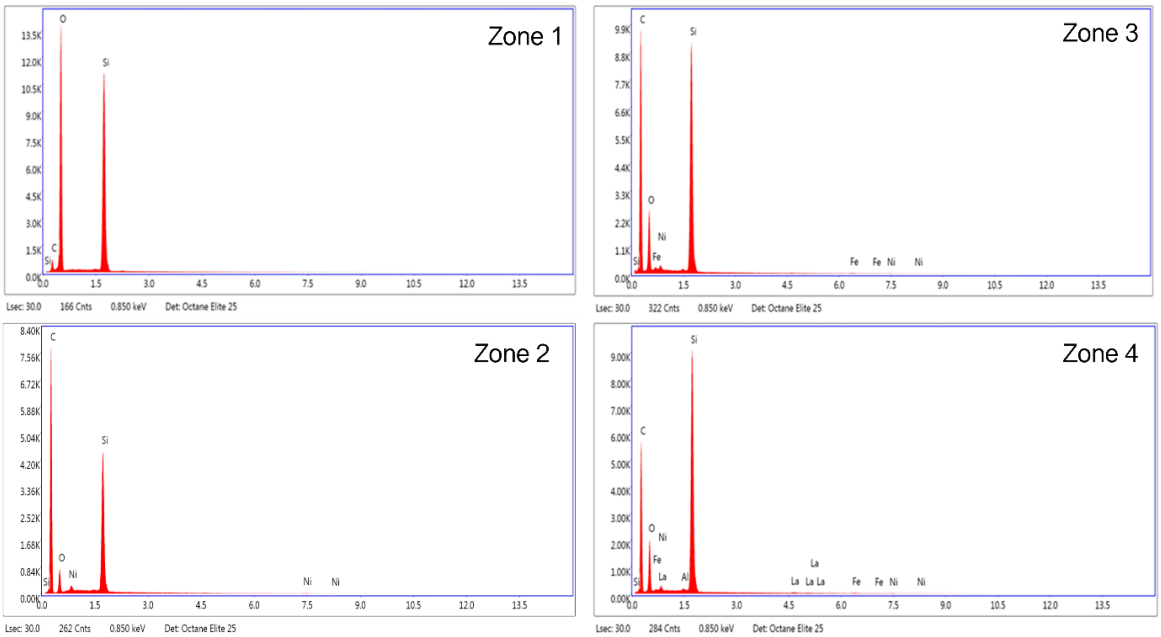

Figure 4.39. EDX analysis of zones remarked for Ni/LSCF$_{prop}$/RSiC 8/5 catalysts post steam reforming of toluene at 550 ºC in ***Figure 4.29***

(iii) Scale – up of the selected structured catalysts

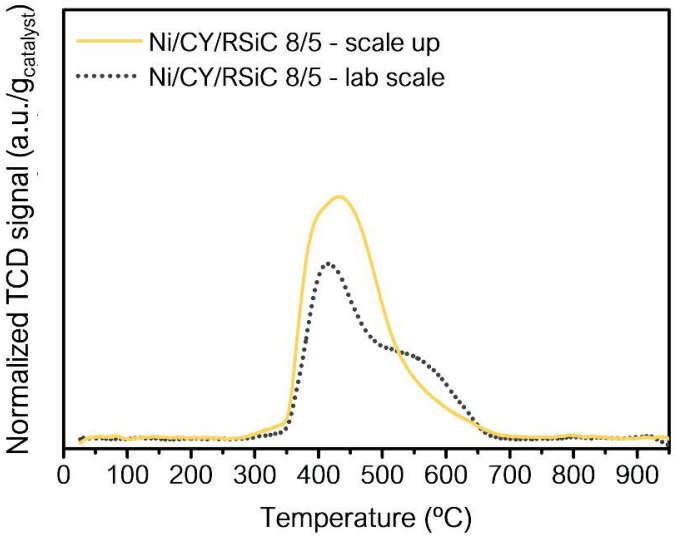

Figure 4.40. H_2-TPR profile of Ni/CY/RSiC 8/5. Effect of the synthesis scale up

CHAPTER 5

CATALYTIC TESTS AT BIOMASS GASIFICATION PILOT PLANT SCALE

Abstract

In this chapter, the catalytic results attained under real biomass gasification conditions for the three structured catalysts prepared at large scale are presented. A catalytic screening under real conditions using wood chips as biomass feedstock is shown in order to determine the catalyst with the best catalytic performance. Additionally, the possible catalytic regeneration of one of the catalytic systems is investigated and discussed.

To complete the research and satisfy the objective of EBIPREP project, catalytic results of the best catalyst under real conditions using a mixture of wood chips and biogas residues as feedstock are displayed.

5.1. Introduction

As presented in General Introduction (*Chapter* 1), the catalytic tar removal can be classified into two types, in function of the location in which tar is eliminated: (i) directly into the gasifier, called primary catalyst or (ii) out the gasifier, called secondary catalyst [34,298]. The former requires an optimization of the properties of the biomass feedstock and design of the gasifier and its operating conditions [25,34,298]. The limits in the feedstock flexibility, the production of waste streams, a decrease in cold gas efficiency and complex gasifier construction are some of the disadvantages displayed by the primary removal methods [34]. An ideal primary catalyst eliminates the need for secondary treatments but, it is expected that complete tar removal is not feasible without applying a secondary removal process [34]. In the case of the secondary catalyst, a downstream cleaning system is used. The use of this type of catalysts would remove the concept of primary treatment and as well can avoid the problems associated to the wastewater treatment. However, a secondary catalytic reactor involves generally a significant increase in the overall gasification process cost.

Primary catalyst, such as dolomite or olivine, minimizes tars and increases both hydrogen and CO_2, avoiding the complex downstream tar removal operations. However, the use of nickel-based catalysts as a primary catalyst has been discouraged due to the fast deactivation of these catalysts in the dusty environment of the gasifier [298]. Corella and co-workers have extensively studied the catalytic performance on tar removal efficiency of Ni-based catalyst as secondary catalyst in a small pilot plant scale (5-25 kg of biomass/h) by using a bubbling fluidized bed reactor. They mainly combined calcined dolomite and commercial Ni-based catalysts. Thus, in some of their studies, the calcined dolomite was introduced directly into the gasifier [299] and in other the calcined dolomite was placed in a first downstream catalytic reactor as a guard bed [300]. In both configurations, the dolomite reduced the tar content in the generated syngas from 12 $g \cdot Nm^{-3}$ to 2-3 $g \cdot Nm^{-3}$ [301]. Afterwards, the use of a secondary catalytic reactor with Ni-based catalyst led to reduce the tar levels from $g \cdot Nm^{-3}$ to the order of $mg \cdot Nm^{-3}$. The use of commercial shaped catalysts (ring, spheres, pellets…) were efficient in tar removal, but they require a syngas without particles. Thereby, they proposed either the use of hot filters before the catalytic bed or monoliths with honeycomb structure that can operate with gases containing particles [302]. Moreover, the open structure of monolithic structure enhances the gas flow yielding low pressure drop and leads to a reasonable external surface area and short diffusion distances. Therefore, nickel-coated structured catalyst such as monoliths, placed in a secondary reactor has been as well studied [302,303]. For these studies, monolithic

structures have been used and additives such as raw dolomite, raw olivine, sintered olivine and Ni/olivine have been added in gasifier bed [302,303]. Part of the catalytic results obtained in these studies will be presented later and compared with those obtained in the present work.

5.2. Partial objective

As described in the general introduction, the role of UNISTRA in EBIPREP project was the development of a catalytic system for post-treatment of the syngas generated from biomass gasification, and its final implementation in a real biomass gasification pilot plant.

In the present chapter, the catalytic tests of the Ni-based structured catalysts prepared at large scale conducted in a small biomass gasification pilot plant located in Hochschule Offenburg in Offenburg (Germany) are presented. As it has been reported in the literature, Ni-based catalysts are commonly used as secondary catalyst in order to limit their catalytic deactivation. In addition, the pilot of Offenburg is equipped with a fixed-bed gasifier reactor and the use of an in-bed catalyst might provoke operational difficulties by accumulation of char and ashes into the gasifier. Considering this, an additional downstream catalytic reactor was used for the catalytic gas cleaning step. Firstly, catalytic tests of the three structured catalysts already selected in *Chapter 4* (Ni/CY/RSiC 8/5, Ni/LSCF/RSiC 8/5 and RuNi/LSCF/RSiC 8/5) under real conditions using wood chips as biomass feedstock was performed in order to determine the best catalytic system in term of catalytic activity and stability. As it has been reported in literature, one of the requirements for the catalytic systems for tar removal is that they should be easily regenerated. Accordingly, in this work, the *in situ* regeneration under air and the subsequent catalytic test at pilot plant, using wood chips as feedstock, has been carried out for Ni/LSCF/RSiC 8/5 catalyst to evaluate its ability to be regenerated.

As presented in *General Introduction* (*Chapter* 1), the aim of EBIPREP project is to combine three biomass conversion processes (gasification, biofermentation and biogas products) and enhance the efficiency of the overall process. One of the purposes is the valorisation of the residues produced from the biotechnological process (bio fermentation and biogas) through their incorporation into the gasifier. Accordingly, in order to elucidate the efficiency of our catalytic system in tar removal in presence of the residues, the best catalyst has been tested using a mixture of wood chips and biogas process as biomass feedstock.

5.3. Experimental set-up and procedure

5.3.1. Pilot plant configuration

The biomass gasification pilot plant configuration is shown in ***Scheme 5.1.*** The main components are:

1. Conveyor belt for automatic feeding of biomass into the gasifier
2. Fixed bed gasifier with a thermocouple to measure the temperature in the reduction zone (T1~800-900 ºC)
3. Platform to measure and control the biomass mass fed into the gasifier
4. Air heat exchanger
5. (A/B) Water heat exchanger
6. Cyclone to remove particles and ashes produced during the biomass gasification process
7. Compressor to suck the generated syngas
8. Ignition torch

A downstream catalytic reactor configuration has been selected and placed in an oven in order to control its temperature. Two lines can be discerned in ***Scheme 5.1,*** the main line in yellow, labelled as raw line, and a secondary line in green for the catalyst, labelled as cata line. In order to evaluate the catalytic efficiency for tar content reduction, two lines, labelled as raw (yellow) and cata (green) line, with two compressors to suck the syngas were used. The temperature of the produced syngas is measured in the raw line (T2) and the temperature of the catalytic bed is followed by using a thermocouple placed at the middle of the reactor (T3). Both lines are equipped with a pressure differential indicator in order to measure the pressure drop (ΔP_1 and ΔP_2). A water circuit was added after the catalytic reactor in the cata line in order to cool down the generated syngas (water-quenching). The real biomass gasification pilot plant is shown in ***Figure 5.1.***

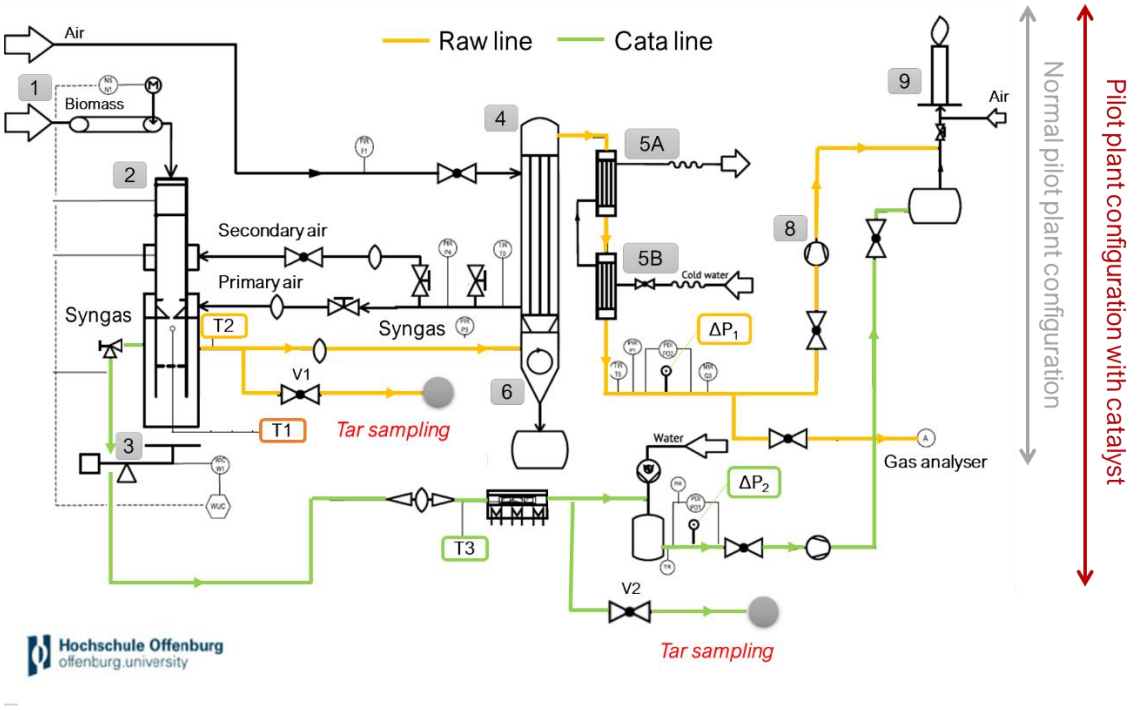

Scheme 5.1. Biomass gasification pilot plant configuration

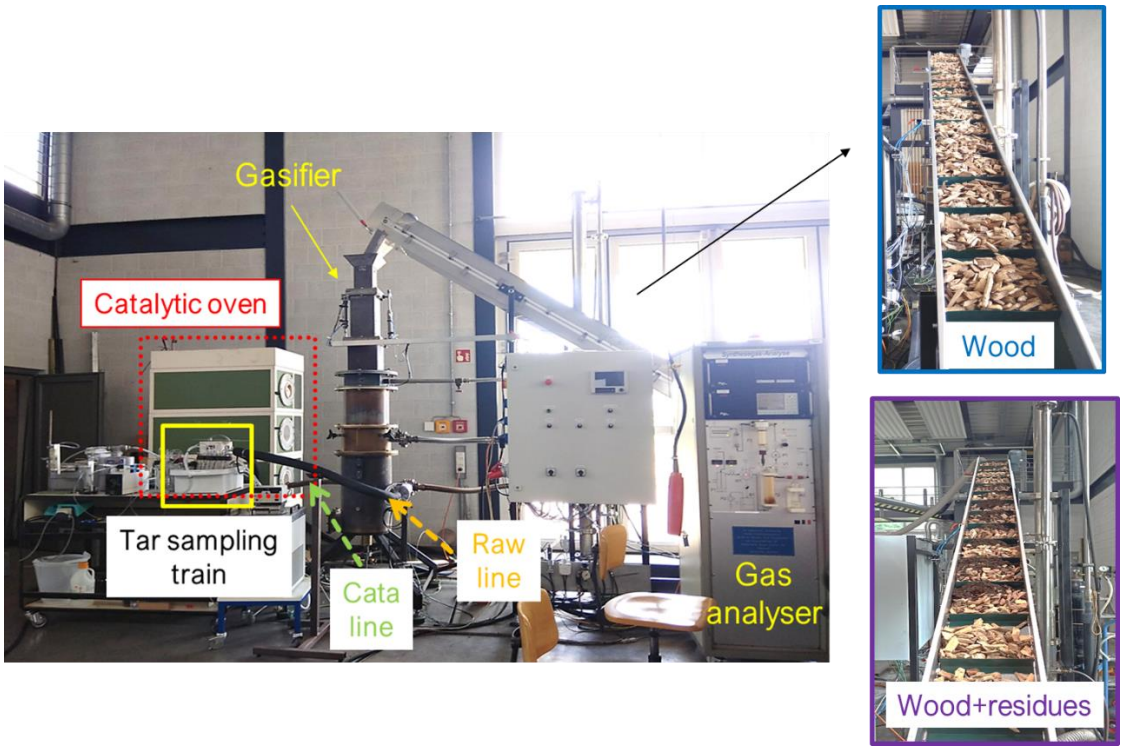

Figure 5.1. Biomass gasification pilot plant rig

A catalytic reactor of 50 cm length with an internal diameter of 7.3 cm was used. The reactor was divided into three different inert pipes and closed with perforated plates as can be seen in ***Figure 5.2***. The catalysts were placed at the middle of the reactor, whereas

the first and last pipe were filled with metallic rasching rings in order to avoid dead spaces and, thereby, reach an equal flow through the catalytic reactor. Moreover, the use of these rings at the inlet of the reactor let to heat up the syngas generated during the biomass gasification before being in contact with the catalyst.

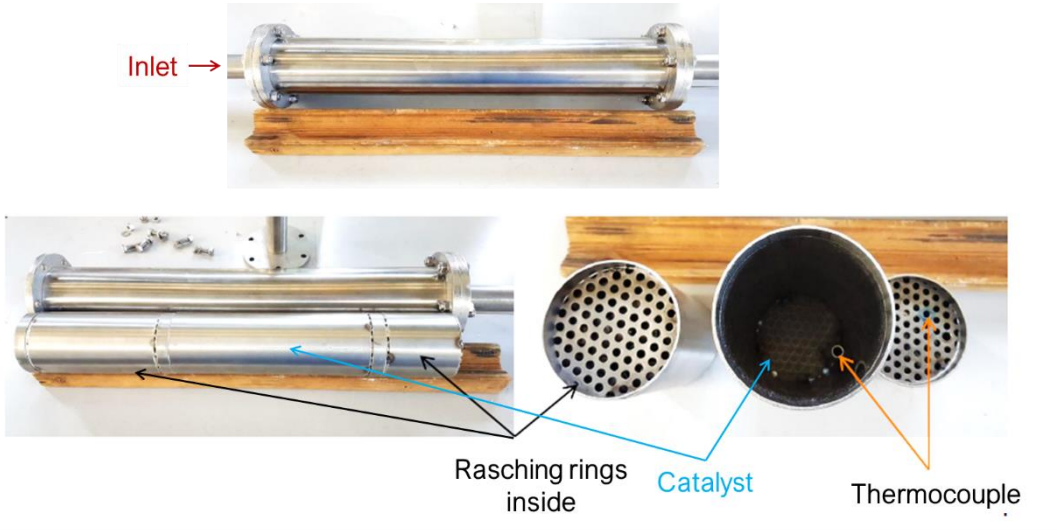

Figure 5.2. Catalytic reactor used at pilot plant scale

5.3.2. Tar collection and analysis

The tars collection was performed following the technical specifications entitled as "Biomass Gasification – tar and particles in product gases – sampling and analysis" (CEN/TS 1534:2006), published by the European Committee for Standardization (BT/TF 143). A general scheme of the CEN/TS sampling train for tar and particles along with a specific scheme of the DIN method for the tar collection is shown in ***Scheme 5.2.*** Thus, four modules are distinguished in the general scheme (***Scheme 5.2 (a)***):

- ***Module 1*** is a gas preconditioning step used for gas cooling and pressure letdown.
- ***Module 2*** consists in a heated filter at high temperature for the separation and collection of solid particles.
- ***Module 3*** is the tar collection step. It could be conducted by DIN method (6 impinger bottles) or using a Peterson column.
- ***Module 4*** is a volume measurementstep. This module consists in a pump for the gas suction, a gas meter, rotameter and barometer. The gas meter is used to determine the volume of sampled gas. In addition, the gas flow is monitored with a rotameter located between the pump and the gas meter, which is used to

adjust and compensate the sample flow. Eventually, the sample gas must be safely vented to atmosphere.

In the present work, the tar collection has been carried out by using the DIN method (***Scheme 5.2 (b)***). A series of six impinger glass bottles of 250 mL volume, the first five containing 100 mL of isopropanol and the last one empty, were placed in a heated bath (1, 2, 4) and a cold bath (3, 5, 6). The temperature of the heated and cold bath was +40 ºC and -20 ºC, respectively. The duration was around 45 min and the gas volume quantified was around 300 - 340 NL for each sampling. Afterwards, the sampling solution was weighed and stored into a dark bottle. The analysis of the samples were carried out *via* gas chromatography equipped with a flame ionization detector (FID). The column and the conditions of the analysis used were the same as at laboratory scale

It should be underlined that two tar sampling trains, each one equipped with six impinger glass bottles was used in order to perform the collection of tar simultaneously in the two operating lines (raw and cata line). This operating mode was used to evaluate the real effect of the catalyst even under non-steady state conditions.

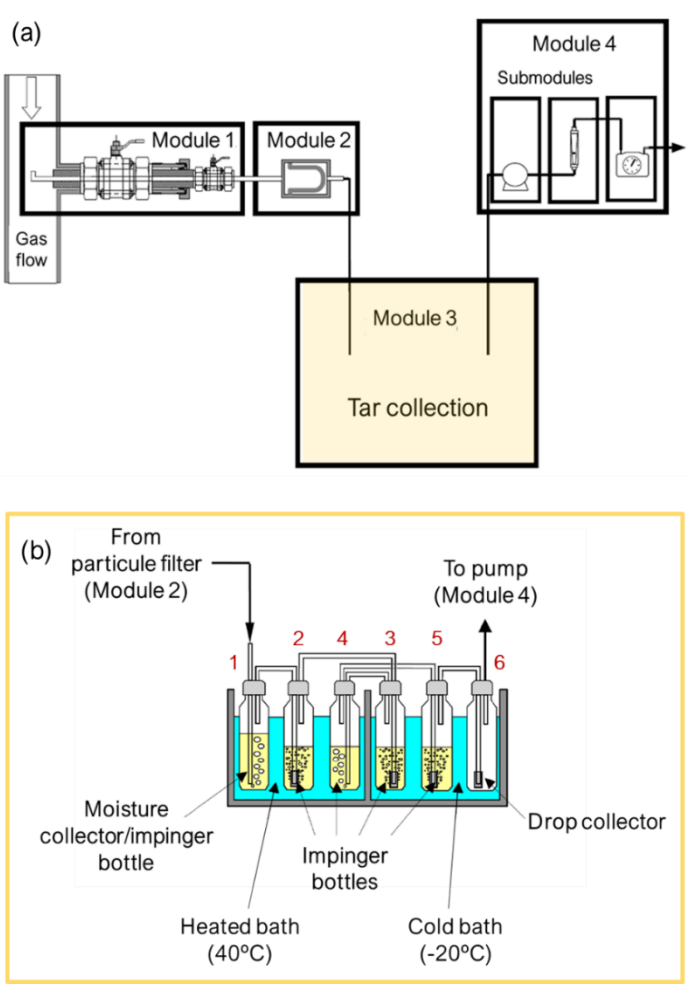

Scheme 5.2. The CEN/TS sampling train set-up (a) general configuration for tar and particles (b) DIN method for tar collection

5.3.3. Catalytic test: procedure and conditions

The main characteristics of the catalytic beds used are listed in ***Table 5.1***. As can be seen, a volume of a 1.0 L with a mass of Ni varied from 3.2 to 5.0 g was introduced into the catalytic reactor for the different catalytic tests. The temperature (T3) as well as the pressure drop (ΔP_2) in the catalytic bed along the time interval were monitored for all the catalytic tests. Moreover, the composition of the generated raw syngas was analyzed on-line through an ABB analyzer.

Before the *in situ* pre-treatment, the catalytic bed was pre-heated until 500 ºC, without syngas passing through it, to avoid the possible condensation of tar present in the produced syngas during the biomass gasification. Once the operating conditions of the gasifier and temperature of the catalytic bed were stable, the produced syngas was introduced through the catalytic bed in order to reduce the catalysts. The time at which the syngas started to pass through the catalysts was considered as time zero of the catalytic

reaction. Thus, the pretreatment under syngas was performed at temperatures around 500 ºC for 2 h. After 1h of test, a tar sampling was performed in order to evaluate if the reduction of the catalysts could be achieved under real operating conditions. Subsequently, the temperature was increased until approximately 550-560 ºC and successive tar samplings were accomplished throughout a period of 4-5 h for all catalysts. Generally, the catalysts were operating 7-8 h under real biomass gasification conditions.

Additionally, the effect of the bare catalytic substrate (β-RSiC 8/5) in thermal tar decomposition in pilot plant conditions has been evaluated before the performance of the catalytic tests. Thus, 1.0 L of bare β-RSiC 8/5 extrudates were introduced in the catalytic reactor and exposed to the product syngas, with a total mass flow of 32 $kg \cdot h^{-1}$, during a time on stream of 3 h at 480 ºC. No tar conversion due to thermal decomposition and no modification of SiC properties after test have been observed and the detailed results are presented and discussed in *Appendix,* at the end of this chapter.

Two biomass feedstocks have been used: (i) wood chips and (ii) a mixture of 85 wt% of wood chips and 15 wt% of biogas residues.

	Feedstock	$m_{cata+ext}$ (g)	V_{ext} (L)	m_{cata} (g)	m_{Ni}^0 (g)	m_{Ru}^0 (g)
Ni/CY/RSiC 8/5	Wood	455	0.9	40	4.8	-
Ni/LSCF/RSiC 8/5	Wood	508	1.0	72	4.3	-
RuNi/LSCF/RSiC 8/5 (1)	Wood	509	1.0	63	3.2	0.5
RuNi/LSCF/RSiC 8/5 (2)	Wood+residues	487	1.0	67	5.2	0.3

Table 5.1. Main characteristic of the catalytic reactor at pilot plant scale

In this chapter, the catalytic test results are presented as:

- ***Conditions at the inlet of the catalytic reactor (or exit the gasifier)***: inlet gas composition (%), obtained by the online analysis using the ABB analyzer, and tar content ($mg \cdot Nm^{-3}$) calculated as follow:

$$tar\ content\ (mg \cdot Nm^{-3}) = \frac{mass\ of\ tar\ (mg)}{V_{gas}\ (Nm^3)} \qquad \textit{(Equation 5.1)}$$

where: $mass\ of\ tar(mg)$ is the amount of a given tar molecule calculated in the raw line for a given tar sampling, estimated by using the GC analysis and; V_{gas} is the corresponding total gas volume measured by the gas meter.

- ***Conditions in the catalytic bed***: temperature (ºC) and $WHSV_{gas}$ (h^{-1}) versus time on stream (h). The masses of deposited catalysts reported in ***Table 5.1*** were

taking into account for the estimation of the $WHSV_{gas}$. Whereas, the total gas mass flow through the catalysts was determined considering the pressure drop (ΔP_2) into the catalytic reactor.

- ***Tar conversion (%):*** the tar conversion calculated is an average value since is a result from a sampling taking in a given time interval (described in prior section). Therefore, the average tar conversion is calculated as follow:

$$\chi_{\text{tar}}(\%) = 1 - \left[\frac{(m_{tar}\cdot Nm^{-3})_{\,cata}}{(m_{tar}\cdot Nm^{-3})_{raw}}\right] \qquad \textit{(Equation 5.2)}$$

where: $m_{tar}\cdot Nm^{-3}$ is the content of tar calculated by mean of the GC analysis of the corresponding samplings recollected through the raw and cata line. Thereby, the $(m_{tar}\cdot Nm^{-3})_{raw/cata}$ is the tar content at the inlet (raw line) and at the outlet (cata line) of the catalytic reactor.

5.4. Catalytic test results

5.4.1. Biomass feedstock: wood chips

The addition of biomass was programmed to maintain a biomass amount interval into the gasifier of 1.6-2.2 kg and is controlled by the platform located under the gasifier (***Scheme 5.1.***). Thus, the biomass flow rate varied from 16 to 19 $kg{\cdot}h^{-1}$ during the test time interval for all catalytic tests. The water content in the wood chips was 8 wt%

5.4.1.1. Ni/CY/RSiC 8/5 catalyst

Figure 5.3. displays the gas composition and the tar content at the inlet of the catalytic reactor versus the time on stream for Ni/CY/RSiC 8/5 catalyst. The grey zones correspond to the time intervals for which the tar samplings were conducted. As it can be seen in ***Figure 5.3 (a)***, the syngas composition remained stable during the catalytic test and is roughly of ~ 20 % CO, 15 % H_2, 12 % CO_2 and 1.4 % CH_4 (dry composition). The tar content was not stable over the duration of the test, a general decrease with time on stream can be observed ***Figure 5.3 (b)***. As reported in literature, the tar generated in biomass gasification is function of many factors such as operating conditions, gasifier type, gasifying agent, etc [35]. Thereby, these modifications in the inlet tar content might be caused by some differences in the operating conditions of the gasifier with the operating time or by different moisture contents in the wood chips used as feedstock. The temperature of the gasifier remained constant during the whole interval of time for this catalytic test (see ***Figure***

5.28 in *Appendix*), indicating stable conditions of the gasifier. Thus, differences of the inlet tar content caused by variations in the operational conditions might be rejected.

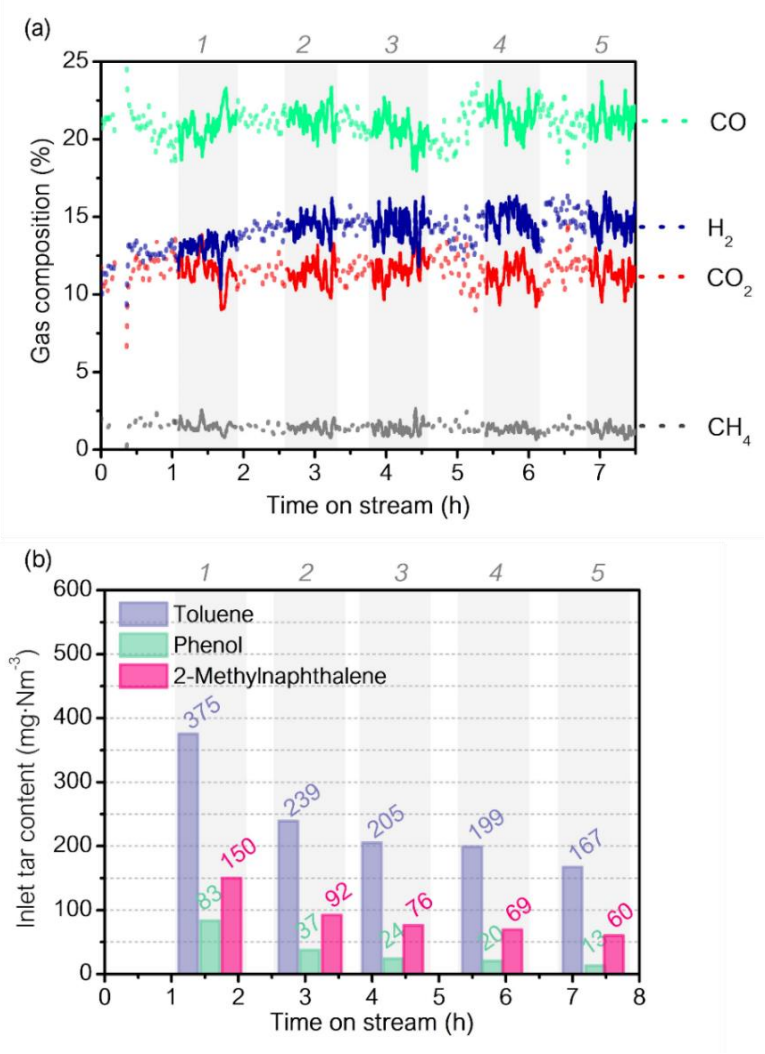

Figure 5.3. Conditions at the inlet of the catalytic reactor (a) inlet gas composition and (b) inlet tar content for each tar sampling versus time on stream

The modifications of temperature as well as the $WHSV_{gas}$ and the average toluene conversion estimated for each tar sampling interval (grey zones) in function of time are plotted in ***Figure 6.4*** for Ni/CY/RSiC 8/5. The average tar conversion of other tar molecules such as phenol, benzene and 2-methylnaphtalene is reported for each tar sampling interval in ***Figure 6.5***. An initial average toluene conversion of 37% is attained after two hours of test at 500-510 ºC and WHSV of 460 h^{-1} (tar sampling 1), outstanding that the reduction of the catalyst under real operating conditions is feasible. A small decrease of the toluene conversion is then observed, followed by a gradual increase of the average toluene conversion in the time interval from 2h to 6h on stream. Thus, successive average toluene conversions of 27%, 42% and 61% are reached for tar samplings 2, 3 and 4, respectively.

During this time interval (from reaction time of 2h to 6h), the reaction temperature was stable at 550-570 ºC, whereas the $WHSV_{gas}$ drastically decreased from 330 to 210 h^{-1} between tar sampling 2 and 3 and, then, it remains stable. This decrease in the $WHSV_{gas}$ along with the slightly lower inlet tar content found for tar sampling 3 compared with sampling 2 (see ***Figure 5.3 (b)***) can, at least partially, elucidate the increase in catalytic activity found in tar sampling 3. Comparable operating conditions in term of $WHSG_{gas}$ (~250 h^{-1}) and inlet tar contents (~200 $mg \cdot m^{-3}$ of toluene, ***Figure 5.3 (b)***) are displayed during the collection of tars in sampling 3 and 4. Therefore, the higher average toluene conversion attained for tar sampling 4 (61%) than sampling 3 (42%) is directly associated to an increase of catalytic activity in tar removal. The lower inlet tar content shown for tar sampling 5 compared to tar sampling 4 (***Figure 5.3 (b)***) might explain the same average toluene conversion (~60%) displayed in both tar samplings, even though the reaction temperature decreases from 570 to 500 ºC. The same tendency with similar values compared to average toluene conversion is achieved for other tar molecules such as phenol, benzene and 2-methylnaphthalene, as it can be found in ***Figure 5.5.***

In conclusion, Ni/CY/RSiC 8/5 is able to be activated under syngas in real conditions and displays relatively good catalytic activity in terms of tar removal under real biomass gasification conditions after roughly 8 h on stream, without apparent catalytic deactivation.

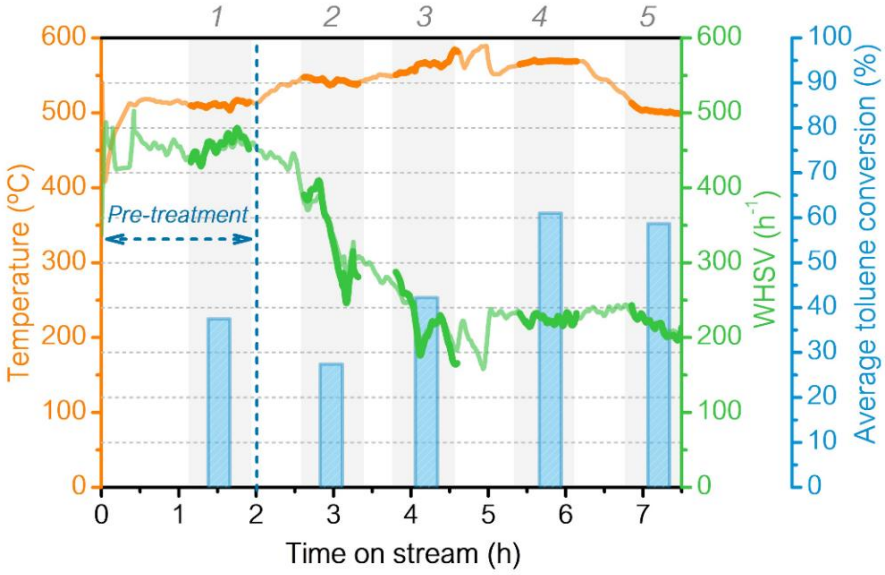

Figure 5.4. Operating conditions in the catalytic bed (T and WHSV) and average toluene conversion at atmospheric pressure for each tar sampling versus time on stream for Ni/CY/RSiC 8/5

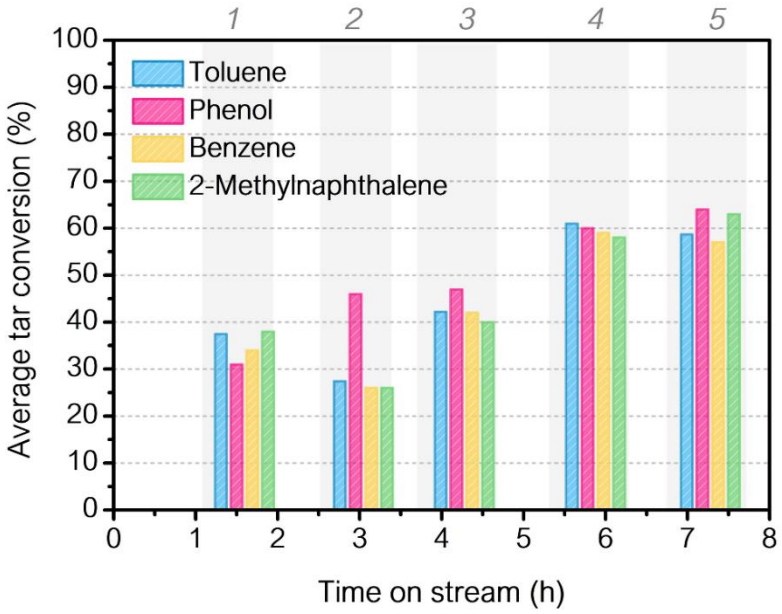

Figure 5.5. Average conversion of different tar molecules for each tar sampling versus time on stream for Ni/CY/RSiC 8/5

The catalytic surface has been characterized after test by scanning electron microscopy (SEM) and by EDX elemental analysis in order to distinguish the changes in morphology and detect the elements present over the surface after tar removal under real biomass gasification conditions. The SEM image as well as the EDX elemental mapping of spent Ni/CY/RSiC 8/5 is shown in ***Figure 5.6.*** As it can be observed, the surface is enriched by inorganic compounds initially contained in the wood chips (Al_2O_3, TiO_2, Fe_2O_3, CaO, MgO, Na_2O, K_2O, SO_3, Cl…). Alkali earth metals such as Mg, Ca are the main deposits noticeable on the surface along with sulfur.

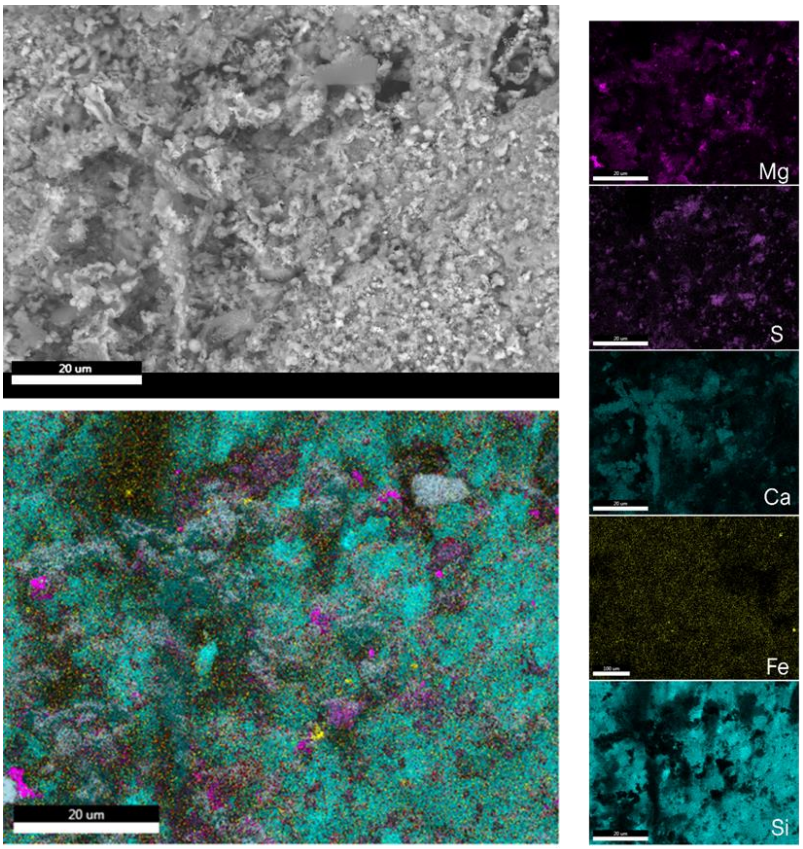

Figure 5.6. EDX element mapping of Ni/CY/RSiC 8/5 post – catalytic test

5.4.1.2. Ni/LSCF/RSiC 8/5 catalyst

The inlet gas composition (%) and tar content for each tar sampling measurement in function of time on stream is reported in ***Figure 5.7*** for Ni/LSCF/RSiC catalyst. As observed, the inlet syngas composition is stable for all the samplings (***Figure 5.7 (a)***) and similar to that attained in the previous catalytic test for Ni/CY/RSiC 8/5 catalyst (***Figure 5.3 (a)***). Thus, the inlet syngas (dry basis) is constituted by around 20.0% CO, 12.5% H_2 and CO_2 and 1.4% CH_4. As concern the inlet tar content (***Figure 5.7 (b)***), similar inlet values are achieved for the two first tar samplings, whereas slightly higher content is reached for the third one.

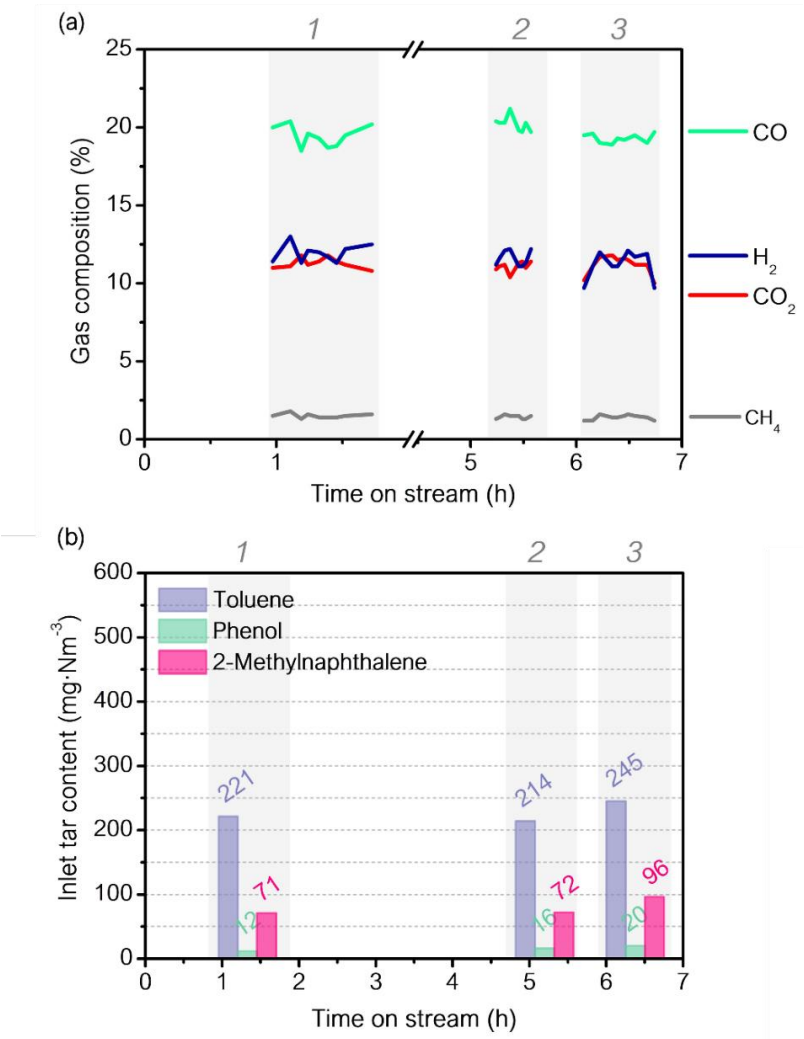

Figure 5.7. Conditions at the inlet of the catalytic reactor (a) inlet gas composition (%) and (b) inlet tar content for each tar sampling versus time on stream

The variations of temperature, $WHSV_{gas}$ and average toluene conversion in function of time is plotted in ***Figure 5.8*** for Ni/LSCF/RSiC 8/5. Additionally, the average tar conversion estimated for different tar molecules is also reported in ***Figure 5.9.*** No initial catalytic activity in term of average tar conversion is observed after 2 h of pre-treatment at 530 ºC and $WHSV_{gas}$ of 250 h^{-1} (tar sampling 1), except for phenol, exhibiting an average conversion of 39% (see ***Figure 5.9***). This fact suggest that the reduction of this catalyst is hard under real conditions and requires a more time on stream. Subsequently, the increase in reaction temperature until 550 ºC along with the decrease in $WHSV_{gas}$ (from 250 to 200 h^{-1}) lead to a boost of the catalytic activity, reaching an average toluene conversion of 65% after 5 h of test (tar sampling 2). Besides, this increase in activity inidicates that Ni/LSCF/RSiC 8/5 catalyst is able to be reduced under real conditions. A severe decrease in the average toluene conversion is noticeable after 6 h on stream (tar sampling 3), despite the softer

operating conditions (higher T and lower $WHSV_{gas}$) attained for this sampling compared to tar sampling 2. This decrease was also observed to the other tar molecules (***Figure 5.9***) and highlights the strong deactivation process undergone by Ni/LSCF/RSiC 8/5 catalyst after 6 h.

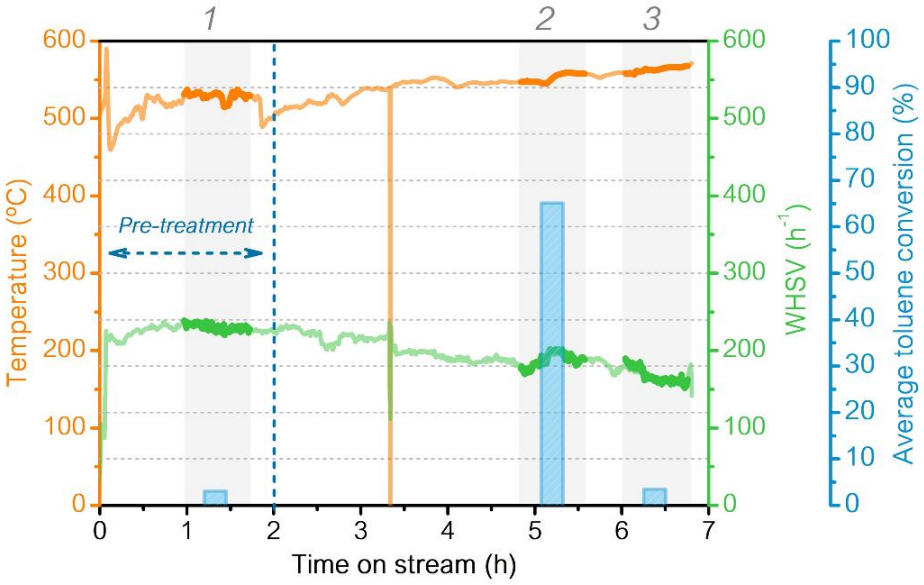

Figure 5.8. Operating conditions in the catalytic bed (T and WHSV) and average toluene conversion at atmospheric pressure for each tar sampling versus time on stream for Ni/LSCF/RSiC 8/5

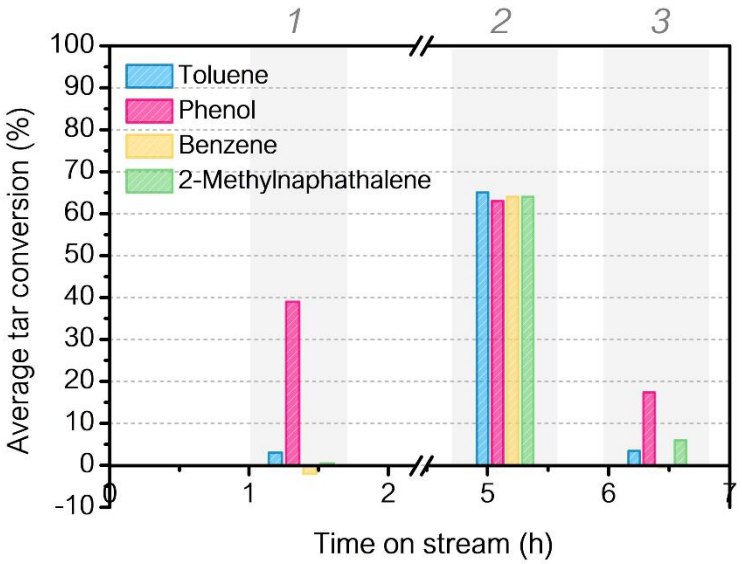

Figure 5.9. Average conversion of different tar molecules for each tar sampling versus time on stream for Ni/LSCF/RSiC 8/5 catalyst

Within literature, sintering of the active phase and/or coke deposition are the main causes of catalytic deactivation found for Ni-based catalysts. As observed in catalytic tests

performed on powdered and structured catalysts, Ni/LSCF is prone to form large amount of coke that could cause its catalytic deactivation under real operating conditions. Nevertheless, the deactivation by sintering as well as the irreversible adsorption of sulphur (present in the woodchips) on metal surface cannot be completely refused. To solve these drawbacks and improve the catalytic activity and stability, some research works reported the addition of transition and noble metals [152,259]. Others investigated catalytic regeneration methods for the deactivated catalysts [304–306].

In this work, the improvement of the catalytic activity and/or stability of Ni/LSCF/RSiC 8/5 catalyst has been investigated by two pathways: (i) *in situ* regeneration of Ni/LSCF/RSiC 8/5 catalyst and (ii) the use of Ru as dopant. The addition of Ru over Ni/LSCF catalyst and its influence in catalytic activity and stability has been prior studied for powdered (*Chapter 3*) and structured catalysts (*Chapter 4*). Likewise, its effect in the catalytic activity and stability under real operating conditions were also evaluated and will be presented in next section (*RuNi/LSCF/RSiC 8/5 (1)*). Regarding the catalytic regeneration, the regeneration method as well as a comparison in catalytic activity between the fresh and regenerated catalysts will be discussed in this section.

5.4.1.2.1. In situ regeneration: fresh vs regenerated Ni/LSCF/RSiC 8/5

Many catalysts regeneration methods have been widely reported in literature, being classified in six categories as follow: reduction with H_2, oxidation with Air or O_2, carbon gasification in steam, regeneration with produced synthesis gases, and combination of oxidation and reduction treatments [304,307]. An *in situ* regeneration under air atmosphere has been carried out for this study, since the carbon deposits seems to be the main factor for the deactivation of Ni/LSCF/RSiC 8/5, as it has been previously observed in catalytic test results at laboratory scale. In addition, it has been reported that temperatures below 600 ºC are enough to remove efficiently the carbon deposits by using air or oxygen atmosphere [307]. Thereby, the use of air could reduce the catalyst sintering compared to other regeneration processes.

In situ regeneration procedure: the regeneration process was conducted in the pilot plant. Without removing the spent Ni/LSCF/RSiC 8/5 catalyst from the set-up, the catalytic reactor was heated from room temperature to 600 ºC under air atmosphere using a total mass flow of 9.2 $kg \cdot h^{-1}$. Afterwards, the catalysts remained at 600 ºC for 1 h under air atmosphere with a total mass flow of 4.2 $kg \cdot h^{-1}$. After the regeneration, a catalytic test was conducted as for the fresh batches.

The inlet tar content versus time on stream for the regenerated catalyst for each tar sampling measurement is presented in ***Figure 5.10.*** As it can be seen in ***Figure 5.10 (a)***, the inlet tar content is stable for tar sampling 1 and 3, whereas it is slightly higher for sampling 2 and lower for sampling 4. Additionally, the inlet tar content decreases in the case of regenerated catalysts compared to the fresh one in all tar samplings (~100 $mg \cdot m^{-3}$ less of toluene) (***Figure 5.10 (b)***). No differences in the inlet gas composition compared to the fresh catalyst was discerned and the comparison of both inlet gas phases are presented in *Appendix (**Figure 5.29***), at the end of the chapter.

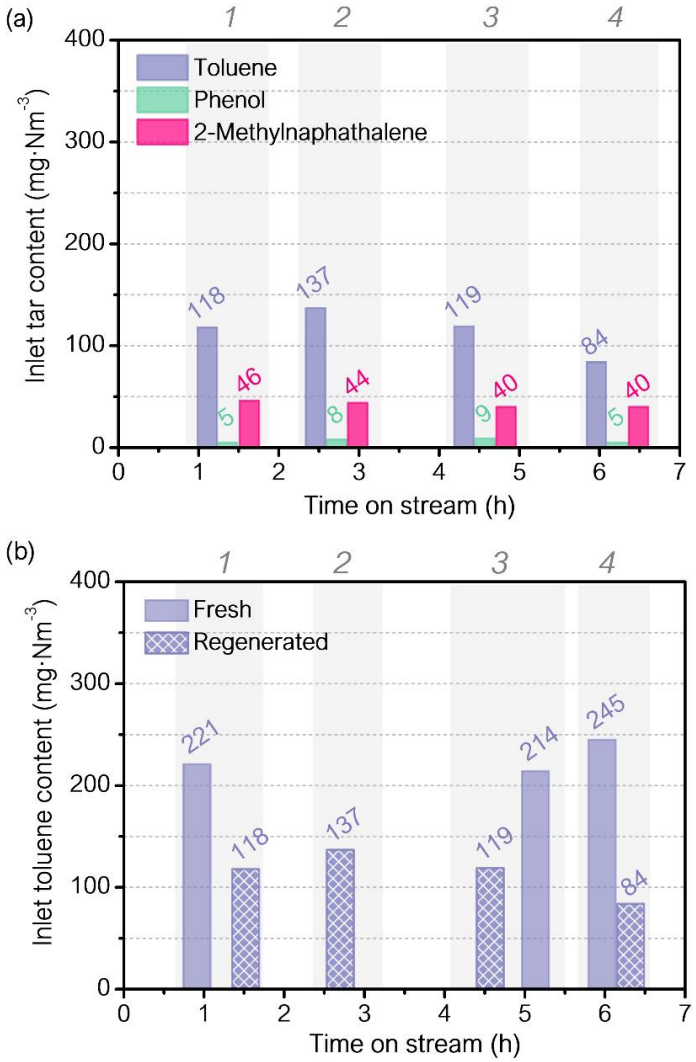

Figure 5.10. (a) Inlet tar content for each tar sampling versus time on stream for regenerated Ni/LSCF/RSiC 8/5 catalyst and (b) comparison between inlet toluene content for fresh and regenerated Ni/LSCF/RSiC 8/5 catalysts

A comparison of the operating conditions between the regenerated and fresh catalyst along the time on stream and the average toluene conversion reached for both

catalysts, regenerated and fresh, are displayed in ***Figure 5.11.*** The average conversions estimated for other tar molecules are shown in ***Figure 5.12*** for the regenerated catalyst. Regarding the operating conditions, a similar and stable reaction temperature is exhibited during the catalytic tests for both catalysts ***(Figure 5.11 (a)***). As expected, a lower $WHSV_{gas}$ is evidenced for the regenerated catalyst by comparing with the fresh one, due to the presence of accumulated particles into the reactor during the prior catalytic test. Alike in the fresh catalyst, the catalytic activity becomes notable after 4 h of test under real conditions, outstanding its low initial catalytic activity (***Figure 5.11 (b)***). This low initial activity can be also appreciated in the average conversion of other molecules in ***Figure 5.12,*** in which only an average phenol conversion of 40% and 25% is attained for tar sampling 1 and 2, respectively. It should be stressed that phenol is more sensitive to thermal decomposition than the rest of hydrocarbons under study, according to literature. Thereby, these initial conversion in phenol should not be only associated to the catalytic activity itself. After 4 h of test, the average toluene conversion was 41% (tar sampling 3) and raised up to 82 % after 6 h on stream (tar sampling 4) for the regenerated catalyst (***Figure 5.11 (b)***). The increase attained in tar sampling 3 might be associated to the decrease of $WHSV_{gas}$ found during this sampling in comparison with the two previous ones (***Figure 5.11 (a)***). The sharp increase in toluene conversion reached in tar sampling 4 can clearly be associated to the lower inlet tar content (***Figure 5.10 (a)***) and $WHSV_{gas}$ (***Figure 5.10 (a)***) evidenced for this sampling compared to tar sampling 3. As can be seen in ***Figure 5.12,*** similar tendency to that described for toluene is found in the average conversion of other tar molecules during tar sampling 3 and 4. The obtained trend can be also verified and supported by comparing the colours of the liquid phase recorded through the raw and cata lines for each tar sampling (***Figure 5.13***). Thus, the noteworthy change of colours between raw and cata line liquid phases appreciated for the last two tar samplings (3 and 4) clearly highlights the catalytic efficiency of the regenerated catalyst under real operating conditions. By comparison with the fresh catalyst (***Figure 5.11 (b)***), the regenerated catalyst shows similar average toluene conversion (41% compared to 45%) after 4 h of test (tar sampling 3), despite the fact that the regenerated catalysts underwent softer operating conditions (lower inlet tar content and $WHSV_{gas}$). This fact suggests that the regenerated catalysts provides lower catalytic activity than the fresh one. However, after 6 h of test, the regenerated catalyst is still active, exhibiting average tar conversion around 80%, whereas the fresh one is strongly deactivated. Thereby, the carbon deposits burned through the *in situ* regeneration method lead to an active catalyst after 6 h on stream with lower catalytic efficiency in tar removal than the fresh one. This decrease in catalytic activity after the regeneration might be

associated to other factors that cannot be regenerated by the regeneration method used. Among these factors are:

(i) catalyst sintering deactivation during the previous catalytic test conducted with the fresh batch [307].

(ii) deposition of elements present in gasification product gases, such as sulfurs, chlorines and alkali metals, on the catalytic surface. These elements can act as catalytic poisons and provokes irreversible loss of catalytic activity [308].

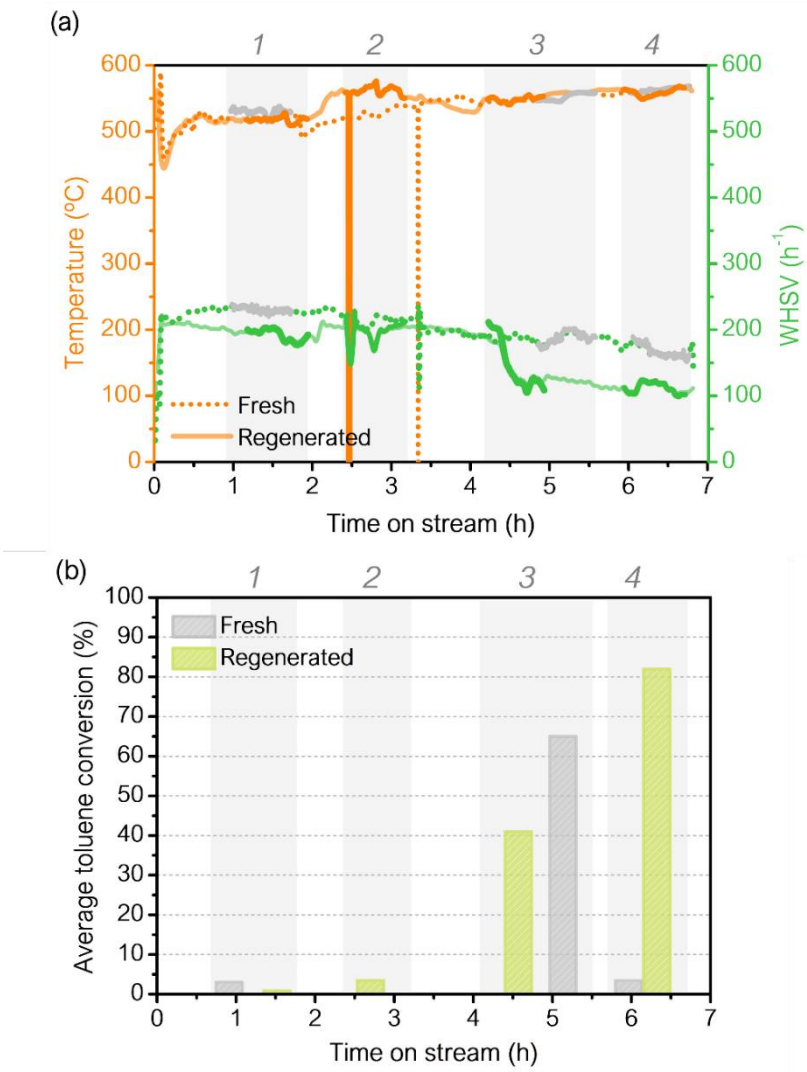

Figure 5.11. (a) Operating conditions in the catalytic bed (T and WHSV) for fresh (dot lines) and regenerated (solid lines) Ni/LSCF/RSiC 8/5 catalyst and (b) comparison of the average toluene conversion for each tar sampling versus time on stream

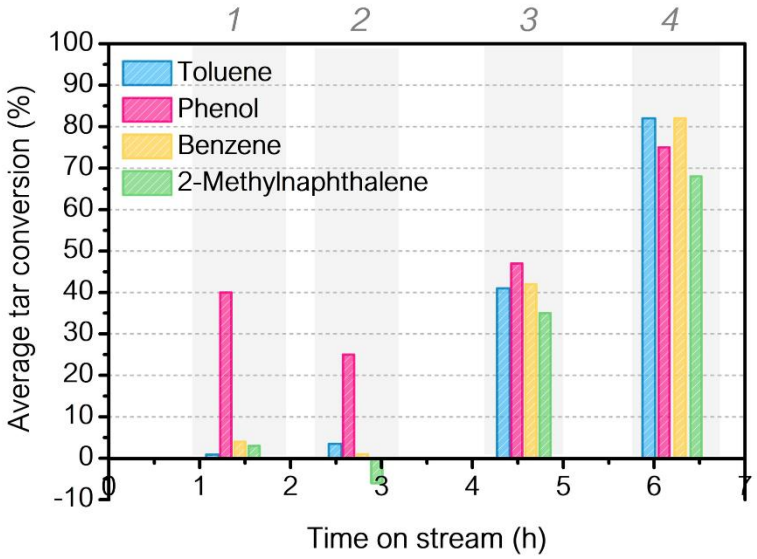

Figure 5.12. Average conversion of different tar molecules for each tar sampling versus time on stream for the regenerated Ni/LSCF/RSiC 8/5 catalyst

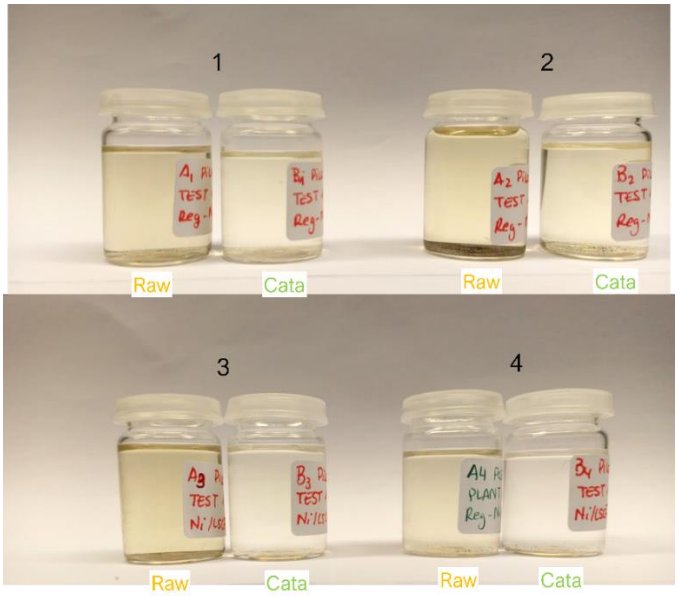

Figure 5.13. Comparison between the colours of the liquid phases obtained through raw and cata line for each tar sampling during the catalytic test of regenerated Ni/LSCF/RSiC 8/5 catalyst

Similarly, the morphology and composition of the catalytic surface for the regenerated Ni/LSCF/RSiC 8/5 after test has been evaluated by SEM and EDX analysis. The resulting SEM image and the EDX elemental analysis are reported in ***Figure 5.14.*** A textural changes surface is found for this catalyst after two catalytic cycles under severe operating conditions (***Figure 5.14 (a)***). In addition, a surface coated by inorganic elements such as Mn, Mg, Ca, P… coming from the initial biomass together with elements associated to the

perovskite support (LSCF) and Ni are revealed by the EDX elemental analysis of the selected zones (*Figure 5.14 (b)*).

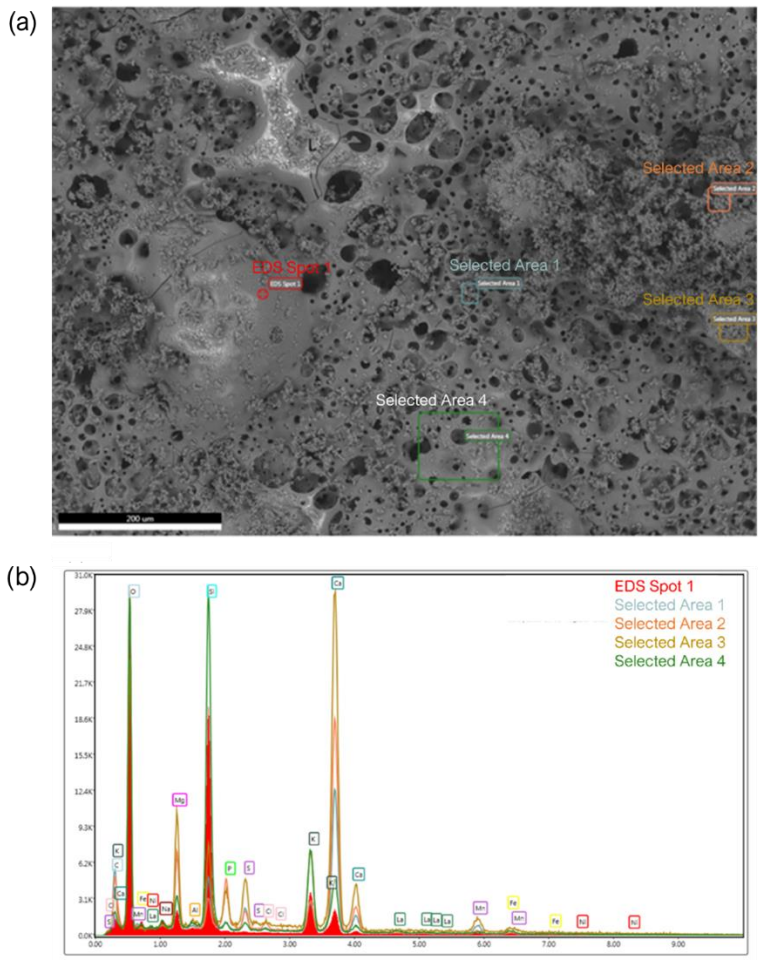

Figure 5.14. (a) SEM image and (b) EDX elemental analysis of regenerated Ni/LSCF/RSiC 8/5 post - catalytic test

5.4.1.3. RuNi/LSCF/RSiC 8/5 catalyst (1)

Similar to the prior studies with powdered and structured catalysts at laboratory scale, the effect of the use of Ru as a catalytic dopant over Ni/LSCF/RSiC 8/5 on the catalytic activity and stability has been also evaluated under pilot plant conditions. The inlet gas composition and the inlet tar content versus the time on stream are presented in ***Figure .15*** for RuNi/LSCF/RSiC 8/5 catalyst. The tendency followed by the syngas composition is constant along the time on stream as evidenced in ***Figure 5.15 (a).*** Moreover, the generated syngas displayed similar composition than that revealed in prior catalytic tests (~ 20% CO, 15% H_2, 12% CO_2 and 1.4% CH_4, dry basis). A slight decrease of the inlet tar content with time on stream is observed from tar sampling 1 to tar sampling 3, whereas an increase of the inlet tar content during tar sampling 4 is seen (***Figure 5.15 (b)***).

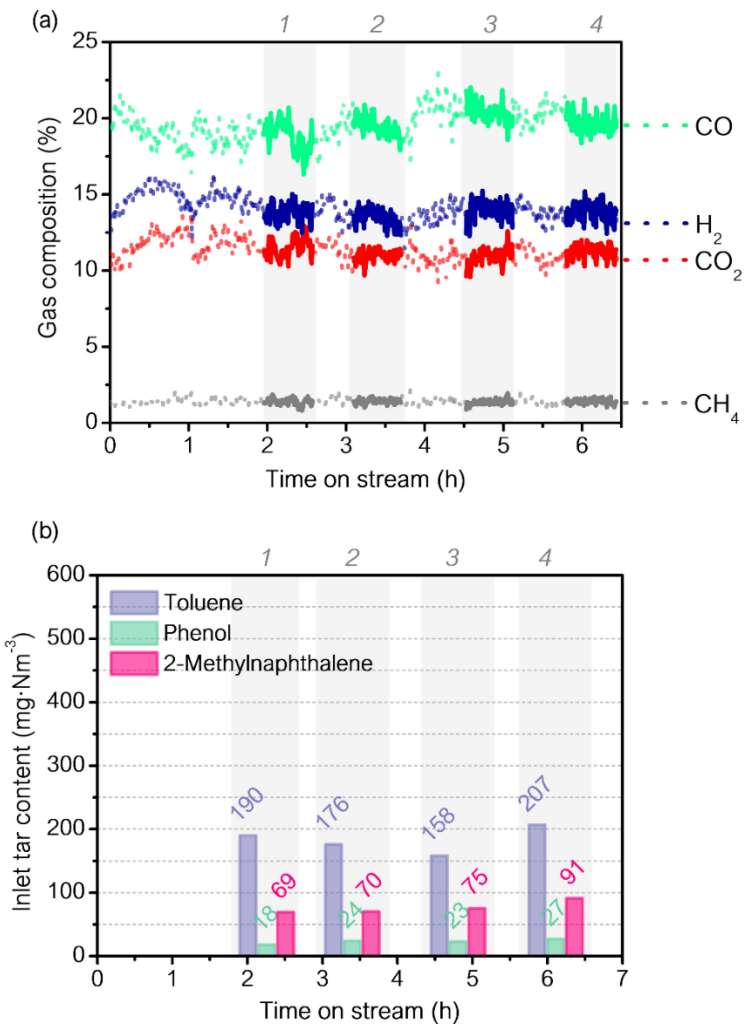

Figure 5.15. Conditions at the inlet of the catalytic reactor (a) inlet gas composition and (b) inlet tar content for each tar sampling versus time on stream

Alike the other catalysts, a pre-treatment process at 470 ºC for 2 h under real syngas composition was also conducted for RuNi/LSCF/RSiC 8/5. The variation of the operating conditions and the average toluene conversion in function of the time on stream is plotted in ***Figure 5.16.*** Afterwards, the temperature was raised up to 550-560 ºC and remained stable during all time interval. Concerning the $WHSV_{gas}$, constant values around 240-260 h^{-1} were attained for the three first tar samplings, whereas a decrease was noticeable during the last tar sampling (tar sampling 4), reaching an average value of 190 h^{-1}. The stable operating conditions attained for the first three tar samplings allow to evaluate the evolution of the catalytic activity and stability with the time on stream for the RuNi/LSCF/RSiC 8/5 catalyst. A relatively high initial catalytic activity is shown after 2-2.5 h of test (tar sampling 1), with an average toluene conversion of 62%. This toluene conversion is maintained after almost 4 h of test with a value of 60% (tar sampling 2). The catalytic

activity slightly decreases after 5 h on stream, with an average toluene conversion of 52% (tar sampling 3). The decrease in $WHSV_{gas}$ found in the tar sampling 4 allows to roughly recover the initial average toluene conversion (65 %). The average tar conversion of other molecules is plotted in ***Figure 5.17*** in function of time on stream. The low average benzene/2-methylnaphthalene conversion reached after 2 h of test (tar sampling 1) compared to toluene/phenol values might suggest the difficulty of these molecules to be reformed or the non-complete reduction of the catalysts after this time on stream. Additionally, the fact that benzene can be a by-product of toluene reforming could be another reason of the low conversion found for the former molecule. compared to the other tar molecules. In general, the RuNi/LSCF/RSiC 8/5 exhibits a much better catalytic activity in term of tar removal and stability compared to the non-Ru doped sample.

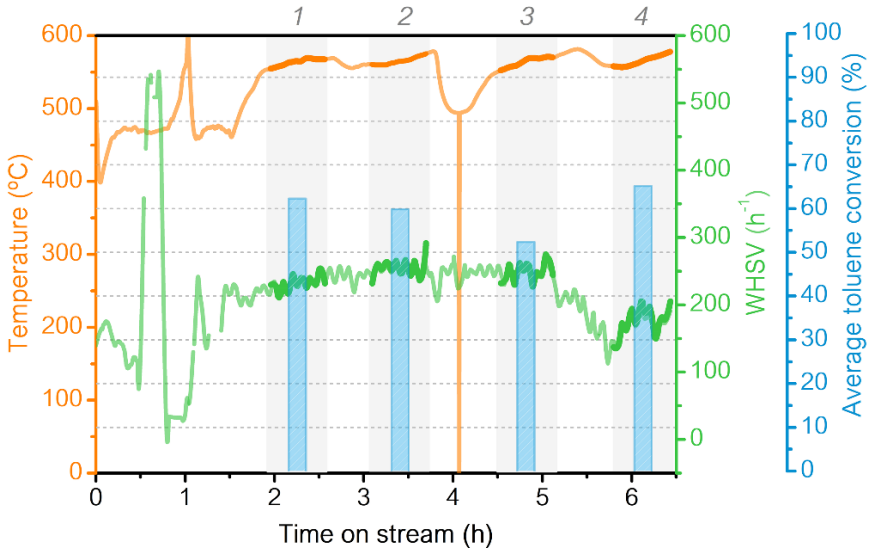

Figure 5.16. Operating conditions in the catalytic bed (T and WHSV) and average toluene conversion for each tar sampling versus time on stream for RuNi/LSCF/RSiC 8/5

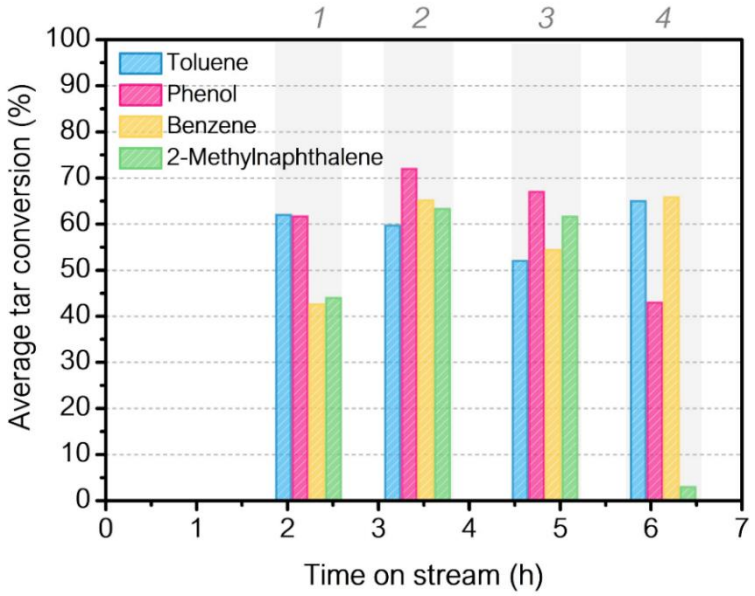

Figure 5.17. Average tar conversion of different tar molecules for each tar sampling versus time on stream for RuNi/LSCF/RSiC 8/5 catalyst

As already presented for the Ni-containing catalysts, the catalytic surface was as well characterized by SEM for RuNi/LSCF/RSiC 8/5 and the corresponding images and EDX elemental analysis are presented in ***Figure 5.18.*** Many carbonaceous deposits can be distinguished in ***Figure 5.18 (a),*** whereas several small dots and a large particle (clear zones), commonly associated to heavy elements such as transition metals, are discerned by chemical contrast mode (***Figure 5.18 (b)***). The EDX elemental mapping reveals that the huge particle and some dots are mainly composed of ruthenium, while the rest of the clear dots were not well identified and might be linked to Ni particles (***Figure 5.18 (c)***). Additionally, inorganic elements such as Mg, Ca and Na are also found on the surface as prior observed in the EDX elemental analysis of Ni/CY/RSiC 8/5 and Ni/LSCF/RSiC 8/5.

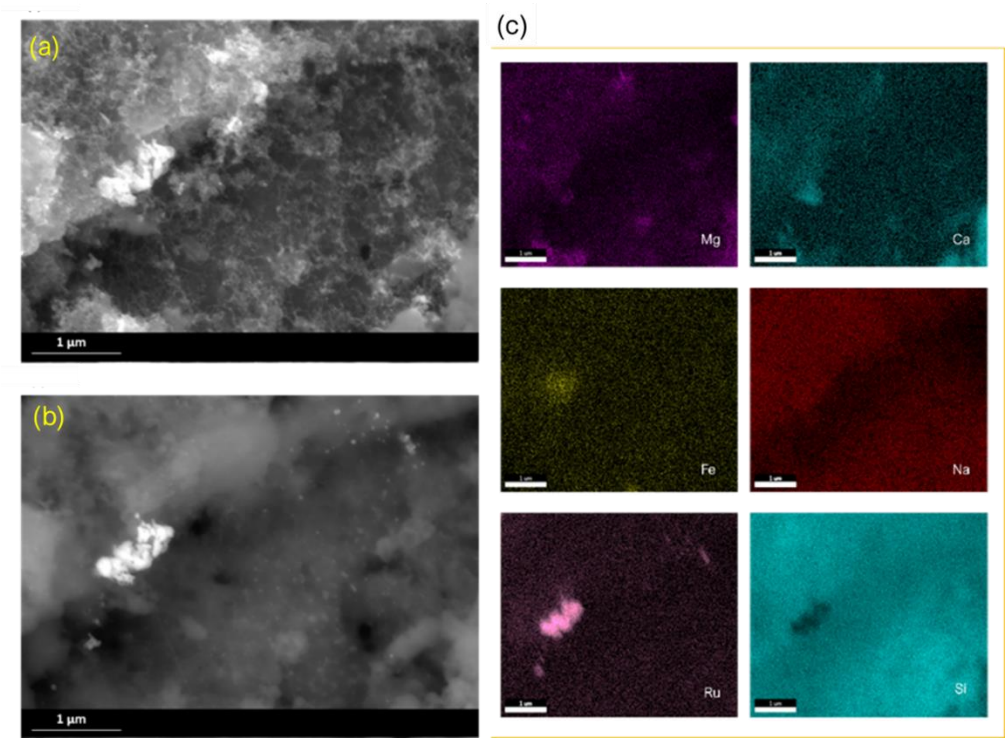

Figure 5.18. (a-b) SEM images and (c) EDX elemental mapping of RuNi/LSCF/RSiC 8/5 post – catalytic test

The catalytic regeneration and the use of noble metal for enhancing the catalytic activity of Ni/LSCF/RSiC 8/5 catalyst have been investigated. The *in situ* regeneration of Ni/LSCF/RSiC 8/5 provided an active catalysts in tar removal after 6 h on stream. As expected, the catalytic activity of the regenerated catalysts was lower than the fresh catalysts, since the fresh catalyst underwent to irreversible catalytic deactivation process during the catalytic test. The use of Ru led to a catalyst with much better catalytic performance, in term of catalytic activity in tar removal and stability, compared to the fresh and regenerated Ni/LSCF/RSiC 8/5 catalyst. Hence, it can be concluded that the use of noble metal result in an enhancement in the catalytic activity of Ni/LSCF/RSiC 8/5 catalyst compared to the regeneration process.

5.4.1.4. Comparison of catalytic performance

A comparison of the average toluene conversion between the three fresh catalytic batches (Ni/CY/RSiC 8/5, Ni/LSCF/RSiC 8/5 and RuNi/LSCF/RSiC 8/5) achieved under similar operating conditions is listed in ***Table 5.2.*** The color codes remark the tar samplings that are comparable, based on time on stream and operating conditions.

A lower initial catalytic activity is clearly displayed for Ni/LSCF/RSiC 8/5 than Ni/CY/RSiC 8/5 catalyst during the pre-treatment (green color), in spite of the softer

operating conditions performed for the former (530 ºC, 250 h^{-1}) than for latter catalyst (500 ºC, 460 h^{-1}). No tar sampling was conducted during the pre-treatment of RuNi/LSCF/RSiC 8/5 material (see ***Figure 5.16***). However, the tar sampling 1 (orange color) displayed for the latter catalyst was conducted instantly after the pre-treatment (2.3 h of test) and can thus give an idea about its initial catalytic activity. The average toluene conversion of 62% is attained at 2.3 h of test for RuNi/LSCF/RSiC 8/5 catalyst, whereas a 42% in average toluene conversion is reached for Ni/CY/RSiC 8/5 under similar operating conditions at 4.2 h on stream (orange color).

After 5-6 h of test, similar values in term of average toluene conversion (~ 50 - 65%) are found for all catalysts (yellow color). It should be underlined that Ni/LSCF/RSiC 8/5 catalyst was submitted to slightly lower $WHSV_{gas}$ (200 h^{-1}) compared to Ni/CY/RSiC 8/5 (220 h^{-1}) during the tar sampling. As can be seen, RuNi/LSCF/RSiC 8/5 exhibits an average conversion close to the initial one after 4.8 h on stream (~52%), highlighting its higher catalytic stability compared to the Ni containing catalysts (Ni/LSCF/RSiC 8/5 and Ni/CY/RSiC 8/5). Indeed, Ni/LSCF/RSiC 8/5 is strongly deactivate after 6.4 h of test under real conditions, whereas the activity remains stable after 7.3 h on stream for Ni/CY/RSiC 8/5 and RuNi/LSCF/RSiC 8/5 catalyst (blue color). Accordingly, the catalytic activity and stability at pilot plant scale decreases as follow: RuNi/LSCF/RSiC 8/5 > Ni/CY/RSiC 8/5 > Ni/LSCF/RSiC 8/5. Therefore, the RuNi/LSCF/RSiC 8/5 is the best catalyst in term of catalytic activity and stability under real biomass gasification conditions.

Catalyst	Tar sampling	Time on stream (h)	T (ºC)	WHSV (h^{-1})	Inlet toluene content ($mg \cdot Nm^{-3}$)	Average toluene conversion (%)
Ni/CY/RSiC	1	1.5	500-510	460	375	37
	3	4.2	550-560	215	205	42
	4	6.0	550-560	220	199	61
	5	7.3	500	220	167	58
Ni/LSCF/RSiC	1	1.3	530	250	221	3
	2	5.2	550-560	200	214	65
	3	6.4	560-570	160	245	4
RuNi/LSCF/RSiC	1	2.3	550-560	240	190	62
	3	4.8	550-560	260	158	52
	4	6.1	550-560	190	207	65

Table 5.2. Comparison of operating conditions and catalytic performances between the fresh catalytic batches

The tendency found is in concordance with what obtained in catalytic tests for powdered and structured catalysts. Indeed, in term of catalytic activity (based in toluene reforming results), the trend for powdered samples was Ni/CY (100%) > RuNi/LSCF (82%) > Ni/LSCF (54%) whereas in term of catalytic stability: RuNi/LSCF > Ni/CY. Within the structured catalyst, the catalytic activity decreased as follow: RuNi/LSCf/RSiC 8/5 > Ni/CY/RSiC 8/5 > Ni/LSCF/RSiC 8/5. In both, powdered and structured catalysts, Ni/LSCF – based catalyst was prone to coke formation, leading to the highest selectivity to coke among the three selected catalysts. This weakness has been associated to the facility of iron element to form stable carbides, generating high amount of carbonaceous species over the catalytic surface. This fact could explain the stronger deactivation attained for Ni/LSCF/RSiC 8/5 catalyst compared to Ni/CY/RSiC 8/5 and RuNi/LSCF/RSiC 8/5 under real conditions at pilot plant scale. In addition, considering the H_2-TPR profiles of the three catalysts prepared at large scale shown in ***Figure 5.19***, an additional reduction peak at low temperature (~ 290 ºC) is displayed for Ni/LSCF/RSiC 8/5, whereas this peak was not noticeable in the other to catalytic systems (the peak at around 200 °C is assigned to RuO reduction for RuNi/LSCF/RSiC 8/5 catalyst). This peak at low temperature has been ascribed to the reduction of NiO species with weak NiO-support-SiC interaction. Within literature, it has been reported that the metal – catalytic support interaction is an important factor to be considered for inhibiting deactivation by sintering process [305,309]. A strong metal – support interaction could avoid the migration of the metal along the catalytic support and, thus, prevent the metal sintering [295]. Accordingly, these NiO species weakly interacting with support-SiC make favourable the deactivation *via* sintering for Ni/LSCF/RSiC 8/5. This fact might explain the fast deactivation suffered by Ni/LSCF/RSiC 8/5 as well as the lower catalytic activity exhibited for the regenerated compared to the fresh catalyst.

Among other factors, the propensity to coke formation by iron element as well as the promotion of metal sintering due to a weak NiO-support-SiC interaction, might justified the low catalytic activity and strong deactivation evidenced for Ni/LSCF/RSiC 8/5 catalyst under real conditions in pilot plant.

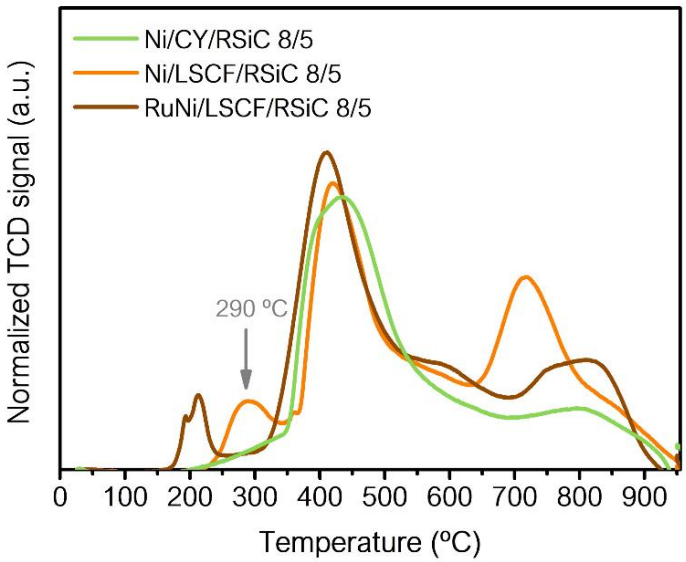

Figure 5.19. H_2-TPR profiles of the selected catalysts prepared at large scale

5.4.2. Biomass feedstock: mixture wood chips and residues

The main objective of the project is the complete utilization of wood as biomass through combination of thermal gasification, biogas and fermentation processes in order to increase the overall efficiency compared to the single processes. In order to investigate the effect of the incorporation with wood chips of these residues from these two biotechnological processes on the catalytic activity and stability, a catalytic test utilizing a mixture of wood chips and residues from biogas process has been carried out.

The best catalytic performances displayed for RuNi/LSCF/RSiC 8/5 catalyst under real conditions using wood chips as feedstock make it the best candidate to perform this catalytic test. In order to evaluate the influence of the addition of residues, a comparison of the operating conditions and the catalytic performance between the use of wood chips and the mixture with residues is presented in this section. Similarly, the biomass flow rate varied from 16 to 19 $kg \cdot h^{-1}$ during the whole intervale of time. The water content in the wood chips and the residues was 8 wt% and 46 wt%, respectively.

The inlet syngas composition and the inlet tar content versus the time on stream are respectively shown in ***Figure 5.20*** and ***Figure 5.21*** for both feedstocks. The addition of residues leads to an increase in H_2 and CO_2 with a decrease in CO compared to the bare wood chips (***Figure 5.20***). This increase could be associated to the higher water content introduced into the gasifier by the mixture wood (8 vol% H_2O) + residues (46 vol% H_2O) allowing high water gas shift reaction rate. As expected, a much greater tar content at the

inlet is attained by using the residues than the bare wood chips (***Figure 5.21***). Therefore, the catalyst was exposed to higher tar content during the catalytic test with residues.

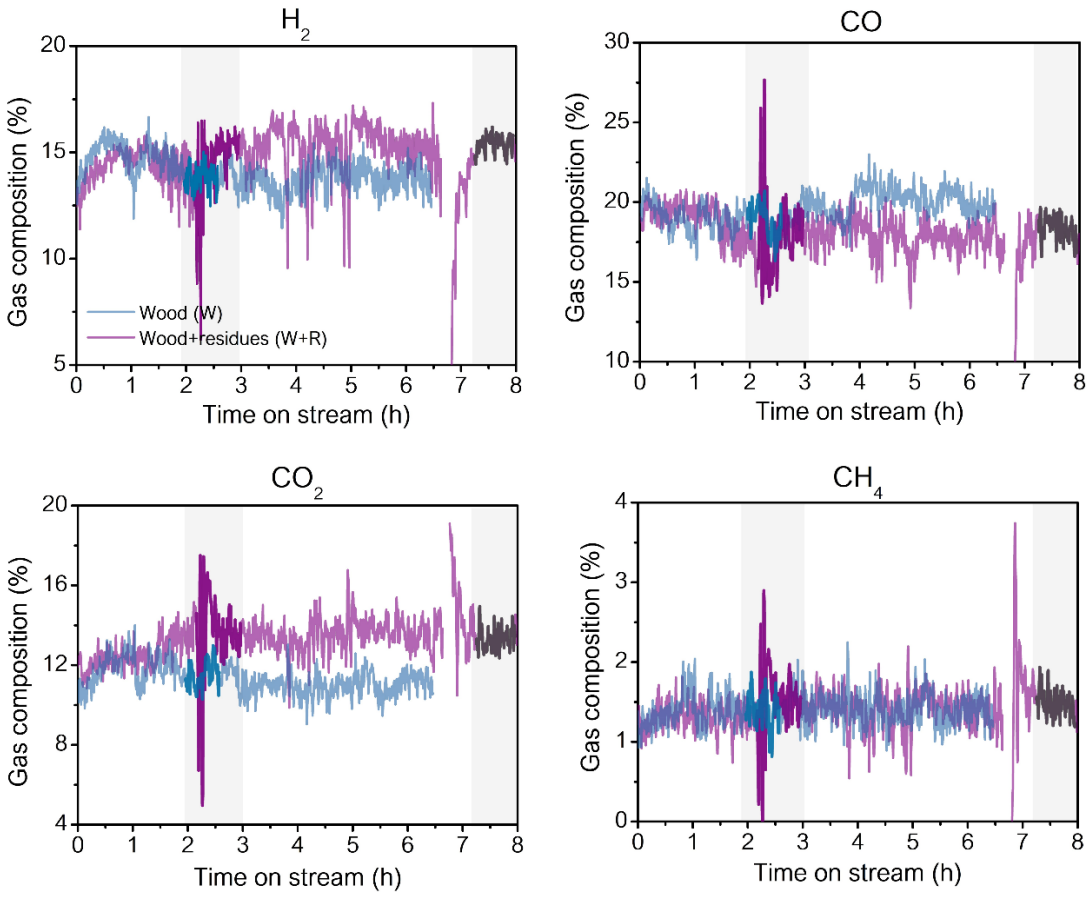

Figure 5.20. Comparison of inlet gas composition between two biomass feedstocks: wood (W) and mixture wood and residues (W+R)

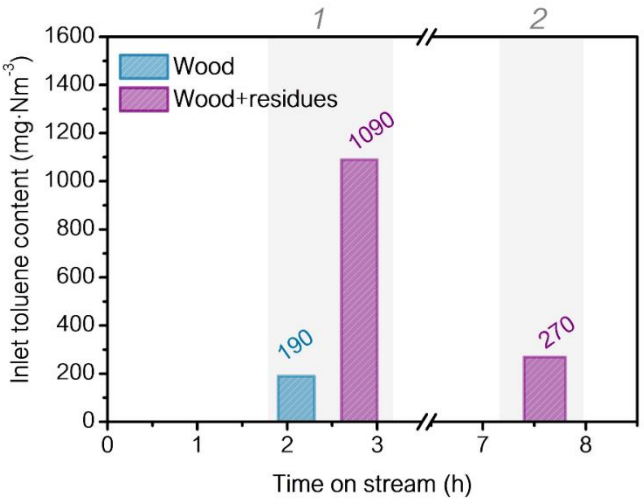

Figure 5.21. Comparison of inlet tar composition between two biomass feedstocks: wood (W) and mixture wood and residues (W+R)

The operating conditions as well as the average tar conversion are presented in ***Figure 5.22.*** Similar to the catalytic test with bare wood, the catalyst underwent a pre-treatment process under generated syngas from the biomass gasification process. The pre-treatment was conducted for 2 h at temperatures around 460-530 ºC (***Figure 5.22 (a)***). Afterwards, the temperature increased until values around 550-565 ºC close to that attained for the catalytic test with wood chips only (***Figure 5.22 (a)***). In addition, a lower $WHSV_{gas}$ was reached for the test with residues in comparison with the bare wood chips and drastically decreases with time on stream (***Figure 5.22 (b)***). This decrease in the $WHSV_{gas}$ is due to the accumulation of ashes and particles into the catalytic bed. Despite the lower $WHSV_{gas}$, the average tar conversion after 2 h of test generally decreased with the introduction of residues (***Figure 5.22 (c)***). Thus, an average conversion of 23% for toluene and 19% for benzene was obtained for the catalyst with residues, much lower than that reached without them (62 % for toluene and 43% for benzene). The lower catalytic efficiency obtained by adding residues can be attributed to the higher tar content into the catalytic reactor than using wood chips as feedstock (***Figure 5.21***). This fact is supported by the oily and dense phase recollected in the first tar sampling through the raw line due to the use of residues, outstanding once again the severe conditions reached (***Figure 5.23***). The phase is not noticeable after tar sampling through the cata line and it might due to the adsorption of these species over the catalytic surface. A second tar sampling was conducted after 7 h of test with residues in order to evaluate the catalytic stability under these conditions. The negligible average tar conversion attained points out that the catalyst underwent strong deactivation when residues were used. Therefore, the addition of residues as feedstock lead to dramatic decrease of the catalytic activity and stability of RuNi/LSCF/RSiC 8/5.

Pictures of catalytic beds bed after test with/without residues are shown in ***Figure 5.24*** together with the particlesfound inside the gasifier generated during the catalytic test with the biogas residues. A blockage of the rings due to the accumulation of particles is clearly observed in ***Figure 5.24 (a)*** for the catalytic bed after test with residues, which can explain the decrease in $WHSV_{gas}$ observed along time on stream (***Figure 5.22 (b)***). In addition, “pebbles” (5-20 cm length, see ***Figure 5.24 (b)***) formed by sintering of the residues are found inside the gasifier after the catalytic test. The formation of these paticles can cause several operational problems in the gasification process, such as blockage and high pressure drops.

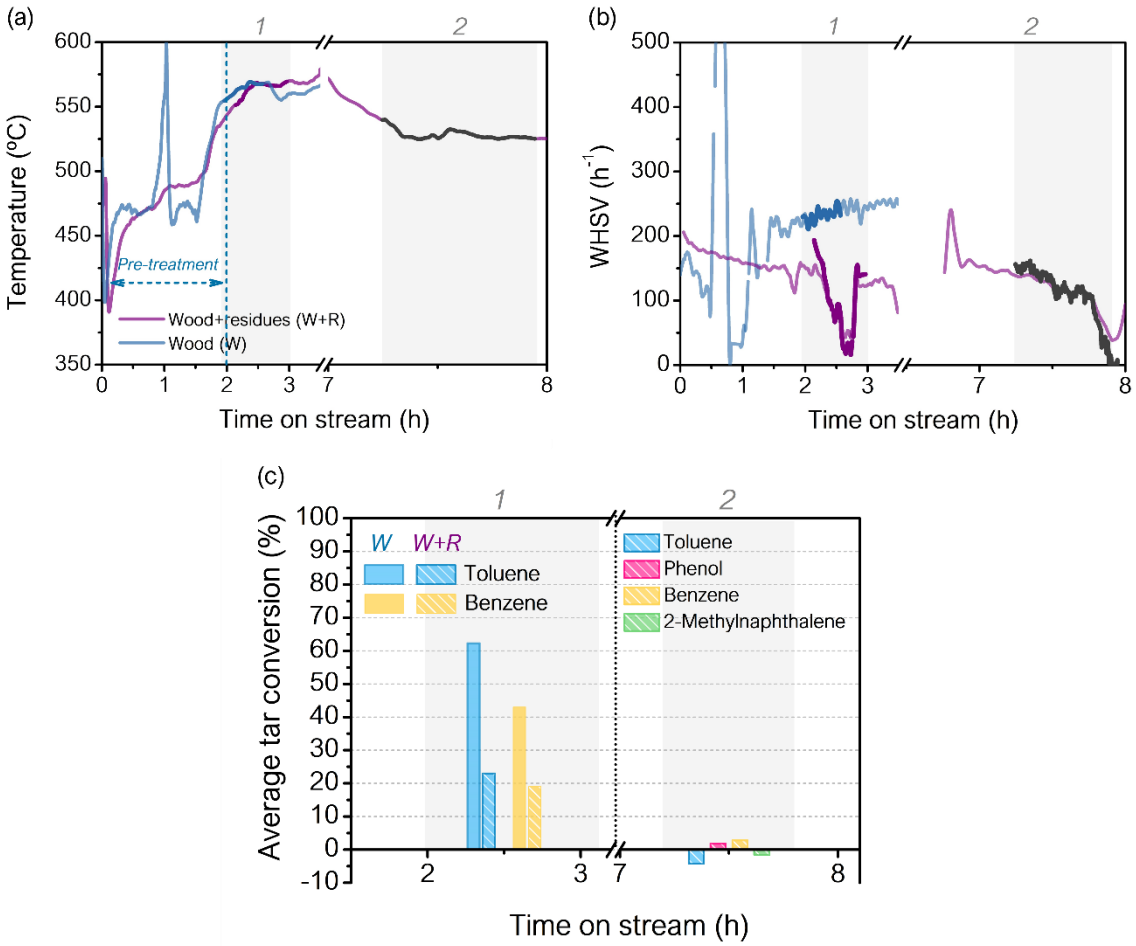

Figure 5.22. (a-b) Operating conditions in the catalytic bed (T and WHSV) and (c) average toluene conversion for each tar sampling versus time on stream for both feedstock (W and W+R)

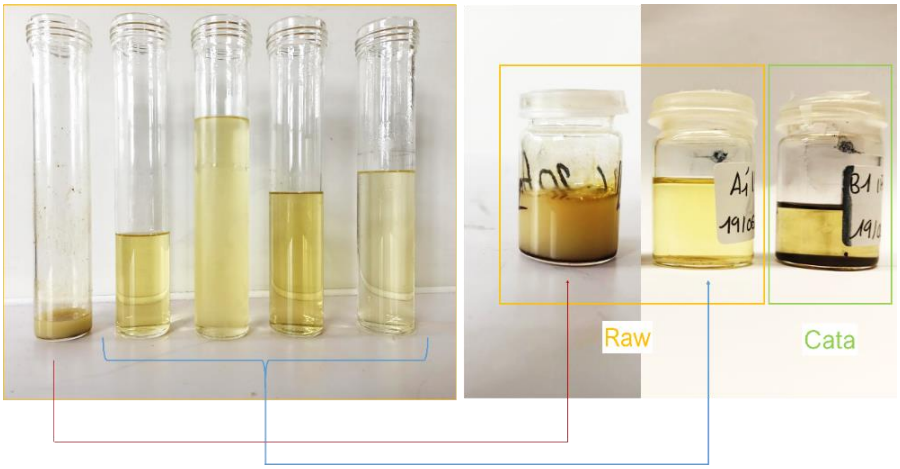

Figure 5.23. First tar sampling recorded through raw line and cata line during catalytic test with resides

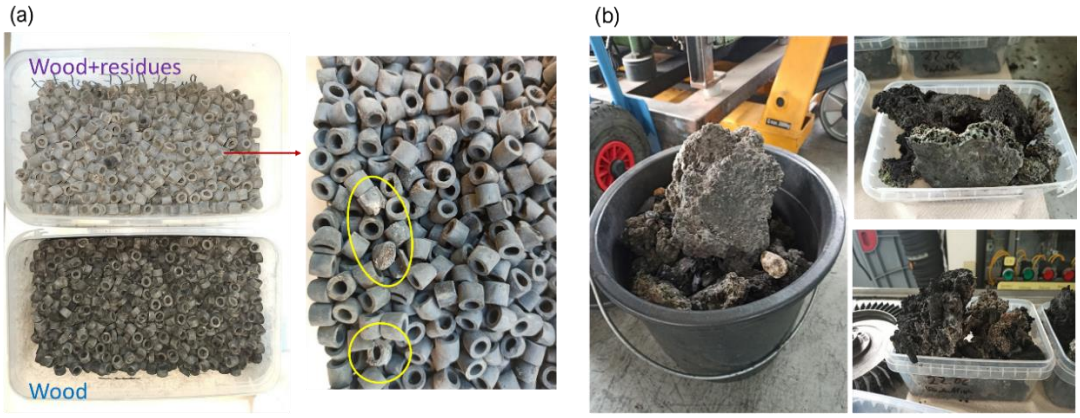

Figure 5.24. (a) Spent RuNi/LSCF/RSiC 8/5 catalyst and (b) stones found inside the gasifier after catalytic test with residues

The SEM images and the EDX elemental mapping of spent RuNi/LSCF catalyst after catalytic tests with residues are displayed in ***Figure 5.25.*** A catalytic surface coated by a sintered layer can be discerned in ***Figure 5.25 (a).*** A completely different surface morphology, with no noticeable carbon deposits, is observed for the spent catalyst post – catalytic test with residues (***Figure 5.25 (b)***) than that attained after test without residues (see ***Figure 5.18 (a)***). Additionally, the EDX mapping analysis corresponding for the surface shown in ***Figure 5.25 (a)*** reveals that the sintered layer is mainly composed of KCl and sulphur, no presence of elements associated to the catalytic support or active phase are noticeable. This fact suggest that the addition of residues results in a complete coverage of the catalytic surface by inorganic elements such as, chlorides and sulfurs, causing its deactivation.

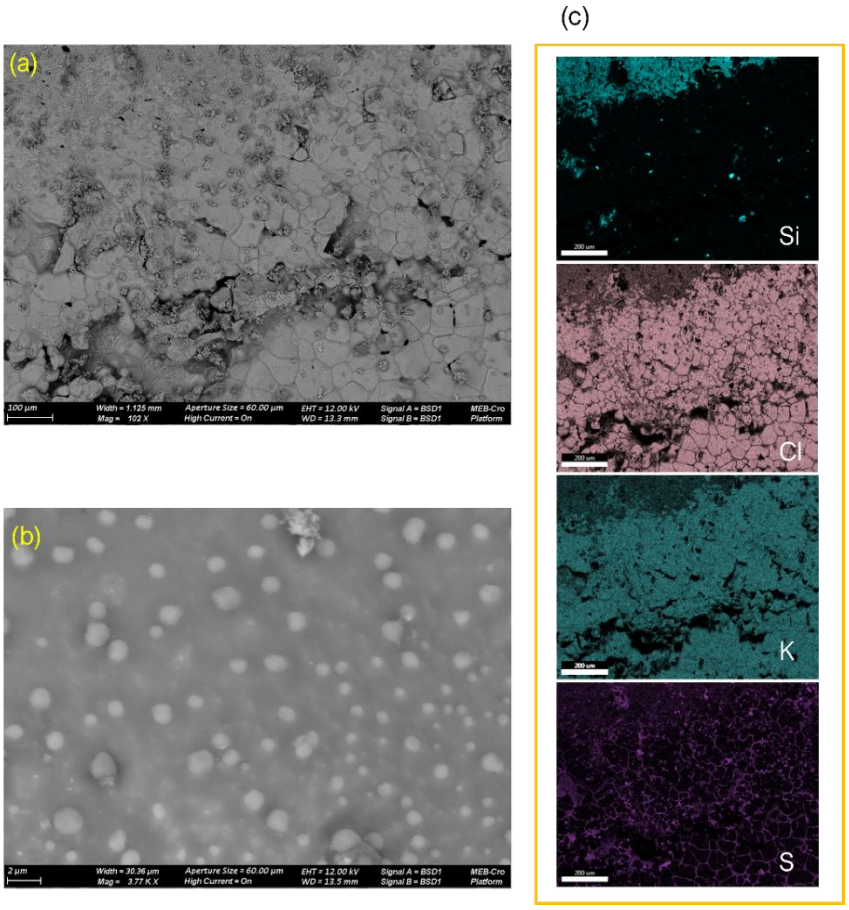

Figure 5.25. (a-b) SEM images and (c) EDX elemental mapping of RuNi/LSCF/RSiC 8/5 post – catalytic test

5.5. Literature comparison

As reported in the introduction of the present chapter, many catalytic tests under real conditions using commercial Ni based catalysts and Ni monoliths in a downstream catalytic reactor has been carried out by Corella and co-workers. The results of two different catalytic tests and the corresponding operating conditions, along with another study performed by using a Fe/olivine catalyst in an in-bed configuration informed by Rapagnà *et al.* [310] are listed in ***Table 5.3.*** It must be remarked that the comparison of results reported by different researchers has to be made carefully since many operation parameters can affect the final tar conversion and an omitted parameter can lead to a wrong conclusion. In the research shown by Corella and co-workers, the addition of dolomite into the gasifier led to introduce a tar content of 2 g·Nm^{-3} in the downstream catalytic reactor [299,303]. In the present work, the inlet tar content in the catalytic reactor was ~1 g·Nm^{-3}. As appreciated in ***Table 5.3***, a tar removal of 96% is attained for a nickel commercial catalysts, ICI 46-1, at 840 ºC whereas a conversion of 53% was displayed by using two monoliths in series, the first at high (800-850 ºC) and the second one at low temperature (400-300 ºC). In the

present work, an average tar conversion of 50-60% is found for RuNi/LSCF/RSiC 8/5 at low temperature (550-560 ºC) without needed a primary guard bed. By comparing operational temperature and GHSV, it can be concluded that the catalyst prepared in the present work performs high catalytic activity in tar removal at low temperatures. However, it should be stressed that the inlet tar content in the investigation reported by Corella was high and the use of dolomite into the gasifier led to a generated syngas with higher content of dust and particles. Tar conversions around 74% have been reported by Rapagnà *et al.* for the in-bed Fe/olivine catalyst. [310]. Olivine also contain active cations in tar reforming, that along with the high temperatures of the gasifier, should displayed better catalytic activity than the catalysts under study. By comparing both catalysts, the similar tar conversion attained in the present work at temperatures 250 ºC lower compared to the in-bed catalyst highlights, once again, the high efficiency of our catalyst in tar removal.

Catayst	Configuration	In-gasifier bed	Biomass flow ($kg \cdot h^{-1}$)	T_{bed} (ºC)	GHVS ($Nm_{wet}^3 \cdot m_{cat}^{-3}\ h^{-1}$)	Tar conversion (%)
In the present work						
RuNi/LSCF	*Downstream*	*Wood chips*	*17*	*550-560*	*52000*	*~50-60*
In literature						
ICI 46-1 [299]	Downstream	Pine wood chips + dolomite	10.7	840	3800	96
2 – layer Ni monoliths [303]	Downstream	Pine wood chips + dolomite	5.5	800-850 (T_1) 400-300 (T_2)	3563 ($GHSV_1$) 4523 ($GHSV_2$)	53
10 wt% Fe/olivine [310]	In-bed	Almond shells	0.3	828*	-	74

* Temperature in the gasifier

Table 5.3. Comparison of catalytic activity in steam reforming of tar conducted by the studied catalysts and other catalysts from the literature

5.6. Conclusions

The catalytic efficiency in tar removal of the selected catalysts prepared at large scale has been evaluated in a biomass gasification pilot plant equipped with a fixed bed gasifier. The catalytic test was carried out using a downstream catalytic reactor at same temperature as that used for the catalytic test at laboratory scale (550-560 ºC). The study was conducted by using two biomass feedstocks, wood chips and mixture of wood and

biogas residues. The three selected catalysts were able to be reduced and displayed catalytic activity in tar removal under real operating conditions using wood chips as biomass feedstock. Both Ni containing catalysts reached an average tar conversion of 60%. However, whereas the Ni/CY/RSiC 8/5 displayed catalytic activity after 6 h on stream, the Ni/LSCF/RSiC 8/5 underwent a strong deactivation. Moreover, a better initial catalytic activity was attained for Ni/CY/RSiC 8/5 compared to Ni/LSCF/RSiC 8/5. The quick catalytic deactivation exhibited by Ni/LSCF/RSiC 8/5 has been associated to its prone to coke formation through the generation of stable iron carbides and to the sintering process favoured by its weak NiO-support-SiC interaction.

In order to improve the catalytic activity and stability of Ni/LSCF/RSiC 8/5 catalyst, two pathways were considered: the *in situ* regeneration under air atmosphere and the addition of Ru. The active catalyst in tar removal after 6h of test attained for the regenerated catalyst through the *in situ* regeneration, highlighted the possible in situ regeneration of this catalyst in real operating conditions. An increase in the catalytic activity and stability was evidenced for the Ru containing catalysts (RuNi/LSCF/RSiC 8/5) compared to the bare Ni containing one (Ni/LSCF/RSiC 8/5), exhibiting a stable average tar conversion around 50-60 % along whole time on stream.

Thus, as observed for powdered and structured catalysts, the catalytic performance among the catalysts under real conditions decreased as follow: RuNi/LSCF/RSiC 8/5 > Ni/CY/RSiC 8/5 > Ni/LSCF/RSiC 8/5, displaying RuNi/LSCF/RSiC the best catalytic performance among the three catalysts.

Eventually, the addition of biogas residues into the gasifier led to a dramatic decrease in catalytic activity and stability for RuNi/LSCF/RSiC 8/5 catalyst. This decrease was associated to the increase in the inlet tar content and in the amount of inorganic elements present in the generated syngas.

Appendix of chapter 5

(i) Reaction blank: bare β-RSiC 8/5 -based extrudates

Table 5.4. shows the average tar conversion calculated for toluene, benzene and phenol after the reaction blank. As expected, no significant conversion due to thermal decomposition is noticeable after 3 h on stream. The conversion of 17% obtained for phenol points out the low thermal stability of the oxygenated compounds compared to the hydrocarbons, according to literature. Additionally, characterization of the spent RSiC 8/5 after the reaction blank has been carried out by using SEM and TGA analysis. The SEM image of the fresh and spent RSiC 8/5 are shown in *Figure 5.26.* No apparent modification of the SiC morphology is caused by the real operating conditions. Eventually, the possible formation of carbon deposits during the blank reaction was evaluated by TGA analysis for the spent RSiC 8/5 and compared to the fresh one (*Figure 5.27*). As it can be clearly seen, a gain of mass due to SiC oxidation process is exhibited for the spent RSiC 8/5 with no noticeable loss of mass associated to carbon deposits.

To conclude, no thermal conversion is found using bare RSiC 8/5 under real conditions and it can be considered as an inert catalytic substrate.

	Average tar conversion (%)
Toluene	-2
Benzene	-1
Phenol	17

Table 5.4. Average tar conversion of different tar molecules after 3h on stream for bare RSiC 8/5

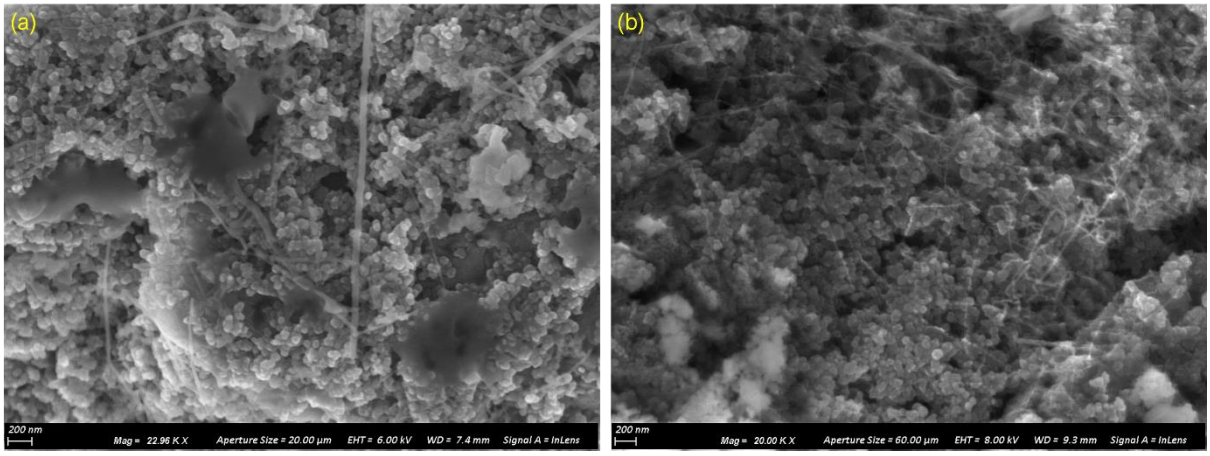

Figure 5.26. SEM images of (a) fresh and (b) spent RSiC 8/5

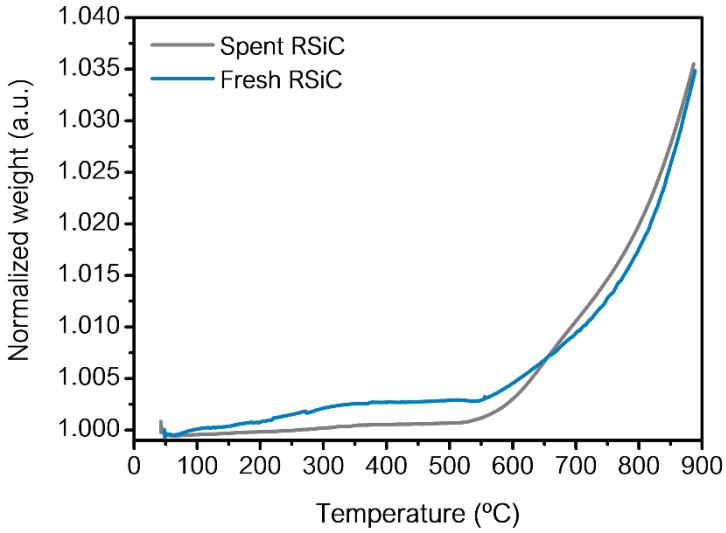

Figure 5.27. TGA analysis of fresh and spent RSiC 8/5

(ii) Catalytic test using wood chips as biomass feedstock

- *Ni/CY/RSiC 8/5 catalyst*

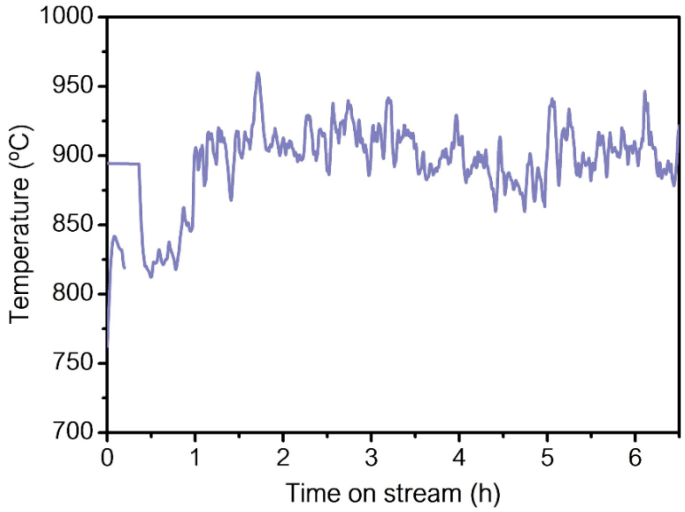

Figure 5.28. Variation of the temperature of the gasifier versus time on stream for catalytic test of Ni/CY/RSiC 8/5 catalyst

- *In situ regeneration of Ni/LSCF/RSiC 8/5*

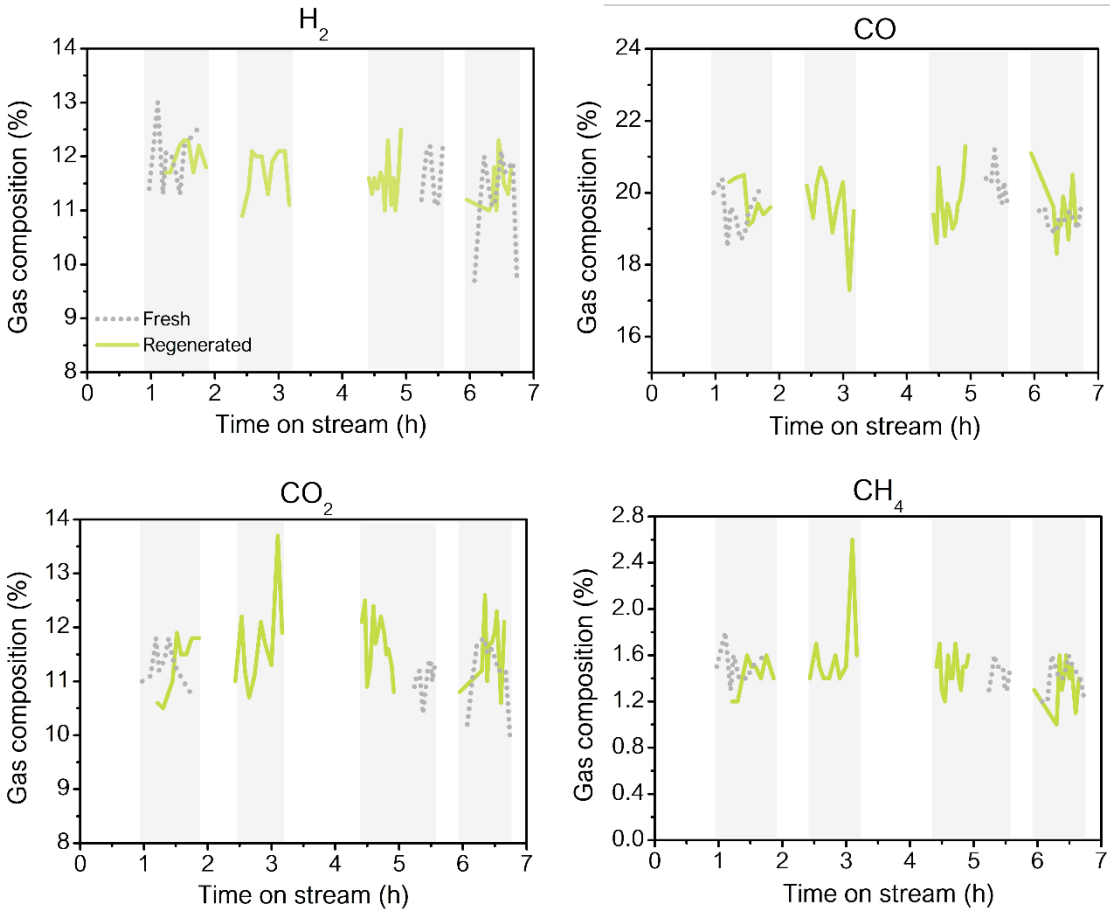

Figure 5.29. Comparison of the inlet gas composition between the fresh and regenerated Ni/LSCF/RSiC 8/5 catalysts for each tar sampling interval

General Conclusions and Perspectives

○ General conclusions

The objective of this PhD work was the development of catalytic systems and the optimization of their catalytic structuration at large scale for tar reforming under real biomass gasification conditions. These objectives are based on those set out in EBIPREP project, about the biomass valorisation by combination of thermochemical and biological processes. To this end, the present work has been divided in two main lines:

1) The synthesis and characterization of powdered catalysts (*Chapter 2*) and their evaluation in tar reforming at laboratory scale (*Chapter 3*)
2) The optimization of the catalytic structuration over SiC extrudates at laboratory scale with the subsequent scale up in batches of 1.1 L (*Chapter 4*) and, the final evaluation of theses batches at large scale in a biomass gasification pilot plant (*Chapter 5*).

Three supports with high oxygen mobility, $Ce_{0.63}Zr_{0.33}Sm_{0.04}O_{2-\delta}$ (CZS), $Ce_2Y_2O_7$ (CY) and $La_{0.6}Sr_{0.4}Co_{0.2}Fe_{0.8}O_{3-\delta}$ (LSCF), have been synthesized through pseudo sol-gel method. Six Ni-based catalysts with 10 %wt metal loading has been prepared using two different Ni addition pathways: (i) wetness impregnation (Ni/CZS, Ni/CY and Ni/LSCF) and (ii) one step pseudo sol-gel (Ni-CZS, Ni-CY and Ni-LSCF). Generally, no significant modifications in the physicochemical properties were found for the impregnated catalyst compared to the supports, whereas the partial insertion of Ni^{2+} species into the support's structures favoured by the one step sol-gel method led to some variations compared to the supports and the impregnated catalysts (*Chapter 2*).

The effect of both addition pathway and support in tar reforming reaction for the six prepared catalysts in powder were investigated (*Chapter 3*). For these studies, the use of two model tar molecules, phenol and toluene, has been used. Moreover, the effect of the reaction temperature (400 and 550 ºC) as well as the pre-treatment procedure (H_2/N_2 vs syngas) in the catalytic performance of these catalysts have been investigated. As expected, lower catalytic activity and higher carbon deposition were attained at low reaction temperature (400 ºC) compared to the high one (550 ºC). The catalytic results attained in phenol and toluene reforming for the six catalysts pre-treated under H_2/N_2 atmosphere revealed differences in reaction mechanism or reactivity over Ni surface between both molecules. Nevertheless, same tendency in catalytic activity and stability were found among the six catalyst for both molecules (Ni/CY > Ni-LSCF > Ni/LSCF ~Ni-CZS > Ni-CY > Ni-CZS). The reduction pre-treatment under syngas atmosphere demonstrated that most of the catalysts were able to be reduced in these conditions, however, the decrease in metallic

surface area along with the carbon deposits generated caused a decline in the catalytic activity toward tar reforming reaction. Considering the catalytic results obtained using H_2/N_2 pre-treatment and the ability of the catalyst to be reduced under syngas atmosphere, three catalysts were selected for their structuration over SiC extrudates (Ni/CY, Ni/LSCF and RuNi/LSCF).

Subsequently, the optimization of the catalytic structuration over SiC extrudates along with the characterization of the final structured catalysts and the evaluation of their catalytic activity in tar reforming at laboratory scale were explored (*Chapter 4*). The influence of the extrudate shapes, the coating concentration solution (0.30 M vs 0.60 M), the individual coating or in batch and the effect of solvent (water-propionic acid) as well as of SiC pre-treatment on the deposition were evaluated. Similar results were attained regardless the extrudate shapes. A diluted concentration solution led to lower deposited mass of support compared to the concentrated one. The use of batches of extrudates provided more accurate results compared to the individual coating. Eventually, the use of water as solvent resulted in a lower mass uptake than for propionic acid and no enhancement in the mass uptake were obtained by the pre-treatment of SiC extrudates. A modification in the crystalline structure and reducibility due to the structuration were observed for the final structured catalysts (Ni/LSCF/SiC and Ni/CY/RSiC) compared to the powdered catalysts. As regard the catalytic activity, the final structured catalysts were reduced under syngas atmosphere and tested in toluene reforming. The reduction of the structure catalysts under syngas was possible and similar average toluene conversion were attained among them, regardless the extrudate shape or the catalytic support, whereas different carbon selectivity was attained for the three extrudates shapes. By comparing with the equivalent catalysts in powder, an improvement of the catalytic activity toward tar reforming reaction were seen for the structured catalysts, and it has been associated to the strong Ni-support-SiC interaction. These catalytic results allowed the choice of the extrudate shape (RSiC 8/5) and the deposition conditions used in the structuration at large scale. Lastly, the scale up of the catalytic structuration indicated that the coating procedure was reproducible but did not allow to master a precise control of the deposited mass. Additionally, modifications in the Ni-support-SiC interaction caused by the preparation at large scale were evidenced.

In the end, the prepared batches of 1.1 L of the three selected catalysts (Ni/CY/RSiC 8/5, Ni/LSCF/RSiC 8/5 and RuNi/LSCF/RSiC 8/5) were tested in a real biomass gasification pilot plant at relatively low temperature (550 ºC) using wood chips and a mixture

of wood chips and residues as biomass feedstock (*Chapter 5*). The catalytic results found for the three catalysts using wood chips as feedstock were consistent with the catalytic behaviour obtained for the powdered and structured catalyst in tar reforming at laboratory scale (RuNi/LSCF/RSiC 8/5 > Ni/CY/RSiC 8/5 > Ni/LSCF/RSiC 8/5). Among them, Ni/LSCF/RSiC 8/5 catalyst underwent to a strong catalytic deactivation under real operating conditions. Thereby, this catalyst was regenerated *in situ* at pilot plant scale and the catalytic results revealed that an active catalyst after 6 h on stream can be attained, but a loss in activity was shown compared to the fresh one. While, an enhancement in the catalytic activity and stability were achieved by adding Ru over Ni/LSCF/RSiC 8/5 catalyst, leading to the best catalytic system among the three chosen. Finally, a decrease in the catalytic activity and stability in tar reforming were clearly discerned when biogas residues were introduced in the feedstock, probably caused by the increase in the tar content in the product syngas as well as in other inorganic elements.

By comparing the catalytic results of the present work with others reported in literature for the same kind of materials and model molecules, it can be seen that, either at laboratory or pilot plant scale, high catalytic activity was achieved in the present work at relatively low temperature (550 ºC). As general conclusion, catalytic systems efficient in tar removal from biomass gasification process have been developed in this research.

○ Future perspectives

Several perspectives can be suggested as results of this PhD work. Regarding the synthesis method, the optimization of the support preparation in order to find a good balance between the crystallinity and the textural properties and, thus, enhance the catalytic activity. In addition, deep characterization of the Ni based catalysts prepared through one step sol-gel in order to clarify "how" is nickel inserted into the mixed oxides with different crystalline structure could allow to explain the differences in physicochemical properties and activity displayed compared to the impregnated catalysts. This understanding may lead to an optimization of the synthesis procedure. Concerning to the structured catalysts, a deep characterization of the fresh and spent catalysts could provide a better understanding of their behaviour under tar reforming reactions. In addition, the optimization of the structuration to improve the catalytic activity can be discerned from these characterization results.

As concern to the tar reforming reactions, the use of operando techniques could be a good alternative to explain the differences between phenol and toluene reforming.

Additionally, the role of the different supports and the influence of the Ni addition can be also clarified from these techniques.

o Conclusion générale

L'objectif de ce travail de doctorat était le développement de systèmes catalytiques et l'optimisation de leur structuration à grande échelle pour le reformage des goudrons dans des conditions réelles de gazéification de la biomasse. Ces objectifs sont basés sur ceux du projet EBIPREP, sur la valorisation de la biomasse par combinaison de processus thermochimiques et biologiques. À cette fin, les travaux ont été divisés en deux grandes lignes :

1) La synthèse et la caractérisation des catalyseurs en poudre (*Chapitre 2*) et leur évaluation en reformage des goudrons à l'échelle du laboratoire (*Chapitre 3*)
2) L'optimisation de la structuration catalytique sur des extrudats de SiC à l'échelle du laboratoire avec la mise à l'échelle ultérieure en lots de 1,1 L (*Chapitre 4*) et l'évaluation catalytique finale de ces lots à grande échelle dans une installation pilote de gazéification de la biomasse (*Chapitre 5*).

Trois supports à haute mobilité d'oxygène, $Ce_{0.63}Zr_{0.33}Sm_{0.04}O_{2-\delta}$ (CZS), $Ce_2Y_2O_7$ (CY) et $La_{0.6}Sr_{0.4}Co_{0.2}Fe_{0.8}O_{3-\delta}$ (LSCF), ont été synthétisés par méthode pseudo sol-gel. Six catalyseurs à base de Ni avec une charge métallique de 10% en poids ont été préparés en utilisant deux voies différentes d'addition du Ni : (i) imprégnation humide (Ni/CZS, Ni/CY et Ni/LSCF) et (ii) synthèse pseudo-sol-gel en une étape (Ni-CZS, Ni-CY et Ni-LSCF). En général, aucune modification significative des propriétés physico-chimiques n'a été constatée pour le catalyseur imprégné par rapport aux supports, alors que l'insertion partielle d'espèces Ni^{2+} dans les structures du support, favorisée par la méthode sol-gel en une étape, a entraîné quelques variations par rapport aux supports et aux catalyseurs imprégnés (*Chapitre 2*).

L'effet de la voie d'addition de Ni et l'effet de la nature du support dans la réaction de reformage des goudrons pour les six catalyseurs préparés en poudre ont été étudiés (*Chapitre 3*). Pour ces études, deux molécules modèles de goudron, le phénol et le toluène, ont été utilisées. En outre, l'effet de la température de réaction (400 et 550 ºC) ainsi que de la procédure de prétraitement (H_2/N_2 ou gaz de synthèse) sur la performance catalytique de ces matériaux ont été étudiés. Comme prévu, une activité catalytique plus faible et un dépôt de carbone plus important ont été obtenus à une température de réaction plus basse (400 ºC) qu'à une température plus élevée (550 ºC). Les résultats catalytiques obtenus en reformage du phénol et du toluène pour les six catalyseurs prétraités sous atmosphère H_2/N_2 ont révélé des différences de mécanisme de réaction ou de réactivité à la surface du

Ni entre les deux molécules. Néanmoins, la même tendance dans l'activité et la stabilité catalytiques a été trouvée parmi les six catalyseurs pour les deux molécules (Ni/CY > Ni-LSCF > Ni/LSCF ~Ni-CZS > Ni-CY > Ni-CZS). Le prétraitement de réduction sous atmosphère de gaz de synthèse a montré que la plupart des catalyseurs pouvaient être réduits dans ces conditions. Cependant, la diminution de la surface métallique ainsi que les dépôts de carbone générés ont provoqué une baisse de l'activité catalytique pour la réaction de reformage du goudron. Compte tenu des résultats catalytiques obtenus grâce au prétraitement H_2/N_2 et de la capacité du catalyseur à être réduit sous atmosphère de gaz de synthèse, trois catalyseurs ont été sélectionnés pour l'étude de la structuration sur des extrudats de SiC (Ni/CY, Ni/LSCF and RuNi/LSCF).

Par la suite, l'optimisation de la structuration catalytique sur des extrudats de SiC ainsi que la caractérisation des catalyseurs structurés finaux et l'évaluation de leur activité catalytique dans le reformage des goudrons à l'échelle du laboratoire ont été explorées (*Chapitre 4*). L'influence de la forme des extrudats, de la concentration de la solution de précuseurs utilisée pour l'enduction (0,30 M contre 0,60 M), l'échelle utilisée (enduction individuelle ou en lot), l'effet de la nature du solvant (acide propionique ou l'eau) ainsi que l'effet du prétraitement du SiC sur le dépôt de la phase catalytique ont été évalués. Des résultats similaires ont été obtenus quelle que soit la forme des extrudats. Une solution de précurseurs de faible concentration a conduit à une masse de support déposée plus faible que celle de la solution concentrée. L'utilisation de lots d'extrudats a permis d'obtenir des résultats plus précis que l'enduction individuelle. Finalement, l'utilisation d'eau comme solvant a entraîné une prise de masse plus faible que pour l'acide propionique et aucune amélioration de prise de masse n'a été obtenue par le prétraitement des extrudats de SiC. Une modification de la structure cristalline et de la réductibilité due à la structuration a été observée pour les catalyseurs structurés finaux (Ni/LSCF/SiC et Ni/CY/RSiC) par rapport aux catalyseurs en poudre. En ce qui concerne l'activité catalytique, les catalyseurs structurés finaux ont été réduits sous atmosphère de gaz de synthèse et testés dans le reformage du toluène. La réduction des catalyseurs structurés sous atmosphère de gaz de synthèse a été possible et une conversion moyenne du toluène similaire a été atteinte, indépendamment de la forme de l'extrudat ou du support catalytique, tandis qu'une sélectivité différente du carbone a été mise en évidence pour les trois formes d'extrudats. En comparant avec les catalyseurs équivalents en poudre, une amélioration de l'activité catalytique vers la réaction de reformage des goudrons a été observée pour les catalyseurs structurés. Elle a été associée à la forte interaction Ni-support-SiC. Ces résultats catalytiques ont permis de choisir la forme de l'extrudat (RSiC 8/5) et les conditions de dépôt

utilisées dans la structuration à grande échelle. Enfin, la mise à l'échelle de la structuration catalytique a indiqué que le procédé d'enduction était reproductible mais ne permettait pas un contrôle fin de la masse déposée. De plus, les modifications de l'interaction Ni-support - SiC causées par la préparation à grande échelle ont été mises en évidence.

Finalement, les lots de 1,1 L préparés pour les trois catalyseurs sélectionnés (Ni/CY/RSiC 8/5, Ni/LSCF/RSiC 8/5 and RuNi/LSCF/RSiC 8/5) ont été testés dans une véritable installation pilote de gazéification de la biomasse en utilisant des copeaux de bois et un mélange de copeaux et de résidus comme matière première de la biomasse (*Chapitre 5*). Les résultats catalytiques obtenus pour les trois catalyseurs, positionnés en sortie du gazéifieur et opérant typiquement à 550 °C, utilisant des copeaux de bois comme matière première étaient conformes au comportement catalytique obtenu pour le catalyseur en poudre et structuré dans le reformage du goudron à l'échelle du laboratoire (RuNi/LSCF/RSiC 8/5 > Ni/CY/RSiC 8/5 > Ni/LSCF/RSiC 8/5). Parmi eux, le catalyseur Ni/LSCF/RSiC 8/5 a subi une forte désactivation catalytique dans des conditions réelles de fonctionnement. Ce catalyseur a ainsi été régénéré in situ à l'échelle pilote et les résultats catalytiques ont révélé qu'un catalyseur actif peut être obtenu après 6 h de fonctionnement, mais qu'il y a une perte d'activité par rapport au catalyseur frais. En revanche, l'ajout de Ru au catalyseur Ni/LSCF/RSiC 8/5 a permis d'améliorer l'activité et la stabilité catalytiques, ce qui a abouti au meilleur système catalytique parmi les trois choisis. Enfin, une diminution de l'activité catalytique et de la stabilité du reformage des goudrons a été clairement observée lors de l'introduction de résidus de biogaz dans la matière première, probablement due à l'augmentation de la teneur en goudron du gaz de synthèse produit ainsi que d'autres éléments inorganiques.

En comparant les résultats catalytiques du présent travail avec ceux rapportés dans la littérature pour le même type de matériaux et de molécules modèles, on peut voir que, soit à l'échelle du laboratoire, soit à celle de l'unité pilote, une activité catalytique élevée a été obtenue dans ce travail, à une température relativement basse (550 ºC). En conclusion générale, des systèmes catalytiques efficaces pour éliminer les goudrons du procédé de gazéification de la biomasse ont été développés dans le cadre de cette recherche.

o Perspectives

Plusieurs perspectives peuvent être suggérées sur la base des résultats de ce travail de doctorat. En ce qui concerne la méthode de synthèse, l'optimisation de la préparation du support afin de trouver un bon équilibre entre la cristallinité et les propriétés texturales et, ainsi, améliorer l'activité catalytique. En outre, la caractérisation approfondie des catalyseurs à base de Ni préparés par sol-gel en une seule étape afin de clarifier "comment" le nickel est inséré dans les oxydes mixtes ayant une structure cristalline différente pourrait permettre d'expliquer les différences de propriétés physico-chimiques et d'activité affichées par rapport aux catalyseurs imprégnés. Cette compréhension pourrait conduire à une optimisation de la procédure de synthèse. En ce qui concerne les catalyseurs structurés, une caractérisation approfondie des catalyseurs frais et usés pourrait permettre de mieux comprendre leur comportement lors des réactions de reformage des goudrons.

En ce qui concerne les réactions de reformage des goudrons, l'utilisation des techniques *operando* pourrait être une bonne alternative pour expliquer les différences entre le reformage du phénol et du toluène. En outre, le rôle des différents supports et l'influence de l'addition de Ni peuvent également être clarifiés grâce à ces techniques.

Referencies

1. Crippa; M.; Oreggioni; G.; Guizzardi; D.; Muntean; Schaaf; E.; Lo Vullo; Solazzo; Monforti-Ferrario; F.; Olivier; J.G.J.; Vignati *JRC SCIENCE FOR POLICY REPORT Fossil CO2 & GHG emissions of all world countries*; 2019; ISBN 9789276110255.

2. Commissariat général au développement durable: Chiffres clés du climat - France, Europe et Monde - Édition 2020. **2020**.

3. Climate Watch - Historical GHG Emissions Available online: https://www.climatewatchdata.org.

4. IEA *Energy Technology Perspectives 2012: Pathways to a Clean Energy System (Paris: OECD/IEA, 2012)*; 2012; ISBN 9789264174887.

5. IN-DEPTH ANALYSIS IN EUROPEAN COMMISSION COMMUNICATION (2018) - A Clean Planet for all A European long-term strategic vision for a prosperous , modern , competitive and climate neutral economy. **2018**.

6. Buck, M.; Redl, C.; Hein, F.; Jones, D. The European Power Sector in 2018. *Agora Energiewende and Sandbag* **2019**.

7. Paletto, A.; Bernardi, S.; Pieratti, E.; Teston, F.; Romagnoli, M. Assessment of environmental impact of biomass power plants to increase the social acceptance of renewable energy technologies. *Heliyon* **2019**, *5*, e02070, doi:10.1016/j.heliyon.2019.e02070.

8. Scarlat, N.; Dallemand, J.-F.; Taylor, N.; Banja, M.; Sanchez Lopez, J.; Avraamides, M. Brief on biomass for energy in the European Union. *EC Publ.* **2019**, 1–8.

9. Scarlat, N.; Dallemand, J.F.; Fahl, F. Biogas: Developments and perspectives in Europe. *Renew. Energy* **2018**, *129*, 457–472, doi:10.1016/j.renene.2018.03.006.

10. Ambec, S.; Crampes, C. Electricity provision with intermittent sources of energy. *Resour. Energy Econ.* **2012**, *34*, 319–336, doi:10.1016/j.reseneeco.2012.01.001.

11. European Commission Directive (EU) 2018/2001 of the European Parliament and of the Council of 11 December 2018 on the promotion of the use of energy from renewable sources. *Off. J. Eur. Union* **2018**, *2018*, 82–209.

12. Zhang, L.; Xu, C. (Charles); Champagne, P. Overview of recent advances in thermo-chemical conversion of biomass. *Energy Convers. Manag.* **2010**, *51*, 969–982, doi:10.1016/j.enconman.2009.11.038.

13. Tursi, A. A review on biomass: importance, chemistry, classification, and conversion. *Biofuel Res. J.* **2019**, *6*, 962–979, doi:10.18331/BRJ2019.6.2.3.

14. Abbasi, T.; Abbasi, S.A. Biomass energy and the environmental impacts associated with its production and utilization. *Renew. Sustain. Energy Rev.* **2010**, *14*, 919–937, doi:10.1016/j.rser.2009.11.006.

15. Baratieri, M.; Baggio, P.; Fiori, L.; Grigiante, M. Biomass as an energy source: Thermodynamic constraints on the performance of the conversion process. *Bioresour. Technol.* **2008**, *99*, 7063–7073,

doi:10.1016/j.biortech.2008.01.006.

16. Ni, M.; Leung, D.Y.C.; Leung, M.K.H.; Sumathy, K. An overview of hydrogen production from biomass. *Fuel Process. Technol.* **2006**, *87*, 461–472, doi:10.1016/j.fuproc.2005.11.003.

17. Williams, R.; Jenkins, B.; Nguyen, D. Solid Waste Conversion: A review and database of current and emerging technologies. *Final report, Dep. Biol.* **2003**, 1–129.

18. Lebaka, V.R. Potential Bioresources as Future Sources of Biofuels Production: An Overview. In *Biofuel Technologies*; Springer Berlin Heidelberg: Berlin, Heidelberg, 2013; pp. 223–258.

19. Maschio, G.; Koufopanos, C.; Lucchesi, A. Pyrolysis, a promising route for biomass utilization. *Bioresour. Technol.* **1992**, *42*, 219–231, doi:10.1016/0960-8524(92)90025-S.

20. Demirbas, M.F.; Balat, M. Biomass pyrolysis for liquid fuels and chemicals: A review. *J. Sci. Ind. Res. (India).* **2007**, *66*, 797–804.

21. Ren, J.; Liu, Y.L.; Zhao, X.Y.; Cao, J.P. Biomass thermochemical conversion: A review on tar elimination from biomass catalytic gasification. *J. Energy Inst.* **2020**, *93*, 1083–1098, doi:10.1016/j.joei.2019.10.003.

22. Damartzis, T.; Zabaniotou, A. Thermochemical conversion of biomass to second generation biofuels through integrated process design-A review. *Renew. Sustain. Energy Rev.* **2011**, *15*, 366–378, doi:10.1016/j.rser.2010.08.003.

23. Heidenreich, S.; Ugo, P. New concepts in biomass gasification. *Prog. Energy Combust. Sci.* **2015**, *46*, 72–95, doi:10.1016/j.pecs.2014.06.002.

24. IEA (International Energy Agency) Bioenergy annual report. **2006**.

25. Valderrama Rios, M.L.; González, A.M.; Lora, E.E.S.; Almazán del Olmo, O.A. Reduction of tar generated during biomass gasification: A review. *Biomass and Bioenergy* **2018**, *108*, 345–370, doi:10.1016/j.biombioe.2017.12.002.

26. Molino, A.; Chianese, S.; Musmarra, D. Biomass gasification technology: The state of the art overview. *J. Energy Chem.* **2016**, *25*, 10–25, doi:10.1016/j.jechem.2015.11.005.

27. Bridgwater, A.. Renewable fuels and chemicals by thermal processing of biomass. *Chem. Eng. J.* **2003**, *91*, 87–102, doi:10.1016/S1385-8947(02)00142-0.

28. Mohd Salleh, M.A.; Kisiki, N.H.; Yusuf, H.M.; Ab Karim Ghani, W.A.W. Gasification of Biochar from Empty Fruit Bunch in a Fluidized Bed Reactor. *Energies* **2010**, *3*, 1344–1352, doi:10.3390/en3071344.

29. Richardson, Y.; Blin, J.; Julbe, A. A short overview on purification and conditioning of syngas produced by biomass gasification: Catalytic strategies, process intensification and new concepts. *Prog. Energy Combust. Sci.* **2012**, *38*, 765–781, doi:10.1016/j.pecs.2011.12.001.

30. Zeng, X.; Ueki, Y.; Yoshiie, R.; Naruse, I.; Wang, F.; Han, Z.; Xu, G. Recent progress in tar removal by char and the applications: A comprehensive analysis. *Carbon Resour. Convers.* **2020**, *3*, 1–18, doi:10.1016/j.crcon.2019.12.001.

31. Burhenne, L.; Rochlitz, L.; Lintner, C.; Aicher, T. Technical demonstration of the novel Fraunhofer ISE biomass gasification process for the production of a tar-free synthesis gas. *Fuel Process. Technol.* **2013**, *106*, 751–760, doi:10.1016/j.fuproc.2012.10.012.

32. Maniatis, K.; Beenackers, A.A.C.M. Tar Protocols. IEA Bioenergy Gasification Task: Introduction. *Biomass and Bioenergy* **2000**, *18*, 1–4, doi:10.1016/S0961-9534(99)00072-0.

33. Devi, L.; Ptasinski, K.J.; Janssen, F.J.J.G. A review of the primary measures for tar elimination in biomass gasification processes. *Biomass and Bioenergy* **2003**, *24*, 125–140, doi:10.1016/S0961-9534(02)00102-2.

34. Anis, S.; Zainal, Z.A. Tar reduction in biomass producer gas via mechanical, catalytic and thermal methods: A review. *Renew. Sustain. Energy Rev.* **2011**, *15*, 2355–2377, doi:10.1016/j.rser.2011.02.018.

35. Guan, G.; Kaewpanha, M.; Hao, X.; Abudula, A. Catalytic steam reforming of biomass tar: Prospects and challenges. *Renew. Sustain. Energy Rev.* **2016**, *58*, 450–461, doi:10.1016/j.rser.2015.12.316.

36. Elliott, D.C. Relation of Reaction Time and Temperature to Chemical Composition of Pyrolysis Oils. In; 1988; pp. 55–65.

37. Evans, R.J.; Milne, T.A. Biomass Gasifier "Tars": Their Nature, Formation and COnversion. *Dev. Thermochem. Biomass Convers.* **1998**, 803–816, doi:10.1007/978-94-009-1559-6_64.

38. El-Rub, Z.Y.K.A. Biomass char as an in-situ catalyst for tar removal in gasification systems, Twente University, Enschede, The Netherlands, 2008.

39. Hanaoka, T.; Inoue, S.; Uno, S.; Ogi, T.; Minowa, T. Effect of woody biomass components on air-steam gasification. *Biomass and Bioenergy* **2005**, *28*, 69–76, doi:10.1016/j.biombioe.2004.03.008.

40. Yu, H.; Zhang, Z.; Li, Z.; Chen, D. Characteristics of tar formation during cellulose, hemicellulose and lignin gasification. *Fuel* **2014**, *118*, 250–256, doi:10.1016/j.fuel.2013.10.080.

41. Yu, Q.; Brage, C.; Chen, G.; Sjöström, K. Temperature impact on the formation of tar from biomass pyrolysis in a free-fall reactor. *J. Anal. Appl. Pyrolysis* **1997**, *40–41*, 481–489, doi:10.1016/S0165-2370(97)00017-X.

42. Zhou, J.; Masutani, S.M.; Ishimura, D.M.; Turn, S.Q.; Kinoshita, C.M. Release of Fuel-Bound Nitrogen during Biomass Gasification. *Ind. Eng. Chem. Res.* **2000**, *39*, 626–634, doi:10.1021/ie980318o.

43. Couto, N.; Rouboa, A.; Silva, V.; Monteiro, E.; Bouziane, K. Influence of the Biomass Gasification Processes on the Final Composition of Syngas. *Energy Procedia* **2013**, *36*, 596–606, doi:10.1016/j.egypro.2013.07.068.

44. Pan, Y..; Roca, X.; Velo, E.; Puigjaner, L. Removal of tar by secondary air in fluidised bed gasification of residual biomass and coal. *Fuel* **1999**, *78*, 1703–1709, doi:10.1016/S0016-2361(99)00118-0.

45. Cao, Y.; Wang, Y.; Riley, J.T.; Pan, W.-P. A novel biomass air gasification process for producing tar-free higher heating value fuel gas. *Fuel Process. Technol.* **2006**, *87*, 343–353, doi:10.1016/j.fuproc.2005.10.003.

46. Galindo, A.L.; Lora, E.S.; Andrade, R.V.; Giraldo, S.Y.; Jaén, R.L.; Cobas, V.M. Biomass gasification in a downdraft gasifier with a two-stage air supply: Effect of operating conditions on gas quality. *Biomass and Bioenergy* **2014**, *61*, 236–244, doi:10.1016/j.biombioe.2013.12.017.

47. Shen, Y.; Yoshikawa, K. Recent progresses in catalytic tar elimination during biomass gasification or pyrolysis - A review. *Renew. Sustain. Energy Rev.* **2013**, *21*, 371–392, doi:10.1016/j.rser.2012.12.062.

48. Belgiorno, V.; De Feo, G.; Della Rocca, C.; Napoli, R.M.A. Energy from gasification of solid wastes. *Waste Manag.* **2003**, *23*, 1–15, doi:10.1016/S0956-053X(02)00149-6.

49. Guan, G.; Kaewpanha, M.; Hao, X.; Zhu, A.; Kasai, Y.; Kakuta, S.; Kusakabe, K.; Abudula, A. Steam reforming of tar derived from lignin over pompom-like potassium-promoted iron-based catalysts formed on calcined scallop shell. *Bioresour. Technol.* **2013**, *139*, 280–284, doi:10.1016/j.biortech.2013.04.007.

50. Guan, G.; Chen, G.; Kasai, Y.; Lim, E.W.C.; Hao, X.; Kaewpanha, M.; Abuliti, A.; Fushimi, C.; Tsutsumi, A. Catalytic steam reforming of biomass tar over iron- or nickel-based catalyst supported on calcined scallop shell. *Appl. Catal. B Environ.* **2012**, *115–116*, 159–168, doi:10.1016/j.apcatb.2011.12.009.

51. Zhang, Z.; Liu, L.; Shen, B.; Wu, C. Preparation, modification and development of Ni-based catalysts for catalytic reforming of tar produced from biomass gasification. *Renew. Sustain. Energy Rev.* **2018**, *94*, 1086–1109, doi:10.1016/j.rser.2018.07.010.

52. Abu El-Rub, Z.; Bramer, E.A.; Brem, G. Review of catalysts for tar elimination in biomass gasification processes. *Ind. Eng. Chem. Res.* **2004**, *43*, 6911–6919, doi:10.1021/ie0498403.

53. Li, D.; Tamura, M.; Nakagawa, Y.; Tomishige, K. Metal catalysts for steam reforming of tar derived from the gasification of lignocellulosic biomass. *Bioresour. Technol.* **2015**, *178*, 53–64, doi:10.1016/j.biortech.2014.10.010.

54. Xu, C.; Donald, J.; Byambajav, E.; Ohtsuka, Y. Recent advances in catalysts for hot-gas removal of tar and NH3 from biomass gasification. *Fuel* **2010**, *89*, 1784–1795, doi:10.1016/j.fuel.2010.02.014.

55. Kikuchi, E.; Tanaka, S.; Yamazaki, Y.; Morita, Y. Steam Reforming of Hydrocarbons on Noble Metal Catalysts - 1. the Catalytic Activity in Methane-Steam Reaction. *Bull Jpn Pet Inst* **1974**, *16*, 95–98.

56. Rostrup-Nielsen, J.R.; Bak Hansen, J.H. CO_2-reforming of methane over transition metals. *J. Catal.* 1993, *144*, 38–49.

57. Qin, D.; Lapszewicz, J. Study of mixed steam and CO_2 reforming of CH_4 to syngas on MgO-supported metals. *Catal. Today* **1994**, *21*, 551–560, doi:10.1016/0920-5861(94)80179-7.

58. Jones, G.; Jakobsen, J.G.; Shim, S.S.; Kleis, J.; Andersson, M.P.; Rossmeisl, J.; Abild-Pedersen, F.; Bligaard, T.; Helveg, S.; Hinnemann, B.; et al. First principles calculations and experimental insight into methane steam reforming over transition metal catalysts. *J. Catal.* **2008**, *259*, 147–160, doi:10.1016/j.jcat.2008.08.003.

59. Tomishige, K.; Miyazawa, T.; Asadullah, M.; Ito, S.; Kunimori, K. Catalyst performance in reforming of tar derived from biomass over noble metal catalysts. *Green Chem.* **2003**, *5*, 399,

doi:10.1039/b303371f.

60. Dayton, D. Review of the literature on catalytic biomass tar destruction; NREL/TP- 510-32815. Golden, CO; NREL; 2002. *Natl. Renew. Energy Lab.* **2002**, 28.

61. Yang, X.; Liu, X.; Guo, T.; Liu, C. Effects of Cu and Fe Additives on Low-Temperature Catalytic Steam Reforming of Toluene Over Ni/AC Catalysts. *Catal. Surv. from Asia* **2019**, *23*, 54–63, doi:10.1007/s10563-018-9260-7.

62. Li, D.; Li, X.; Gong, J. Catalytic Reforming of Oxygenates: State of the Art and Future Prospects. *Chem. Rev.* **2016**, *116*, 11529–11653, doi:10.1021/acs.chemrev.6b00099.

63. Caballero, M.A.; Aznar, M.P.; Gil, J.; Martín, J.A.; Francés, E.; Corella, J. Commercial Steam Reforming Catalysts to Improve Biomass Gasification with Steam-Oxygen Mixtures. 1. Hot Gas Upgrading by the Catalytic Reactor. *Ind. Eng. Chem. Res.* **1997**, *36*, 5227–5239, doi:10.1021/ie970149s.

64. Coll, R.; Salvadó, J.; Farriol, X.; Montané, D. Steam reforming model compounds of biomass gasification tars: conversion at different operating conditions and tendency towards coke formation. *Fuel Process. Technol.* **2001**, *74*, 19–31, doi:10.1016/S0378-3820(01)00214-4.

65. Yung, M.M.; Jablonski, W.S.; Magrini-Bair, K.A. Review of catalytic conditioning of biomass-derived syngas. *Energy and Fuels* **2009**, *23*, 1874–1887, doi:10.1021/ef800830n.

66. Park, S.Y.; Oh, G.; Kim, K.; Seo, M.W.; Ra, H.W.; Mun, T.Y.; Lee, J.G.; Yoon, S.J. Deactivation characteristics of Ni and Ru catalysts in tar steam reforming. *Renew. Energy* **2017**, *105*, 76–83, doi:10.1016/j.renene.2016.12.045.

67. Laosiripojana, N.; Assabumrungrat, S. Catalytic steam reforming of ethanol over high surface area CeO_2: The role of CeO_2 as an internal pre-reforming catalyst. *Appl. Catal. B Environ.* **2006**, *66*, 29–39, doi:10.1016/j.apcatb.2006.01.011.

68. Sehested, J. Four challenges for nickel steam-reforming catalysts. *Catal. Today* **2006**, *111*, 103–110, doi:10.1016/j.cattod.2005.10.002.

69. Ashok, J.; Dewangan, N.; Das, S.; Hongmanorom, P.; Wai, M.H.; Tomishige, K.; Kawi, S. Recent progress in the development of catalysts for steam reforming of biomass tar model reaction. *Fuel Process. Technol.* **2020**, *199*, 106252, doi:10.1016/j.fuproc.2019.106252.

70. Artetxe, M.; Alvarez, J.; Nahil, M.A.; Olazar, M.; Williams, P.T. Steam reforming of different biomass tar model compounds over Ni/Al_2O_3 catalysts. *Energy Convers. Manag.* **2017**, *136*, 119–126, doi:10.1016/j.enconman.2016.12.092.

71. Li, Z.; Hu, X.; Zhang, L.; Liu, S.; Lu, G. Steam reforming of acetic acid over Ni/ZrO_2 catalysts: Effects of nickel loading and particle size on product distribution and coke formation. *Appl. Catal. A Gen.* **2012**, *417–418*, 281–289, doi:10.1016/j.apcata.2012.01.002.

72. Yue, B.; Wang, X.; Ai, X.; Yang, J.; Li, L.; Lu, X.; Ding, W. Catalytic reforming of model tar compounds from hot coke oven gas with low steam/carbon ratio over $Ni/MgO-Al_2O_3$ catalysts. *Fuel Process. Technol.* **2010**, *91*, 1098–1104, doi:10.1016/j.fuproc.2010.03.020.

73. Park, H.J.; Park, S.H.; Sohn, J.M.; Park, J.; Jeon, J.K.; Kim, S.S.; Park, Y.K. Steam reforming of biomass gasification tar using benzene as a model compound over various Ni supported metal oxide catalysts. *Bioresour. Technol.* **2010**, *101*, 101–103, doi:10.1016/j.biortech.2009.03.036.

74. Wang, K.; Dou, B.; Jiang, B.; Zhang, Q.; Li, M.; Chen, H.; Xu, Y. Effect of support on hydrogen production from chemical looping steam reforming of ethanol over Ni-based oxygen carriers. *Int. J. Hydrogen Energy* **2016**, *41*, 17334–17347, doi:10.1016/j.ijhydene.2016.07.261.

75. Menezes, J.P. da S.Q.; Dias, A.P. dos S.; da Silva, M.A.P.; Souza, M.M.V.M. Effect of alkaline earth oxides on nickel catalysts supported over γ-alumina for butanol steam reforming: Coke formation and deactivation process. *Int. J. Hydrogen Energy* **2020**, *45*, 22906–22920, doi:10.1016/j.ijhydene.2020.06.187.

76. Adnan, M.A.; Muraza, O.; Razzak, S.A.; Hossain, M.M.; De Lasa, H.I. Iron Oxide over Silica-Doped Alumina Catalyst for Catalytic Steam Reforming of Toluene as a Surrogate Tar Biomass Species. *Energy and Fuels* **2017**, *31*, 7471–7481, doi:10.1021/acs.energyfuels.7b01301.

77. Koo, K.Y.; Roh, H.S.; Jung, U.H.; Yoon, W.L. CeO_2 promoted Ni/Al_2O_3 catalyst in combined steam and carbon dioxide reforming of methane for gas to liquid (GTL) process. *Catal. Letters* **2009**, *130*, 217–221, doi:10.1007/s10562-009-9867-4.

78. de Castro, T.P.; Silveira, E.B.; Rabelo-Neto, R.C.; Borges, L.E.P.; Noronha, F.B. Study of the performance of Pt/Al_2O_3 and $Pt/CeO_2/Al2O_3$ catalysts for steam reforming of toluene, methane and mixtures. *Catal. Today* **2018**, *299*, 251–262, doi:10.1016/j.cattod.2017.05.067.

79. Montero, C.; Ochoa, A.; Castaño, P.; Bilbao, J.; Gayubo, A.G. Monitoring Ni 0 and coke evolution during the deactivation of a Ni/La_2O_3 – a Al_2O_3 catalyst in ethanol steam reforming in a fluidized bed. *J. Catal.* **2015**, *331*, 181–192, doi:10.1016/j.jcat.2015.08.005.

80. Constantinou, D.A.; Fierro, J.L.G.; Efstathiou, A.M. A comparative study of the steam reforming of phenol towards H_2 production over natural calcite, dolomite and olivine materials. *Appl. Catal. B Environ.* **2010**, *95*, 255–269, doi:10.1016/j.apcatb.2010.01.003.

81. Gil, J.; Caballero, M.A.; Martín, J.A.; Aznar, M.P.; Corella, J. Biomass gasification with air in a fluidized bed: Effect of the in-bed use of dolomite under different operation conditions. *Ind. Eng. Chem. Res.* **1999**, *38*, 4226–4235, doi:10.1021/ie980802r.

82. Gusta, E.; Dalai, A.K.; Uddin, M.A.; Sasaoka, E. Catalytic decomposition of biomass tars with dolomites. *Energy and Fuels* **2009**, *23*, 2264–2272, doi:10.1021/ef8009958.

83. Hu, G.; Xu, S.; Li, S.; Xiao, C.; Liu, S. Steam gasification of apricot stones with olivine and dolomite as downstream catalysts. *Fuel Process. Technol.* **2006**, *87*, 375–382, doi:10.1016/j.fuproc.2005.07.008.

84. Chang, A.C.C.; Chang, L.S.; Tsai, C.Y.; Chan, Y.C. Steam reforming of gasification-derived tar for syngas production. *Int. J. Hydrogen Energy* **2014**, *39*, 19376–19381, doi:10.1016/j.ijhydene.2014.07.133.

85. Xu, T.; Xu, F.; Moyo, G.G.; Sun, Y.; Chen, Z.; Xiao, B.; Wang, X.; Hu, Z. Comparative study of M_xO_y (M = Cu, Fe and Ni) supported on dolomite for syngas production via chemical looping reforming with

toluene. *Energy Convers. Manag.* **2019**, *199*, doi:10.1016/j.enconman.2019.111937.

86. Devi, L.; Ptasinski, K.J.; Janssen, F.J.J.G. Pretreated olivine as tar removal catalyst for biomass gasifiers: Investigation using naphthalene as model biomass tar. *Fuel Process. Technol.* **2005**, *86*, 707–730, doi:10.1016/j.fuproc.2004.07.001.

87. Rapagnà, S.; Jand, N.; Kiennemann, A.; Foscolo, P.U. Steam-gasification of biomass in a fluidised-bed of olivine particles. *Biomass and Bioenergy* **2000**, *19*, 187–197, doi:10.1016/S0961-9534(00)00031-3.

88. Świerczyński, D.; Libs, S.; Courson, C.; Kiennemann, A. Steam reforming of tar from a biomass gasification process over Ni/olivine catalyst using toluene as a model compound. *Appl. Catal. B Environ.* **2007**, *74*, 211–222, doi:10.1016/j.apcatb.2007.01.017.

89. Michel, R.; Łamacz, A.; Krzton, A.; Djéga-Mariadassou, G.; Burg, P.; Courson, C.; Gruber, R. Steam reforming of α-methylnaphthalene as a model tar compound over olivine and olivine supported nickel. *Fuel* **2013**, *109*, 653–660, doi:10.1016/j.fuel.2013.03.017.

90. Corma, A. State of the art and future challenges of zeolites as catalysts. *J. Catal.* **2003**, *216*, 298–312, doi:10.1016/S0021-9517(02)00132-X.

91. Qiu, S.B.; Gong, L.; Liu, L.; Hong, C.G.; Yuan, L.X.; Li, Q.X. Hydrogen production by low-temperature steam reforming of bio-oil over Ni/HZSM-5 catalyst. *Chinese J. Chem. Phys.* **2011**, *24*, 211–217, doi:10.1088/1674-0068/24/02/211-217.

92. Buchireddy, P.R.; Bricka, R.M.; Rodriguez, J.; Holmes, W. Biomass gasification: Catalytic removal of tars over zeolites and nickel supported zeolites. *Energy and Fuels* **2010**, *24*, 2707–2715, doi:10.1021/ef901529d.

93. Sinağ, A.; Sungur, M.; Canel, M. Effect of experimental conditions on the yields during the copyrolysis of Mustafa Kemal Paşa (MKP) lignite (Turkey) with low-density polyethylene. *Energy and Fuels* **2006**, *20*, 1609–1613, doi:10.1021/ef060108l.

94. Li, W.; Zhao, Z.; Guo, X.; Wang, G. Employing a Nickel-Containing Supramolecular Framework as Ni Precursor for Synthesizing Robust Supported Ni Catalysts for Dry Reforming of Methane. *ChemCatChem* **2016**, *8*, 2939–2952, doi:10.1002/cctc.201600448.

95. Tang, W.; Cao, J.P.; Yang, F.L.; Feng, X.B.; Ren, J.; Wang, J.X.; Zhao, X.Y.; Zhao, M.; Cui, X.; Wei, X.Y. Highly active and stable HF acid modified HZSM-5 supported Ni catalysts for steam reforming of toluene and biomass pyrolysis tar. *Energy Convers. Manag.* **2020**, *212*, doi:10.1016/j.enconman.2020.112799.

96. Ye, M.; Tao, Y.; Jin, F.; Ling, H.; Wu, C.; Williams, P.T.; Huang, J. Enhancing hydrogen production from the pyrolysis-gasification of biomass by size-confined Ni catalysts on acidic MCM-41 supports. *Catal. Today* **2018**, *307*, 154–161, doi:10.1016/j.cattod.2017.05.077.

97. Ashok, J.; Subrahmanyam, M.; Venugopal, A. Hydrotalcite structure derived Ni-Cu-Al catalysts for the production of H_2 by CH_4 decomposition. *Int. J. Hydrogen Energy* **2008**, *33*, 2704–2713, doi:10.1016/j.ijhydene.2008.03.028.

98. Li, D.; Wang, L.; Koike, M.; Nakagawa, Y.; Tomishige, K. Steam reforming of tar from pyrolysis of

biomass over Ni/Mg/Al catalysts prepared from hydrotalcite-like precursors. *Appl. Catal. B Environ.* **2011**, *102*, 528–538, doi:10.1016/j.apcatb.2010.12.035.

99. Chen, T.; Liu, H.; Shi, P.; Chen, D.; Song, L.; He, H.; Frost, R.L. CO_2 reforming of toluene as model compound of biomass tar on Ni/Palygorskite. *Fuel* **2013**, *107*, 699–705, doi:10.1016/j.fuel.2012.12.036.

100. Li, S.; Gong, J. Strategies for improving the performance and stability of Ni-based catalysts for reforming reactions. *Chem. Soc. Rev.* **2014**, *43*, 7245–7256, doi:10.1039/C4CS00223G.

101. Tsipis, E. V.; Kharton, V. V. Electrode materials and reaction mechanisms in solid oxide fuel cells: A brief review : I Performance-determining factors. *J. Solid State Electrochem.* **2008**, *12*, 1039–1060, doi:10.1007/s10008-007-0468-0.

102. Vernoux, P.; Lizarraga, L.; Tsampas, M.N.; Sapountzi, F.M.; De Lucas-Consuegra, A.; Valverde, J.L.; Souentie, S.; Vayenas, C.G.; Tsiplakides, D.; Balomenou, S.; et al. Ionically conducting ceramics as active catalyst supports. *Chem. Rev.* **2013**, *113*, 8192–8260, doi:10.1021/cr4000336.

103. Laguna-Bercero, M.A. Recent advances in high temperature electrolysis using solid oxide fuel cells: A review. *J. Power Sources* **2012**, *203*, 4–16, doi:10.1016/j.jpowsour.2011.12.019.

104. Laobuthee, A.; Veranitisagul, C.; Wattanathana, W.; Koonsaeng, N.; Laosiripojana, N. Activity of Fe supported by $Ce_{1-x}Sm_xO_{2-\delta}$ derived from metal complex decomposition toward the steam reforming of toluene as biomass tar model compound. *Renew. Energy* **2015**, *74*, 133–138, doi:10.1016/j.renene.2014.08.001.

105. Ashok, J.; Ang, M.L.; Kawi, S. Enhanced activity of CO_2 methanation over Ni/CeO_2-ZrO_2 catalysts: Influence of preparation methods. *Catal. Today* **2017**, *281*, 304–311, doi:10.1016/j.cattod.2016.07.020.

106. Zhang, L.; Wu, W.; Zhang, Y.; Zhou, X. Clean synthesis gas production from municipal solid waste via catalytic gasification and reforming technology. *Catal. Today* **2018**, *318*, 39–45, doi:10.1016/j.cattod.2018.02.050.

107. Ashok, J.; Kawi, S. Steam reforming of toluene as a biomass tar model compound over CeO_2 promoted Ni/CaO–Al_2O_3 catalytic systems. *Int. J. Hydrogen Energy* **2013**, *38*, 13938–13949, doi:10.1016/j.ijhydene.2013.08.029.

108. García-García, I.; Acha, E.; Bizkarra, K.; Martínez de Ilarduya, J.; Requies, J.; Cambra, J.F. Hydrogen production by steam reforming of m-cresol, a bio-oil model compound, using catalysts supported on conventional and unconventional supports. *Int. J. Hydrogen Energy* **2015**, *40*, 14445–14455, doi:10.1016/j.ijhydene.2015.07.155.

109. Reddy, B.M.; Saikia, P.; Bharali, P.; Yamada, Y.; Kobayashi, T.; Muhler, M.; Grünert, W. Structural Characterization and Catalytic Activity of Nanosized Ceria−Terbia Solid Solutions. *J. Phys. Chem. C* **2008**, *112*, 16393–16399, doi:10.1021/jp806131r.

110. Li, P.; Chen, X.; Li, Y.; Schwank, J.W. A review on oxygen storage capacity of CeO_2 -based materials: Influence factors, measurement techniques, and applications in reactions related to catalytic automotive

emissions control. *Catal. Today* **2019**, *327*, 90–115, doi:10.1016/j.cattod.2018.05.059.

111. Usmen, R.K.; Graham, G.W.; Watkins, W.L.H.; McCabe, R.W. Incorporation of La^{3+} into a $Pt/CeO_2/Al_2O_3$ catalyst. *Catal. Letters* **1995**, *30*, 53–63, doi:10.1007/BF00813672.

112. Bernal, S.; Blanco, G.; Cauqui, M.A.; Corchado, M.P.; Larese, C.; Pintado, J.M.; Rodŕiguez-Izquierdo, J.M. Cerium–terbium mixed oxides as alternative components for three-way catalysts: a comparative study of $Pt/CeTbO_x$ and Pt/CeO_2 model systems. *Catal. Today* **1999**, *53*, 607–612, doi:10.1016/S0920-5861(99)00148-0.

113. Kehoe, A.B.; Scanlon, D.O.; Watson, G.W. Role of lattice distortions in the oxygen storage capacity of divalently doped CeO_2. *Chem. Mater.* **2011**, *23*, 4464–4468, doi:10.1021/cm201617d.

114. Kanazawa, T.; Suzuki, J.; Takada, T.; Suzuki, T.; Morikawa, A.; Suda, A.; Sobukawa, H.; Sugiura, M. 91 Development of three-way catalyst using composite alumina-ceria-zirconia. In; 2003; pp. 415–418.

115. Reddy, B.M.; Thrimurthulu, G.; Katta, L. Design of efficient $Ce_xM_{1-x}O_{2-\delta}$ (M = Zr, Hf, Tb and Pr) nanosized model solid solutions for CO oxidation. *Catal. Letters* **2011**, *141*, 572–581, doi:10.1007/s10562-010-0484-z.

116. Maia, T.A.; Assaf, E.M. Catalytic features of Ni supported on CeO_2-ZrO_2 solid solution in the steam reforming of glycerol for syngas production. *RSC Adv.* **2014**, *4*, 31142–31154, doi:10.1039/c4ra02886d.

117. Ocampo, F.; Louis, B.; Roger, A.C. Methanation of carbon dioxide over nickel-based $Ce_{0.72}Zr_{0.28}O_2$ mixed oxide catalysts prepared by sol-gel method. *Appl. Catal. A Gen.* **2009**, *369*, 90–96, doi:10.1016/j.apcata.2009.09.005.

118. Vinodkumar, T.; Naga Durgasri, D.; Reddy, B.M.; Alxneit, I. Synthesis and Structural Characterization of Eu_2O_3 Doped CeO_2: Influence of Oxygen Defects on CO Oxidation. *Catal. Letters* **2014**, *144*, 2033–2042, doi:10.1007/s10562-014-1367-5.

119. VINODKUMAR, T.; DURGASRI, D.N.; MALOTH, S.; REDDY, B.M. Tuning the structural and catalytic properties of ceria by doping with Zr^{4+}, La^{3+} and Eu^{3+} cations. *J. Chem. Sci.* **2015**, *127*, 1145–1153, doi:10.1007/s12039-015-0891-1.

120. Lucid, A.K.; Keating, P.R.L.; Allen, J.P.; Watson, G.W. Structure and Reducibility of CeO_2 Doped with Trivalent Cations. *J. Phys. Chem. C* **2016**, *120*, 23430–23440, doi:10.1021/acs.jpcc.6b08118.

121. Harshini, D.; Kim, Y.; Nam, S.W.; Lim, T.H.; Hong, S.A.; Yoon, C.W. Influence of terbium doping on oxygen storage capacity of Ceria-zirconia supports: Enhanced durability of ni catalysts for propane steam reforming. *Catal. Letters* **2013**, *143*, 49–57, doi:10.1007/s10562-012-0944-8.

122. Prasad, D.H.; Park, S.Y.; Ji, H.I.; Kim, H.R.; Son, J.W.; Kim, B.K.; Lee, H.W.; Lee, J.H. Structural characterization and catalytic activity of $Ce_{0.65}Zr_{0.25}RE_{0.1}O_{2-\delta}$ nanocrystalline powders synthesized by the glycine-nitrate process. *J. Phys. Chem. C* **2012**, *116*, 3467–3476, doi:10.1021/jp207107j.

123. Anirban, S.; Paul, T.; Dutta, A. Vacancy mediated ionic conduction in Dy substituted nanoceria: a structure–property correlation study. *RSC Adv.* **2015**, *5*, 50186–50195, doi:10.1039/C5RA06730H.

124. Royer, S.; Duprez, D.; Can, F.; Courtois, X.; Batiot-Dupeyrat, C.; Laassiri, S.; Alamdari, H. Perovskites as Substitutes of Noble Metals for Heterogeneous Catalysis: Dream or Reality. *Chem. Rev.* **2014**, *114*, 10292–10368, doi:10.1021/cr500032a.

125. Zhu, H.; Zhang, P.; Dai, S. Recent Advances of Lanthanum-Based Perovskite Oxides for Catalysis. *ACS Catal.* **2015**, *5*, 6370–6385, doi:10.1021/acscatal.5b01667.

126. Oemar, U.; Ang, M.L.; Chin, Y.C.; Hidajat, K.; Kawi, S. Role of lattice oxygen in oxidative steam reforming of toluene as a tar model compound over Ni/$La_{0.8}Sr_{0.2}AlO_3$ catalyst. *Catal. Sci. Technol.* **2015**, *5*, 3585–3597, doi:10.1039/c5cy00412h.

127. Oemar, U.; Ming Li, A.; Hidajat, K.; Kawi, S. Mechanism and kinetic modeling for steam reforming of toluene on $La_{0.8}Sr_{0.2}Ni_{0.8}Fe_{0.2}O_3$ catalyst. *AIChE J.* **2014**, *60*, 4190–4198, doi:10.1002/aic.14573.

128. Natile, M.M.; Ugel, E.; Maccato, C.; Glisenti, A. $LaCoO_3$: Effect of synthesis conditions on properties and reactivity. *Appl. Catal. B Environ.* **2007**, *72*, 351–362, doi:10.1016/j.apcatb.2006.11.011.

129. Ngamou, P.H.T.; Bahlawane, N. Influence of the Arrangement of the Octahedrally Coordinated Trivalent Cobalt Cations on the Electrical Charge Transport and Surface Reactivity. *Chem. Mater.* **2010**, *22*, 4158–4165, doi:10.1021/cm1004642.

130. Mefford, J.T.; Rong, X.; Abakumov, A.M.; Hardin, W.G.; Dai, S.; Kolpak, A.M.; Johnston, K.P.; Stevenson, K.J. Water electrolysis on $La_{1-x}Sr_xCoO_{3-\delta}$ perovskite electrocatalysts. *Nat. Commun.* **2016**, *7*, doi:10.1038/ncomms11053.

131. Mueller, D.N.; MacHala, M.L.; Bluhm, H.; Chueh, W.C. Redox activity of surface oxygen anions in oxygen-deficient perovskite oxides during electrochemical reactions. *Nat. Commun.* **2015**, *6*, doi:10.1038/ncomms7097.

132. Ferri, D. Methane combustion on some perovskite-like mixed oxides. *Appl. Catal. B Environ.* **1998**, *16*, 119–126, doi:10.1016/S0926-3373(97)00065-9.

133. Ponce, S.; Peña, M.A.; Fierro, J.L.G. Surface properties and catalytic performance in methane combustion of SR-substituted lanthanum manganites. *Appl. Catal. B Environ.* **2000**, *24*, 193–205, doi:10.1016/S0926-3373(99)00111-3.

134. Oemar, U.; Ang, M.L.; Hee, W.F.; Hidajat, K.; Kawi, S. Perovskite $La_xM_{1-x}Ni_{0.8}Fe_{0.2}O_3$ catalyst for steam reforming of toluene: Crucial role of alkaline earth metal at low steam condition. *Appl. Catal. B Environ.* **2014**, *148–149*, 231–242, doi:10.1016/j.apcatb.2013.10.001.

135. Sekine, Y.; Mukai, D.; Murai, Y.; Tochiya, S.; Izutsu, Y.; Sekiguchi, K.; Hosomura, N.; Arai, H.; Kikuchi, E.; Sugiura, Y. Steam reforming of toluene over perovskite-supported Ni catalysts. *Appl. Catal. A Gen.* **2013**, *451*, 160–167, doi:10.1016/j.apcata.2012.11.005.

136. Wang, L.; Li, D.; Koike, M.; Watanabe, H.; Xu, Y.; Nakagawa, Y.; Tomishige, K. Catalytic performance and characterization of Ni–Co catalysts for the steam reforming of biomass tar to synthesis gas. *Fuel* **2013**, *112*, 654–661, doi:10.1016/j.fuel.2012.01.073.

137. Li, D.; Lu, M.; Aragaki, K.; Koike, M.; Nakagawa, Y.; Tomishige, K. Characterization and catalytic

performance of hydrotalcite-derived Ni-Cu alloy nanoparticles catalysts for steam reforming of 1-methylnaphthalene. *Appl. Catal. B Environ.* **2016**, *192*, 171–181, doi:10.1016/j.apcatb.2016.03.052.

138. Wang, L.; Hisada, Y.; Koike, M.; Li, D.; Watanabe, H.; Nakagawa, Y.; Tomishige, K. Catalyst property of Co–Fe alloy particles in the steam reforming of biomass tar and toluene. *Appl. Catal. B Environ.* **2012**, *121–122*, 95–104, doi:10.1016/j.apcatb.2012.03.025.

139. Nahar, G.; Dupont, V.; Twigg, M. V.; Dvininov, E. Feasibility of hydrogen production from steam reforming of biodiesel (FAME) feedstock on Ni-supported catalysts. *Appl. Catal. B Environ.* **2015**, *168–169*, 228–242, doi:10.1016/j.apcatb.2014.12.036.

140. Blanco, P.H.; Wu, C.; Onwudili, J.A.; Williams, P.T. Characterization and evaluation of Ni/SiO_2 catalysts for hydrogen production and tar reduction from catalytic steam pyrolysis-reforming of refuse derived fuel. *Appl. Catal. B Environ.* **2013**, *134–135*, 238–250, doi:10.1016/j.apcatb.2013.01.016.

141. Jafarbegloo, M.; Tarlani, A.; Mesbah, A.W.; Muzart, J.; Sahebdelfar, S. NiO–MgO Solid Solution Prepared by Sol–Gel Method as Precursor for Ni/MgO Methane Dry Reforming Catalyst: Effect of Calcination Temperature on Catalytic Performance. *Catal. Letters* **2016**, *146*, 238–248, doi:10.1007/s10562-015-1638-9.

142. Baudouin, D.; Szeto, K.C.; Laurent, P.; De Mallmann, A.; Fenet, B.; Veyre, L.; Rodemerck, U.; Copéret, C.; Thieuleux, C. Nickel–Silicide Colloid Prepared under Mild Conditions as a Versatile Ni Precursor for More Efficient CO_2 Reforming of CH_4 Catalysts. *J. Am. Chem. Soc.* **2012**, *134*, 20624–20627, doi:10.1021/ja3111797.

143. Ashok, J.; Kathiraser, Y.; Ang, M.L.; Kawi, S. Ni and/or Ni–Cu alloys supported over SiO_2 catalysts synthesized via phyllosilicate structures for steam reforming of biomass tar reaction. *Catal. Sci. Technol.* **2015**, *5*, 4398–4409, doi:10.1039/C5CY00650C.

144. Luo, X.; Hong, Y.; Wang, F.; Hao, S.; Pang, C.; Lester, E.; Wu, T. Development of nano Ni_xMg_yO solid solutions with outstanding anti-carbon deposition capability for the steam reforming of methanol. *Appl. Catal. B Environ.* **2016**, *194*, 84–97, doi:10.1016/j.apcatb.2016.04.031.

145. Wang, H.; Miller, J.T.; Shakouri, M.; Xi, C.; Wu, T.; Zhao, H.; Akatay, M.C. XANES and EXAFS studies on metal nanoparticle growth and bimetallic interaction of Ni-based catalysts for CO_2 reforming of CH_4. *Catal. Today* **2013**, *207*, 3–12, doi:10.1016/j.cattod.2012.09.015.

146. Ocampo, F.; Louis, B.; Kiennemann, A.; Roger, A.C. CO_2 methanation over Ni-Ceria-Zirconia catalysts: Effect of preparation and operating conditions. *IOP Conf. Ser. Mater. Sci. Eng.* **2011**, *19*, 012007, doi:10.1088/1757-899X/19/1/012007.

147. Xie, C.; Chen, Y.; Engelhard, M.H.; Song, C. Comparative study on the sulfur tolerance and carbon resistance of supported noble metal catalysts in steam reforming of liquid hydrocarbon fuel. *ACS Catal.* **2012**, *2*, 1127–1137, doi:10.1021/cs200695t.

148. Salehi, E.; Azad, F.S.; Harding, T.; Abedi, J. Production of hydrogen by steam reforming of bio-oil over Ni/Al_2O_3 catalysts: Effect of addition of promoter and preparation procedure. *Fuel Process. Technol.* **2011**, *92*, 2203–2210, doi:10.1016/j.fuproc.2011.07.002.

149. Chen, J.; Tamura, M.; Nakagawa, Y.; Okumura, K.; Tomishige, K. Promoting effect of trace Pd on hydrotalcite-derived Ni/Mg/Al catalyst in oxidative steam reforming of biomass tar. *Appl. Catal. B Environ.* **2015**, *179*, 412–421, doi:10.1016/j.apcatb.2015.05.042.

150. Profeti, L.P.R.; Dias, J.A.C.; Assaf, J.M.; Assaf, E.M. Hydrogen production by steam reforming of ethanol over Ni-based catalysts promoted with noble metals. *J. Power Sources* **2009**, *190*, 525–533, doi:10.1016/j.jpowsour.2008.12.104.

151. Profeti, L.P.R.; Ticianelli, E.A.; Assaf, E.M. Production of hydrogen via steam reforming of biofuels on Ni/CeO_2-Al_2O_3 catalysts promoted by noble metals. *Int. J. Hydrogen Energy* **2009**, *34*, 5049–5060, doi:10.1016/j.ijhydene.2009.03.050.

152. Morales-Cano, F.; Lundegaard, L.F.; Tiruvalam, R.R.; Falsig, H.; Skjøth-Rasmussen, M.S. Improving the sintering resistance of Ni/Al_2O_3 steam-reforming catalysts by promotion with noble metals. *Appl. Catal. A Gen.* **2015**, *498*, 117–125, doi:10.1016/j.apcata.2015.03.016.

153. Nishikawa, J.; Nakamura, K.; Asadullah, M.; Miyazawa, T.; Kunimori, K.; Tomishige, K. Catalytic performance of Ni/CeO_2/Al_2O_3 modified with noble metals in steam gasification of biomass. *Catal. Today* **2008**, *131*, 146–155, doi:10.1016/j.cattod.2007.10.066.

154. Roger, A.C.; Petit, C.; Kiennemann, A. Effect of metallo-organic precursors on the synthesis of Sm-Sn pyrochlore catalysts: Application to the oxidative coupling of methane. *J. Catal.* **1997**, *167*, 447–459, doi:10.1006/jcat.1997.1601.

155. Vargas, J.C.; Libs, S.; Roger, A.C.; Kiennemann, A. Study of Ce-Zr-Co fluorite-type oxide as catalysts for hydrogen production by steam reforming of bioethanol. *Catal. Today* **2005**, *107–108*, 417–425, doi:10.1016/j.cattod.2005.07.118.

156. Sinquin, G.; Petit, C.; Hindermann, J.P.; Kiennemann, A. Study of the formation of $LaMO_3$ (M = Co, Mn) perovskites by propionates precursors: Application to the catalytic destruction of chlorinated VOCs. *Catal. Today* **2001**, *70*, 183–196, doi:10.1016/S0920-5861(01)00417-5.

157. Gosavi, P. V.; Biniwale, R.B. Pure phase $LaFeO_3$ perovskite with improved surface area synthesized using different routes and its characterization. *Mater. Chem. Phys.* **2010**, *119*, 324–329, doi:10.1016/j.matchemphys.2009.09.005.

158. Bedel, L.; Roger, A.C.; Estournes, C.; Kiennemann, A. Co^0 from partial reduction of La(Co,Fe)O_3 perovskites for Fischer-Tropsch synthesis. *Catal. Today* **2003**, *85*, 207–218, doi:10.1016/S0920-5861(03)00388-2.

159. Al-Fatesh, A.S.; Arafat, Y.; Ibrahim, A.A.; Kasim, S.O.; Alharthi, A.; Fakeeha, A.H.; Abasaeed, A.E.; Bonura, G.; Frusteri, F. Catalytic behaviour of Ce-doped Ni systems supported on stabilized zirconia under dry reforming conditions. *Catalysts* **2019**, *9*, 473, doi:10.3390/catal9050473.

160. Fang, X.; Zhang, X.; Guo, Y.; Chen, M.; Liu, W.; Xu, X.; Peng, H.; Gao, Z.; Wang, X.; Li, C. Highly active and stable Ni/$Y_2Zr_2O_7$ catalysts for methane steam reforming: On the nature and effective preparation method of the pyrochlore support. *Int. J. Hydrogen Energy* **2016**, *41*, 11141–11153, doi:10.1016/j.ijhydene.2016.04.038.

161. Kido, H.; Komarneni, S.; Roy, R. Preparation of $La_2Zr_2O_7$ by Sol—Gel Route. *J. Am. Ceram. Soc.* **1991**, *74*, 422–424, doi:10.1111/j.1151-2916.1991.tb06899.x.

162. Gaur, S.; Haynes, D.J.; Spivey, J.J. Rh, Ni, and Ca substituted pyrochlore catalysts for dry reforming of methane. *Appl. Catal. A Gen.* **2011**, *403*, 142–151, doi:10.1016/j.apcata.2011.06.025.

163. Sutthiumporn, K.; Maneerung, T.; Kathiraser, Y.; Kawi, S. CO2 dry-reforming of methane over $La_{0.8}Sr_{0.2}Ni_{0.8}M_{0.2}O_3$ perovskite (M = Bi, Co, Cr, Cu, Fe): Roles of lattice oxygen on C-H activation and carbon suppression. *Int. J. Hydrogen Energy* **2012**, *37*, 11195–11207, doi:10.1016/j.ijhydene.2012.04.059.

164. Shannon, R.D. Revised effective ionic radii and systematic studies of interatomic distances in halides and chalcogenides. *Acta Crystallogr. Sect. A* **1976**, *32*, 751–767, doi:10.1107/S0567739476001551.

165. Kim, D. Lattice Parameters, Ionic Conductivities, and Solubility limits in Fluorite-Structure MO_2 Oxide. *J. Am. Chem. Soc.* **1989**, *72*, 1415–1421, doi:10.1111/j.1151-2916.1989.tb07663.x.

166. Marrocchelli, D.; Bishop, S.R.; Tuller, H.L.; Yildiz, B. Understanding chemical expansion in non-stoichiometric oxides: Ceria and zirconia case studies. *Adv. Funct. Mater.* **2012**, *22*, 1958–1965, doi:10.1002/adfm.201102648.

167. Iglesias, I.; Baronetti, G.; Alemany, L.; Mariño, F. Insight into $Ni/Ce_{1-x}Zr_xO_{2-\delta}$ support interplay for enhanced methane steam reforming. *Int. J. Hydrogen Energy* **2019**, *44*, 3668–3680, doi:10.1016/j.ijhydene.2018.12.112.

168. Choya, A.; de Rivas, B.; González-Velasco, J.R.; Gutiérrez-Ortiz, J.I.; López-Fonseca, R. Oxidation of lean methane over cobalt catalysts supported on ceria/alumina. *Appl. Catal. A Gen.* **2020**, *591*, 117381, doi:10.1016/j.apcata.2019.117381.

169. De Rivas, B.; Sampedro, C.; Ramos-Fernández, E. V.; López-Fonseca, R.; Gascon, J.; Makkee, M.; Gutiérrez-Ortiz, J.I. Influence of the synthesis route on the catalytic oxidation of 1,2-dichloroethane over CeO_2/H-ZSM5 catalysts. *Appl. Catal. A Gen.* **2013**, *456*, 96–104, doi:10.1016/j.apcata.2013.02.026.

170. Giordano, F.; Trovarelli, A.; De Leitenburg, C.; Giona, M. A Model for the Temperature-Programmed Reduction of Low and High Surface Area Ceria. *J. Catal.* **2000**, *193*, 273–282, doi:10.1006/jcat.2000.2900.

171. Trovarelli, A.; Zamar, F.; Llorca, J.; Leitenburg, C. de; Dolcetti, G.; Kiss, J.T. Nanophase Fluorite-Structured CeO_2–ZrO_2 Catalysts Prepared by High-Energy Mechanical Milling. *J. Catal.* **1997**, *169*, 490–502, doi:10.1006/jcat.1997.1705.

172. da Silva, A.A.A.; Bion, N.; Epron, F.; Baraka, S.; Fonseca, F.C.; Rabelo-Neto, R.C.; Mattos, L. V.; Noronha, F.B. Effect of the type of ceria dopant on the performance of Ni/CeO_2 SOFC anode for ethanol internal reforming. *Appl. Catal. B Environ.* **2017**, *206*, 626–641, doi:10.1016/j.apcatb.2017.01.069.

173. Li, L.; Chen, F.; Lu, J.Q.; Luo, M.F. Study of defect sites in $Ce_{1-x}M_xO_{2-\delta}$ (x = 0.2) solid solutions using raman spectroscopy. *J. Phys. Chem. A* **2011**, *115*, 7972–7977, doi:10.1021/jp203921m.

174. Wang, J.B.; Tai, Y.-L.; Dow, W.-P.; Huang, T.-J. Study of ceria-supported nickel catalyst and effect of

yttria doping on carbon dioxide reforming of methane. *Appl. Catal. A Gen.* **2001**, *218*, 69–79, doi:10.1016/S0926-860X(01)00620-2.

175. Fang, W.; Pirez, C.; Dhepe, P.L.; Dumeignil, F.; Jalowiecki-duhamel, L. RSC Advances Ce – Ni mixed oxide as efficient catalyst for H_2 production and nanofibrous carbon material from ethanol in the presence of water. **2012**, 9626–9634, doi:10.1039/c2ra21701e.

176. Meeyoo, V.; Panchan, N.; Phongprueksathat, N.; Traitangwong, A.; Guo, X.; Li, C.; Rirksomboon, T. Low Temperature Methanation of CO_2 on High Ni Content Ni-Ce-ZrO_δ Catalysts Prepared via One-Pot Hydrothermal Synthesis. *Catalysts* **2019**, *10*, 32, doi:10.3390/catal10010032.

177. Roh, H.S.; Jun, K.W.; Dong, W.S.; Chang, J.S.; Park, S.E.; Joe, Y. Il Highly active and stable Ni/Ce-ZrO_2 catalyst for H_2 production from methane. *J. Mol. Catal. A Chem.* **2002**, *181*, 137–142, doi:10.1016/S1381-1169(01)00358-2.

178. Yamazaki, S.; Matsui, T.; Ohashi, T.; Arita, Y. Defect structures in doped CeO_2 studied by using XAFS spectrometry. *Solid State Ionics* **2000**, *136–137*, 913–920, doi:10.1016/S0167-2738(00)00569-5.

179. Ao, M.; Pham, G.H.; Sage, V.; Pareek, V. Structure and activity of strontium substituted $LaCoO_3$ perovskite catalysts for syngas conversion. *J. Mol. Catal. A Chem.* **2016**, *416*, 96–104, doi:10.1016/j.molcata.2016.02.020.

180. Wang, H.; Dong, X.; Zhao, T.; Yu, H.; Li, M. Dry reforming of methane over bimetallic Ni-Co catalyst prepared from $La(Co_xNi_{1-x})_{0.5}Fe_{0.5}O_3$ perovskite precursor: Catalytic activity and coking resistance. *Appl. Catal. B Environ.* **2019**, *245*, 302–313, doi:10.1016/j.apcatb.2018.12.072.

181. Guo, S.; Puleo, F.; Wang, L.; Wu, H.; Liotta, L.F. $La_{0.6}Sr_{0.4}Co_{0.2}Fe_{0.79}M_{0.01}O_{3-\delta}$ (M = Ni, Pd) perovskites synthesized by Citrate-EDTA method: Oxygen vacancies effect on electrochemical properties. *Adv. Powder Technol.* **2018**, *29*, 2804–2812, doi:10.1016/j.apt.2018.07.029.

182. Morales, M.; Segarra, M. Applied Catalysis A : General Steam reforming and oxidative steam reforming of ethanol over production. *"Applied Catal. A, Gen.* **2015**, *502*, 305–311, doi:10.1016/j.apcata.2015.05.036.

183. Yakovleva, I.S.; Isupova, L.A.; Rogov, V.A. Oxygen species and their reactivity in the mechanochemically prepared substituted perovskites $La_{1-X}Sr_xCoO_{3-Y}$ (x = 0-1). *Kinet. Catal.* **2009**, *50*, 275–283, doi:10.1134/S0023158409020190.

184. Lin, K.H.; Wang, C. Bin; Chien, S.H. Catalytic performance of steam reforming of ethanol at low temperature over $LaNiO_3$ perovskite. *Int. J. Hydrogen Energy* **2013**, *38*, 3226–3232, doi:10.1016/j.ijhydene.2013.01.005.

185. Oemar, U.; Ang, P.S.; Hidajat, K.; Kawi, S. Promotional effect of Fe on perovskite $LaNi_xFe_{1-x}O_3$ catalyst for hydrogen production via steam reforming of toluene. *Int. J. Hydrogen Energy* **2013**, *38*, 5525–5534, doi:10.1016/j.ijhydene.2013.02.083.

186. Pereñíguez, R.; González-DelaCruz, V.M.; Holgado, J.P.; Caballero, A. Synthesis and characterization of a LaNiO3 perovskite as precursor for methane reforming reactions catalysts. *Appl. Catal. B Environ.* **2010**, *93*, 346–353, doi:10.1016/j.apcatb.2009.09.040.

187. Zhao, B.; Liu, P.; Li, S.; Shi, H.; Jia, X.; Wang, Q.; Yang, F.; Song, Z.; Guo, C.; Hu, J.; et al. Bimetallic Ni-Co nanoparticles on SiO_2 as robust catalyst for CO methanation: Effect of homogeneity of Ni-Co alloy. *Appl. Catal. B Environ.* **2020**, *278*, doi:10.1016/j.apcatb.2020.119307.

188. Wu, G.; Li, S.; Zhang, C.; Wang, T.; Gong, J. Glycerol steam reforming over perovskite-derived nickel-based catalysts. *Appl. Catal. B Environ.* **2014**, *144*, 277–285, doi:10.1016/j.apcatb.2013.07.028.

189. Nabgan, W.; Tuan Abdullah, T.A.; Mat, R.; Nabgan, B.; Triwahyono, S.; Ripin, A. Hydrogen production from catalytic steam reforming of phenol with bimetallic nickel-cobalt catalyst on various supports. *Appl. Catal. A Gen.* **2016**, *527*, 161–170, doi:10.1016/j.apcata.2016.08.033.

190. Huang, L.; Bassir, M.; Kaliaguine, S. Reducibility of Co^{3+} in perovskite-type $LaCoO_3$ and promotion of copper on the reduction of Co^{3+} in perovskite-type oxides. *Appl. Surf. Sci.* **2005**, *243*, 360–375, doi:10.1016/j.apsusc.2004.09.079.

191. Szabo, V.; Bassir, M.; Van Neste, A.; Kaliaguine, S. Perovskite-type oxides synthesized by reactive grinding. *Appl. Catal. B Environ.* **2002**, *37*, 175–180, doi:10.1016/S0926-3373(01)00328-9.

192. Huang, L.; Bassir, M.; Bousselham, E.; Kaliaguine, S. Comparative Studies on the Properties of New and Conventional Perovskite-Type $LaCoO_3$. *Bull. Chem. Soc. Jpn.* **2005**, *78*, 1450–1456, doi:10.1246/bcsj.78.1450.

193. Wu, X.; Fan, J.; Ran, R.; Weng, D. Effect of preparation methods on the structure and redox behavior of platinum-ceria-zirconia catalysts. *Chem. Eng. J.* **2005**, *109*, 133–139, doi:10.1016/j.cej.2005.04.003.

194. Medina, O.E.; Gallego, J.; Restrepo, L.G.; Cortés, F.B.; Franco, C.A. Influence of the Ce^{4+}/Ce^{3+} redox-couple on the cyclic regeneration for adsorptive and catalytic performance of NiO-PdO/$CeO_{2\pm\delta}$ nanoparticles for n-C7 asphaltene steam gasification. *Nanomaterials* **2019**, *9*, 734, doi:10.3390/nano9050734.

195. Wang, J.; Shen, M.; Wang, J.; Yang, M.; Wang, W.; Ma, J.; Jia, L. Effects of Ni-doping of ceria-based materials on their micro-structures and dynamic oxygen storage and release behaviors. *Catal. Letters* **2010**, *140*, 38–48, doi:10.1007/s10562-010-0420-2.

196. Sunding, M.F.; Hadidi, K.; Diplas, S.; Løvvik, O.M.; Norby, T.E.; Gunnæs, A.E. XPS characterisation of in situ treated lanthanum oxide and hydroxide using tailored charge referencing and peak fitting procedures. *J. Electron Spectros. Relat. Phenomena* **2011**, *184*, 399–409, doi:10.1016/j.elspec.2011.04.002.

197. Ogugua, S.N.; Swart, H.C.; Ntwaeaborwa, O.M. The influence of post-preparation annealing atmospheres on the optical properties and energy transfer between Pr^{3+} and Dy^{3+} in mixed lanthanum-yttrium oxyorthosilicate hosts. *Opt. Mater. (Amst).* **2018**, *76*, 125–140, doi:10.1016/j.optmat.2017.12.032.

198. Imada, S.; Jo, T. Effects of hybridization on multiplet structures in 3d- and 4d-core photoemission spectra in light rare earth compounds. *Phys. Scr.* **1990**, *41*, 115–119, doi:10.1088/0031-8949/41/1/028.

199. Deka, D.J.; Gunduz, S.; Fitzgerald, T.; Miller, J.T.; Co, A.C.; Ozkan, U.S. Production of syngas with controllable H_2/CO ratio by high temperature co-electrolysis of CO_2 and H_2O over Ni and Co- doped lanthanum strontium ferrite perovskite cathodes. *Appl. Catal. B Environ.* **2019**, *248*, 487–503, doi:10.1016/j.apcatb.2019.02.045.

200. Chen, Y.S.; Kang, J.F.; Chen, B.; Gao, B.; Liu, L.F.; Liu, X.Y.; Wang, Y.Y.; Wu, L.; Yu, H.Y.; Wang, J.Y.; et al. Microscopic mechanism for unipolar resistive switching behaviour of nickel oxides. *J. Phys. D. Appl. Phys.* **2012**, *45*, doi:10.1088/0022-3727/45/6/065303.

201. Turner, N.H.; Single, A.M. Determination of peak positions and areas from wide-scan XPS spectra. *Surf. Interface Anal.* **1990**, *15*, 215–222, doi:10.1002/sia.740150305.

202. Dickinson, M.; Scott, T.B.; Crane, R.A.; Riba, O.; Barnes, R.J.; Hughes, G.M. The effects of vacuum annealing on the structure and surface chemistry of iron:nickel alloy nanoparticles. *J. Nanoparticle Res.* **2010**, *12*, 2081–2092, doi:10.1007/s11051-009-9767-y.

203. Sutthiumporn, K.; Kawi, S. Promotional effect of alkaline earth over Ni-La_2O_3 catalyst for CO_2 reforming of CH_4: Role of surface oxygen species on H_2 production and carbon suppression. *Int. J. Hydrogen Energy* **2011**, *36*, 14435–14446, doi:10.1016/j.ijhydene.2011.08.022.

204. Huang, T.J.; Wang, C.H. Methane decomposition and self de-coking over gadolinia-doped ceria-supported Ni catalysts. *Chem. Eng. J.* **2007**, *132*, 97–103, doi:10.1016/j.cej.2007.01.024.

205. Chen, D.L.; Pan, K.L.; Chang, M.B. Catalytic removal of phenol from gas streams by perovskite-type catalysts. *J. Environ. Sci. (China)* **2017**, *56*, 131–139, doi:10.1016/j.jes.2016.04.031.

206. Kudo, Y.; Yoshida, N.; Fujimoto, M.; Tanaka, K. Acid-Dissociation Behavior of para-Hydroxyl Group in the N,N,O-Terdentate Ligand, 4-(4-Methyl-2-pyridylazo)resorcinol Coordinated to a Transition Metal Iron. *Bull. Chem. Soc. Jpn.* **1986**, *59*, 1481–1486.

207. WALDVOGEL, A. Mise au point d'un catalyseur performant pour la chaîne de procédé Power to Methane et étude cinétique, University of Strasbourg, 2017.

208. González Tejuca, L.; Bell, A.T.; Fierro, J.L.G.; Peña, M.A. Surface behaviour of reduced $LaCoO_3$ as studied by TPD of CO, CO_2 and H_2 probes and by XPS. *Appl. Surf. Sci.* **1988**, *31*, 301–316, doi:10.1016/0169-4332(88)90095-5.

209. Simell, P.A.; Hepola, J.O.; Krause, A.O.I. Effects of gasification gas components on tar and ammonia decomposition over hot gas cleanup catalysts. *Fuel* **1997**, *76*, 1117–1127, doi:10.1016/S0016-2361(97)00109-9.

210. Czernik, S.; Evans, R.; French, R. Hydrogen from biomass-production by steam reforming of biomass pyrolysis oil. *Catal. Today* **2007**, *129*, 265–268, doi:10.1016/j.cattod.2006.08.071.

211. Zhang, Z.; Ou, Z.; Qin, C.; Ran, J.; Wu, C. Roles of alkali/alkaline earth metals in steam reforming of biomass tar for hydrogen production over perovskite supported Ni catalysts. *Fuel* **2019**, *257*, 116032, doi:10.1016/j.fuel.2019.116032.

212. Jess, A. Mechanisms and kinetics of thermal reactions of aromatic hydrocarbons from pyrolysis of solid

fuels. *Fuel* **1996**, *75*, 1441–1448, doi:10.1016/0016-2361(96)00136-6.

213. Liu, L.; Zhang, Z.; Das, S.; Kawi, S. Reforming of tar from biomass gasification in a hybrid catalysis-plasma system: A review. *Appl. Catal. B Environ.* **2019**, *250*, 250–272, doi:10.1016/j.apcatb.2019.03.039.

214. Zhao, B.; Zhang, X.; Chen, L.; Qu, R.; Meng, G.; Yi, X.; Sun, L. Steam reforming of toluene as model compound of biomass pyrolysis tar for hydrogen. *Biomass and Bioenergy* **2010**, *34*, 140–144, doi:10.1016/j.biombioe.2009.10.011.

215. Zhang, R.; Wang, Y.; Brown, R.C. Steam reforming of tar compounds over Ni/olivine catalysts doped with CeO_2. *Energy Convers. Manag.* **2007**, *48*, 68–77, doi:10.1016/j.enconman.2006.05.001.

216. Srinakruang, J.; Sato, K.; Vitidsant, T.; Fujimoto, K. Highly efficient sulfur and coking resistance catalysts for tar gasification with steam. *Fuel* **2006**, *85*, 2419–2426, doi:10.1016/j.fuel.2006.04.026.

217. Oh, G.; Park, S.Y.; Seo, M.W.; Ra, H.W.; Mun, T.Y.; Lee, J.G.; Yoon, S.J. Combined steam-dry reforming of toluene in syngas over CaNiRu/Al_2O_3 catalysts. *Int. J. Green Energy* **2019**, *16*, 333–349, doi:10.1080/15435075.2019.1566729.

218. Łamacz, A.; Babiński, P.; Łabojko, G. The impact of components of synthesis gas from coal gasification on conversion of model tar compounds over Ni/$CeZrO_2$ catalyst. *Fuel* **2019**, *236*, 984–992, doi:10.1016/j.fuel.2018.09.075.

219. Swierczynski, D.; Courson, C.; Kiennemann, A. Study of steam reforming of toluene used as model compound of tar produced by biomass gasification. *Chem. Eng. Process. Process Intensif.* **2008**, *47*, 508–513, doi:10.1016/j.cep.2007.01.012.

220. Josuinkas, F.M.; Quitete, C.P.B.; Ribeiro, N.F.P.; Souza, M.M.V.M. Steam reforming of model gasification tar compounds over nickel catalysts prepared from hydrotalcite precursors. *Fuel Process. Technol.* **2014**, *121*, 76–82, doi:10.1016/j.fuproc.2014.01.007.

221. Liu, X.; Yang, X.; Liu, C.; Chen, P.; Yue, X.; Zhang, S. Low-temperature catalytic steam reforming of toluene over activated carbon supported nickel catalysts. *J. Taiwan Inst. Chem. Eng.* **2016**, *65*, 233–241, doi:10.1016/j.jtice.2016.05.006.

222. Wang, S.; Li, X.; Zhang, F.; Cai, Q.; Wang, Y.; Luo, Z. Bio-oil catalytic reforming without steam addition: Application to hydrogen production and studies on its mechanism. *Int. J. Hydrogen Energy* **2013**, *38*, 16038–16047, doi:10.1016/j.ijhydene.2013.10.032.

223. Koike, M.; Li, D.; Watanabe, H.; Nakagawa, Y.; Tomishige, K. Comparative study on steam reforming of model aromatic compounds of biomass tar over Ni and Ni-Fe alloy nanoparticles. *Appl. Catal. A Gen.* **2015**, *506*, 151–162, doi:10.1016/j.apcata.2015.09.007.

224. Constantinou, D.A.; Efstathiou, A.M. Low-temperature purification of gas streams from phenol by steam reforming over novel supported-Rh catalysts. *Appl. Catal. B Environ.* **2010**, *96*, 276–289, doi:10.1016/j.apcatb.2010.02.007.

225. Constantinou, D.A.; Álvarez-Galván, M.C.; Fierro, J.L.G.; Efstathiou, A.M. Low-temperature conversion

of phenol into CO, CO_2 and H_2 by steam reforming over La-containing supported Rh catalysts. *Appl. Catal. B Environ.* **2012**, *117–118*, 81–95, doi:10.1016/j.apcatb.2012.01.005.

226. Peng, Q.; Tao, Y.; Ling, H.; Wu, Z.; Zhu, Z.; Jiang, R.; Zhao, Y.; Wang, Y.; Ji, C.; Liao, X.; et al. Tuning Hydrogen and Carbon Nanotube Production from Phenol Steam Reforming on Ni/Fe-Based Nanocatalysts. *ACS Sustain. Chem. Eng.* **2017**, *5*, 2098–2108, doi:10.1021/acssuschemeng.6b01936.

227. Hwang, K.R.; Lee, C.B.; Park, J.S. Advanced nickel metal catalyst for water-gas shift reaction. *J. Power Sources* **2011**, *196*, 1349–1352, doi:10.1016/j.jpowsour.2010.08.084.

228. Ang, M.L.; Oemar, U.; Kathiraser, Y.; Saw, E.T.; Lew, C.H.K.; Du, Y.; Borgna, A.; Kawi, S. High-temperature water-gas shift reaction over Ni/xK/CeO_2 catalysts: Suppression of methanation via formation of bridging carbonyls. *J. Catal.* **2015**, *329*, 130–143, doi:10.1016/j.jcat.2015.04.031.

229. Panagiotopoulou, P.; Kondarides, D.I.; Verykios, X.E. Selective methanation of CO over supported Ru catalysts. *Appl. Catal. B Environ.* **2009**, *88*, 470–478, doi:10.1016/j.apcatb.2008.10.012.

230. Wang, T.; Porosoff, M.D.; Chen, J.G. Effects of oxide supports on the water-gas shift reaction over PtNi bimetallic catalysts: Activity and methanation inhibition. *Catal. Today* **2014**, *233*, 61–69, doi:10.1016/j.cattod.2013.09.037.

231. Shinde, V.M.; Madras, G. Water gas shift reaction over multi-component ceria catalysts. *Appl. Catal. B Environ.* **2012**, *123–124*, 367–378, doi:10.1016/j.apcatb.2012.05.007.

232. Hu, D.; Gao, J.; Ping, Y.; Jia, L.; Gunawan, P.; Zhong, Z.; Xu, G.; Gu, F.; Su, F. Enhanced Investigation of CO Methanation over Ni/Al_2O_3 Catalysts for Synthetic Natural Gas Production. *Ind. Eng. Chem. Res.* **2012**, *51*, 4875–4886, doi:10.1021/ie300049f.

233. Wang, D.; Montané, D.; Chornet, E. Catalytic steam reforming of biomass-derived oxygenates: acetic acid and hydroxyacetaldehyde. *Appl. Catal. A Gen.* **1996**, *143*, 245–270, doi:10.1016/0926-860X(96)00093-2.

234. Artetxe, M.; Nahil, M.A.; Olazar, M.; Williams, P.T. Steam reforming of phenol as biomass tar model compound over Ni/Al_2O_3 catalyst. *Fuel* **2016**, *184*, 629–636, doi:10.1016/j.fuel.2016.07.036.

235. Gai, C.; Zhang, F.; Lang, Q.; Liu, T.; Peng, N.; Liu, Z. Facile one-pot synthesis of iron nanoparticles immobilized into the porous hydrochar for catalytic decomposition of phenol. *Appl. Catal. B Environ.* **2017**, *204*, 566–576, doi:10.1016/j.apcatb.2016.12.005.

236. Wu, G.; Zhang, C.; Li, S.; Han, Z.; Wang, T.; Ma, X.; Gong, J. Hydrogen production via glycerol steam reforming over Ni/Al_2O_3: Influence of nickel precursors. *ACS Sustain. Chem. Eng.* **2013**, *1*, 1052–1062, doi:10.1021/sc400123f.

237. Ye, F.; Mori, T.; Ou, D.R.; Zou, J.; Drennan, J.; Nakayama, S.; Miyayama, M. Effect of nickel diffusion on the microstructure of Gd-doped ceria (GDC) electrolyte film supported by Ni-GDC cermet anode. *Solid State Ionics* **2010**, *181*, 646–652, doi:10.1016/j.ssi.2010.03.012.

238. Wang, X.; Shen, M.; Wang, J.; Fabris, S. Enhanced oxygen buffering by substitutional and interstitial Ni point defects in ceria: A first-principles DFT+U study. *J. Phys. Chem. C* **2010**, *114*, 10221–10228,

doi:10.1021/jp101100f.

239. De Souza, E.F.; Chagas, C.A.; Manfro, R.L.; Souza, M.M.V.M.; Bicca De Alencastro, R.; Schmal, M. Combined DFT and experimental study of the dispersion and interaction of copper species in Ni-CeO_2 nanosized solid solutions. *RSC Adv.* **2016**, *6*, 5057–5067, doi:10.1039/c5ra23139f.

240. Carrasco, J.; Lõpez-Durán, D.; Liu, Z.; Duchoň, T.; Evans, J.; Senanayake, S.D.; Crumlin, E.J.; Matolín, V.; Rodríguez, J.A.; Ganduglia-Pirovano, M.V. In situ and theoretical studies for the dissociation of water on an active Ni/CeO_2 Catalyst: Importance of strong metal-support interactions for the cleavage of O-H bonds. *Angew. Chemie - Int. Ed.* **2015**, *54*, 3917–3921, doi:10.1002/anie.201410697.

241. Łamacz, A.; Matus, K.; Liszka, B.; Silvestre-Albero, J.; Lafjah, M.; Dintzer, T.; Janowska, I. The impact of synthesis method of CNT supported $CeZrO_2$ and Ni-$CeZrO_2$ on catalytic activity in WGS reaction. *Catal. Today* **2018**, *301*, 172–182, doi:10.1016/j.cattod.2017.03.035.

242. Da Silva, A.L.M.; Den Breejen, J.P.; Mattos, L. V.; Bitter, J.H.; De Jong, K.P.; Noronha, F.B. Cobalt particle size effects on catalytic performance for ethanol steam reforming - Smaller is better. *J. Catal.* **2014**, *318*, 67–74, doi:10.1016/j.jcat.2014.07.020.

243. Sun, J.; Mei, D.; Karim, A.M.; Datye, A.K.; Wang, Y. Minimizing the Formation of Coke and Methane on Co Nanoparticles in Steam Reforming of Biomass-Derived Oxygenates. *ChemCatChem* **2013**, *5*, 1299–1303, doi:10.1002/cctc.201300041.

244. Kim, J.-H.; Suh, D.J.; Park, T.-J.; Kim, K.-L. Effect of metal particle size on coking during CO_2 reforming of CH_4 over Ni–alumina aerogel catalysts. *Appl. Catal. A Gen.* **2000**, *197*, 191–200, doi:10.1016/S0926-860X(99)00487-1.

245. TAKANABE, K.; NAGAOKA, K.; NARIAI, K.; AIKA, K. Titania-supported cobalt and nickel bimetallic catalysts for carbon dioxide reforming of methane. *J. Catal.* **2005**, *232*, 268–275, doi:10.1016/j.jcat.2005.03.011.

246. Horiuchi, T.; Sakuma, K.; Fukui, T.; Kubo, Y.; Osaki, T.; Mori, T. Suppression of carbon deposition in the CO_2-reforming of CH_4 by adding basic metal oxides to a Ni/Al_2O_3 catalyst. *Appl. Catal. A Gen.* **1996**, *144*, 111–120, doi:10.1016/0926-860X(96)00100-7.

247. Zhuang, Q.; Qin*, Y.; Chang, L. Promoting effect of cerium oxide in supported nickel catalyst for hydrocarbon steam-reforming. *Appl. Catal.* **1991**, *70*, 1–8, doi:10.1016/S0166-9834(00)84149-4.

248. Tomishige, K.; Li, D.; Tamura, M.; Nakagawa, Y. Nickel-iron alloy catalysts for reforming of hydrocarbons: Preparation, structure, and catalytic properties. *Catal. Sci. Technol.* **2017**, *7*, 3952–3979, doi:10.1039/c7cy01300k.

249. Kim, S.H.; Nam, S.W.; Lim, T.H.; Lee, H.I. Effect of pretreatment on the activity of Ni catalyst for CO removal reaction by water-gas shift and methanation. *Appl. Catal. B Environ.* **2008**, *81*, 97–104, doi:10.1016/j.apcatb.2007.12.009.

250. Gohier, A.; Ewels, C.P.; Minea, T.M.; Djouadi, M.A. Carbon nanotube growth mechanism switches from tip- to base-growth with decreasing catalyst particle size. *Carbon N. Y.* **2008**, *46*, 1331–1338, doi:10.1016/j.carbon.2008.05.016.

251. Souza, M.D.M.V.M.; Clavé, L.; Dubois, V.; Perez, C.A.C.; Schmal, M. Activation of supported nickel catalysts for carbon dioxide reforming of methane. *Appl. Catal. A Gen.* **2004**, *272*, 133–139, doi:10.1016/j.apcata.2004.05.026.

252. He, L.; Hu, S.; Jiang, L.; Liao, G.; Chen, X.; Han, H.; Xiao, L.; Ren, Q.; Wang, Y.; Su, S.; et al. Carbon nanotubes formation and its influence on steam reforming of toluene over Ni/Al_2O_3 catalysts: Roles of catalyst supports. *Fuel Process. Technol.* **2018**, *176*, 7–14, doi:10.1016/j.fuproc.2018.03.007.

253. Rieck, J.S.; Bell, A.T. The influence of dispersion on the interactions of H_2 and CO with Pd SiO_2. *J. Catal.* **1987**, *103*, 46–54, doi:10.1016/0021-9517(87)90091-1.

254. Xu, J.; Bartholomew, C.H. Temperature-programmed hydrogenation (TPH) and in situ mössbauer spectroscopy studies of carbonaceous species on silica-supported iron fischer-tropsch catalysts. *J. Phys. Chem. B* **2005**, *109*, 2392–2403, doi:10.1021/jp048808j.

255. Du, Z.Y.; Zhang, Z.H.; Xu, C.; Wang, X.B.; Li, W.Y. Low Temperature Steam Reforming of Toluene and Biomass Tar over Biochar-Supported Ni Nanoparticles. *ACS Sustain. Chem. Eng.* **2019**, *7*, 3111–3119, doi:10.1021/acssuschemeng.8b04872.

256. Courson, C.; Makaga, E.; Petit, C.; Kiennemann, A. Development of Ni catalysts for gas production from biomass gasification. Reactivity in steam- and dry-reforming. *Catal. Today* **2000**, *63*, 427–437, doi:10.1016/S0920-5861(00)00488-0.

257. Musumeci, A.W.; Silva, G.G.; Martens, W.N.; Waclawik, E.R.; Frost, R.L. Thermal decomposition and electron microscopy studies of single-walled carbon nanotubes. *J. Therm. Anal. Calorim.* **2007**, *88*, 885–891, doi:10.1007/s10973-006-7563-9.

258. Matas Güell, B.; Babich, I. V.; Lefferts, L.; Seshan, K. Steam reforming of phenol over Ni-based catalysts - A comparative study. *Appl. Catal. B Environ.* **2011**, *106*, 280–286, doi:10.1016/j.apcatb.2011.05.012.

259. Zou, X.; Chen, T.; Zhang, P.; Chen, D.; He, J.; Dang, Y.; Ma, Z.; Chen, Y.; Toloueinia, P.; Zhu, C.; et al. High catalytic performance of Fe-Ni/Palygorskite in the steam reforming of toluene for hydrogen production. *Appl. Energy* **2018**, *226*, 827–837, doi:10.1016/j.apenergy.2018.06.005.

260. Mukai, D.; Tochiya, S.; Murai, Y.; Imori, M.; Sugiura, Y.; Sekine, Y. Structure and activity of $Ni/La_{0.7}Sr_{0.3}AlO_{3-\delta}$ catalyst for hydrogen production by steam reforming of toluene. *Appl. Catal. A Gen.* **2013**, *464–465*, 78–86, doi:10.1016/j.apcata.2013.05.023.

261. Cybulski, A.; Moulijn, J.A. *Structured Catalysts and Reactors*; CRC Press, T.F.G., Ed.; 2nd editio.; Taylor Francis Group, 2006;

262. Brussino, P.; Banús, E.D.; Ulla, M.A.; Bortolozzi, J.P. NiO-based ceramic structured catalysts for ethylene production: Substrates and active sites. *Catal. Today* **2020**, doi:10.1016/j.cattod.2020.09.005.

263. Sanz, O.; Echave, F.J.; Romero-Sarria, F.; Odriozola, J.A.; Montes, M. Advances in Structured and Microstructured Catalytic Reactors for Hydrogen Production. In *Renewable Hydrogen Technologies*; Elsevier, 2013; pp. 201–224.

264. Bortolozzi, J.P.; Banús, E.D.; Milt, V.G.; Miro, E.E. New formulations of Ni-containing ceramic papers to enhance the catalytic performance for the oxidative dehydrogenation of ethane. *Ind. Eng. Chem. Res.* **2014**, *53*, 17570–17579, doi:10.1021/ie503154f.

265. Frey, M.; David, E.; Roger, A.C. Optimization of structured cellular foam-based catalysts for low-temperature carbon dioxide methanation in a platelet milli-reactor. **2015**, *18*, 283–292.

266. Barbero, B.P.; Costa-Almeida, L.; Sanz, O.; Morales, M.R.; Cadus, L.E.; Montes, M. Washcoating of metallic monoliths with a MnCu catalyst for catalytic combustion of volatile organic compounds. *Chem. Eng. J.* **2008**, *139*, 430–435, doi:10.1016/j.cej.2007.12.033.

267. Santos, D.F.M.; Soares, O.S.G.P.; Figueiredo, J.L.; Sanz, O.; Montes, M.; Pereira, M.F.R. Preparation of ceramic and metallic monoliths coated with cryptomelane as catalysts for VOC abatement. *Chem. Eng. J.* **2020**, *382*, 122923, doi:10.1016/j.cej.2019.122923.

268. Avila, P.; Montes, M.; Miró, E.E. Monolithic reactors for environmental applications: A review on preparation technologies. *Chem. Eng. J.* **2005**, *109*, 11–36, doi:10.1016/j.cej.2005.02.025.

269. Brussino, P.; Bortolozzi, J.P.; Sanz, O.; Montes, M.; Ulla, M.A.; Banús, E.D. Fecralloy monoliths coated with Ni/Al_2O_3 applied to the low-temperature production of ethylene. *Catalysts* **2018**, *8*, doi:10.3390/catal8070291.

270. Ugues, D.; Specchia, S.; Saracco, G. Optimal Microstructural Design of a Catalytic Premixed FeCrAlloy Fiber Burner for Methane Combustion. *Ind. Eng. Chem. Res.* **2004**, *43*, 1990–1998, doi:10.1021/ie034202q.

271. Nguyen, P.; Pham, C. Innovative porous SiC-based materials: From nanoscopic understandings to tunable carriers serving catalytic needs. *Appl. Catal. A Gen.* **2011**, *391*, 443–454, doi:10.1016/j.apcata.2010.07.054.

272. Díaz, J.A.; Calvo-Serrano, M.; De La Osa, A.R.; García-Minguillán, A.M.; Romero, A.; Giroir-Fendler, A.; Valverde, J.L. β-Silicon carbide as a catalyst support in the fischer-tropsch synthesis: Influence of the modification of the support by a pore agent and acidic treatment. *Appl. Catal. A Gen.* **2014**, *475*, 82–89, doi:10.1016/j.apcata.2014.01.021.

273. Lacroix, M.; Dreibine, L.; De Tymowski, B.; Vigneron, F.; Edouard, D.; Bégin, D.; Nguyen, P.; Pham, C.; Savin-Poncet, S.; Luck, F.; et al. Silicon carbide foam composite containing cobalt as a highly selective and re-usable Fischer-Tropsch synthesis catalyst. *Appl. Catal. A Gen.* **2011**, *397*, 62–72, doi:10.1016/j.apcata.2011.02.012.

274. Ledoux, M.J.; Hantzer, S.; Pham-Huu, C.; Guille, J.; Desaneaux, M.P. New synthesis and uses of high-specific-surface SiC as a catalytic support that is chemically inert and has high thermal resistance. *J. Catal.* **1988**, *114*, 176–185, doi:10.1016/0021-9517(88)90019-X.

275. Lillebø, A.; Håvik, S.; Blekkan, E.A.; Holmen, A. Fischer-tropsch synthesis on SiC-supported cobalt catalysts. *Top. Catal.* **2013**, *56*, 730–736, doi:10.1007/s11244-013-0032-3.

276. De Tymowski, B.; Liu, Y.; Meny, C.; Lefèvre, C.; Begin, D.; Nguyen, P.; Pham, C.; Edouard, D.; Luck, F.; Pham-Huu, C. Co-Ru/SiC impregnated with ethanol as an effective catalyst for the Fischer-Tropsch

synthesis. *Appl. Catal. A Gen.* **2012**, *419–420*, 31–40, doi:10.1016/j.apcata.2012.01.004.

277. de la Osa, A.R.; Romero, A.; Dorado, F.; Valverde, J.L.; Sánchez, P. Influence of cobalt precursor on efficient production of commercial fuels over FTS Co/SiC catalyst. *Catalysts* **2016**, *6*, doi:10.3390/catal6070098.

278. Frey, M.; Romero, T.; Roger, A.C.; Edouard, D. Open cell foam catalysts for CO_2 methanation: Presentation of coating procedures and in situ exothermicity reaction study by infrared thermography. *Catal. Today* **2016**, *273*, 83–90, doi:10.1016/j.cattod.2016.03.016.

279. Frey, M.; Romero, T.; Roger, A.C.; Edouard, D. An intensification of the CO_2 methanation reaction: Effect of carbon nanofiber network on the hydrodynamic, thermal and catalytic properties of reactors filled with open cell foams. *Chem. Eng. Sci.* **2019**, *195*, 271–280, doi:10.1016/j.ces.2018.11.028.

280. García-Moncada, N.; Jurado, L.; Martínez-Tejada, L.M.; Romero-Sarria, F.; Odriozola, J.A. Boosting water activation determining-step in WGS reaction on structured catalyst by Mo-doping. *Catal. Today* **2020**, *In Press*, doi:10.1016/j.cattod.2020.06.003.

281. Martínez Tejada, L.M.; Domínguez, M.I.; Sanz, O.; Centeno, M.A.; Odriozola, J.A. Au/CeO_2 metallic monolith catalysts: Influence of the metallic substrate. *Gold Bull.* **2013**, *46*, 221–231, doi:10.1007/s13404-013-0102-0.

282. González-Castaño, M.; Saché, E. Le; Ivanova, S.; Romero-Sarria, F.; Centeno, M.A.; Odriozola, J.A. Tailoring structured WGS catalysts: Impact of multilayered concept on the water surface interactions. *Appl. Catal. B Environ.* **2018**, *222*, 124–132, doi:10.1016/j.apcatb.2017.10.018.

283. Sanz, O.; Almeida, L.C.; Zamaro, J.M.; Ulla, M.A.; Miró, E.E.; Montes, M. Washcoating of Pt-ZSM5 onto aluminium foams. *Appl. Catal. B Environ.* **2008**, *78*, 166–175, doi:10.1016/j.apcatb.2007.09.024.

284. Lee, J.; Kong, K.Y.; Jung, C.R.; Cho, E.; Yoon, S.P.; Han, J.; Lee, T.G.; Nam, S.W. A structured Co-B catalyst for hydrogen extraction from NaBH4 solution. *Catal. Today* **2007**, *120*, 305–310, doi:10.1016/j.cattod.2006.09.019.

285. Echave, F.J.; Sanz, O.; Velasco, I.; Odriozola, J.A.; Montes, M. Effect of the alloy on micro-structured reactors for methanol steam reforming. *Catal. Today* **2013**, *213*, 145–154, doi:10.1016/j.cattod.2013.02.027.

286. Burgos, N.; Paulis, M.; Montes, M. Preparation of Al_2O_3/Al monoliths by anodisation of aluminium as structured catalytic supports. *J. Mater. Chem.* **2003**, *13*, 1458, doi:10.1039/b212242a.

287. Thommes, M.; Kaneko, K.; Neimark, A. V.; Olivier, J.P.; Rodriguez-Reinoso, F.; Rouquerol, J.; Sing, K.S.W. Physisorption of gases, with special reference to the evaluation of surface area and pore size distribution (IUPAC Technical Report). *Pure Appl. Chem.* **2015**, *87*, 1051–1069, doi:10.1515/pac-2014-1117.

288. Medri, V.; Ruffini, A. The influence of process parameters on in situ inorganic foaming of alkali-bonded SiC based foams. *Ceram. Int.* **2012**, *38*, 3351–3359, doi:10.1016/j.ceramint.2011.12.045.

289. Deng, J.; Dai, H.; Jiang, H.; Zhang, L.; Wang, G.; He, H.; Chak Tong, A.U. Hydrothermal Fabrication

and Catalytic Properties of $La_{1-x}Sr_xM_{1-y}Fe_yO_3$ (M = Mn, Co) That Are Highly Active for the Removal of Toluene. *Environ. Sci. Technol.* **2010**, *44*, 2618–2623, doi:10.1021/es9031997.

290. Jacobson, N.S.; Myers, D.L. Active oxidation of SiC. *Oxid. Met.* **2011**, *75*, 1–25, doi:10.1007/s11085-010-9216-4.

291. Socha, R.P.; Laajalehto, K.; Nowak, P. Influence of the surface properties of silicon carbide on the process of SiC particles codeposition with nickel. *Colloids Surfaces A Physicochem. Eng. Asp.* **2002**, *208*, 267–275, doi:10.1016/S0927-7757(02)00153-X.

292. Jin, G.; Gu, F.; Liu, Q.; Wang, X.; Jia, L.; Xu, G. Highly stable Ni / SiC catalyst modified by Al_2O_3 for CO methanation reaction †. **2016**, 9631–9639, doi:10.1039/c5ra19940a.

293. Jiao, Z.F.; Dong, L.L.; Guo, X.N.; Jin, G.Q.; Guo, X.Y.; Wang, X.M. Methane catalytic combustion over Ni/SiC, Fe/SiC and Co/SiC modified by $Zr_{0.5}Ce_{0.5}O_2$ solid solution. *Wuli Huaxue Xuebao/ Acta Phys. - Chim. Sin.* **2014**, *30*, 1941–1946, doi:10.3866/PKU.WHXB201408181.

294. He, S.; Jing, Q.; Yu, W.; Mo, L.; Lou, H.; Zheng, X. Combination of CO_2 reforming and partial oxidation of methane to produce syngas over Ni/SiO_2 prepared with nickel citrate precursor. *Catal. Today* **2010**, *148*, 130–133, doi:10.1016/j.cattod.2009.03.009.

295. Guo, P.F.; Jin, G.Q.; Guo, C.X.; Wang, Y.Y.; Tong, X.L.; Guo, X.Y. Effects of Yb_2O_3 promotor on the performance of Ni/SiC catalysts in CO_2 reforming of CH_4. *Ranliao Huaxue Xuebao/Journal Fuel Chem. Technol.* **2014**, *42*, 719–726, doi:10.1016/s1872-5813(14)60033-5.

296. Zhan, H.J.; Shi, X.Y.; Huang, X.; Zhao, N. Highly coke-resistant ordered mesoporous Ni/SiC with large surface areas in CO_2 reforming of CH_4. *Ranliao Huaxue Xuebao/Journal Fuel Chem. Technol.* **2019**, *47*, 942–948, doi:10.1016/s1872-5813(19)30039-8.

297. Clause, O.; Bonneviot, L.; Che, M. Effect of the preparation method on the thermal stability of silica-supported nickel oxide as studied by EXAFS and TPR techniques. *J. Catal.* **1992**, *138*, 195–205, doi:10.1016/0021-9517(92)90017-C.

298. Torres, W.; Pansare, S.S.; Goodwin, J.G. Hot gas removal of tars, ammonia, and hydrogen sulfide from biomass gasification gas. *Catal. Rev. - Sci. Eng.* **2007**, *49*, 407–456, doi:10.1080/01614940701375134.

299. Caballero, M.A.; Corella, J.; Aznar, M.P.; Gil, J. Biomass gasification with air in fluidized bed. Hot gas cleanup with selected commercial and full-size nickel-based catalysts. *Ind. Eng. Chem. Res.* **2000**, *39*, 1143–1154, doi:10.1021/ie990738t.

300. Corella, J.; Orío, A.; Toledo, J.M. Biomass gasification with air in a fluidized bed: Exhaustive tar elimination with commercial steam reforming catalysts. *Energy and Fuels* **1999**, *13*, 702–709, doi:10.1021/ef980221e.

301. Corella, J.; Aznar, M.P.; Gil, J.; Caballero, M.A. Biomass gasification in fluidized bed: Where to locate the dolomite to improve gasification? *Energy and Fuels* **1999**, *13*, 1122–1127, doi:10.1021/ef990019r.

302. Corella, J.; Toledo, J.M.; Padilla, R. Catalytic Hot Gas Cleaning with Monoliths in Biomass Gasification

in Fluidized Beds. 1. Their Effectiveness for Tar Elimination. *Ind. Eng. Chem. Res.* **2004**, *43*, 2433–2445, doi:10.1021/ie0307683.

303. Toledo, J.M.; Corella, J.; Molina, G. Catalytic hot gas cleaning with monoliths in biomass gasification in fluidized beds. 4. Performance of an advanced, second-generation, two-layers-based monolithic reactor. *Ind. Eng. Chem. Res.* **2006**, *45*, 1389–1396, doi:10.1021/ie051171l.

304. Furusawa, T.; Saito, K.; Kori, Y.; Miura, Y.; Sato, M.; Suzuki, N. Steam reforming of naphthalene/benzene with various types of Pt- and Ni-based catalysts for hydrogen production. *Fuel* **2013**, *103*, 111–121, doi:10.1016/j.fuel.2011.09.026.

305. Du, J.; Gao, J.; Gu, F.; Zhuang, J.; Lu, B.; Jia, L.; Xu, G.; Liu, Q.; Su, F. A strategy to regenerate coked and sintered Ni/Al_2O_3 catalyst for methanation reaction. *Int. J. Hydrogen Energy* **2018**, *43*, 20661–20670, doi:10.1016/j.ijhydene.2018.09.128.

306. Zhao, X.; Lu, G. Improving catalytic activity and stability by in-situ regeneration of Ni-based catalyst for hydrogen production from ethanol steam reforming via controlling of active species dispersion. *Int. J. Hydrogen Energy* **2016**, *41*, 13993–14002, doi:10.1016/j.ijhydene.2016.05.042.

307. Qingli, X.; Peng, F.; Wei, Q.; Kai, H.; Shanzhi, X.; Yongjie, Y. Catalyst deactivation and regeneration during CO_2 reforming of bio-oil. *Int. J. Hydrogen Energy* **2019**, *44*, 10277–10285, doi:10.1016/j.ijhydene.2019.02.156.

308. Bain, R.L.; Dayton, D.C.; Carpenter, D.L.; Czernik, S.R.; Feik, C.J.; French, R.J.; Magrini-Bair, K.A.; Phillips, S.D. Evaluation of catalyst deactivation during catalytic steam reforming of biomass-derived syngas. *Ind. Eng. Chem. Res.* **2005**, *44*, 7945–7956, doi:10.1021/ie050098w.

309. Zhang, C.; Yue, H.; Huang, Z.; Li, S.; Wu, G.; Ma, X.; Gong, J. Hydrogen production via steam reforming of ethanol on phyllosilicate- derived Ni/SiO_2: Enhanced metal-support interaction and catalytic stability. *ACS Sustain. Chem. Eng.* **2013**, *1*, 161–173, doi:10.1021/sc300081q.

310. Rapagnà, S.; Virginie, M.; Gallucci, K.; Courson, C.; Di Marcello, M.; Kiennemann, A.; Foscolo, P.U. Fe/olivine catalyst for biomass steam gasification: Preparation, characterization and testing at real process conditions. *Catal. Today* **2011**, *176*, 163–168, doi:10.1016/j.cattod.2010.11.098.

311. Ebnesajjad, S. Surface and Material Characterization Techniques. In *Surface Treatment of Materials for Adhesive Bonding*; Elsevier, 2014; pp. 39–75.

312. Inkson, B.J. Scanning electron microscopy (SEM) and transmission electron microscopy (TEM) for materials characterization. In *Materials Characterization Using Nondestructive Evaluation (NDE) Methods*; Elsevier: New York, 2016; pp. 17–43.

ANNEX

CHARACTERIZATION TECHNIQUES

A. Introduction

The main aim of the use of characterization techniques in the area of heterogeneous catalysis research is to well understand the physicochemical properties of the catalysts and, through them, elucidate the differences on the catalytic performances. Moreover, the obtained results could provide additional information to enhance catalytic systems for the future works.

In the present chapter, an overview of the theoretical principles of the experimental characterization techniques applied during this thesis are described. Besides, general description of the technique specifications, as used instruments and methods, for the study of the catalytic materials are also reported.

B. Nitrogen physisorption

Theoretical principle. The textural properties as specific surface area, porosity and pore shape and size distribution are important parameters to consider for a solid sample. These properties can be evaluated by nitrogen physisorption analysis. During this non-destructive analysis, a physisorbed amount of an inert compound over the surface is measured as a function of relative pressure (P/P_0), where P_0 is the saturation pressure. Subsequently, an isotherm characteristic of the surface area but also of the porous system is obtained. Generally, the pores have been grouped by their size as macropores ($\geq$ 50 nm), mesopores (2-50 nm) and micropores ($\leq$ 2 nm) in concordance with IUPAC.

Many kinds of adsorption isotherms related to a wide variety of porous solids have been reported in the literature. Despite this diversity, these isotherms can be classified into six categories according to the IUPAC (***Figure 1***)[287]. Thus, type I isotherm is characteristic of microporous materials; type II isotherm is widely observed for non-porous or microporous solid; type III isotherm is typical of materials with weak adsorbent/absorbate interactions; type IV isotherm is related to mesoporous samples, where the pore filling mechanism is led by the capillary condensation; type V isotherm is similar to type III in the low P/P_0, common for weak absorbent/absorbate interactions, whereas in high P/P_0 the molecular clustering is followed by pore filling leading to one or several step(s), typically observed for water adsorption on hydrophobic microporous and mesoporous adsorbents and, lastly, type VI isotherm is the less common and is mainly associated to absorption layer by layer over non porous materials. In the present work, type II isotherm related to non-porous materials and type IV isotherm linked to mesoporous materials have been evidenced.

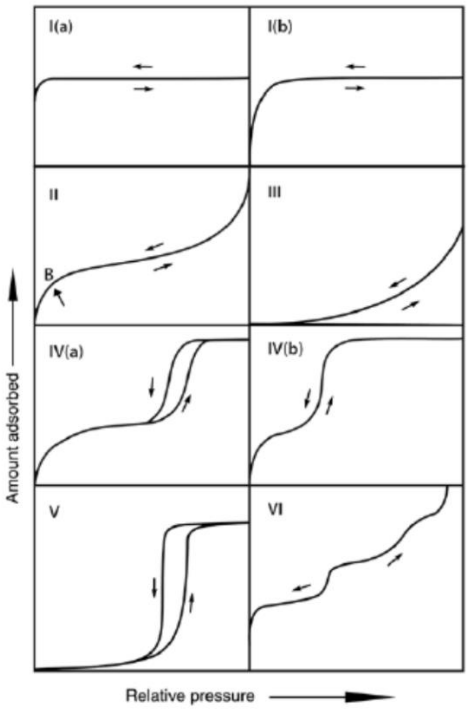

Figure 1. Classification of adsorption isotherms (IUPAC) [287]

In addition, a hysteresis loop in the adsorption-desorption isotherm, generally associated with the capillary condensation, can appear. This hysteresis, among other factors, could be influenced by the pore's structure/geometry. Similarly, based on their forms, the hysteresis loops have been classified by the IUPAC into six groups (*Figure 2*)[287]. The H1 type loop is observed for absorbents with narrow pore distribution, i.e., MCM-41 materials, or for spherical particles with homogeneous size and distribution; the H2 type is associated to samples with complex pore structures linked to blockage of pores; the H3 type is characteristic of non-rigid pores aggregates, i.e., some clay structures, but also could be encountered for macroporous materials which are not completely filled with pore condensate; the H4 type is typical of microporous solids as zeolites and micro-mesoporous carbons and, the H5 type, atypical, shows a particular shape related to pore structures including open and partially blocked mesopores.

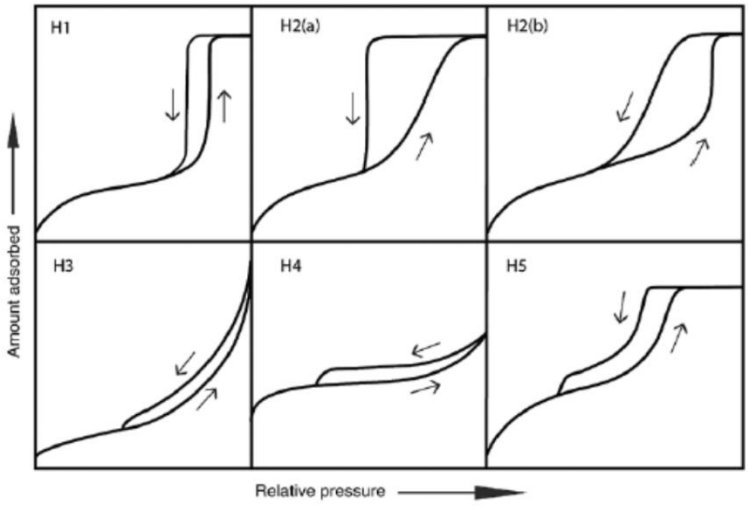

Figure 2. Classification of hysteresis loops (IUPAC)

Instrument and method. In this work, the textural properties were measured by nitrogen physisorption at 77 K through a relative pressure (P/P_0) range between 0 and 1 using the Brunauer-Emmet-Teller (BET) method with a Micromiretrics sorptometer Tri Star 3000. Prior to analysis, all samples were pre-treated through a degassing process under vacuum at 250 ºC for 3h in order to remove the physisorbed water and carbonates species present over the surface. An amount around 250 mg of sample were used for the analysis.

Type of information. The Brunauer-Emmet-Teller (BET) formula (Equation 1), associated to the adsorption isotherm for a relative pressure range between 0.05 and 0.30, was used for the treatment of the resulting data.

$$\frac{1}{\left[V_a\left(\frac{P_0}{P}-1\right)\right]} = \frac{C-1}{V_m C} \times \frac{P}{P_0} + \frac{1}{V_m C} \qquad \textit{Equation 1}$$

Where,

P (Pa): partial pressure of the adsorbate (N_2) in equilibrium with the surface at boiling temperature of nitrogen at atmospheric pressure

P_0 (Pa): saturation vapor pressure of the absorbate (N_2)

V_0 (mL): absorbed gas volume under standard conditions (273 K, P_{atm})

V_m ($mL \cdot g^{-1}$): adsorbed gas volume needed to generate a monolayer at the surface under standard conditions

C: adimensional constant linked to the adsorption enthalpy ratio of the first and the next layers (generally > 1).

Thereby, when $1/\left[V_a\left(\frac{P_0}{P}-1\right)\right]$ is plotted *versus* P_0/P, a linear graph with $(C-1)/V_mC$ as slope and $1/V_mC$ as intercept is obtained. From these values, V_m is determined as 1/(slope+intercept) whereas C is calculated as (slope/intercept) +1. Afterwards, the specific surface area SSA ($m^2 \cdot g^{-1}$) can be estimated through the following equation:

$$SSA = \frac{V_m N_a A}{V} \qquad \textit{Equation 2}$$

Where N_a is Avogadro's number ($6.023 \cdot 10^{23}$ mol^{-1}), A is the adsorption cross section of the absorbate (16,2 $Å^2$ in the case of nitrogen) and V is the molar volume of the adsorbate (N_2) in standard conditions of temperature and pressure (22 400 $cm^3 \cdot mol^{-1}$).

Additionally, the pore size distribution has been estimated using Barrett, Joyner, Halenda (BJH) method. This method determines the modifications in the thickness of absorbed layer from the decrease of relative pressure in the desorption branch. Considering each decrement as a result from the evaporation of the largest pores from the capillary condensate, as well as a reduction in thickness of the physisorbed layer. The calculation of the pore area and volume for each decrement is also possible through Kelvin's law. The addition of these values leads to a cumulative specific surface area and pore volume. The pore volume ($cm^3 \cdot g^{-1}$), V_p, is derived from the amount of adsorbed gas at P/P_0 close to the unity, by assuming that the gas adsorbed is fully condensed into the pores [287]. Thus, the pore volume can be calculated as follows:

$$V_p = \left(\frac{V_{P/P_0=0.99}}{V}\right) \cdot V_{liq} \qquad \textit{Equation 3}$$

Where $V_{P/P_0=0.99}$ is the gas adsorbed volume at relative pressure of 0.99, V is the molar volume of the adsorbate (N_2) in standard conditions of temperature and pressure (22 400 $cm^3 \cdot mol^{-1}$) and $V_{(liq)}$ is the liquid molar volume of the adsorbate (N_2).

As regard to the average pore diameter (D_p), the calculation is conducted by assuming pores with cylindrical geometry with a total cumulated length (L) at P/P_0 close to the unity. Therefore, the corresponding pore volume could be defined as:

$$V_p = \frac{\pi}{4} \cdot D_p^2 \cdot L \qquad \textit{Equation 4}$$

Considering only the lateral surface of the pores and assuming that it is correspond to the BET specific surface area (SSA), i.e., $SSA = \pi \cdot D \cdot L$, the average pore diameter can be estimated using the following equation:

$$D = \frac{V_p}{4 \cdot SSA} \qquad \textit{Equation 5}$$

C. X-ray Diffraction (XRD)

Theoretical principle. X-ray diffraction is a non-destructive technique based on the constructive interference of monochromatic X-rays diffracted by the planes in a crystalline sample. Taking into account one line of equidistant atoms and the Bragg's law (*Equation 6*), the angle between the incident X-ray beam and the sample is equal to the angle between the diffracted beam and the sample. Given a second line of atoms, the incident beam would be similarly diffracted and the constructive interaction between both diffracted beams leads to its maximum intensity. Thereby, a diffraction peak, related to a specific reticular plane family, is obtained when the Bragg's law is satisfied. This law links the wavelength of radiation (λ) to the demi-diffraction angle (θ) and the lattice spacing (d_{hkl}) between two reticular planes hkl in the sample. These parameters are linked as expressed by Equation 6.

$$n\lambda = 2d_{hkl}sin\theta \qquad \textit{Equation 6}$$

where n is an integer linked to the order of diffraction, and it is often the unity.

Consequently, all diffraction directions of the lattice should be detected by scanning it through a range of 2θ angle. The resulted curve, called diffractogram, represents the intensity versus the diffracted angle, 2θ. ***Figure 3*** shows a general scheme in order to better explain the fundamental principle.

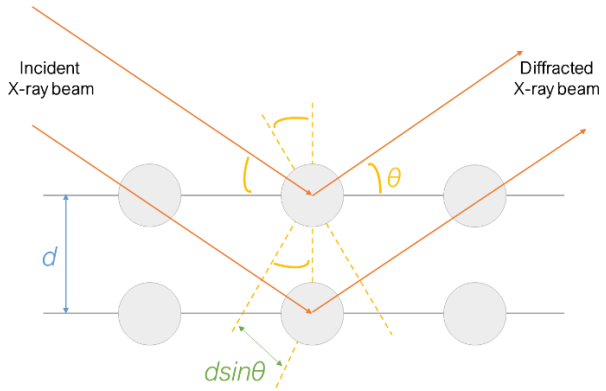

Figure 3. Theoretical principle of X-ray diffraction

The composition and crystalline structure of the studied materials could be determined comparing the diffraction peaks position and their relative intensities between the obtained diffractogram and the database. In this work, the crystalline phases have been

identified using files from International Center for Diffraction Data (ICDD), ex-JCPDS (Joint Committee on Powder Diffraction Standards).

Instrument and method. The samples were ground and, afterwards, placed over a glass plate as a support. The analysis were carried out on a Bruker D8 Advance diffractometer with LynxEye detector side and Ni filtered Cu Kα radiation (λ = 1.5418 Å). In this work, three different catalytic support were investigated: two Ce-based fluorite and La-based perovskite. Therefore, the diffractograms were recorded using a step size of 0.050º and step time of 0.16 s over a 2θ range of 20-110º and 20-85º for Ce-based fluorites and La-based perovskite, respectively.

Type of information. Besides the composition and crystalline structure of the materials, the lattice parameter as well as crystalline particle size can be also determined through this technique. A shift of the diffractograms through 2θ angle due to experimental measurement (low ammount of sample, sample not well placed…) could interfere in these calculations. Then, an internal standard (KBr) was used for all samples in order to avoid possible errors. In this work, the lattice parameter of Ce-based fluorites, face centered cubic structure, was calculated using the Miller index hkl of the corresponding reticular planes through the following equation:

$$a_{cubic} = d_{hkl}\sqrt{h^2 + k^2 + l^2} \qquad \textit{Equation 7}$$

Considering that the La-based perovskite shows a orthorhombic structure, a lattice parameter related to an elemental perovskite into a cubic system, called reduced lattice parameter, was estimated. Then, this reduced parameter was determined by the cube root of the normilized perovskite cell volumes (V/z) being $z = 4$ for orthorhombic systems (Equation 8).

$$a_{reduced} = \sqrt[3]{V/z} \qquad \textit{Equation 8}$$

Thereby, the reticular parameters a, b, c were calculated using the Miller index of three different reticular planes (Equation 9).Then, the cell volume related to a orthorhombic system has been attained ($V = abc$).

$$\frac{1}{{d_{hkl}}^2} = \frac{h^2}{a^2} + \frac{k^2}{b^2} + \frac{l^2}{c^2} \qquad \textit{Equation 9}$$

In addition, the crystalline particle size (d) has been also determined for all the samples. This parameter is related to the width at half height of an X-ray diffraction peak by means of Debye-Scherrer formula:

$$d = \frac{k\lambda}{\beta\, cos\theta} \qquad \textit{Equation10}$$

Where k is the adimensional factor used for spherical particles (k = 0.9), λ is wavenumber of the electromagnetic beam ($\lambda_{K\alpha(Cu)}$=1.5418 Å) and β is the width at half height of the diffraction peak in radian.

D. Temperature Programmed Reduction (TPR)

Theoretical principle. Valuable information as the different reducible species present in the materials, their resulting reducibility and the reduction temperature of these oxidized species can be well defined by this technique. As well, the supported phases - supports interaction can be also evidenced. A constant gas flow of diluted hydrogen in argon cross the sample located in a quartz U-reactor. The reactor is heated from room temperature until the desired temperature at a determined heating ramp. The consumption of hydrogen is detected by a thermal conductivity detector (TCD) in function of temperature and/or running time. A trap cooled at -10 ºC placed before the TCD was used in order to condense the water produces during the reduction reactions.

Instrument and methods. In the present work, the temperature programmed reduction were carried out on a Micromiretics AutoChem II. An ammount around 50 mg of powdered sample was used for all the measurements. In the case of the structured catalysts, the extrudates were crushed and the suitable amount of total extrudates to introduce around 50 mg of deposited catalysts was used. Both, powdered and structured samples were heated from room temperature to 950 ºC at a heating ramp of 15 ºC·min^{-1} under 10 mol% H_2/Ar atmosphere using a total gas flow of 50 mL·min^{-1}. The obtained TPR profile were normalized to the mass of catalyst in order to easily compare all the materials. All TPR profiles were plotted as normalized TCD signal (arbitrary units (a.u.)/$g_{catalyst}$) as a function of temperature.

Type of information. Generally, a normalized TCD signal (a.u /$g_{catalyst}$) shows different peaks as function of temperature. Each peak can be related to one or several reduction process and is located at determined temperature, called reduction temperature. The reduction temperature provides useful information about the interaction between supported metals and support for a studied material. Thereby, the stronger is the metal-support interaction the higher is the reduction temperature. Moreover, the reducibility of the sample can be defined as:

$$\%\, Reducibility = \frac{Experimental\ H_2\ consumption\ (mol)}{Theoretical\ H_2\ consumption\ (mol)} \qquad \textit{Equation 11}$$

The experimental consumption is obtained by integration of the TPR curve, while the theoretical one is the amount of H_2 needed to reduce all the reducing species present in the material.

In the present work, the reducibility of the synthesized materials has been reported as "support reducibility" and its calculation is based on the assumption of the complete reduction of the nominal supported metal content (10 %wt Ni^0 or 1 %wt Ru^0 – 10 %wt Ni^0) and the rest of consumed hydrogen is associated to the reduction of the reducible species present in the support in its oxidized form.

E. X-ray Photoelectron Spectroscopy (XPS)

Theoretical principle. The X-ray photoelectron spectroscopy is a surface sensitive spectroscopic technique based on the photoelectric effect. The XPS spectra are obtained by measuring the kinetic energy and number of emitted electrons from the upper top 0 to 10 nm of the material surface when the sample is irradiated with an X-ray beam. Then, any electron with lower binding energy than hv is released, becoming a photoelectron. Thus, its kinetic energy is the subtraction between hv and its initial binding energy and it is characteristic of the atomic energy levels of the different elements present in the sample.

Instrument and method. The XPS spectra were acquired by an ultra-high vacuum spectrometer with a VSW Class WA as electrostatic hemispherical analyser and a double anode (Al K_α, 1486.6 eV) as X-ray source. The powdered samples were dispersed on a carbon tape using a sample holder with dimensions of 0.8 x 0.8 cm^2. Prior the analysis, the samples underwent in ultrahigh vacuum overnight to reach a pressure of 10^{-9} mbar. The binding energy values were corrected from the charge effects using the C(1s) peak at 284.6 eV as reference (carbon contamination). The different peak zones have been interpreted using a Shirley background and the surface atomic composition has been calculated by using peaks areas corrected with the correlated relative sensitivity factor for each element.

Type of information. Valuable information about the surface of the materials since the binding energy of the resulting photoelectrons depend on the chemical environment of the atom. Therefore, elemental surface composition, coordination and the chemical oxidation state of the different components of the material surface can be obtained by this technique.

F. H_2 chemisorption and Temperature Programmed Desorption (H_2-TPD)

Theoretical principle. The exposed metallic surface of the active phase as result of a defined pre-treatment under reducing atmosphere is other parameter to study in order to understand the catalytic activity of a given material. Firstly, the material is subjected to a certain reduction pre-treatment, usually prior defined through TPR analysis. Afterwards, the samples are cooled to a define temperature under inert atmosphere and then the surface is saturated under determined adsorption conditions over the metal phase by means of probe molecule such as hydrogen. This surface saturation involved chemisorption phenomena and could be carried out either by passing a hydrogen flow, or by injection of hydrogen pulses using a loop with a well-known volume, which has the advantage to make more accurate the quantification of the amount chemisorbed. The hydrogen pulses are recorded using a TCD detector and the outlet hydrogen can be estimated by their corresponding areas. Chemisorbed hydrogen can then be evaluated by the difference between injected and outlet amounts. A flow of inert gas is then used to remove weakly adsorbed hydrogen and the sample is heated under inert gas flow employing a constant heating ramp. The desorbed hydrogen is also analysed through a TCD detector leading to a TPD curve. The same amount of hydrogen should be found through the total desorbed hydrogen calculated by integration of the TPD curve and the chemisorbed hydrogen from the integration of pulses. Thus, the metallic surface generated during a given reduction pre-treatment can be calculated from the resulting amount of chemisorbed/desorbed hydrogen (Equation 12).

Instrument and method. Measurements were also performed on a Micromiretics AutoChem II. An amount of around 100 mg of powdered catalyst loaded in a quartz U-reactor was used and the pre-reduction temperature was the same than the one employed for the pre-treatment applied prior the catalytic reaction. Similar to H_2-TPR analysis, the structured catalysts were crushed and a total amount of extrudate corresponding to a deposited catalysts mass approximately 100 mg was used. All samples were pre-reduced under a mixture 10 mol% H_2/Ar with a total gas flow of 50 mL·min^{-1} at 600 ºC for 2 h using a heating ramp of 2 ºC·min^{-1}. In order to remove the possible physisorbed hydrogen, the sample was subjected to Ar gas flow (50 mL·min^{-1}) for 90 min at the same temperature. The temperature was decreased to 50 ºC and, then, 15 pulses of 10 mol% H_2/Ar at atmospheric pressure were injected employing a loop of 50 µL and remaining an Ar gas flow of 50 mL·min^{-1} as a carrier gas. Lastly, the system was kept under Ar flow for 30 min at 50 ºC to remove the hydrogen weakly adsorbed and well-define the baseline before the desorption

accomplished up to 900 ºC under Ar with a heating ramp of 10 ºC·min^{-1}. In addition, a blank of the supports were performed to quantify the desorbed hydrogen from their surfaces and, thereby, prevent errors in the calculation of the metal surface.

For samples pre-treated under syngas atmosphere, prior the H_2-chemisorption pulse and H_2-TPD, the samples were exposed to a mixture of 10 mol % H_2/Ar with a total gas flow of 50 Nml·min^{-1} at 300 ºC for 30 min using a heating ramp of 5 ºC·min^{-1}. Afterwards, same protocol as for the samples reduced under H_2/Ar mixture for the H_2-chimisorption and H_2-TPD has been followed.

In the present work, TPD curves were normalized to the mass of catalyst in order to easily compare all the materials. All TPD profiles are plotted as normalized TCD signal as a function of the temperature.

Type of information. Both, hydrogen chemisorption and desorption programed temperature of hydrogen, can be used for the estimation of the metal surface exhibited at catalyst surface, either nickel or ruthenium, by Equation 12.

$$S_{metallic} = \nu \cdot n_{H_2} \cdot N_a \cdot a_m \qquad \textit{Equation 12}$$

Where, ν is the chemisorption stoichiometry, that is the number of chemisorbed H per metallic atom for one H_2 molecule. This factor is 2 for the studied active phases since $H_{adsorbed}$/Ni is 1:1. n_{H_2} is the number of moles of chemisorbed hydrogen on the metallic nickel or ·ruthenium surface, calculated either from TPD curve or hydrogen pulses; N_a is Avogadro's number (mol^{-1}); and, a_m is exposed surface of the corresponding metallic atom, determined by means of the reticular planes (111), (100) and (110) of a face-centered cubic structure (6.51 Å^2 for Ni)

Additionally, different Ni-surface chemical bonds and, thus, different Ni environment can be also deduced from the desorption peaks evidenced at different temperatures in the TPD curve.

G. Scanning Electron Microscopy (SEM) and microanalysis by Energy Dispersive X-Ray Spectroscopy (EDXS)

Theoretical principle. The scanning electron microscopy is a high-resolution technique based on the electrons-sample interaction to provide morphological information of the sample surface. The sample is irradiated by an electron beam in a vacuum generating secondary electrons, backscattered electrons, characteristic X-rays and other signals (Figure 4). Mainly secondary and backscattered electrons signals provide the image of the

surface. Secondary electrons (SE) are produced near the sample surface and the resulting image upon detecting these electron replicates the topographical and morphological structure of surface sample. Meanwhile, the backscattered electrons (BSE) are those displayed upon hitting the atoms within the sample, and the number of these electrons is linked to the composition of sample (atomic number, crystal orientation…). Therefore, BSE image shows the surface composition of the sample. Additionally, the specific wavelengths of X-ray emissions, characteristic of the atomic structure of the elements, can be analysed by an energy dispersive detector. Then, the elements are identified, resulting in the elemental surface composition of the specimen surface. This procedure is well-known as Energy Dispersive X-ray Spectroscopy (EDXS) [311].

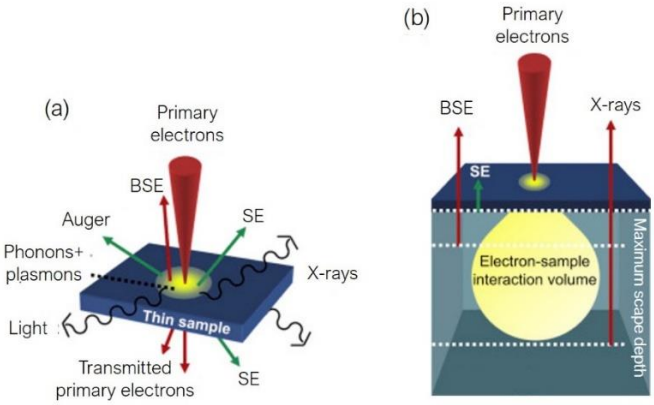

Figure 4. Useful signals produced by electron-sample interactions [312]

Instrument and method. In this work, SEM analysis was performed on a Zeiss GeminiSEM 500 microscope with an electron source based on FEG Schottky. It is equipped with five different detectors for imaging and an X-ray detector for elementary microanalysis by EDXS. All samples have been deposited on a carbon layer in order to avoid charge effects generated by electron accumulation at the surface.

Type of information. SEM images caused by the analysis of secondary electrons allows the study of the topography and morphology of the surface, whereas the analysis of backscattered electrons leads to images in which the contrast is directly linked to the chemical composition at the surface. In addition, the X-ray spectra generated by EDXS shows the relative intensity as function of the binding energy. Each X-ray emission is related to an electronic transition of a specific element and the characteristic X-ray obtained leads to the identification of the elements present at the surface.

H. Thermogravimetric analysis (TGA)

Theoretical principle. The thermogravimetric analysis is a destructive and quantitative technique used to study the physical and/or chemical changes of a sample when it is heated under a determined atmosphere and temperature ramp. Important information such as thermal stability, oxidation process, chemical composition can be deduced by this technique. Generally, a sample pan supported by a micro-balance is heated under defined atmosphere into an oven and the variation of its mass is monitored during the experiment leading to a thermogram as a result. A thermogram is a graph in which the sample mass change is plotted versus the temperature or time.

Instrument and method. In present work, the TG analyses were carried out on a Q5000IR from TA Instruments. An amount of around 3 mg of tested sample was employed. The analysis was executed up to 900 ºC with a heating ramp of 10 ºC·min^{-1} under synthetic air using a total gas flow of 25 NmL·min^{-1}.

Type of information. The amount of deposited carbon over the catalyst surface generated during tar reforming reaction has been determined by the evaluation of the loss of mass of the spent catalysts. Likewise, the total number of moles deposited carbon was defined as:

$$mol_{deposited\ coke} = \frac{m_{coke,TGA}\,(g)\cdot m_{cata,reactor}(g)}{m_{cata,TGA}\,(g)\cdot At.wt\ \ (g\cdot mol^{-1})} \qquad \textit{Equation 13}$$

Dolores JURADO FUENTES

Etude de catalyseurs structurés pour le post-traitement du gaz de synthèse issu de la gazéification de bois pressé

Résumé

La gazéification semble être une technologie prometteuse de conversion de la biomasse en raison de la valeur énergétique du gaz produit, connu sous le nom de gaz de synthèse. Néanmoins, d'importantes quantités d'hydrocarbures lourds indésirables, définis comme goudrons, sont généralement produites. Ces goudrons peuvent causer plusieurs problèmes opérationnels en raison de leur condensation dans différentes parties du procédé en aval (turbines, tubes...). De plus, ils peuvent limiter le pouvoir énergétique du gaz de synthèse produit. C'est pourquoi l'intégration d'une étape de nettoyage de gaz dans le procédé de gazéification afin d'éliminer ces goudrons est visée. Dans le cadre des travaux actuels, le développement de systèmes catalytiques pour le reformage des goudrons et la génération d'un gaz de synthèse de haute qualité a été réalisé. Ainsi, la synthèse et la caractérisation de six catalyseurs à base de nickel sur support d'oxydes mixtes à haute conductivité de l'oxygène (structure fluorite à base de cérine et pérovskites à base de lanthane) ont été réalisées. Par la suite, l'activité catalytique en reformage du goudron a été évaluée à l'échelle du laboratoire en utilisant le phénol et le toluène comme molécules modèles des goudrons. La structuration catalytique sur des extrudats à base de SiC a été optimisée à l'échelle de quelques extrudés avant d'être réalisée à grande échelle (lots d'extrudats de 1L). Finalement, les catalyseurs structurés préparés à grande échelle ont été testés dans des conditions réelles dans une unités pilote de gazéification de la biomasse.

Mots clés : gazéification de la biomasse, reformage à la vapeur, goudrons, catalyseurs à base de Ni, structuration catalytique

Abstract

Biomass gasification seems to be a promising biomass conversion technology due to the valuable product gas obtained, well-known as syngas. Nevertheless, a mixture of high hydrocarbons, defined as tars, are produced as by-products. This mixture can cause several operational problems due to its condensation in different parts of the industrial process (turbines, tubes…) and, moreover, it can limit the downstream use of the final product gas. Thereby, the integration of a cleaning gas step in the gasification process to remove these tars are aimed. In the present work, the development of catalytic systems to reform tars and generate a high-quality syngas has been carried out. Thus, the synthesis and characterization of six nickel-based catalysts supported over mixed oxides with high oxygen conductivity, based on doped-ceria fluorites and La-based perovskite, were performed. Afterwards, the catalytic activity in tar reforming was evaluated at laboratory scale using phenol and toluene as tar model molecules. The catalytic structuration over SiC based extrudates was optimized and subsequently, its structuration at large scale (batch extrudates of 1L) was conducted. Eventually, the structured catalysts prepared at large scale were tested under real conditions at biomass gasification pilot plant scale.

Keywords: biomass gasification, steam reforming, tars, Ni-based catalysts, catalytic structuration